Transactions of the ASME®

Technical Editor
ARTHUR J. WENNERSTROM
Senior Associate Technical Editor
G. K. SEROVY
Associate Technical Editors
Advanced Energy Systems
M. J. MORAN
Environmental Control
H. E. HESKETH
Fuels and Combustion Technologies
R. E. BARRETT
Gas Turbine
S. KUO
Internal Combustion Engine
K. J. SPRINGER
Nuclear Engineering
S. M. CHO
Power
R. W. PORTER

BOARD ON COMMUNICATIONS
Chairman and Vice-President
K. N. REID, JR.

Members-at-Large
J. T. COKONIS
M. FRANKE
M. KUTZ
F. LANDIS
J. R. LLOYD
T. C. MIN
R. E. NICKELL
R. E. REDER
R. ROCKE
F. W. SCHMIDT
W. O. WINER

President, R. ROSENBERG
Executive Director,
D. L. BELDEN
Treasurer, ROBERT A. BENNETT

PUBLISHING STAFF
Mng. Dir., Publ., JOS. SANSONE
Managing Editor,
CORNELIA MONAHAN
Sr. Production Editor,
VALERIE WINTERS
Editorial Prod. Asst.,
MARISOL ANDINO

Transactions of the ASME, Journal of Turbomachinery (ISSN 0889-504X) is published quarterly (Jan., Apr., July, Oct.) for $95 per year by The American Society of Mechanical Engineers, 345 East 47th Street, New York, NY 10017. Second-class postage paid at New York, NY and additional mailing offices. POSTMASTER: Send address change to The Journal of Turbomachinery, c/o The AMERICAN SOCIETY OF MECHANICAL ENGINEERS, 22 Law Drive, Box 2300, Fairfield, NJ 07007-2300."

CHANGES OF ADDRESS must be received at Society headquarters seven weeks before they are to be effective. Please send old label and new address.

PRICES: To members, $27.00, annually; to nonmembers, $95.00. Add $12.00 for postage to countries outside the United States and Canada.

INDEXED by Applied Mechanics Reviews and Engineering Information, Inc.

Journal of Turbomachinery

Published Quarterly by The American Society of Mechanical Engineers

VOLUME 110 • NUMBER 2 • APRIL 1988

TECHNICAL PAPERS

DISCUSSION

ANNOUNCEMENTS

The Inertial Deposition of Fog Droplets on Steam Turbine Blades

J. B. Young
Whittle Laboratory,
University of Cambridge,
Cambridge, United Kingdom

K. K. Yau
GEC Turbine Generators Ltd.,
Urmston, Manchester, United Kingdom

A theoretical approach for calculating the rate of deposition of fog droplets on steam turbine blades by inertial impaction is described. Deposition rates are computed by tracking a number of droplet path lines through a specified blade-to-blade vapor flowfield and identifying the limiting trajectories that just intersect the blade surface. A new technique for performing the calculations efficiently has been developed whereby the mathematical stiffness of the governing equations is removed, thus allowing the numerical integration to proceed stably with comparatively large time increments. For high accuracy, the vapor flowfield is specified by a quasi-three-dimensional flow calculation involving both meridional and blade-to-blade plane calculations. Results are presented for two representative "test cases," namely the final stage blading of the low-pressure cylinder of a 500 MW turbine and a typical stage in a high-pressure wet steam turbine. The effect on the deposition rate of fog droplet size and blade profile geometry is investigated for both on- and off-design flowfields. Comparisons are made with the predictions of a simplified theory for inertial deposition and the effect of blade rotation in flows with high pitch angles is discussed.

1 Introduction

Water in steam turbines exists in two fundamentally different forms, namely fog droplets and coarse water (Moore and Sieverding, 1976). The fog consists of very fine spherical droplets (0.03 μm $< r <$ 1 μm) formed in the core of the flow by spontaneous nucleation in the vapor phase. The coarse water consists of considerably larger droplets ($r >$ 20 μm), but contains a much smaller proportion by mass of the total liquid present. Most of the coarse water originates from the deposition of the fog onto the blading, the subsequent coalescence into films and rivulets, and the detachment of these rivulets at the trailing edges in the form of large droplets.

Both inertial impaction and turbulent diffusional mechanisms are responsible for the transportation of the fog to the blade surfaces. Deposition by inertial impaction is a laminar flow phenomenon caused by the inability of the droplets to follow exactly the curved vapor streamlines within the blade passage. Diffusional deposition, on the other hand, is the process by which droplets, entrained in the (usually) turbulent boundary layers, migrate to the blade surfaces under the influence of random fluctuations in the flow. This paper deals with the calculation of deposition by inertial impaction only. The calculation of deposition by turbulent diffusion has been discussed by Yau and Young (1987).

Few papers in the literature are directly concerned with fog droplet deposition in steam turbines. Two notable exceptions, however, are the work of Gyarmathy (1962) and a comprehensive study by Crane (1973). In recent years, the related topic of solid particle erosion in gas turbines has spawned a number of papers, but none deal with the rather special problems specific to steam turbines only.

The rate of deposition is a strong function of the fog droplet radius, and the paucity of information in the literature is largely a reflection of the difficulty of measuring fog droplet size in steam turbines. In recent years, however, a major breakthrough in experimental wet steam research has been made by the introduction of optical probes capable of measuring the size and number of fog droplets present within the turbine (Walters and Skingley, 1979). Computational methods for calculating the droplet size due to spontaneous nucleation in the flow are also appearing (Moheban and Young, 1985). It would therefore appear to be an opportune time for a reconsideration of the mechanics of deposition and the application of modern computational techniques to its calculation.

2 The Calculation of Deposition by Inertial Impaction

2.1 Equation of Motion of a Droplet. Fog droplets are assumed to be spherical particles moving in a continuous vapor flowfield and unaffected by the proximity of other droplets. The effects of condensation and evaporation are neglected and the mass and radius of a droplet are assumed to be constant. Because the vapor density is always much less than the liquid density, the only nonnegligible contribution to the force on a droplet is that due to the steady-state viscous drag. The equation of motion can thus be written

$$\mathbf{D} = \frac{4}{3}\,\pi\, r^3 \rho_l \frac{d\mathbf{V}_l}{dt_l} \tag{1}$$

where d/dt_l represents differentiation with respect to time following a droplet, i.e., $(\partial/\partial t + \mathbf{V}_l \cdot \nabla)$.

Contributed by the Power Division for publication in the JOURNAL OF TURBOMACHINERY. Manuscript received by the Power Division August 14, 1987.

The form of the drag force **D** depends on the flow regime. Gyarmathy (1962) proposed a composite formula

$$\mathbf{D}=\frac{6\pi\, r\mu_g(\mathbf{V}_g-\mathbf{V}_l)}{[\phi(\mathrm{Re})+2.7\ \mathrm{Kn}]} \tag{2}$$

where ϕ (Re) is a function of the slip Reynolds number

$$\mathrm{Re}=\frac{2r\rho_g|\mathbf{V}_g-\mathbf{V}_l|}{\mu_g} \tag{3}$$

and is given by the empirical formula

$$\phi(\mathrm{Re})=[1+0.197\ \mathrm{Re}^{0.63}+0.00026\ \mathrm{Re}^{1.38}]^{-1} \tag{4}$$

In the continuum regime (Kn $\ll$ 1) when Re $\ll$ 1, equation (2) reduces to the Stokes drag law, while deviations from this behavior at higher values of Re are accounted for by the introduction of the factor ϕ (Re) (which is accurate for Re $<$ 5 $\times$ 10^4). In the free molecular regime (Kn $\gg$ 1), equation (2) reduces to the expression given by kinetic theory.

Equation (1) can alternatively be written

$$\frac{d\mathbf{V}_l}{dt_l}=\frac{\mathbf{V}_g-\mathbf{V}_l}{\tau} \tag{5}$$

where the *inertial relaxation time* τ is defined by

$$\tau=\frac{2r^2\rho_l}{9\mu_g}[\phi(\mathrm{Re})+2.7\ \mathrm{Kn}] \tag{6}$$

2.2 Analytical Integration of the Equation of Motion. For any specified vapor flowfield $\mathbf{V}_g$, equation (5) can, in principle, be integrated numerically to give the trajectory of any droplet introduced into the flow. Problems arise, however, because the inertial relaxation times of fog droplets are often very small compared with characteristic flow transit times. Equation (5) then becomes mathematically stiff and integration increments Δt_l of the same order of magnitude as τ are required to ensure numerical stability.

One possibility for overcoming this problem is to integrate equation (5) analytically over periods that may be long compared with the inertial relaxation time, but are short inasmuch as the flow properties can be approximated by suitable average values, which are assumed to remain constant over the increment. To this end equation (5) is rewritten in terms of the slip velocity

$$\Delta\mathbf{V}=\mathbf{V}_g-\mathbf{V}_l \tag{7}$$

thus giving

$$\frac{d}{dt_l}(\Delta\mathbf{V})+\frac{\Delta\mathbf{V}}{\tau}=\frac{d\mathbf{V}_g}{dt_l} \tag{8}$$

Equation (8) can be integrated over a time step Δt_l, the only restriction being that $(d\mathbf{V}_g/dt_l)$ should remain approximately constant over this increment. Assuming this is so,

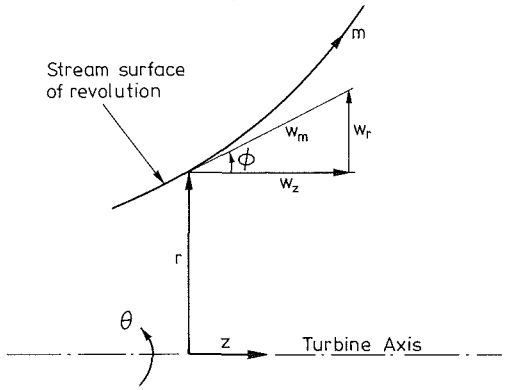

Fig. 1 Meridional plane representation of the coordinate system

$$\Delta\mathbf{V}_2=\Delta\mathbf{V}_1e^{-(\Delta t_l/\tau)}+\tau\frac{d\mathbf{V}_g}{dt_l}[1-e^{-(\Delta t_l/\tau)}] \tag{9}$$

where the subscripts 1 and 2 represent conditions at the start and end of the increment, respectively.

2.3 Choice of Coordinate System. When calculating deposition rates on moving blades, it is convenient to work in a frame of reference rotating with the same angular velocity Ω as the turbine. The vapor and liquid velocities relative to the blades, $\mathbf{W}_g$ and $\mathbf{W}_l$, are therefore given by

$$\mathbf{W}_g=\mathbf{V}_g-(\Omega\times\mathbf{R})$$
$$\mathbf{W}_l=\mathbf{V}_l-(\Omega\times\mathbf{R}) \tag{10}$$

where **R** is the position vector measured from the origin of the coordinate system.

For turbomachinery calculations, it is convenient to adopt a cylindrical polar coordinate system (r, θ, z) as shown in Fig. 1. Writing the components of velocity in the rotating frame as (W_r, W_θ, W_z), the three components of the slip velocity are given by

$$\Delta W_r=W_{gr}-W_{lr}$$
$$\Delta W_\theta=W_{g\theta}-W_{l\theta}$$
$$\Delta W_z=W_{gz}-W_{lz} \tag{11}$$

The three scalar equations of motion corresponding to equation (9) can now be obtained by transforming to the rotating coordinate system. The manipulation is standard and the result is

$$\Delta W_{r2}=\Delta W_{r1}\beta+\tau(1-\beta)\left[\frac{dW_{gr}}{dt_l}-\frac{V_{l\theta}^2}{r}\right]$$

Nomenclature

c = axial or meridional chord length
$\mathbf{D}^*$ = drag force on a droplet
F_I = fractional inertial deposition rate
f_I = inertial deposition distribution function
Kn = Knudsen number = $l_g/2r$
l_g = mean free path of a gas molecule
P = blade pitch
R = leading edge radius
$\mathbf{R}$ = position vector
Re = slip Reynolds number
r = droplet radius, streamsurface radius
St = Stokes number = $\tau W_g/c$
t = time
$\mathbf{V}$ = absolute flow velocity
$\Delta\mathbf{V}$ = slip velocitiy
$\mathbf{W}$ = relative flow velocity
β_0 = relative inlet flow angle
μ = dynamic viscosity
ρ = density
τ = inertial relaxation time
ϕ = pitch angle
Ω = turbine rotational speed

Subscripts

g = vapor phase
I = inertial
l = liquid phase
m = meridional coordinate
r = radial coordinate
z = axial coordinate
θ = circumferential coordinate

*Symbols in bold-face type denote vector quantities.

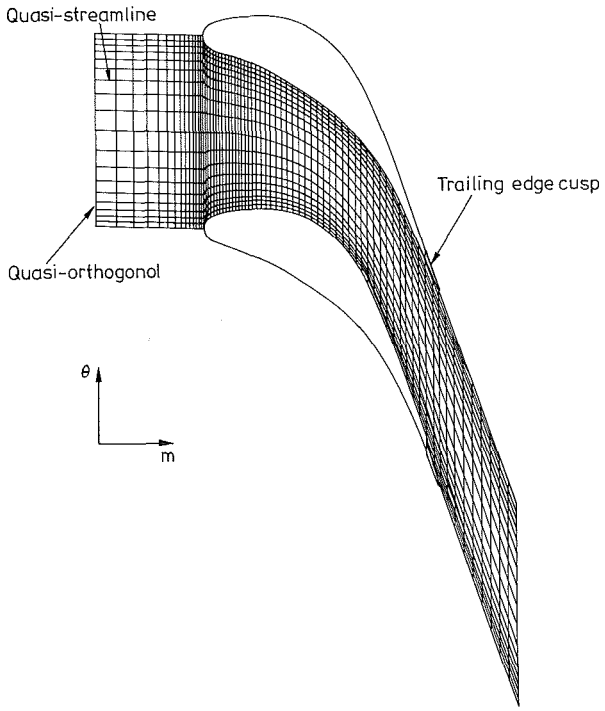

Fig. 2 Geometric details of the computational grid

$$\Delta W_{\theta 2} = \Delta W_{\theta 1}\beta + \tau(1-\beta)\left[\frac{dW_{g\theta}}{dt_l} + \frac{W_{lr}W_{l\theta}}{r} + 2\Omega W_{lr}\right] \quad (12)$$

$$\Delta W_{z2} = \Delta W_{z1}\beta + \tau(1-\beta)\left[\frac{dW_{gz}}{dt_l}\right]$$

where

$$\beta = \exp(-\Delta t_l/\tau)$$

The terms in square brackets are understood to be average values for the increment Δt_l.

Although procedures are available for predicting three-dimensional inviscid flow through turbine blade passages, all the calculations presented in this report are two-dimensional in nature and assume that the flow streamsurfaces are surfaces of revolution with respect to the turbine axis. It is further assumed that fog droplet streamsurfaces are identical to vapor streamsurfaces.

Transforming equations (12) to (m, θ) coordinates, where m is the distance measured along the streamsurface in the meridional plane (see Fig. 2), results in

$$\Delta W_{m2} = \Delta W_{m1}\beta + \tau(1-\beta)\left[\frac{dW_{gm}}{dt_l} - \frac{V_{l\theta}^2}{r}\sin\phi\right]$$

$$\Delta W_{\theta 2} = \Delta W_{\theta 1}\beta + \tau(1-\beta)\left[\frac{dW_{g\theta}}{dt_l} + W_{lm}\sin\phi\left(\frac{W_{l\theta}}{r} + 2\Omega\right)\right] \quad (13)$$

where ϕ is the pitch angle of the streamsurface in the meridional plane and

$$\Delta W_m = W_{gm} - W_{lm} \quad (14)$$

Equations (13) are the required form describing the variation of slip velocity of a specific droplet along its trajectory path. By setting $\Omega = 0$, they become applicable to the flow through stationary blade passages. By setting $\phi = 0$, they reduce to the equations for plane two-dimensional flow.

2.4 Numerical Solution Procedure. Inertial deposition rates were calculated by tracking the path lines of a large number of droplets introduced into the flowfield upstream of the blade row and identifying the limiting trajectories intersecting the blade surfaces. The vapor flowfield was specified by an inviscid computational procedure, which assumed the steam to be in thermal and velocity equilibrium at all times.

For high-pressure turbines with small casing flare angles, it was sufficiently accurate to adopt a plane two-dimensional calculation procedure. Such flowfields were computed using the inviscid transonic blade-to-blade time-marching program described by Denton (1983). In low-pressure turbines with large casing flare angles, a quasi-three-dimensional approach was adopted. This involved calculating the position of the streamsurfaces in the meridional plane using the axisymmetric streamline curvature throughflow program described by Denton (1978) and then obtaining the blade-to-blade velocity field using a version of the time-marching program that included the effects of varying streamsurface radius and streamtube divergence.

However the flowfield was calculated, the final result was a set of velocity components (W_{gm}, $W_{g\theta}$) specified at each node of a grid similar to that shown in Fig. 2. Neither the spacing in the axial nor the pitchwise direction was required to be uniform and, indeed, for accurate trajectory calculations it was necessary to employ a very fine grid close to the blade surface, especially in the vicinity of the leading edge. (In passing, it should be noted that, in contrast to many methods, the flow calculation procedure could deal with quite extensive regions of reversed flow caused by movement of the stagnation point away from the nose at off-design flow incidence angles.)

The droplet trajectory calculations were initiated by specifying a starting position and velocity of the droplet (normally half an axial chord length upstream of the blade row and zero velocity slip). A suitable time increment Δt_l was adopted and the droplet trajectory computed by successive application of equations (14). This was achieved using a second-order accurate predictor-corrector algorithm described in detail by Yau (1986).

As the droplet approached the blade surface (and in other regions where the velocity gradients were high), the time increment Δt_l was automatically reduced to maintain computational accuracy. If the droplet impinged on the blade surface, the calculation was terminated and the intersection point recorded.

3 Definition of Deposition Parameters

Deposition data are best represented in terms of the fraction of the fog entering the blade passage that is deposited on the blade surfaces.

Consider the mass flow rate of water entering a blade row through a streamtube of thickness dr situated a radial distance r from the turbine axis. The *Fractional Inertial Deposition Rate* of fog droplets F_I is defined as the fraction of this water flow rate that is deposited on the blades by inertial deposition. In machines with high aspect ratio blading, F_I may vary significantly in the spanwise direction, but in machines with short blades a single value of F_I may be sufficient to characterize the deposition process adequately.

In order to represent the distribution of deposited water on the blading, it is useful to introduce the *Inertial Deposition Distribution Function* f_I. This is defined such that the fraction of the total mass flow rate of water deposited on the blade by inertial deposition in an axial element of length dz between z and $z + dz$ on either the pressure or the suction surface is given by $f_I d(z/c)$, where c is the axial chord length of the blade.

From the definition of f_I, it is evident that

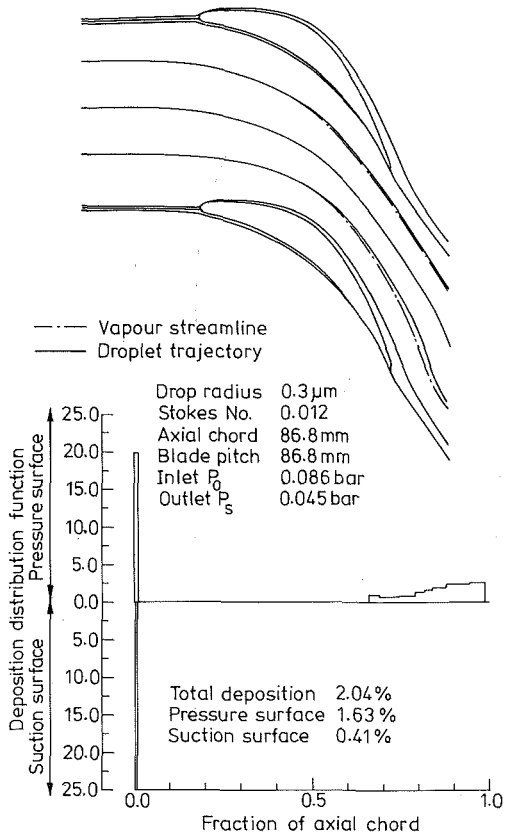

Fig. 3 Droplet trajectories and deposition distribution for a low-pressure turbine stator blade

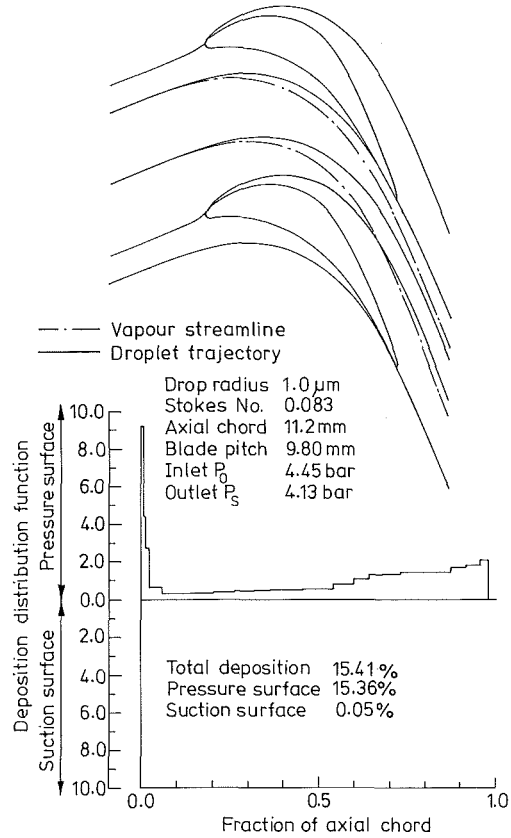

Fig. 4 Droplet trajectories and deposition distribution for a high-pressure turbine blade

$$\int_0^1 f_I d(z/c) + \int_0^1 f_I d(z/c) = 1 \qquad (15)$$

(P.S.) (S.S.)

where z is measured from the leading edge and (P.S.) and (S.S.) stand for pressure surface and suction surface, respectively.

In calculating deposition rates, it was assumed throughout that all droplets incident on the blading adhere to the surface. The bouncing of droplets depends on the impact velocity, the angle of incidence, and the structure of the surface and is very difficult to predict theoretically. Gyarmathy (1962) states that if the surfaces are wet, then all small droplets deposited at oblique angles are believed to be caught in the surface films. His evidence, however, appears to be slight and it should be remembered that all deposition rates presented below are upper limiting values.

4 Some General Results

Figure 3 shows the results of trajectory calculations for a typical low-pressure turbine stator blade. The calculations were performed for droplets of radius 0.3 μm and the liquid phase was assumed to be distributed uniformly at cascade inlet. All relevant details are given in the figure.

It can be seen that inertial deposition tends to occur in two distinct regions: around the leading edge of the blade in the vicinity of the stagnation point and on the pressure surface toward the trailing edge. Small droplets having correspondingly small relaxation times (i.e., Stokes numbers St $\ll$ 1) tend to follow the vapor streamlines very closely and pressure surface deposition, in some cases, may be completely absent. Certainly, for small droplets, values of F_I are very dependent on blade profile shape. With increase in droplet size, the area over which deposition occurs increases toward the leading edge and, for large droplets whose trajectories deviate considerably from the vapor streamlines, deposition may occur over the whole of the pressure surface. Values of F_I in such cases are much less dependent on specific details of the profile shape.

The latter type of behavior is illustrated in Fig. 4, which shows the results of trajectory calculations for a much smaller turbine blade operating with higher pressure stream. The calculations were performed for droplets of radius 1 μm and the relevant data can be found in the figure. The larger droplets and shorter chord length of the blade result in a higher Stokes number and hence increased velocity slip between the phases. The inertial deposition rate is therefore much higher: 16 percent as opposed to 2 percent in the previous example.

Figure 4 also illustrates a phenomenon that may have a significant effect on the thermal nonequilibrium characteristics of wet steam turbines. This is the "bunching" of droplet trajectories during their passage through the cascade. Bunching results from the fact that the vapor velocities and streamline curvatures are much greater near the suction surface than near the pressure surface. Droplets following trajectories that narrowly avoid the suction surface therefore tend to slip more in the pitchwise direction than those closer to the pressure surface. The net result is that the flow downstream of the cascade is nonuniform and separates into two distinct regions of wet and dry steam, respectively. The following blade row then experiences an unsteady approach flow, consisting of alternate wet and dry regions, which is periodic at the blade passing frequency. The effect may be considerable for larger droplets; for example, in Fig. 4, 45 percent of the blade outflow is dry steam.

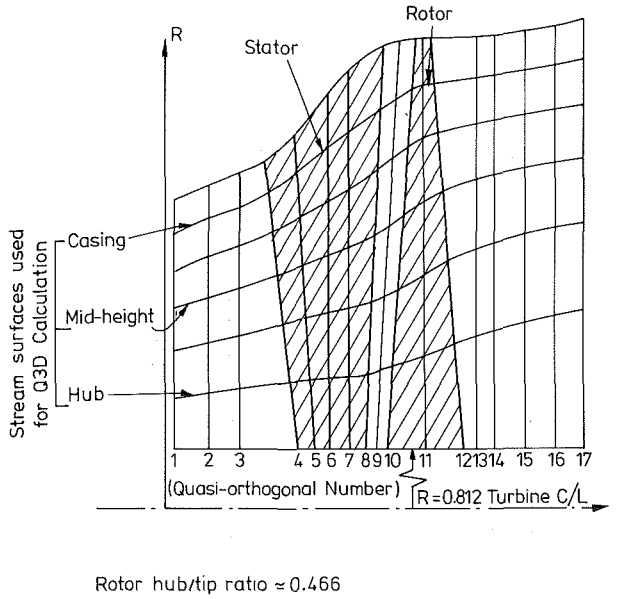

Fig. 5 Final stage geometry and computed stream surfaces for the 500 MW turbine

5 A Simple Theory of Inertial Deposition

The calculation procedure described in the previous sections suffers from the disadvantage that the data preparation and calculation of the vapor flowfields can be very time consuming. If the flowfields are available as the result of a basic blade design exercise, then the computational effort is greatly reduced, but, in cases where this is not so, a simplified calculation procedure giving good, approximate estimates of deposition rates would be of considerable value. In particular, a short analytical calculation method might usefully be incorporated into the axisymmetric throughflow procedures that currently form the starting point for all steam turbine design.

Throughflow calculations are performed during the initial stages of design when detailed blade profiles have not been finalized. A necessary criterion for any simplified deposition calculation is therefore that it should depend only on the gross blade geometric details such as the inlet and outlet angles, axial chord length, etc. Gyarmathy (1962) has proposed a method that fulfills these requirements precisely. His calculation is divided into two sections. The leading edge of a blade is modeled as a circular cylinder in a uniform, parallel flow and the pressure surface is modeled as a parabolic profile in a flow with constant axial velocity.

Gyarmathy's original theory is deficient in two respects. Firstly, it does not include the effect of rotation in moving blade rows, and secondly, it assumes that the viscous drag on a droplet is independent of the slip Reynolds number, an approximation leading to significant error for large fog droplets, especially in high-pressure flows. The authors have extended Gyarmathy's original theory to include both these effects, however, and details can be found in the Appendix. There it is shown that the effects of blade rotation are comparatively small. Typically, for machines with high casing flare angles and rotating at 50 Hz, the deposition rates are altered by less than 20 percent from the predictions of the original theory.

How well the simplified theory agrees with the more exact calculations depends largely on the importance of blade profile shape in determining the deposition rate. This aspect is explored in the case studies of the following sections.

6 Case Study 1. Deposition on the Final Stage Blading of the LP Cylinder of a 500 MW Turbine

In order to illustrate both qualitative and quantitative aspects of deposition in low-pressure turbines, a complete analysis for the final (sixth) stage of the LP cylinder of a currently operating 500 MW turbine was performed.

	Stator		Rotor	
	Mean Pitch (mm)	Axial Chord (mm)	Mean Pitch (mm)	Axial Chord (mm)
Hub	162.0	180.0	67.0	133.0
Mid-height	208.5	236.0	89.5	87.0
Casing	246.5	322.0	107.0	37.7

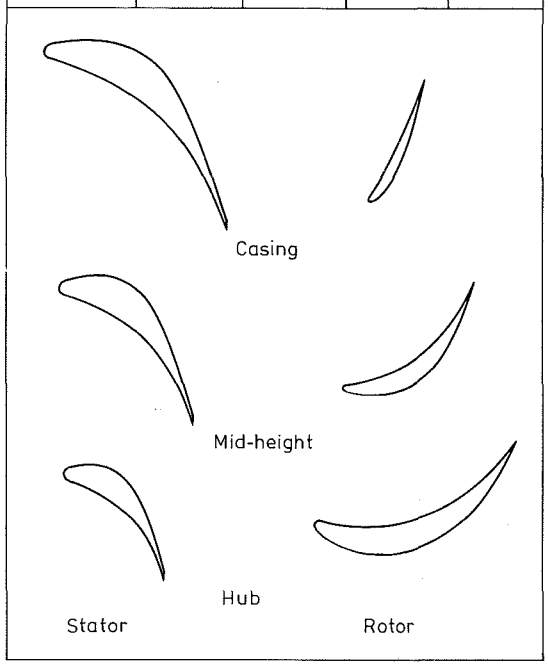

Fig. 6 Interpolated quasi-three-dimensional blade profiles for the 500 MW turbine

6.1 Calculation of the Velocity Flowfields. The meridional plane geometry of the turbine stage is shown in Fig. 5. Initially, an equilibrium, axisymmetric throughflow analysis was performed to locate the positions of the streamsurfaces of revolution. These also are shown in Fig. 5.

Blade-to-blade data were available in the form of the two-dimensional geometry of profiles formed by the intersection of the blades with a number of cylindrical surfaces of revolution. For the deposition calculations, however, blade-to-blade flowfields based on the true streamsurfaces and including the effects of streamsurface divergence and change of radius were required. (Large errors in deposition rates result from using a two-dimensional rather than a quasi-three-dimensional profile in turbine stages having strong radial variation of flow properties.) Accordingly, a geometric interpolation procedure was developed for estimating the required quasi-three-dimensional profiles from the existing two-dimensional data. This was achieved by connecting points on the two-dimensional profiles having the same "fraction of axial chord" coordinate by parabolic curves and interpolating for the required streamsurface. In this way six quasi-three-dimensional profiles were generated, three for the stator and three for the rotor blade. The three streamsurfaces will be referred to as the hub, midheight, and casing streamsurfaces, respectively, and are shown in Fig. 5. The six profiles are shown in Fig. 6.

Blade-to-blade calculations based on the quasi-three-dimensional profiles were performed using the time-marching program mentioned previously. Very fine grid networks were employed (typically 80 × 25) in order to obtain good definition in regions of rapid change. In particular, the density of

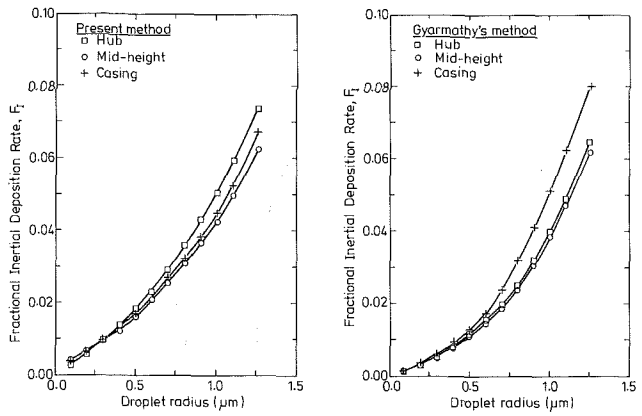

Fig. 7 Inertial deposition on the stator blade of the 500 MW, LP turbine (on-design calculation)

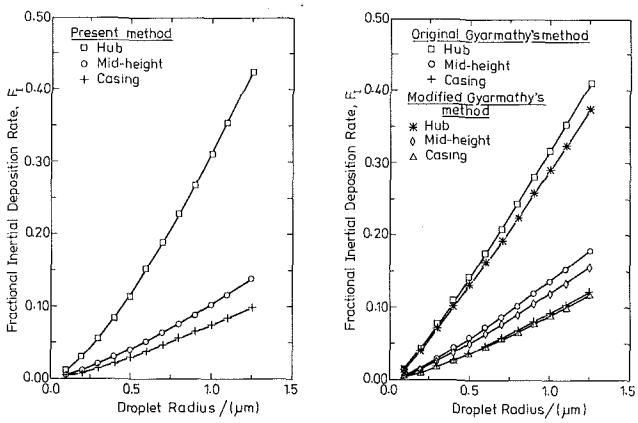

Fig. 8 Inertial deposition on the rotor blade of the 500 MW, LP turbine (on-design calculation)

grid points was very high in the vicinity of the leading edge and near the pressure surface of the blade. This was absolutely essential for the accurate computation of the trajectories of the smaller droplets, for it was found that too coarse a grid system could give rise to very large errors in the overall deposition rate.

6.2 On-Design Calculations of Inertial Deposition Rate. Inertial deposition rates were calculated by tracking the droplet trajectories as described previously. For each droplet size, approximately 200 trajectories were required to give an accurate representation of the distribution of deposited water over the blade surface. On-design conditions were assumed (zero degrees incidence) and the calculations were undertaken for a range of droplet radii varying from 0.1 μm to 1.25 μm. For droplet radii less than 0.1 μm, the deposition rates are very low and discretization errors can become significant even for very fine grid networks.

The results for the stator blade are shown in Fig. 7. The blade twist is small and there is little variation in deposition rate in the spanwise direction. Also shown are the results of using Gyarmathy's simplified method. The method evidently tends to underestimate the deposition rates of the smaller droplets and this discrepancy is easily traceable to the influence of the detailed profile geometry. As shown in the Appendix, for small droplets, Gyarmathy's method predicts a uniform distribution of deposited water with axial coordinate on the pressure surface of the blade. In practice, however, the distribution is more typically as shown in Fig. 3, with increased deposition toward the trailing edge. Despite this shortcoming, however, Gyarmathy's method predicts surprisingly accurate results considering the extreme simplicity of the analysis.

Inertial deposition rates on the rotor blade are shown in Fig. 8. The rates are greatly enhanced over those for the stator (note the different scales) due to the increased flow turning and reduced axial chord length. There is also a much greater variation in the spanwise direction due to the large twist of the blade. Gyarmathy's method overestimates the deposition rates slightly, but is very successful in displaying the important effects of variation in blade profile geometry. The effect of the Coriolis acceleration in rotating blade rows is slight, as can be seen in Fig. 8 by comparing the results of Gyarmathy's original theory with the modified version of the Appendix.

6.3 Off-Design Calculations of Inertial Deposition Rate. Calculations were also performed on several blade profiles at a number of different flow incidence angles. Figure 9 shows the results for the midheight streamsurface of the rotor blade. It is evident that deposition is slightly increased by small positive flow incidence angles and reduced by negative ones. Figure 9 also shows the results using Gyarmathy's method, and this is

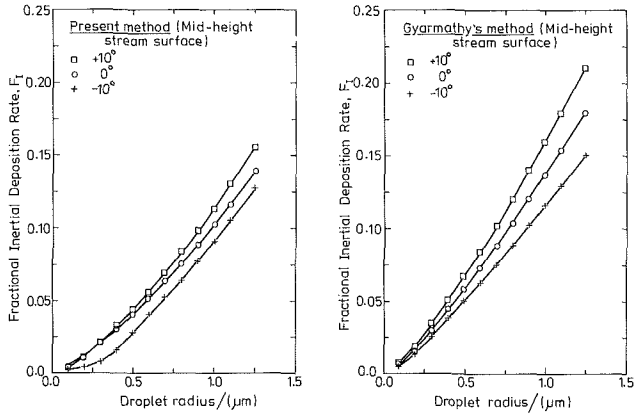

Fig. 9 Inertial deposition on the rotor blade of the 500 MW, LP turbine (midheight stream surface, off-design calculation)

obviously successful in predicting the correct trends of the off-design behavior.

7 Case Study 2. Deposition in a High-Pressure, Wet-Steam Turbine

A second case study was undertaken based on a typical stage of a 500 MW, high-pressure, nuclear, wet-steam turbine. The geometry of the profile selected was identical to that shown in Fig. 4, but the axial chord length was 33.6 mm and the inlet pressure was 40 bar.

7.1 Calculation of the Flowfield. Because of the small casing flare angle of the turbine, a full quasi-three-dimensional analysis was not required and the flow was assumed to be two-dimensional in the blade-to-blade plane with negligible streamtube divergence and change of radius. Furthermore, the blade profiles of the stators and rotors were identical.

7.2 Calculations of Inertial Deposition Rate. Deposition by inertial impaction was computed as before and values of F_I as a function of droplet radius are shown in Fig. 10. It can be seen that a significant improvement over Gyarmathy's original equation is obtained by including the correction for the slip Reynolds number.

A comparison of Fig. 10 with Figs. 7 and 8 shows that, in general, the inertial deposition rate on the high-pressure blade is lower than that on the low-pressure blades for the same droplet size. This is, perhaps, surprising considering the shorter chord length of the HP blade and is due to the reduced curvature of the flow streamlines and differences in profile geometry, especially at the leading edge. Furthermore, as the

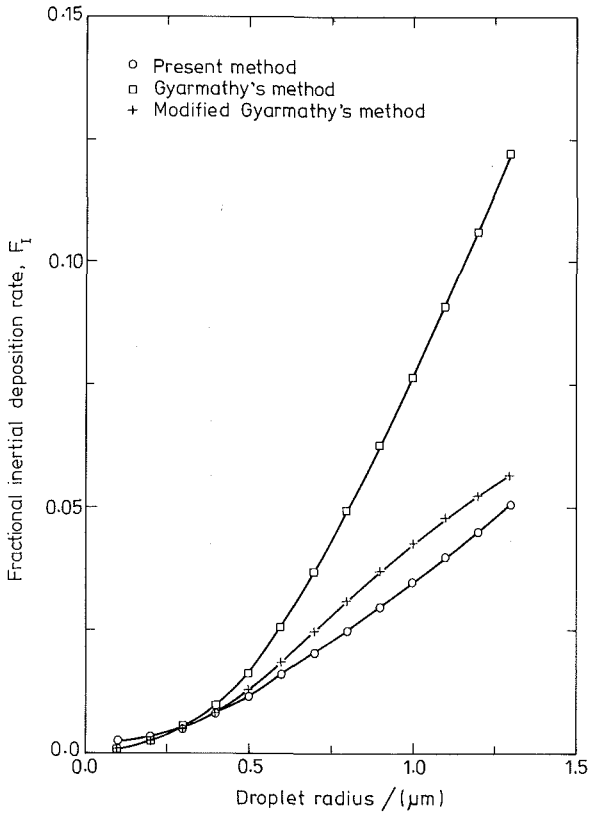

Fig. 10 Inertial deposition on the HP turbine blade

pressure is increased, the Knudsen number becomes smaller (tending toward continuum flow) and the drag force on a droplet of given radius is increased.

7.3 Trajectory Bunching. At this point, it is of interest to present results concerning the phenomenon of "trajectory bunching" described previously. This information is automatically generated during a deposition calculation and the profiles selected for analysis here were the rotor hub section of the LP turbine and the HP blade discussed above. Figure 11 shows the results, presented as graphs of the volume fraction of the flow downstream of the cascade, which is dry steam versus droplet radius. Also shown are curves of F_I taken from Figs. 8 and 10. Evidently, for the larger droplets, the downstream flow is highly nonuniform despite the comparatively low deposition rates.

8 Conclusions

1 Deposition by inertial impaction depends on the detailed profile geometry and can only be calculated accurately by flowfield calculation and particle tracking.

2 Gyarmathy's simplified approach is very suitable for initial estimates. The theory is reasonably reliable for the larger fog droplets, but errors in deposition rate of 50 percent or more may be incurred for small droplet radii.

3 The effect of the Coriolis acceleration in rotating blade rows with high pitch angles is unlikely to alter deposition rates by more than 20 percent.

4 Large pitchwise variations within the blade passage can cause trajectory bunching, resulting in a nonuniform cascade exit flow.

5 For identical droplet radii, deposition rates on low and high-pressure blading are comparable. However, the increased number of wet stages in nuclear HP turbines suggests that the quantities of coarse water are much higher in HP cylinders.

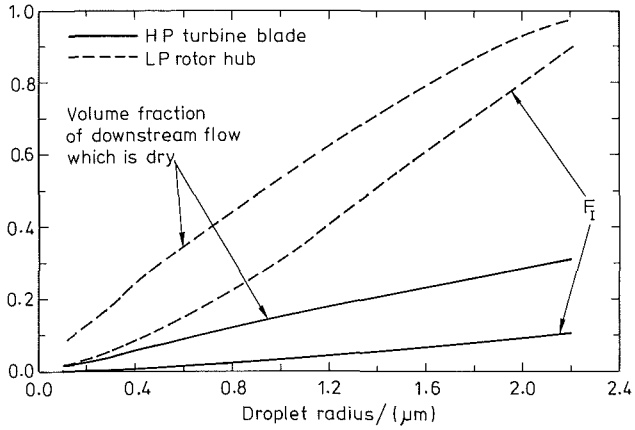

Fig. 11 Trajectory bunching in LP and HP turbines

Acknowledgments

The work was carried out at the Whittle Laboratory, University of Cambridge, and was supported by a grant from the Central Electricity Research Laboratory, Leatherhead (organized by Dr. M. J. Moore), for which the authors express their gratitude. They are also grateful to Dr. J. D. Denton for allowing them free access to his flow calculation computer programs. One of the authors (KKY) was supprted by a Croucher Foundation Scholarship during the course of the work.

References

Crane, R. I., 1973, "Deposition of Fog Drops on Low Pressure Steam Turbine Blades," *Int. J. Mech. Sci.*, Vol. 15, pp. 613–631.

Denton, J. D., 1978, "Throughflow Calculations for Transonic Axial Flow Turbines," ASME *Journal of Engineering for Power*, Vol. 100, pp. 212–218.

Denton, J. D., 1983, "An Improved Time-Marching Method for Turbomachinery Flow Calculation," ASME *Journal of Engineering for Power*, Vol. 105, pp. 514–524.

Gyarmathy, G., 1962, "Bases of a Theory for Wet Steam Turbines," Bull. 6. Inst. for Thermal Turbomachines, Federal Technical University, Zurich, CEGB Translation T-781.

Moheban, M., and Young, J. B., 1985, "A Study of Thermal Nonequilibrium Effects in Low-Pressure Wet-Steam Turbines Using a Blade-to-Blade Time-Marching Technique," *Int. J. Heat and Fluid Flow*, Vol. 6, pp. 269–278.

Moore, M. J., and Sieverding, C., 1976, *Two-Phase Steam Flow in Turbines and Separators*, Hemisphere, Washington, DC.

Walters, P. T., and Skingley, P. C., 1979, "An Optical Instrument for Measuring the Wetness Fraction and Droplet Size of Wet Steam Flows in LP Turbines," *Steam Turbines for the 1980s*, IMechE, London, Paper No. C141/79, pp. 337–348.

Yau, K. K.,1986, "Fog Droplet Deposition and Movement of Coarse Water in Steam Turbines," Ph.D. Thesis, Dept. of Eng., Univ. of Cambridge.

Yau, K. K., and Young, J. B., 1987, "The Deposition of Fog Droplets on Steam Turbine Blades by Turbulent Diffusion," ASME JOURNAL OF TURBOMACHINERY, Vol. 109, pp. 429–435.

APPENDIX

A Simplified Theory of Deposition by Inertial Impaction

***(a)* Leading Edge Deposition.** To estimate the inertial deposition rate on a blade leading edge, Gyarmathy (1962) assumed that the vapor flowfield could be approximated by a circular cylinder in a uniform parallel incompressible flow. No analytical solution for the droplet trajectories in such a flowfield is known and hence deposition rates were computed numerically. For Re $\ll$ 1, the collection efficiency η_c of a circular cylinder is a function only of the Stokes number and is shown in Fig. 12(*a*). The fractional inertial deposition rate on the leading edge is given by

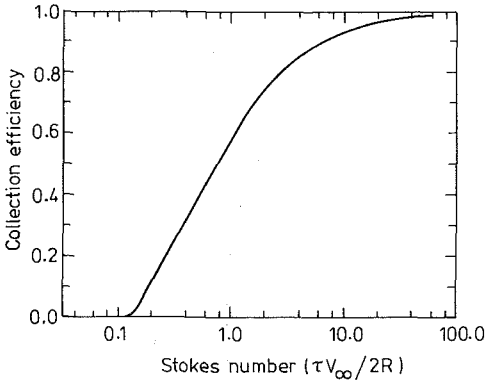

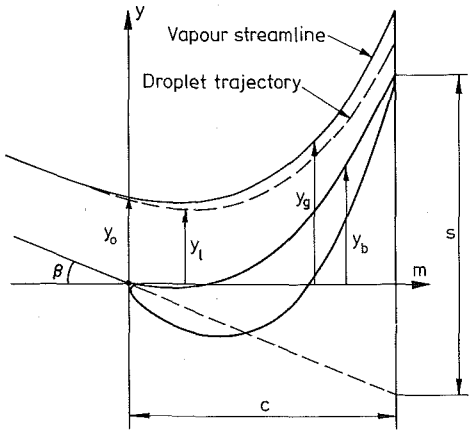

Fig. 12 *(a)* **Collection efficiency for a circular cylinder in a uniform parallel flow; (*b*) geometric details for Gyarmathy's theory of pressure surface deposition**

$$F_I = \eta_c \frac{2R}{P} \tag{A1}$$

where R is the equivalent leading edge radius and P is the blade pitch.

(*b*) Pressure Surface Deposition. Gyarmathy's original analysis started from the assumption that the flow was plane two-dimensional with zero radial component of velocity. A similar analysis can be performed in cylindrical coordinates for axisymmetric flow, but the improvement in accuracy hardly justifies the increased complexity of the algebra. The influence of the Coriolis component of acceleration in rotating blade rows can be included without difficulty, however, and hence it is here assumed that the flow is plane two-dimensional, but inclined at a constant pitch angle ϕ to the turbine axis.

With reference to Fig. 12(*b*), the vapor streamlines are approximated by the parabolas

$$y_g = y_o - m \tan \beta_o + sm^2/c^2 \tag{A2}$$

where c is the meridional chord length and β_o is the relative inlet flow angle. It is further assumed that the meridional velocity is constant and the velocity slip in this direction is zero. The slip velocity in the circumferential direction can be obtained from equation (13) by discarding the term $W_{l\theta}/r$. In the notation of Fig. 12(*b*)

$$W_{gy} - W_{ly} = \tau[(1 - \exp(-m/W_m\tau)] \times \left[W_m \frac{dW_{gy}}{dm} + 2\Omega W_m \sin \phi\right] \tag{A3}$$

assuming that $\Delta W_y = 0$ at $m = 0$. The circumferential components of velocity are given by

$$W_{gy} = W_m \frac{dy_g}{dm}, \qquad W_{ly} = W_m \frac{dy_l}{dm} \tag{A4}$$

Substituting equations (A2) and (A4) into (A3) gives a first-order differential equation for the droplet trajectory having solution

$$y_l = y_b + y_o - 2s(\mathrm{St})(1-\alpha)[(m/c) - \mathrm{St}(1 - e^{-m/c\mathrm{St}})] \tag{A5}$$

where y_b is the blade coordinate (obtained by putting $y_o = 0$ in equation (A2)) and St is the Stokes number ($\tau W_m/c$). The dimensionless parameter

$$\alpha = \frac{\Omega c^2 \sin \phi}{sW_m} \tag{A6}$$

represents the effect of the Coriolis acceleration on the droplet trajectory.

The limiting trajectory that just grazes the trailing edge of the blade is obtained by setting $y_l = y_b$ at $m = c$. This trajectory therefore has a y_o value given by

$$y_o = 2s(\mathrm{St})(1-\alpha)[1 - \mathrm{St}(1 - e^{-1/\mathrm{St}})] \tag{A7}$$

and the fractional inertial deposition rate on the pressure surface is

$$F_I = \frac{2s}{P}(1-\alpha)[(\mathrm{St}) - (\mathrm{St})^2(1 - e^{-1/\mathrm{St}})] \tag{A8}$$

Equation (A8) is the same as Gyarmathy's expression except for the term $(1 - \alpha)$. Insertion of typical values shows that α is rarely greater than 0.2 even for quite large pitch angles. For larger droplets in high-pressure flows it is important to include the correction ϕ (Re) when calculating a suitable value of τ from equation (6). This may be done by obtaining an initial estimate of a mean value of ΔW_y from equation (A3).

For any droplet trajectory passing through the point $m = 0$, $y = y_o$, the point of intersection with the blade $m = m_b$, $y = y_b$ can be found from equation (A5), that is,

$$y_o = 2s(\mathrm{St})(1-\alpha)[(m_b/c) - \mathrm{St}(1 - e^{-m_b/c\mathrm{St}})] \tag{A9}$$

The deposition distribution function f_I can then be obtained from its definition

$$\frac{dy_o}{y_o} = f_I \frac{dm_b}{c} \tag{A10}$$

Hence

$$f_I = \frac{2s}{y_o}(\mathrm{St})(1-\alpha)(1 - e^{-m_b/c\mathrm{St}}) \tag{A11}$$

For small values of St, which is usually the case in practice, Gyarmathy's theory predicts that the distribution function is effectively constant over the blade pressure surface.

Fog Droplet Deposition and Coarse Water Formation in Low-Pressure Steam Turbines: a Combined Experimental and Theoretical Analysis

J. B. Young
Whittle Laboratory,
Cambridge University Engineering Department,
Cambridge, CB3 0DY, United Kingdom

K. K. Yau
GEC Turbine Generators Ltd.,
Urmston, Manchester, M31 2LD,
United Kingdom

P. T. Walters
Central Electricity Research Laboratories,
Leatherhead, Surrey, United Kingdom

The paper describes a theoretical and experimental study of fog droplet deposition and coarse water formation in the LP cylinders of two 500 MW steam turbines. Measurements of coarse water flow rates entering and leaving the final stage of each turbine were performed using a new design of water absorbent probe. From these measurements it was possible to deduce the rate of deposition of fog droplets onto the last stage blading of each machine. Aerodynamic and optical traverses provided experimental data on the fog droplet mean diameter and wetness faction, and the application of an inversion procedure generated an approximation to the droplet size spectrum itself. Using these data and theoretical methods for predicting inertial and diffusional deposition rates, a second estimate was obtained for the stage deposition rates. The two different approaches show excellent agreement, in contrast with previously published work, which was unable to reconcile (to within one order of magnitude) deposition theory with measured fog droplet sizes and coarse water quantities.

Introduction

Condensation in low-pressure (LP) steam turbines occurs primarily by spontaneous nucleation in the vapor phase, producing a dense fog of very fine droplets. The droplets, although tiny, do not follow the vapor streamlines exactly and a small percentage is deposited on the blading both by inertial and diffusional mechanisms. The deposited water is drawn toward the trailing edges by the drag of the steam and is reentrained into the flow in the form of coarse water droplets having diameters in the range 10–100 μm. It is the latter that cause erosion damage to the blades.

Previous research has uncovered a serious inconsistency between theory and experiment in this area. Light extinction measurements of the mean fog droplet size (Walters, 1985) indicate that the fog droplets in turbines usually have Sauter mean diameters in the range 0.1–0.5 μm. Deposition calculations based on such droplet sizes predict that only a very small fraction of the fog (less than 1 percent) is deposited on the blade surfaces (Crane, 1973). In contrast, however, direct measurements of coarse water quantities using catchpot probes (Williams and Lord, 1973) indicate that some 5–10 percent of the water exists in this coarse form. It therefore appears impossible to reconcile the fog and coarse water measurements with deposition theory and this has led to speculation concerning the inadequacy of the theory or the possibility of large systematic errors in the measurements.

In this paper, results are presented that demonstrate how theory and experiment can be brought into good agreement. Firstly, a recent development in light extinction technique show that fog droplets in LP turbines are not monodispersed. Instead, the size distribution is negatively skewed, having a "tail" extending to droplets of about 1 μm diameter, which make a significant contribution to the overall wetness fraction. Secondly, measurements of coarse water quantities undertaken with a new design of probe suggest that the coarse water fraction in some turbines may be lower than previous measurements have indicated. When both these effects are taken into consideration, calculations of inertial and diffusional deposition based on conventional theories prove to be perfectly compatible with experimental measurements.

General Description

Experimental measurements were performed on two 500 MW turbines, 'A' and 'B', both currently in operation in the UK. The low-pressure cylinder of each machine had six stages and radial traverses from hub to casing were carried out upstream and downstream of each final stage. The meridional plane geometry and the position of the traverse lines are shown in Figs. 1 and 2.

Contributed by the Power Division for publication in the JOURNAL OF TURBOMACHINERY. Manuscript received by the Power Division May 22, 1987.

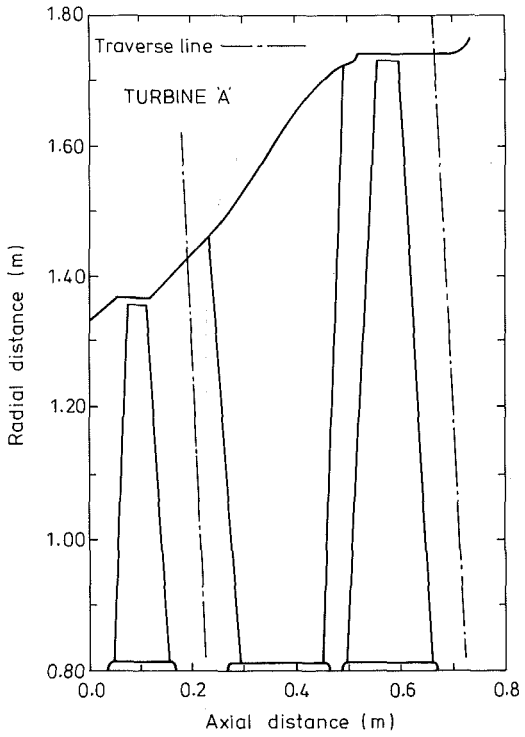

Fig. 1 Meridional plane geometry and position of traverse lines for Turbine A

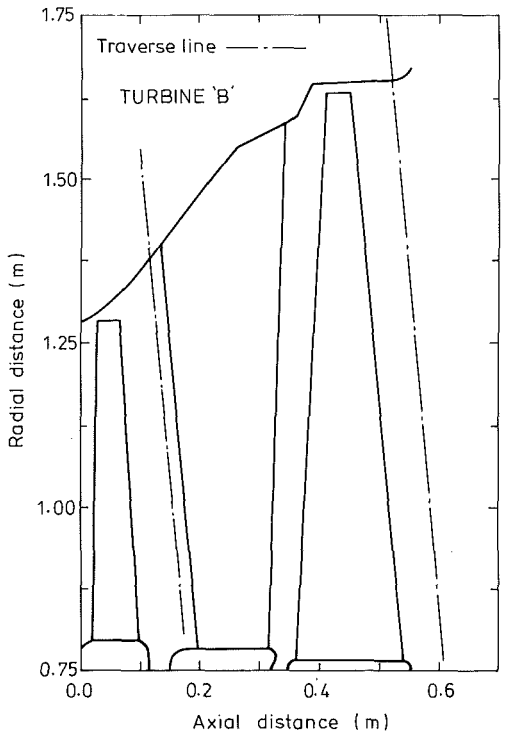

Fig. 2 Meridional plane geometry and position of traverse lines for Turbine B

The following measurements were carried out at each traverse:

1 Total static pressures, and steam flow yaw and pitch angles using the instrumentation described by Moore and Sculpher (1969).

2 Fog droplet Sauter mean diameter and wetness fraction using the optical technique described by Walters (1985).

3 Coarse water and casing film flow rates using a new design of probe described below.

Together, the three sets of measurements allowed the individual flow rates of fog and coarse water entering and leaving each stage to be calculated. Details of the analysis are presented in subsequent sections, but a brief outline of the main argument may be useful at this point.

If it is assumed that all coarse water orginates by the reentrainment of fog droplest deposited on the blades (rather than by direct condensation on the blade surfaces or by the agglomeration of fog droplets in the main stream), then the difference between the coarse water mass flow rate leaving and entering the stage is equal to the mass rate of fog deposition onto the blading. (It is, of course, necessary to include any water film flowing on the turbine casing under the general heading of coarse water.) The stage deposition rate can thus be obtained directly from experimental measurements of coarse water flow rates.

The optical measurements allow the calculation of the spanwise distribution of the fog wetness fraction and Sauter mean diameter upstream and downstream of the stage. The application of an inversion procedure (Walters, 1980) then generates an approximation for the droplet size spectrum at each traverse location. Armed with this information and a knowledge of the blade geometry, theoretical calculations of the rate of deposition of the fog onto the blading can be performed.

In this way, it is possible to arrive at two independent estimates for the stage deposition rate, the first solely from experimental measurements and the second by theoretical calculation based on measured fog droplet sizes.

Nomenclature

C = velocity of coarse water droplet
D = droplet diameter
d = coarse water probe diameter
F_c = integrated coarse water fractional flow rate
f_c = local coarse water fractional flow rate
F_D = fractional diffusional deposition rate
F_I = fractional inertial deposition rate
h = coarse water probe height
M_c = mass collection rate of coarse water by probe
M_f = mass collection rate of fog by probe
M_t = total mass collection rate of liquid by probe
m_c = axial mass flux of coarse water
m_f = axial mass flux of fog
$N(D)$ = number density distribution function of coarse water
$n(D)$ = number density distribution function of fog
p_0 = stagnation pressure
p_s = static pressure
SDR = stage deposition rate
V = steam velocity
y_f = fog wetness fraction
α = coarse water yaw angle relative to axial direction
β = steam yaw angle relative to axial direction
γ = inclination of probe to radial direction
ϕ = steam pitch angle
ψ = coarse water pitch angle
ρ_g = gas density
ρ_l = liquid density
η_c = collection efficiency
τ = inertial relaxation time

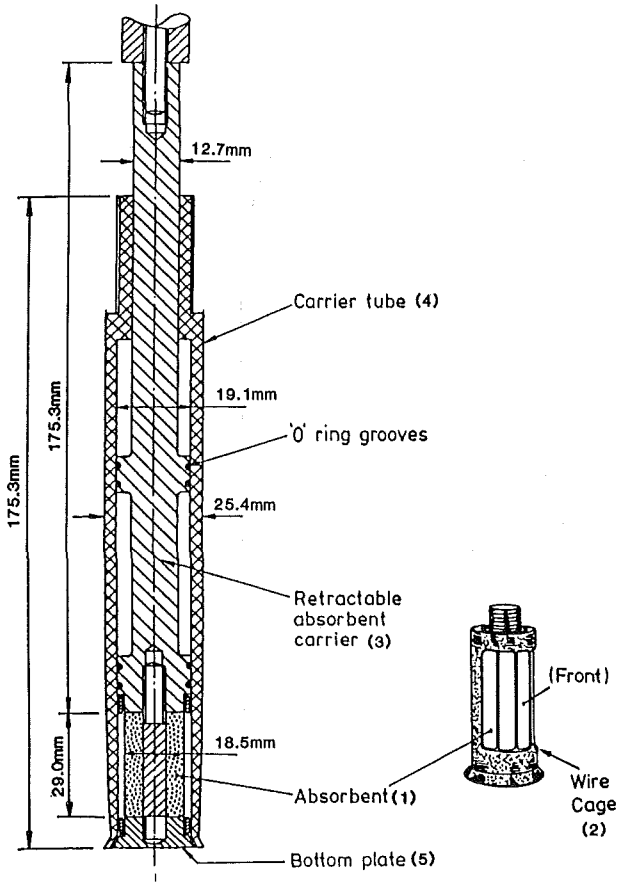

Fig. 3 Details of the coarse water probe

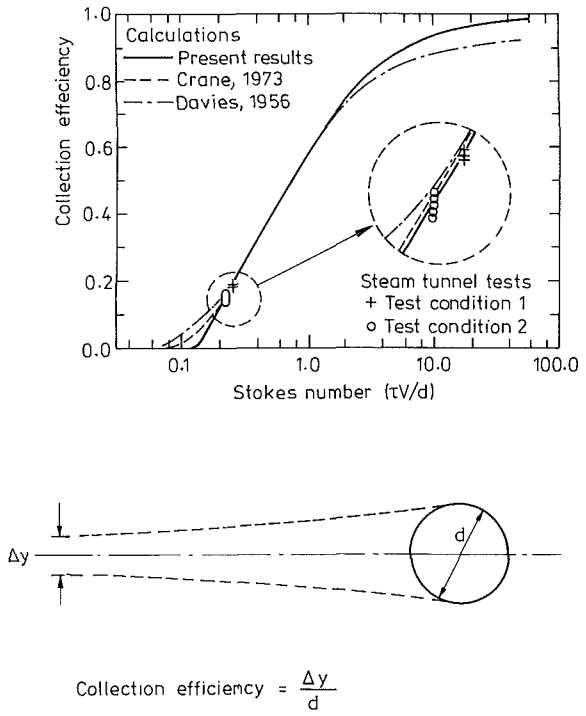

Fig. 4 Collection efficiency of a circular cylinder in a parallel flow

Aerodynamic Measurements

Traverses from hub to casing upstream and downstream of the final stage of both turbines were carried out using the instrumentation described by Moore and Sculpher (1969). The traverses involved measurements of total and static pressure (p_0 and p_s), and steam flow yaw and pitch angles (β and ϕ). The velocity of the two-phase flow was obtained from the measured total and static pressures assuming frozen vapor flow and applying the correction suggested by Crane and Moore (1972) for the momentum of droplets destroyed during stagnation.

Optical Measurements

Similar traverses were performed using the light extinction probe described by Walters (1985). This probe measures the attenuation of a beam of light traversing a short section of the wet steam flow within the turbine at a number of monochromatic wavelengths in the range 0.35–1.05 μm. Light scattering theory may then be used to interpret these data to provide both the mean droplet size and suspended mass fraction of the fog droplet component of the wetness. Recently, the application of linear inversion techniques to optical transmission data has also provided an approximation to the fog droplet size spectrum as described by Walters (1980).

Coarse Water Measurements

Measurements of coarse water and casing film flow rates were performed with a new design of probe shown in Fig. 3. The principle of operation involved exposing a cylindrical sample of tightly rolled absorbent paper to the wet steam flow for a measured period of time. After subtracting a correction for the mass of fog collected by the probe, the increase in mass of the sample could be related to the local axial mass flux of coarse water in the turbine.

With reference to Fig. 3, the absorbent sample (1) was loaded into a removable wire cage (2), screwed onto the end of the long central rod (3). The latter was free to slide inside the guide tube (4), which was inserted in the turbine through an access hole and clamped in position at the required traverse location. On insertion, the wire cage was retracted into the body of the guide tube so that the absorbent was not exposed to the steam environment. Good sealing was provided by the beveled edge of the bottom plate (5). Once in position, the sample was exposed to the flow for a prescribed period of time by operating the control rod like a piston. The orientation of the wire cage was independent of the flow yaw angle and it was only necessary to ensure that the small supporting plate was aligned approximately with the downstream direction.

The exposure time depended on the local wetness fraction and aerodynamic conditions, but typically 1–2 min was sufficient to collect about 1 g of liquid. A number of trials showed this to be the optimum increase in mass, being sufficient to ensure good accuracy when measured with an electronic balance, but insufficient to saturate the absorbent sample. Between each measurement it was necessary to remove the probe from the turbine to reload the sample, but this could be accomplished rapidly enough to allow a data collection rate of 20 points per hour.

Testing and Calibration of the Coarse Water Probe

Probe development was carried out in two laboratory test facilities. These were a 35-cm-dia low-speed air tunnel at the Whittle Laboratory, Cambridge, and the wet steam test facility at the Central Electricity Research Laboratories, Leatherhead, described by Moore et al. (1973).

Experiments in the air tunnel were mainly visual. The flow velocity could be varied to a maximum of 60 m/s and provision was made for generating a coarse water spray (mean droplet diameter about 100 μm) upstream of the probe using a commercial aerosol.

Table 1 Experimental results and theoretical calculations for the fog collection efficiency of the coarse water probe

TEST CONDITION 1			TEST CONDITION 2		
y = 2.5%	D_{30} = 0.62μm D_{32} = 0.92μm D_{43} = 1.10μm		y = 1.1%	D_{30} = 0.49μm D_{32} = 0.68μm D_{43} = 0.80μm	
p_s(bar)	V(m/s)	η_c(%)	p_s(bar)	V(m/s)	η_c(%)
0.120	374	18.8	0.063	303	14.8
0.137	337	19.0	0.063	296	15.5
0.119	384	19.1	0.063	296	16.2
0.138	335	18.6	0.063	298	14.2
Experimental average		18.9	0.064	304	13.5
			0.060	335	14.8
			Experimental average		14.8
THEORETICAL CALCULATIONS OF COLLECTION EFFICIENCY					
Full spectrum		18.7	Full spectrum		15.0
Monodispersed (D_{30})		0.2	Monodispersed (D_{30})		0.4
Monodispersed (D_{32})		11.4	Monodispersed (D_{32})		9.6
Monodispersed (D_{43})		18.9	Monodispersed (D_{43})		15.4

After testing with various probe orientations from vertical to horizontal, the following conclusions were drawn:

1 All water incident on the absorbent sample was absorbed immediately. Water films or rivulets did not form on the surface.

2 All water incident on the guide tube was drawn by the air flow to the rear, where it was re-entrained into the flow. No unwanted water was absorbed by the sample even when the probe was aligned vertically.

3 With sample withdrawn into the guide tube, sealing was effectively complete.

Experiments conducted in the CERL tunnel were performed in a genuine wet-steam environment. This was obtained by passing the steam through a turbine upstream of the test section and adjusting the turbine inlet temperature so that fog nucleation occurred within the blade passages (Moore et al., 1973). The exhaust wetness and mean droplet size were not independent, but essentially two different test section conditions could be obtained by varying the turbine mass flow rate. The flow velocity in the working section was deduced from measurements of total and static pressure and the steam wetness and Sauter mean droplet diameter were obtained from light extinction measurements (Walters, 1973).

The droplet size distribution was estimated by applying the inversion procedure described by Walters (1980) and the analysis revealed that the droplet spectrum in both cases was of similar shape to that shown in Fig. 7. It was assumed that the coarse water content in the central part of the tunnel was negligible and this was confirmed by previous tests conducted at CERL. Details of the two flow conditions can be found in Table 1. The various mean droplet diameters D_{ab} were calculated numerically from the distribution using the definition

$$D_{ab} = \left(\frac{\int_0^{D_{max}} n(D) D^a dD}{\int_0^{D_{max}} n(D) D^b dD} \right)^{1/(a-b)} \quad (1)$$

where $n(D)\ dD$ is the number density of droplets having diameters in the range D to $D+dD$.

The collection efficiency η_c of a circular cylinder situated in a uniform, parallel flow is defined as the ratio of the mass collection rate of water by the cylinder to the mass flow rate of water passing through the projected area of the cylinder in its absence (see Fig. 4). A number of measurements of collection efficiency of the probe were made at each of the two tunnel operating conditions and these are also tabulated in Table 1. It can be seen that the reproducibility of the readings is good.

Theoretical calculations of the collection efficiency of a circular cylinder were performed by computing the inviscid gas flowfield around the forward part of the cylinder and tracking individual droplets through this flowfield by numerically integrating the Lagrangian equation of motion of the droplet along its trajectory. Full details of the procedure can be found in Yau (1986). For small droplet Reynolds numbers, such as are found in the present application, the collection efficiency is a function only of the Stokes number $\tau V/d$ (Crane, 1973). Figure 4 shows this universal curve and compares the present calculations with similar ones reported in the literature (Crane, 1973; Davies and Peetz, 1956). In general the agreement is excellent but in regions where small discrepancies exist, it is believed that the present calculations are more accurate as great care was taken to ensure that the flowfield discretization was very fine in sensitive regions such as around the forward stagnation point.

Knowing the droplet size distribution in the steam tunnel, the collection efficiencies for the two test conditions were obtained from Fig. 4 by numerically integrating over the droplet spectrum. The results, shown in Table 1, compare very favorably with the average experimental values in both cases. This is believed to be the first experimental confirmation of theoretically derived results for the collection efficiency of a circular cylinder.

The experimental results are also included in Fig. 4 for visual comparison with the theoretical curve. Both tests fall in the range of low η_c and no verification is available for the upper part of the curve. Despite this shortcoming, it is felt that the available evidence goes a considerable way to validating the operation of the probe in a foggy, high-speed flow.

When dealing with polydispersed droplet flows, it is often expedient to perform calculations with an equivalent monodispersion. In the case of inertial deposition there are sound theoretical reasons (Yau, 1986) for adopting the weighted mean diameter D_{43} to characterize the distribution. The results of Table 1 show this to be an excellent approximation in the case of deposition on a circular cylinder. The importance of using the correct mean diameter can be appreciated by comparing the above results with those based on the mass mean diameter D_{30} and the Sauter mean diameter D_{32} also presented in Table 1. Both approximations seriously underestimate the experimental results and, indeed, and adoption of D_{30} predicts almost zero collection efficiency in both cases.

Analysis of the Coarse Water Measurements

During its exposure to the flow in a turbine, the probe collects both fog and coarse water. The mass collection rate of coarse water M_c is therefore obtained by subtracting the mass collection rate of fog M_f from the total mass collection rate of liquid M_t

$$M_c = M_t - M_f \quad (2)$$

The calculation of the fog collection rate M_f is straightforward and is described in the appendix. In general it is a small fraction of M_t, but in regions of high velocity and wetness fraction, such as near the casing, the correction becomes appreciable and must be included.

From the knowledge of M_c, it is now necessary to compute the axial mass flux of coarse water m_c at the local probe position. The main difficulty in interpreting the results now emerges, because the coarse droplets, unlike the fog, cannot be assumed to be traveling in the same direction as the vapor phase. The analysis is presented in the appendix, where it is shown that m_c is given by

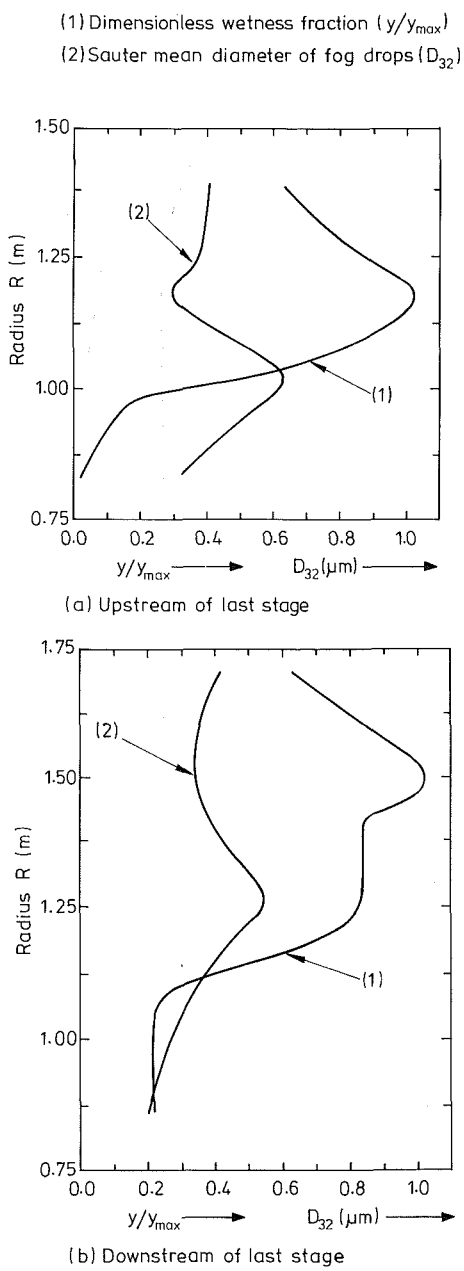

Fig. 5 Measured fog wetness fraction and mean droplet size distribution for Turbine A

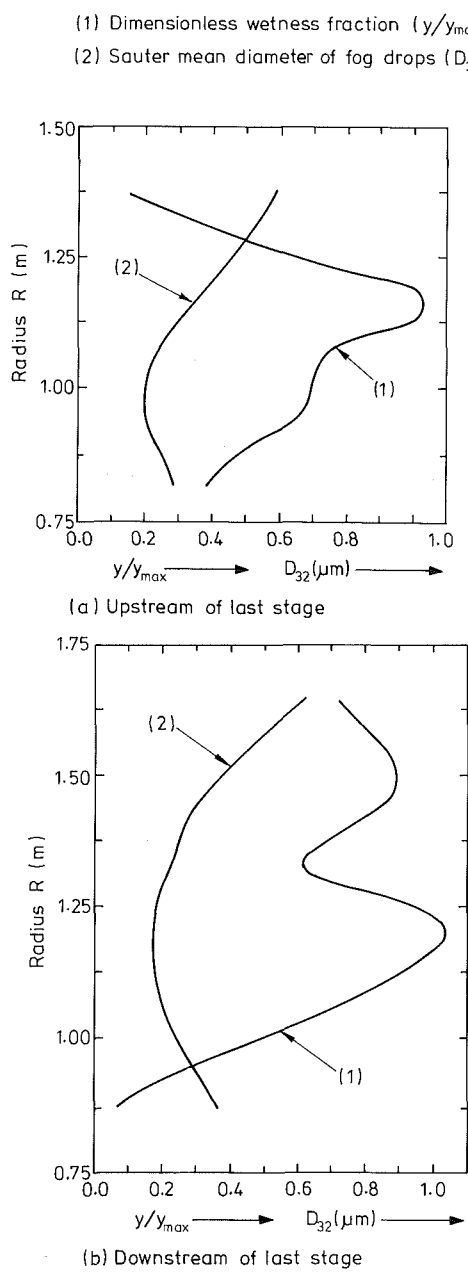

Fig. 6 Measured fog wetness fraction and mean droplet size distribution for Turbine B

$$m_c = \frac{M_c}{hd} \cos(\bar{\alpha}) \tag{3}$$

where h and d are the height and diameter of the absorbent sample, respectively, and $\bar{\alpha}$ is the mean yaw angle (with respect to the axial direction) of the coarse water droplets. In deriving equation (3), it has been assumed that the collection efficiency for all coarse water droplets is unity. Calculation of the relevant Stokes numbers and a study of Fig. 4 shows this to be effectively correct for all droplets having diameters greater than 10 μm.

In order to evaluate the mean coarse water yaw angle $\bar{\alpha}$, it was necessary to assume a size distribution function for the coarse droplets and to estimate the yaw angle for each class of droplet at the probe position. As no direct measurements were made of either of these quantities, it was decided to utilize the experimental data of Stastny (1979), who performed a most detailed study of the structure of the coarse water in a 200 MW turbine. Stastny measured the coarse droplet size spectrum by exposing a probe coated in magnesium oxide to the wet flow for a short period of time and then analyzing the craters formed by the impingement of the droplets. He also measured the mean droplet flow angle by using soft, spherical targets that were selectively eroded by the coarse droplets.

Stastny's measured distributions were discretized into a number of droplet groups and trajectory calculations were performed to estimate the yaw angle of each droplet group at the probe position and hence the mean coarse water yaw angle. The drag coefficient for large drops was computed from the correlation given by Moore and Sieverding (1976) and calculations were initiated at the trailing edges of the rotor blades assuming the droplets to be stripped off with zero relative velocity.

The results of the calculations indicated that, because of the strong radial acceleration, the droplets moved rapidly toward the casing and passed through the traverse plane of the probe with a pitch angle much higher than that of the steam. Projection of the trajectories in the cascade plane also revealed that

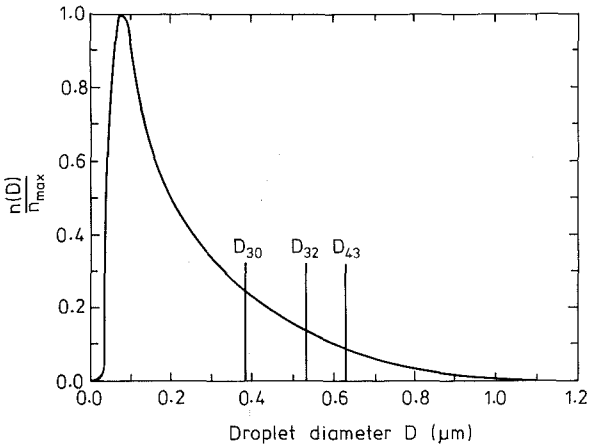

Fig. 7 Droplet size distribution in the exhaust of Turbine A

differences in mean yaw angle of up to 25 deg existed between the larger coarse droplets and the steam depending on the radial position. This finding is indirectly corroborated by Stastny (1979), who measured the mean coarse water flow angle in a different turbine and recorded deviations from the steam flow angle of between 20 and 40 deg. The trajectory calculations also showed that the variation of yaw angle with droplet diameter at each measuring station was small, the standard deviation from the mean being of the order of 5 deg.

The coarse water probe was also used to estimate the water film flow rate on the turbine casing. For this measurement the absorbent sample was positioned with its center at the level of the casing inner surface. Fog deposition on the probe was assumed to be negligible because of the low steam velocity near the casing wall. The probe therefore collected the surface water film together with some coarse water from the main flow. The rate of collection of the latter was estimated by averaging the measurements at nearby points. In computing the axial mass flow rate of the casing water film, it was as-

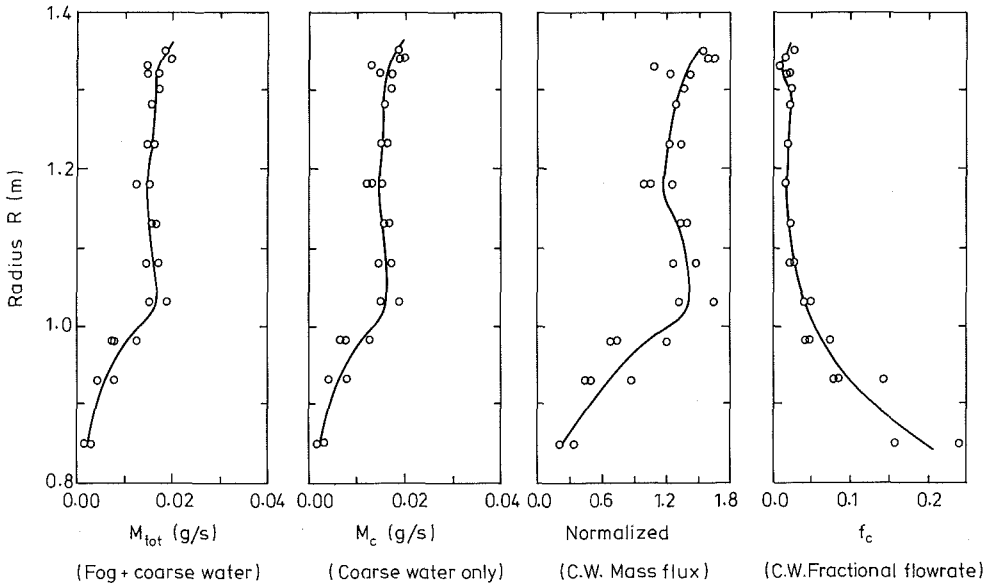

Fig. 8 Measured coarse water results for Turbine A (upstream traverse)

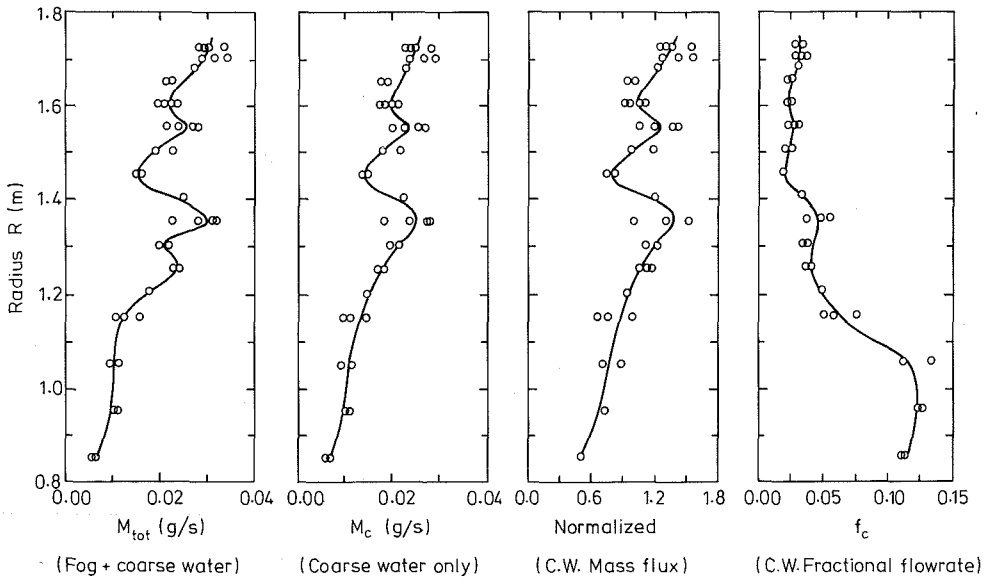

Fig. 9 Measured coarse water results for Turbine A (downstream traverse)

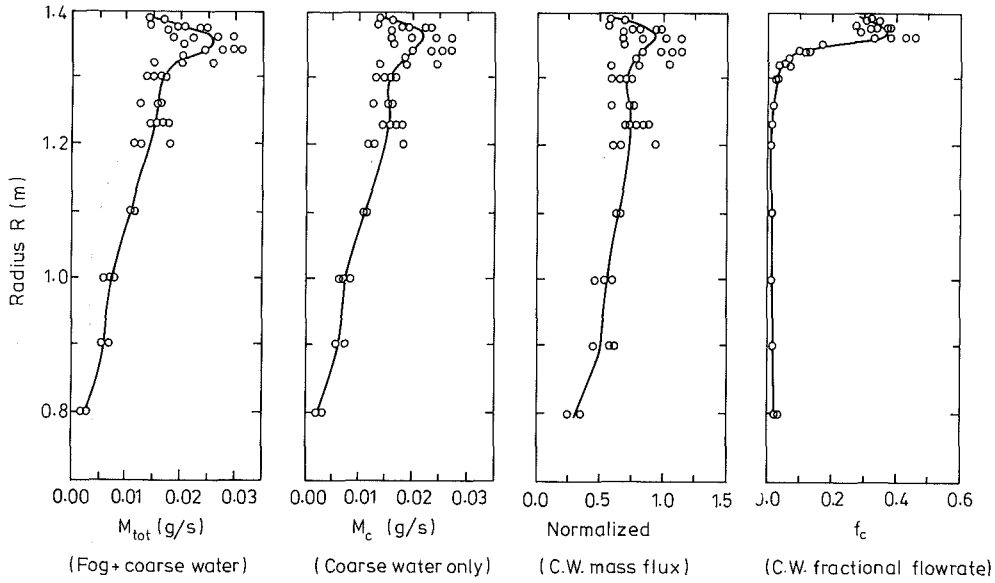

Fig. 10 Measured coarse water results for Turbine B (upstream traverse)

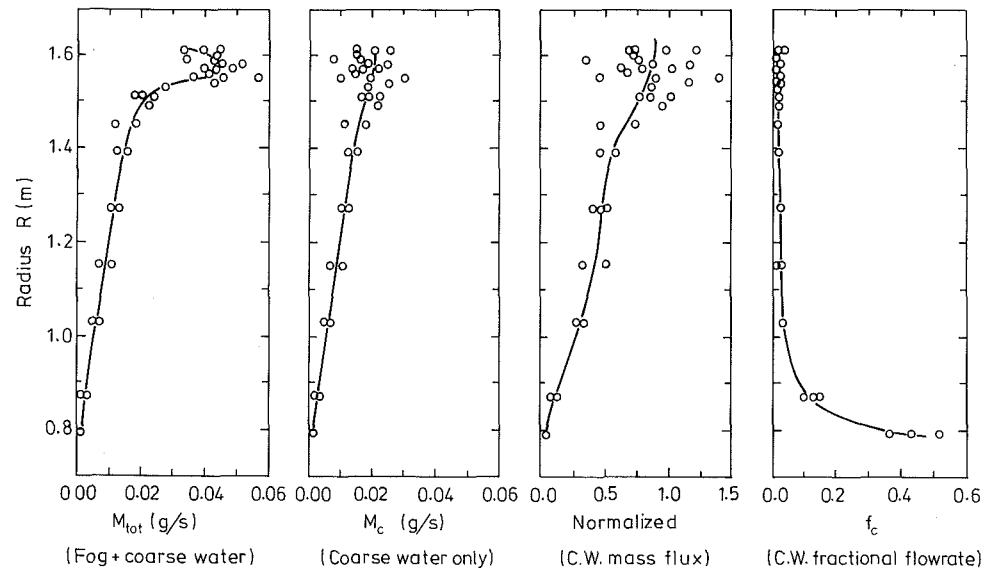

Fig. 11 Measured coarse water results for Turbine B (downstream traverse)

sumed that the flow angle of the film was equal to the measured steam angle at the point nearest the casing and also that the collection efficiency for the water film was unity.

Experimental Results

Experiments on Turbine A were performed during a period when the unit was operating with a load of 500 MW and a back pressure of 67 mbar. Measurements on Turbine B were taken during a particularly warm spell when the back pressure was 86 mbar, well above the design value. As the final stage was choked, it is unlikely that deposition rates and coarse water quantities were affected, but the exhause fog wetness fraction was lower than under normal operating conditions. Fog wetness fraction and Sauter mean droplet diameter obtained from the optical measurements are plotted in Figs. 5 and 6 for Turbines A and B, respectively. In each case, the shapes of the profiles upstream and downstream of the final stage are similar. The absolute value of wetness fraction is information confidential to the CEGB and wetnesses are presented in dimensionless form only.

The fog droplet size distribution at each measuring station was computed by the inversion procedure. The distribution was approximately constant over each traverse and Fig. 7 shows the exhaust distribution for Turbine A. It may be seen that the distribution peaks at a comparatively small droplet diameter, but there is a "tail" extending to diameters of about 1 μm. The fact that this tail makes a significant contribution to the wetness fraction is shown by the position of the mean diameters D_{30}, D_{32}, and D_{43}.

The results of the coarse water measurements appear in Figs. 8–11. Figures 8 and 9 show the results of the upstream and downstream traverses, respectively, for Turbine A and Figs. 10 and 11 show similar results for Turbine B. The four graphs labeled (*a*) to (*d*) in each figure are now discussed in turn:

***(a)* The Total Mass Collection Rate of Liquid M_t.** There is a general trend toward higher collection rates near the casing

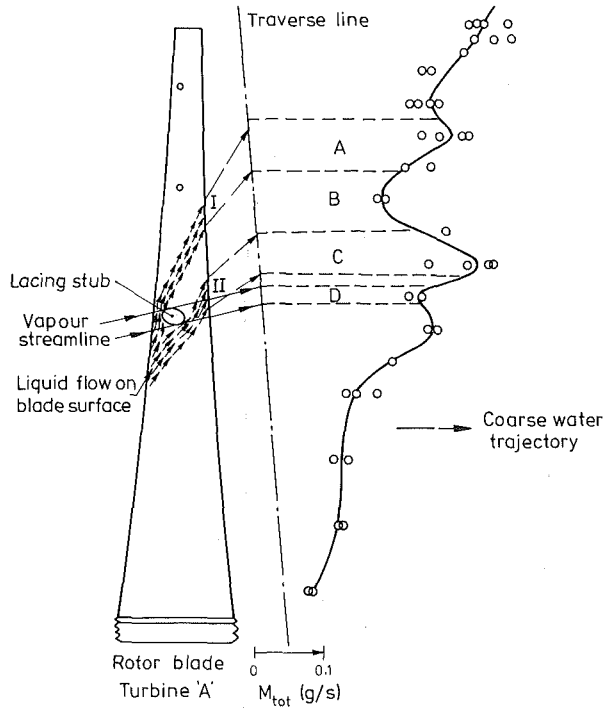

Fig. 12 Influence of lacing-stub on the coarse water distribution of Turbine A

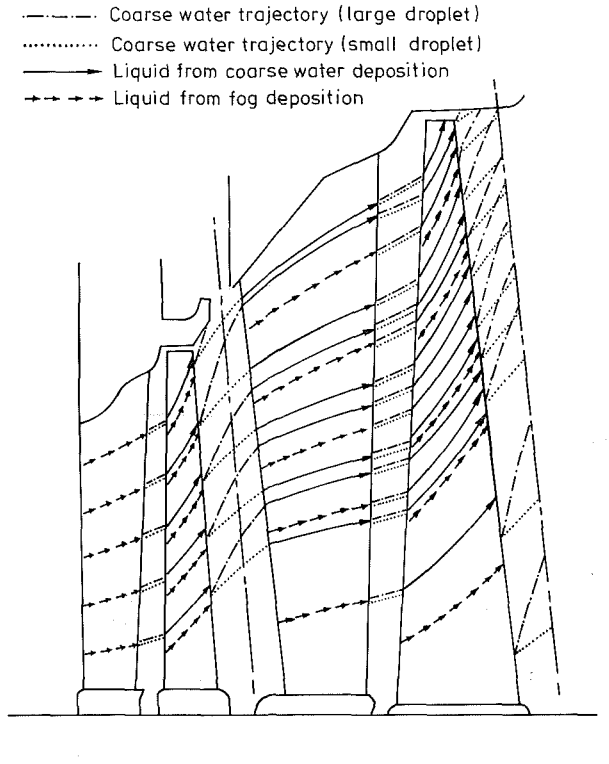

Fig. 13 Computed trajectories for the secondary liquid phase in Turbine A

in agreement with other measurements in steam turbines (Williams and Lord, 1976). This results from the movement of the secondary liquid phase on and after the rotor blades where it is subjected to strong centrifugal acceleration. The rather discontinuous distribution of Fig. 9(*a*) was produced not by experimental error, but by the presence of a lacing-stub on the last stage rotor of Turbine A (see Fig. 12). The liquid film on the blade evidently detached from the trailing edge at locations I and II, giving rise to the high concentrations *A* and *C* and low concentration *B* of coarse water at the traverse line. Another point of low concentration *D* existed at about the same level as the stub. This was caused by shielding of the fog by the stub itself.

Table 2 Integrated experimental results for Turbines A and B

	TURBINE 'A'		TURBINE 'B'	
	Upstream Traverse	Downstream Traverse	Upstream Traverse	Downstream Traverse
$(F_c)_{bulk}$ x 100%	2.5	3.4	1.7	2.0
$(F_c)_{film}$ x 100%	0.0	0.7	0.0	1.1
F_c x 100%	2.5	4.1	1.7	3.1
SDR x 100%	3.0		2.1	

For Turbine B, Figs. 10(*a*) and 11(*a*) show coarse water peaks near the casing for both upstream and downstream traverses. The same feature was observed by Williams and Lord (1976), who suggested there was a correlation between the tip leakage jet and the peaks. An alternative explanation is suggested below, however.

(*b*) The Mass Collection Rate of Coarse Water M_c. This was obtained by subtracting the collection rate of fog M_f from the total mass collection rate M_t. The curves are similar to those of graphs (*a*) and, in general, fog deposition on the probe was only found to be significant near the casing.

In connection with Turbine B, it is interesting to note that, after subtracting the fog collection rate, a peak in the coarse water distribution remained in the upstream but not the downsteam traverse (compare Figs. 10*b* and 11*b*). This may be related to the different casing profiles shrouding the rotor tips in stages 5 and 6 of Turbine B (see Fig. 2). Coarse water originating from the stator of the penultimate stage may conceivably move through the rotor tip leakage gap under the action of the steam flow and be sensed by the probe as a peak in the coarse water distribution, (Fig. 10*b*). In all other cases Figs. 8(*b*), 9(*b*), and 11(*b*), the coarse water is more likely to be deposited on the rotor blade tips or centrifuged directly to the casing.

It is therefore concluded that peaks in a coarse water traverse as observed by Williams and Lord (1976) are probably due to enhanced fog collection rather than coarse water tip leakage jets. In this respect it is significant that no fog correction was applied to the results reported by these authors as the fog droplet size could not be measured.

(*c*) The Axial Mass Flux of Coarse Water M_c. These profiles are similar to those of graphs (*b*) and were plotted after estimating the mean coarse water yaw angle $\bar{\alpha}$. A normalized scale has been used as the absolute values are data confidential to the CEGB.

(*d*) The Local Coarse Water Fraction f_c. This is the ratio of the local coarse water flow rate to the local total water flow rate (fog plus coarse water). It can be seen that f_c is always very small, of the order of 2–4 percent. (The higher values near the hub are misleadingly enhanced due to the low overall steam flow rates in these regions.)

The curves in Figs. 8–11 can be integrated over the blade height to give the total water flow rates entering and leaving each turbine final stage. The results are summarized in Table 2. If the mass flow rate of coarse water in the bulk flow is denoted by $(m_c)_{bulk}$, the mass flow rate of water on the casing

Table 3 Theoretical calculations of deposition rate for Turbines A and B

	TURBINE 'A'		TURBINE 'B'	
	STATOR	ROTOR	STATOR	ROTOR
F_I x 100%	0.78	1.25	0.41	0.45
F_D x 100%	1.25	1.03	0.68	1.19
$(F_I + F_D)$ x 100%	2.03	2.28	1.09	1.64
SDR x 100%	4.3		2.7	

by $(m_c)_{\text{film}}$, and the mass flow rate of fog by m_f, then the *integrated coarse water fraction* F_c is defined by

$$F_c = \frac{m_c}{m_c + m_f} \tag{4}$$

where m_c is the total coarse water flow rate, $(m_c)_{\text{bulk}} + (m_c)_{\text{film}}$. No particular significance is attached to the fraction of coarse water flowing on the casing. Coarse droplets are rapidly centrifuged toward the casing, as can be seen from the computed trajectories in Fig. 13, and the film flow rate is entirely dependent on the traverse position. Both turbines had steam extraction belts sited between stages 5 and 6 and hence the casing film flow rate was zero for both upstream traverses. The Stage Deposition Rate (SDR), also tabulated in Table 2, is the fraction of the fog mass flow rate entering the stage that is deposited on the blading. Thus

$$\text{SDR} = \frac{(m_c)_D - (m_c)_U}{(m_f)_U} \tag{5}$$

where subscripts D and U stand for downstream and upstream, respectively.

Comparison With Theory

Knowing the droplet size distribution at inlet to the final stage, together with details of the blade geometry for both stators and rotors, it is possible to calculate theoretically the deposition rate of fog droplets onto the blading. Calculations of deposition by inertial impaction were performed using the techniques described by Young and Yau (1988) and deposition by turbulent diffusion using the methods of Yau and Young (1987). Full details of the procedures and a comprehensive discussion of the results are presented in both references and will not be repeated here. Note, however, that Case Study 1 in the two references refers to the same geometry and flow conditions as Turbine A in the present report.

A summary of the results of the calculations is given in Table 3. F_I is the fractional inertial deposition rate and is defined as the fraction of the fog mass flow rate entering the stage under consideration that is deposited on the blading by inertial impaction. F_D is the fractional diffusional deposition rate and is defined similarly. The values of F_I, F_D, and the Stage Deposition Rate were computed from the full droplet size spectrum obtained from the light extinction measurements by the inversion procedure. Calculations with an equivalent monodispersion gave similar results when D_{43} was used to characterize the distribution, but the use of D_{32} or, especially, D_{30}, underestimated both types of deposition very significantly.

A comparison of the values of F_I and F_D in Table 3 suggests that inertial and diffusional deposition play comparable roles LP steam turbines. The deposition rates on the stationary and moving blades are also seen to be very similar. The Stage Deposition Rates should be compared with the experimental values of Table 2. Considering that previously published research was unable to reconcile theory and experiment to within one order of magnitude, the agreement is obviously excellent.

Discussion and Conclusions

The work described in this report has demonstrated that measurements of fog droplet size, wetness fraction, and coarse water quantities are consistent with present theories of inertial and diffusional deposition. Previous disagreement in the literature is explained by the assumption of a monodispersed fog droplet population based on the Sauter mean diameter D_{32}. The fog in LP turbines is polydispersed and it is the tail of the distribution which is mainly responsible for deposition on the blading. In performing deposition calculations with an equivalent monodispersion, the mean diameter D_{43} gives results compatible with a treatment using the full droplet spectrum.

Measurements of coarse water quantities using a new design of probe resulted in lower exhaust coarse water fractions than measurements by Williams and Lord (1976) using a catchpot probe (3–4 percent as opposed to 5–10 percent). It is not clear at this stage whether or not these figures constitute a disagreement. The results of Williams and Lord (1976) were based on fog wetness fractions estimated from the turbine condition line and were generally higher than values measured in the present work. Higher wetness levels imply higher deposition rates and therefore larger coarse water quantities. On the other hand, the design of catchpot type probes may result in reduced accuracy when traversing takes place insufficiently far downstream of the rotor trailing edge for the coarse droplets to have become aligned with the steam flow.

In summary, the authors believe that the results demonstrate the fundamental correctness of both theoretical methods and experimental measuring techniques in this area of wet steam research. They hope that the work will stimulate renewed interest in formulating theoretical prediction methods for wetness loss and turbine blade erosion.

Acknowledgments

The work was carried out jointly by the Whittle Laboratory, Cambridge University Engineering Department, and the Central Electricity Research Laboratories, Leatherhead. It was sponsored by a grant from the Central Electricity Generating Board. One of the authors (KKY) was supported by a Croucher Foundation Scholarship. Thanks are due to Dr. M. J. Moore of CERL for supporting the work, to Mr. R. Langford of CERL for performing the aerodynamic traverse measurements, and to NEI Parsons Ltd. for supplying the turbine blade geometric details.

References

Crane, R. I., and Moore, M. J., 1972, "Interpretation of Pitot Pressure in Compressible Two-Phase Flow," *J. Mech. Eng. Sci.*, Vol. 14, pp. 128–133.

Crane, R. I., 1973, "Deposition of Fog Drops on Low Pressure Steam Turbine Blades," *Int. J. Mech. Sci.*, Vol. 15, pp. 613–631.

Davies, C. N., and Peetz, C. V., 1956, "Impingement of Particles on a Transverse Cylinder," *Proc. Roy. Soc., London*, Vol. A234, p. 269.

Moore, M. J., and Sculpher, P., 1969, "Conditions Producing Concentrated Erosion in Large Steam Turbines," *Proc. IMechE*, Vol. 184, Pt. 3G (III), p. 45.

Moore, M. J., Walters, P. T., Crane, R. I., and Davidson, B. J., 1973, "Predicting the Fog Drop Size in Wet Steam Flows," *IMechE Conference on Heat and Fluid Flow in Steam and Gas Turbine Plant*, University of Warwick, Paper No. C37/73.

Moore, M. J., and Sieverding, C. H., 1976, *Two-Phase Steam Flow in Turbines and Separators*, Hemisphere, Washington, DC.

Stastny, M., 1979, "Structure of Secondary Liquid Phase Downstream of

Moving Blades in LP Cylinder Stages of Steam Turbines," *IMechE, Conference on Steam Turbines for the 1980's*, London, Paper No. C188/79, pp. 371–384.

Walters, P. T., 1973, "Optical Measurements of Water Droplets in Wet Steam Flows," *IMechE, Conference on Heat and Fluid Flow in Steam and Gas Turbine Plant*, University of Warwick, Paper No. C37/73.

Walters, P. T., 1980, "Practical Applications of Inverting Spectral Turbidity Data to Provide Aerosol Size Distributions," *Applied Optics*, Vol. 19, pp. 2353–2365.

Walters, P. T., 1985, "Wetness and Efficiency Measurements in L. P. Turbines With an Optical Probe as an Aid to Improving Performance," ASME/IMEE Power Generation Conference, Milwaukee, Paper No. 85-JPGC-GT-9.

Williams, G. J., and Lord, M. J., 1976, "Measurements of Coarse Water Distribution in the LP Cylinders of Operating Steam Turbines," *Proc. Instn. Mech. Engnrs.*, Vol. 190 (4/76), pp. 59-69.

Yau, K. K., and Young, J. B., 1987, "Deposition of Fog Droplets on Steam Turbine Blades by Turbulent Diffusion," ASME JOURNAL OF TURBOMACHINERY, Vol. 109, pp. 429–435.

Young, J. B., and Yau, K. K., 1988, "The Inertial Deposition of Fog Droplets on Steam Turbine Blades," ASME JOURNAL OF TURBOMACHINERY, Vol. 110, this issue.

APPENDIX

1 Calculation of the Mass Collection Rate of Fog by the Coarse Water Probe

The fog wetness fraction y_f and the local droplet size distribution were obtained from the optical measurements and the inversion procedure. The aerodynamic measurements gave the flow velocity V and the steam pitch angle ϕ. Assuming the fog to travel with the same velocity as the vapor, a valid assumption for submicron droplets, then

$$M_f = \bar{\eta}_c \left(\frac{y_f}{1-y_f}\right) \rho_g V\, h\, d\, \cos(\phi - \lambda) \tag{6}$$

where $\sin\lambda = \sin\gamma\cos\beta$ and γ is the inclination of the probe to the radial direction. $\bar{\eta}_c$ is the mean fog collection efficiency

$$\bar{\eta}_c = \frac{\int_0^{D_{\max}} \eta_c n(D) D^3 dD}{\int_0^{D_{\max}} n(D) D^3 dD} \tag{7}$$

and can be computed numerically from the known droplet size distribution and the universal collection efficiency curve (Fig. 4).

2 Calculation of the Axial Mass Flux of Coarse Water

Let $N(D)dD$ be the number density of coarse droplets having diameters in the range D to $D+dD$. Furthermore, let these be traveling with velocity $C(D)$, pitch angle $\psi(D)$, and yaw angle $\alpha(D)$ at the probe position. The mass collection rate of these droplets by the probe is then given by

$$dM_c = \eta_c \rho_l N(D) \left(\frac{\pi D^3}{6}\right) h\, d\, C(D)\, \cos[\psi(D) - \lambda(D)] dD \tag{8}$$

where $\sin\lambda(D) = \sin\gamma\cos\alpha(D)$. Their contribution to the axial mass flux is given by

$$dm_c = \rho_l N(D) \left(\frac{\pi D^3}{6}\right) C(D) \cos[\psi(D) - \lambda(D)] \cos\alpha(D) dD \tag{9}$$

Combining the two equations and setting $\eta_c = 1$ for coarse droplets gives

$$dm_c = \frac{\cos\alpha(D)}{hd} dM_c \tag{10}$$

The total axial mass flux of coarse water is therefore given by

$$m_c = \frac{1}{hd} \int_{D_{\min}}^{D_{\max}} \cos\alpha(D) dM_c = \frac{M_c \cos(\bar{\alpha})}{hd} \tag{11}$$

where $\bar{\alpha}$ is the mean coarse water yaw angle defined by

$$\cos(\bar{\alpha}) = \frac{1}{M_c} \int_{D_{\min}}^{D_{\max}} \cos\alpha(D) dM_c \tag{12}$$

R. Maier
Research Engineer.

J. Wachter[1]
Director.

Institut für Thermische Strömungsmaschinen
und Maschinenlaboratorium,
Universität Stuttgart,
Stuttgart, Federal Republic of Germany

Shock-Induced Flow Oscillations in Steam Turbine Diffusers

In exhaust diffusers of steam turbines pressure oscillations may occur at certain operating conditions, due to shock–boundary layer interactions. These self-excited flow oscillations are caused by the high-speed clearance flow between blade tip and outer contour, leading to an excitation of the running blades. The paper describes the behavior of this unsteady flow phenomenon in the diffuser, identified with steady state and unsteady measurements at the wall, along with probe measurements behind the runner blading. A deeper physical understanding was gained by simulation of this flow pattern on the base of the water analogy.

Introduction

The design of exhaust diffusers of large steam turbines in view of optimal pressure recovery is subjected to a significant limitation regarding the axial length of the diffuser. The two design criteria of maximum diffuser efficiency on one hand and minimum length on the other require an acceptable tradeoff, which can be sufficiently achieved by axial-radial diffusers (Wachter and Maier, 1985).

However, the flow conditions in diffusers of this type are extremely complicated. The strong deflection of the flow out of the axial to the radial direction in a relatively short distance leads to a local acceleration at the outer contour and deceleration at the inner contour. The relatively poor passage flow of the last stage around the hub causes large regions of separation, especially in partial load operation. Leaving the rotor, the flow into the diffuser also has a strong rotational momentum, which, however, may be of use for better pressure recovery (Kruse and Quest, 1980). Furthermore, the condenser underneath the turbine contributes to the strongly three-dimensional type of the diffuser flow. In addition, a clearance flow develops between the tip of the running blades and the outer casing, which, apart from reducing the stage efficiency, has a significant influence on the diffuser flow at the outer contour. The clearance flow, caused by the high pressure difference at the moving blades, forms a large region of supersonic flow in the diffuser, which is additionally accelerated by the curved outer diffuser shell, due to a Prandtl–Meyer expansion. This supersonic flow region is consequentially limited by a shock, caused by the back pressure, which is determined by the condenser pressure (Fig. 1).

At the point where a shock wave hits a solid wall, the boundary layer thickness increases or the flow may even separate because the boundary layer cannot cope with high pressure gradients. In addition, unsteady flow phenomena, known as self-excited shock-boundary layer oscillations, may occur. In this case, the shock causes a strong boundary layer separation affecting the downstream pressure, which in turn determines the actual position of the shock. The original position of the shock becomes unstable and the shock moves upstream, dragging its own flow separation behind, which, again, makes the shock move upstream even more. At the same time the shock intensity decreases and at a critical strength the flow reattaches completely, which happens at the latest when the shock reaches the rotor. An acceleration phase follows next and the original supersonic region is formed again. The shock wave limiting the supersonic region grows again and the entire process starts again.

Measurements in the exhaust diffuser of the last stage test stand at the Institut für Thermische Strömungsmaschinen, University of Stuttgart (Wachter and Jarosch, 1980), have

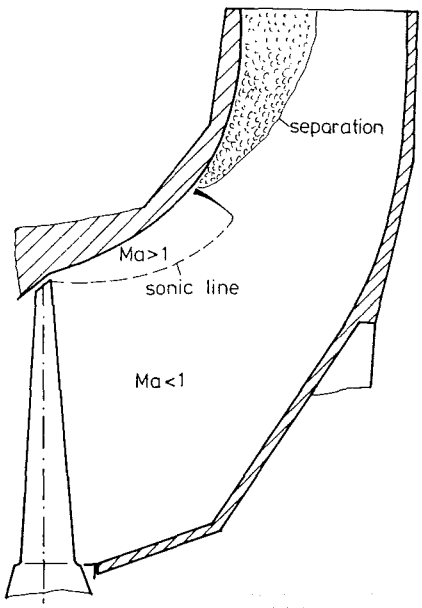

Fig. 1 Tip clearance flow in an exhaust diffuser

[1]Deceased in March 1986.

Contributed by the Gas Turbine Division of THE AMERICAN SOCIETY OF MECHANICAL ENGINEERS and presented at the 32nd International Gas Turbine Conference and Exhibit, Anaheim, California, May 31–June 4, 1987. Manuscript received at ASME Headquarters February 10, 1987. Paper No. 87-GT-124.

shown that under certain operational conditions of the turbine, strong pressure oscillations with specific frequencies occur, leading to an excitation of the runner blade. These pressure fluctuations are a consequence of the self-excited shock oscillations mentioned above. Additionally, this unsteady flow pattern is clearly noticeable acoustically by a strong buzzing noise, for this reason also called "diffuser buzz" (Dibelius et al., 1982).

In this paper some experimental results are presented that describe the behavior of the unsteady diffuser flow. The studies were carried out at three different diffusers to investigate the influence of different contours on the formation of this oscillating flow pattern.

Literature

The fundamental studies of Ackeret et al. (1946) on the influence of shocks on laminar and turbulent boundary layers have been followed by many research projects on this field. Most of these studies deal with the problem of transonic flow past airfoils, where shock-induced flow separation at the trailing edge severely affects the circulation and the aerodynamic lift. A detailed summary on this field is given by Deleres and Marvin (1986). The interactions of supersonic or hypersonic flow fields with regard to the flow around aircraft and ramjets are treated by Deleres and Marvin (1986) and Hankey and Holden (1975). Also, investigations on the unsteady flow past airfoils, called "buffeting," are presented widely in the literature. These unsteady flow conditions develop at Mach numbers about 0.8 to 0.9, causing a strong vibration of the aircraft. Therefore, so-called vibration limits of airfoil profiles have often been treated in earlier studies (Thomas, 1966). An extensive survey on this field is given by Finke (1977). However, similar flow phenomena could also be observed in other fields of applications. Fatigue failure of turbine blades occurred during investigations by Lawaczek and Amecke (1970), possibly caused by shock wave oscillations. The unsteady flow formation in linear blade cascades was examined by Araki et al. (1981), where shock-induced pressure oscillations could be observed in partial load operation. Henne et al. (1985) presented investigations on shock-boundary layer interactions and shock wave oscillations along with their aero-elastic interaction with the blades at single profiles and cascades. Meier (1974) showed that shock oscillations can also develop in curved channels and laval nozzles. Evans (1983) also took measurements at laval nozzles in order to examine the nature of self-excited shock oscillations in dry and wet steam where a strong effect on the condensation process was found. Finke (1977) observed similar phenomena in the transonic flow past biconvex circular arc airfoils and circular cylinders.

Few publications treat unsteady flow phenomena in diffusers. Extensive studies on a two-dimensional model were done by Bogar et al. (1983) and Sabjen et al. (1977, 1981) with the intention of obtaining information on the flow behavior of inlet diffusers of supersonic jet engines.

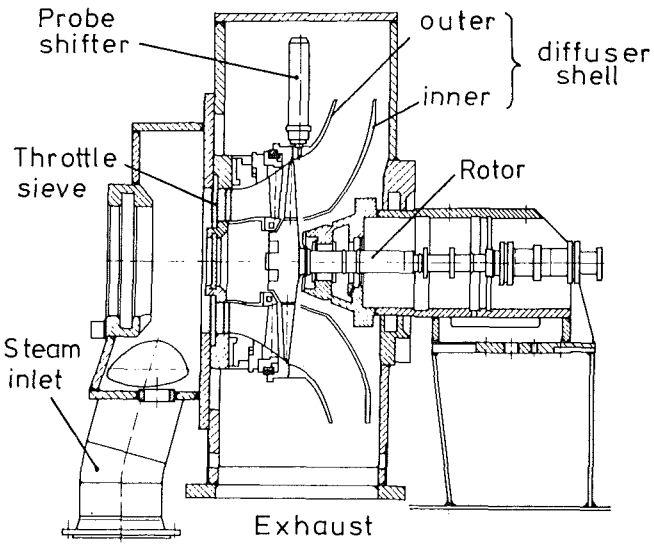

Fig. 2 Last-stage test stand

On shock wave oscillations in exhaust diffusers, no appreciable contributions can be found in the literature. Actually the phenomenon of "diffuser buzz" is already known, but it has only been treated in the context of acoustics (Dibelius et al., 1982). A possible reason for the lack of investigations in the steam turbine field could be the fact that these unsteady flow effects appear only at certain Mach numbers, which very often are reached only in operation beyond the design point, so that the diffuser buzz seldom arises in regular operating conditions. In addition, measuring this flow pattern in steam is very difficult and common methods to make shock oscillations visible, such as schlieren optics or density-gradient methods, are not applicable, mainly because of missing accessibility. Furthermore, experiments on large steam turbines under special operating conditions far beyond the design point are extremely difficult and expensive or often not feasible. A remedy consists in studies on model turbines that allow simulation of all possible operating states under practical conditions.

Experimental Setup

The last-stage test stand of the Institut für Thermische Strömungsmaschinen was designed and built in order to investigate the flow and vibration characteristics of the last stages of large steam turbines under practical conditions (Wachter and Eyb, 1982). The diffuser investigations were carried out with a single-stage version of the model turbine using a 1:4.21 model of a 10 m^2 last stage with a hub ratio of 0.41. The prestages were simulated by throttle sieves at the inlet (Fig. 2).

The unsteady flow behavior was examined at three different diffusers, two of them having an inlet aperture of the outer contour of 15 deg but different blade tip angles of 40 deg and

Nomenclature

A = amplitude
c = flow velocity
f = frequency
L = diffuser length
M = Mach number
p = pressure
u = rotational velocity
η = efficiency
ϕ = volumetric flow coefficient $= c_{2ax}/u_2$
ω = rotational frequency

Subscripts

ax = axial
b = blade
$cond$ = condenser
e = excitation
o = oscillation
$stat$ = static
tot = total

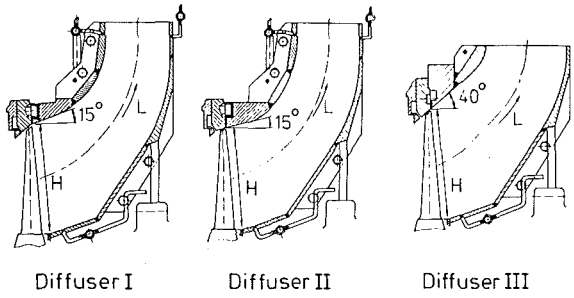

Fig. 3 Investigated diffusers

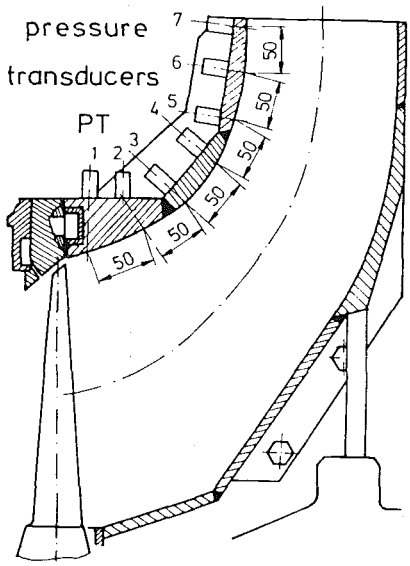

Fig. 4 Unsteady measurement technique

15 deg, respectively. Consequently the flow deflection in diffuser II is smoother than that in diffuser I. The smaller blade tip angle also allows a reduction of the clearance up to 60 percent, whereas the investigated diffuser II has only a 25 percent smaller clearance. The outer contour of diffuser III has a completely different design. Due to the 40 deg inlet aperture of the outer hood the flow through the moving blades has a greater radial component leading to a clear decrease of the stage efficiency (Wachter and Maier, 1985). On the other hand, the flow deflection in this diffuser is smaller than that in the 15 deg diffusers. At the same time the outer diffuser shell becomes considerably shorter.

Experimental Results

In order to study the oscillating behavior, unsteady pressure measurements as well as steady-state measurements were taken along the outer diffuser contour and at the diffuser inlet and outlet.

Unsteady Measurements at Diffuser I. In the following, the behavior of the unsteady diffuser flow is shown, using diffuser I as an example. The shock wave oscillations were measured with seven high-response pressure transducers mounted in the outer contour of diffuser I (Fig. 4). The natural frequency of the transducers was between 1000 and 1400 Hz, depending on the diffuser wall thickness, and was therefore an order of magnitude higher than the measured signals.

To get a better idea of the operating conditions for which shock oscillations occur, the operational range of the investigated last stage with diffuser I is shown in Fig. 5. The

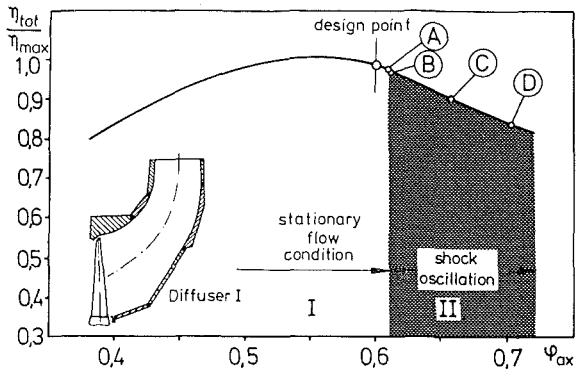

Fig. 5 Operational range of the last stage with diffuser I

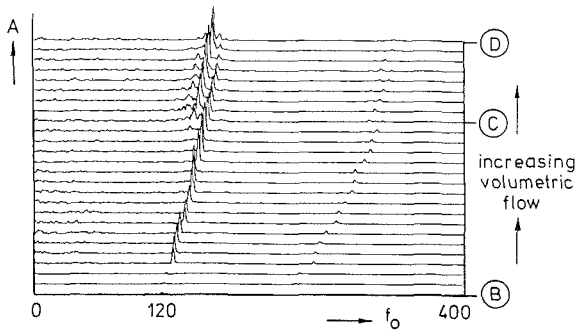

Fig. 6 Oscillation frequency at raised flow rate

design point of the last stage lies in the range of maximum efficiency at a volumetric flow coefficient of $\phi_{ax} = 0.6$.

If the mass flow through the last stage is increased, i.e., the volumetric flow is raised, pressure oscillations with frequencies around 100 Hz suddenly start to become effective at an operational state right beyond the design point (state A). These pressure oscillations begin at a volumetric flow coefficient ϕ_{ax} of approximately 0.61 and initially show short stochastic oscillations of a few cycles with heavy varying frequencies of 90 to 116 Hz. A very slight increase of the volumetric flow rate leads to a stable oscillation with an exactly triggered frequency of 120 Hz (state B). Figure 6 shows the oscillation behavior for a further increase of the volumetric flow rate.

It can be seen that an increase of the volumetric flow leads to higher oscillation frequencies and rapidly growing amplitudes. At a frequency of approximately 160 Hz a second frequency suddenly appears, which is about 10 Hz lower and increases parallel to the first frequency for a further increasing volumetric flow rate. At the same time the amplitude of the oscillation with the upper frequency decreases while the amplitude of the lower frequency steadily increases and finally becomes dominant. A reason for this behavior might be the development of not only a single shock, but of two successive shocks of different strength and position. For an increasing volumetric flow rate the initial major shock loses intensity, while the strength of the second shock grows until it takes the dominant role. A similar behavior was observed by Sabjen et al. (1977). For a further increase of the volumetric flow the oscillation suddenly stops at frequencies of approximately 176 Hz.

Figure 7 shows the real time signals of the seven high-response pressure transducers for different volumetric flow rates. Evidently, the shock oscillation initiates around pressure transducer 4, i.e., around the middle of the diffuser length. At a ϕ_{ax} of 0.615 only PT4 shows a noticeable signal of 132 Hz, while the other transducers show comparatively small amplitudes or no signals at all.

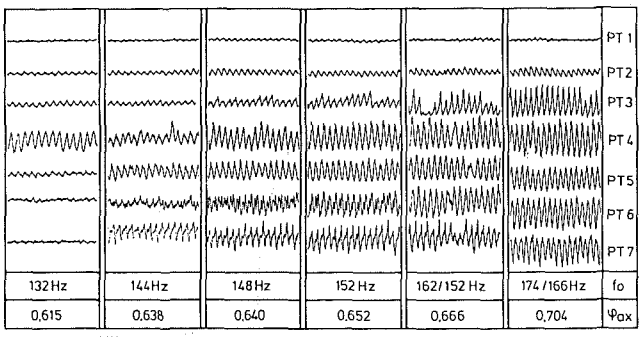

Fig. 7 Real time signals of high-response pressure transducers at different flow rates

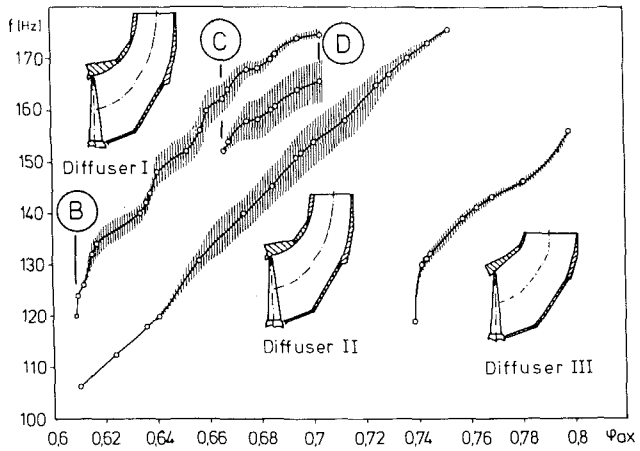

Fig. 8 Oscillation behavior of different diffusers

An increasing volumetric flow up to a ϕ_{ax} of 0.638 initially leads to an amplitude rise of the transducers downstream of PT4, while the pressure transducers upstream still show small amplitudes only. For a further increased volumetric flow rate of $\phi_{ax} = 0.64$ and a frequency of 148 Hz, pressure transducer PT3 also starts to oscillate, which indicates that, during the oscillation, the shock moves more and more upstream toward the tip clearance. At the same time the responses of transducer 6 and 7 additionally show oscillations of higher frequency.

Increasing the mass flow up to $\phi_{ax} = 0.704$ (Fig. 5, state D) leads to the double oscillations with frequencies of 174 and 166 Hz that were mentioned above. Especially for $\phi_{ax} = 0.666$, this behavior can be seen in the real time signals as a beating. In this state all transducers 3 to 7 show practically uniform fluctuations; the secondary frequencies at PT6 and PT7 have vanished. Clear signals also come from PT2, while PT1, located right behind the clearance, shows only very small pressure amplitudes. The reason is that up to the location of this transducer no noticeable supersonic velocities can develop. Consequently a shock wave that moves upstream toward the tip clearance steadily loses intensity, as the steady pressure measurements along the outer contour, given below, show more clearly.

Oscillation Behavior of Different Diffuser Contours. The two other diffusers show pressure fluctuations similar to that one observed in diffuser I. A comparison of the frequency and amplitude behavior of the three different diffusers is shown in Fig. 8.

In diffuser II the shock oscillations start approximately at the same volumetric flow rate as in diffuser I but the frequency is about 15 to 20 Hz lower. This frequency difference remains the same for an increasing flow rate. Apparently this behavior is a consequence of the smoother diffuser wall curvature, along with the resulting lower local flow acceleration and the smaller tip clearance. In diffuser II the oscillations also end at approximately 176 Hz. The behavior of the oscillation amplitudes of the diffusers I and II is practically identical; however, a double oscillation mode, as described for diffuser I, did not occur in diffuser II.

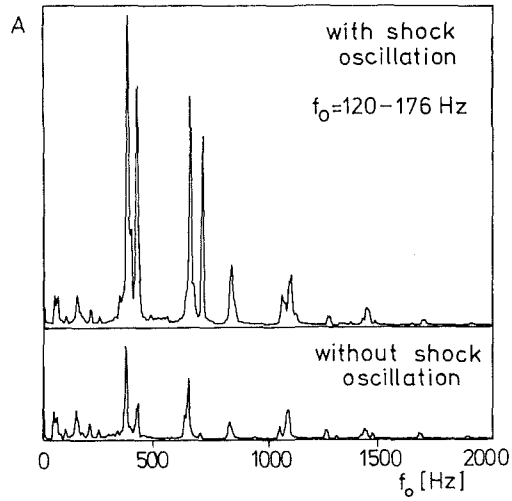

Fig. 9 Frequency spectra of a single blade without and with shock oscillations

The behavior of diffuser III is clearly different. In this diffuser pressure oscillations start to develop for considerably higher volumetric flow rates. The initial frequency, however, is also about 120 Hz. In comparison, the oscillations already vanish at 151 Hz. Also, the amplitudes of the pressure fluctuations are much lower than the amplitudes observed in diffuser I and II.

Effects on Running Blades. The influence of the moving shock on the flow is not restricted on the outer diffuser contour. The strong flow separation behind the shock leads to significant changes in the effective diffuser cross section, thus steadily forcing the main flow to move inward. Therefore, the oscillations affect the entire flow domain in the diffuser in such a manner that at every point in the diffuser, including the inner wall, pressure fluctuations with high amplitudes occur. The consequence is an alternating pressure wave acting on the running blades and causing forced vibrations of the blades.

According to Pfeiffer (1985), the superposition of any periodically fluctuating flow field of defined frequency with multiples of the rotational frequency may lead to resonances of the blades. This relation can be expressed in the intermodulation formula

$$f_e = m \cdot (j \cdot f_o \pm k \cdot \omega) \qquad m,\ k,\ j = 1,\ 2,\ 3,\ldots \qquad (1)$$

It follows from equation (1) that a single oscillation frequency f_o includes a whole spectrum of excitation frequencies f_e. Within the frequency range of the diffuser buzz from approximately 120 Hz to 176 Hz the blades are exposed to a multitude of excitation frequencies. Consequently, resonances are unavoidable when the turbine is running within or through the oscillation range. Figure 9 shows the comparison of the frequency spectra of a single blade without and with shock wave oscillations, the latter being recorded by going through the entire oscillation range of 120 to 176 Hz. The plots show that within this range four resonance frequencies of the blade were excited, causing vibration stresses three to eight times higher than without shock wave oscillations.

The enormous frequency bandwidth of the diffuser buzz makes it practically impossible to avoid resonances by tuning the running blades. The intensity of the vibration stresses, however, depends only on the intensity of the pressure oscilla-

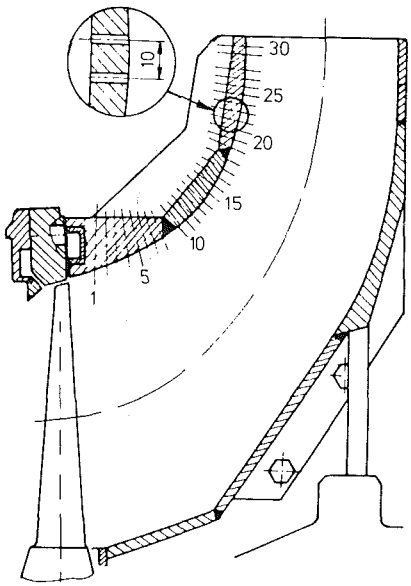

Fig. 10 Steady-state measurement technique

tions. All the investigations carried out so far have shown that although there are clearly increased alternating stresses, there occurred no dangerous stresses in the investigated blades.

Steady-State Flow Measurements at Diffuser II. The unsteady pressure measurements discussed so far are not sufficient to describe the phenomena in the exhaust diffuser completely. Therefore it is necessary to obtain some insight into the general behavior of the diffuser flow, too. For this reason, additional steady-state measurements at the diffuser II were carried out.

Static Pressure Distribution at the Outer Diffuser Contour. In order to locate the shock at the outer wall and to get an idea of the formation of the supersonic region, 30 static wall pressure bores were installed along the outer wall (Fig. 10). The static pressure distributions along the outer contour were measured for steady-state flow conditions (Fig. 5, state I) as well as for the existence of shock wave oscillations (Fig. 5, state II). Figure 11(*a*) illustrates the formation of the supersonic region for operating conditions of the turbine in state I, where the ratio of static pressure and condenser pressure is plotted versus the diffuser length L. The static pressure distribution for no-load operation at $\phi_{ax} = 0.39$ (upper curve) initially shows a slight pressure decrease behind the rotor, which is caused mainly by the local acceleration resulting from the strong deflection of the flow out of the axial to the radial direction.

Due to the present low-pressure difference at the running blade, no supersonic region can develop in this state. Beginning at $\phi_{ax} = 0.51$, the loading of the last stage, i.e., the increasing volumetric flow, leads to a distinct decrease of the static pressure with a pressure minimum located at about 20 percent of the diffuser length. For increasing volumetric flow rate, this local supersonic region becomes more and more dominant and at $\phi_{ax} = 0.63$ the region takes already more than 40 percent of the diffuser length. The static pressure is then only about 40 percent of the condenser pressure.

The end of the supersonic region, characterized by extremely low pressure, shows a very sharp pressure increase. However, due to the boundary layer interaction of the shock wave, the pressure distribution at the wall does not show a distinct jump. In the subsonic part of the boundary layer near the wall, a pressure disturbance can move upstream with sonic speed, which cannot be the case in the adjacent supersonic part. Therefore, the boundary layer already thickens a certain

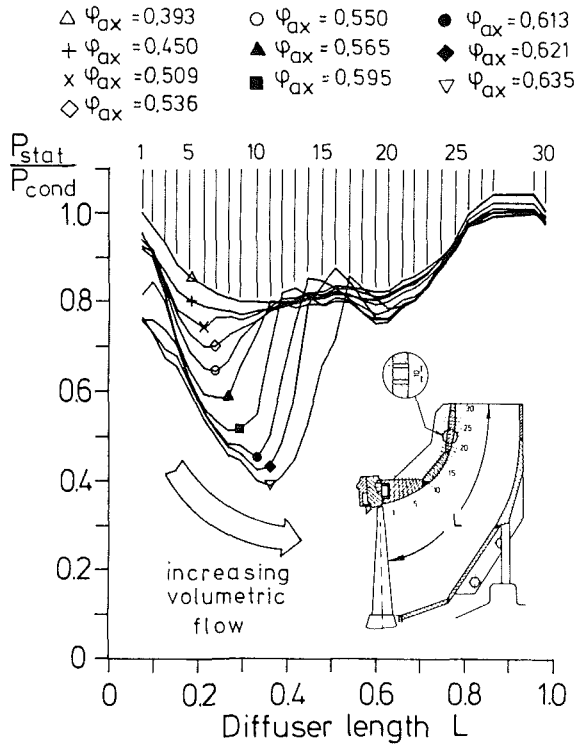

Fig. 11(*a*) Static pressure along the outer diffuser wall at different flow rates (state I)

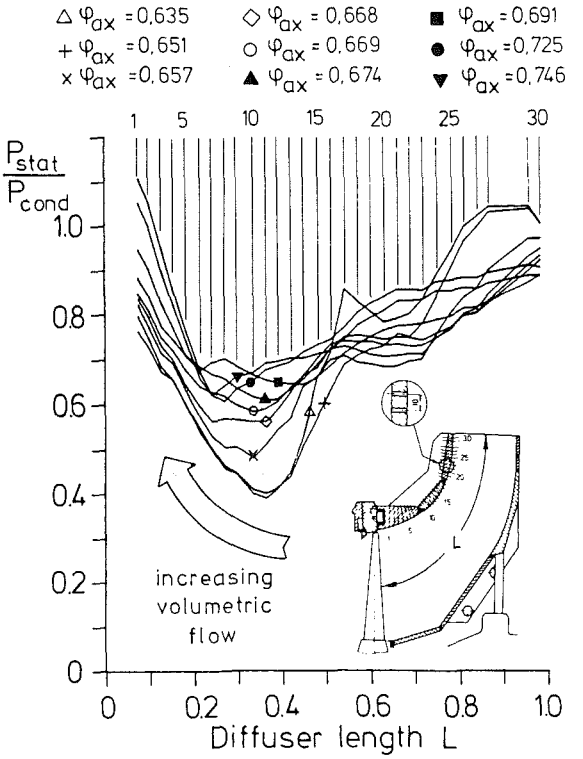

Fig. 11(*b*) Static pressure along the outer diffuser wall at different flow rates (state II)

distance upstream of the actual main shock as a consequence of the pressure increase moving ahead of the shock, leading to a typical λ shock. Thus the boundary layer widens the sharp pressure increase, which makes it difficult to determine the position of the shock exactly. Measurements of the pressure gradients at different distances to the wall (Deleres and Marvin, 1986) clearly show this behavior. Figure 11(*a*) also shows that the pressure minimum, i.e., the maximum of the velocity

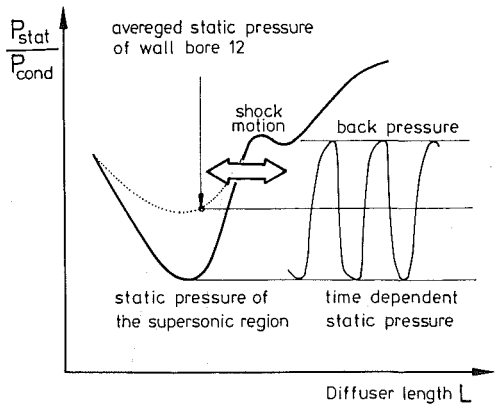

Fig. 12 Averaging of the pressure oscillations of the steady measuring static wall bores

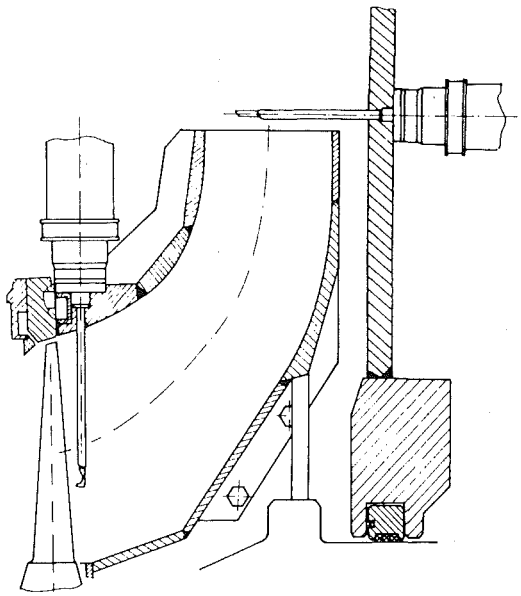

Fig. 13 Flow measurement technique

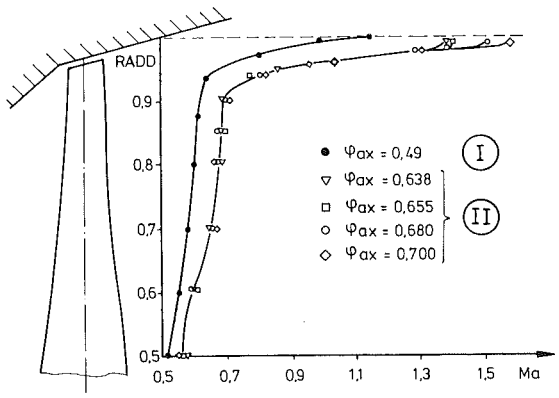

Fig. 14 Mach number distribution at the rotor exit at different flow rates

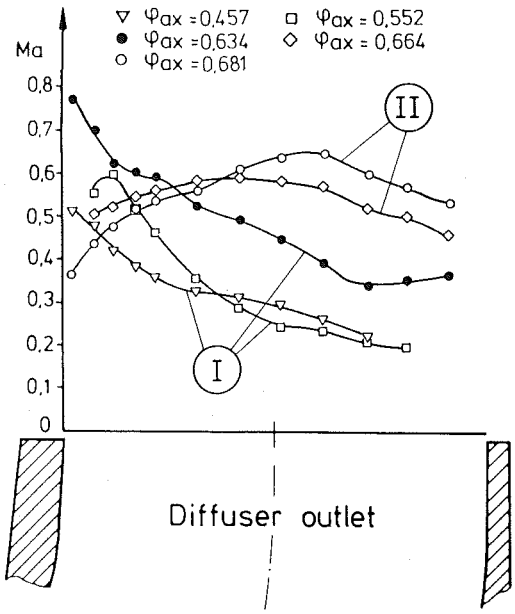

Fig. 15 Mach number distribution at diffuser exit at different volumetric flow rates

in the supersonic region, and therefore the steady shock also move toward the diffuser exit for an increasing volumetric flow rate. The continuation of the turbine loading from Fig. 11(*a*) in the range of the shock wave oscillation (state II) is shown in Fig. 11(*b*).

Starting with $\phi_{ax} = 0.62$ the shock front, located at about 50 percent of the diffuser length, clearly starts to move slightly upstream. As a consequence, the steady-state measuring static wall bores are able to show only averaged pressure values of the time-dependent supersonic and subsonic flow (Fig. 12). The more the shock front moves upstream for higher volumetric flow rates, the more the measured pressure values increase in the region of supersonic flow. This behavior is evident in Fig. 11(*b*).

It can be seen that for increasing volumetric flow rate the supersonic region and the adjacent shock become less distinct. At the same time the pressure at the exit of the runner wheel increases compared to the pressure at the diffuser outlet, which can be attributed to a choking of the diffuser II. In this state of choking, a raised mass flow is only possible by increasing the pressure upstream of the choked cross section. The relation of mass flow and static pressure then becomes linear (Wachter and Maier, 1985).

Flow Conditions at the Diffuser Inlet and Outlet. Apart from the static pressure distribution at the wall, the flow formation at the diffuser inlet and outlet is also of interest for obtaining information about the range of the tip clearance flow and the separation region. The flow measurements at the diffuser exit were carried out using a steady measuring wedge probe, whereas the measurements at the inlet were taken with a slightly smaller five-hole probe with a probe head diameter of 2.5 mm (Fig. 13).

Figure 14 shows the distribution of the absolute Mach numbers at the exit of the rotor for various volumetric flow rates in the range from 50 percent span to the outer wall.

The measurements for volumetric flow rates greater than 0.61 were carried out in the range of the pressure oscillations (state II), which coincides with the range of choking in the diffuser. The effect is that the flow properties cannot change any more, even for a high increase of the mass flow rate. This may be noted in Fig. 14. The Mach numbers at the rotor exit are practically identical for all of the four states. However, the Mach number at the tip clearance behind the rotor shows a different behavior: It keeps growing for an increasing mass flow rate. It can also be seen that in the cross-sectional measurement plane of the probe, located 20 mm behind the rotor, the tip clearance flow has already expanded up to a relative blade span of 0.92, which corresponds to a thickness of approximately 20 mm. The measurements taken in partial load operation (state I, $\phi_{ax} = 0.49$) show slightly lower Mach numbers along the blade height on the whole. The clearance flow in particular is much less developed in this state. It must

be mentioned that although the flow measurements were carried out in the state of shock wave oscillations, the measurement errors, resulting from averaging the pressure fluctuations, are negligible because of the low pressure amplitudes at this measuring point (compare Fig. 7).

The distribution of the Mach numbers at the diffuser exit for various volumetric flow rates is plotted in Fig. 15.

It is evident that for low volumetric flow rates (state I, $\phi_{ax} = 0.4$–0.6) the maximum outlet velocity occurs directly at the outer diffuser wall. This is a consequence of the strong deflection of the flow, which causes a high acceleration of the flow at the outer contour. For the measurements in the state of the diffuser buzz (state II), the steady measuring wedge probe is exposed to a fluctuating flow, which means that in one phase of the oscillation cycle the flow around the probe has its

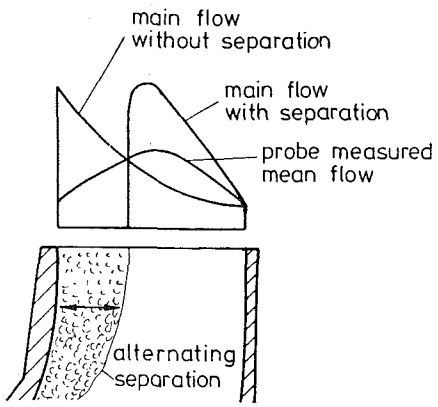

Fig. 16 Probe averaging of the oscillating flow

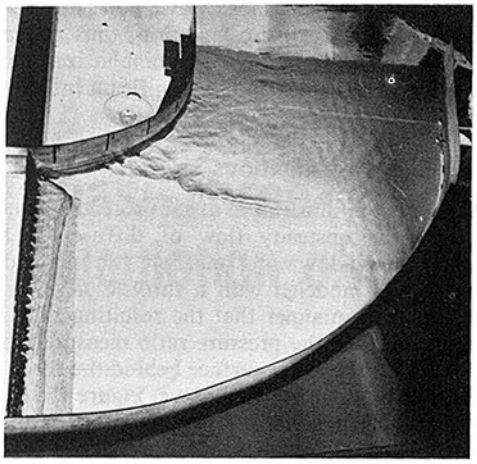

Fig. 17 Shallow water model of diffuser II

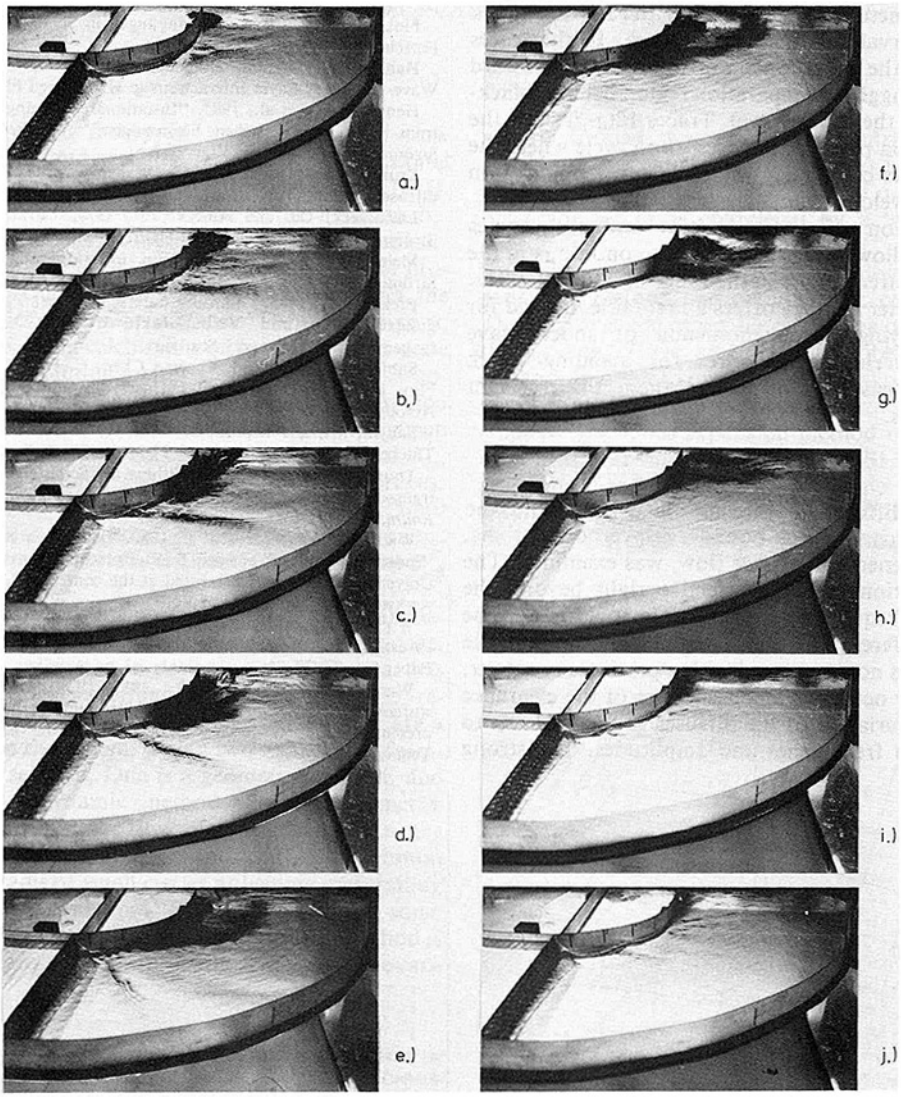

Fig. 18(*a-j*) Self-excited shock-boundary layer oscillation in the shallow water model of diffuser II ($\Delta t = 0.5$ s)

maximum velocity, whereas only a moment later the probe lies in the separation region. Therefore, the steady measuring wedge probe can only show an average value of the oscillating flow (Fig. 16). This finally becomes apparent in the velocity distribution; the maximum velocity is no longer located at the outer wall but is found in the middle of the diffuser exit. The measurements show that the separation region at the outer wall, caused by the moving shock wave, takes up to 50 percent of the entire diffuser exit cross section, thus displacing the main flow toward the inner wall. This emphasizes the effect of the unsteady flow behavior and its significant influence on the entire diffuser flow.

Shallow Water Investigations

To obtain a better illustration of the unsteady phenomena in the diffuser, the unsteady flow of diffuser II has been simulated by the shallow water analogy. The energy difference at the rotor was modeled with a throttle sieve, which was designed in such a manner that the resulting ratio of water levels corresponds to the pressure ratio measured in the turbine. To stabilize the water surface behind the throttle sieve a wire mesh was put on top of the sieve. Figure 17 shows a picture of the shallow water model with the developing tip clearance flow at the upper wall, which can be identified by the extremely sharp decrease of the water level and a shock (hydraulic jump in the water level) at the end.

In the following picture series photos of the moving shock wave, taken in intervals of 0.5 s, are shown. In the traces 18(*a–f*) one can see the shock wave moving upstream toward the throttle sieve, dragging its separation region behind (black-colored flow behind the shock wave). Traces 18(*g–j*) show the following acceleration phase of the oscillation cycle where the separation disappears completely while the supersonic region (low water level) develops again.

The transformation of the velocities and frequencies measured at the shallow water model to the conditions in the turbine gave similar frequencies in the range of 130 to 150 Hz. Thus the shallow water analogy offers a favorable method for systematically studying the phenomenon of shock wave oscillations and developing measures for avoiding shock oscillations or at least for displacing them to irrelevant operating conditions.

Summary

In the exhaust diffuser of the last-stage test stand the behavior of self-excited shock-boundary layer oscillations, caused by the high-energy clearance flow, was examined. The shock wave oscillations become effective right beyond the design point with frequencies from 120 Hz to 176 Hz. The comparison of different diffuser contours shows that the unsteady behavior is not connected with a particular contour, but that it generally occurs as a consequence of the clearance flow. However, a variation of the diffuser geometry leads to different oscillation frequencies and amplitudes. The strong flow separation behind the shock and the resulting effect on the entire diffuser flow leads to an excitation of the runner blades. In running the turbine through the oscillation range, several resonance frequencies of the blades were excited. A consequence is a clearly increased alternating stress which, however, is not dangerous for the blades in the considered case. Simulation of the unsteady phenomena with the shallow water analogy allows systematic studies to develop appropriate measures for diminishing shock wave oscillations in diffusers or displacing them into irrelevant operating conditions.

References

Ackeret, J., Feldmann, F., and Rott, N., 1946, "Untersuchungen an Verdichtungsstössen und Grenzschichten in schnell bewegten Gasen," Mitt. Inst. f. Aerotechnik E. T. H., Zürich.

Araki, T., et al., 1981, "Self-Excited Flow Oscillations in the Low Pressure Steam Turbine Cascade," *Proc. of the 2nd International Symposium on Aeroelasticity in Turbomachines*, P. Suter, ed., Juris Verlag.

Bogar, T. J., Sabjen, M., and Kroutil, J. C., 1983, "Charateristic Frequencies of Transonic Diffuser Flow Oscillations," *AIAA Journal*, Vol. 21, No. 9.

Deleres, J., and Marvin, J. G., 1986, "Shock-Wave Boundary Layer Interactions," AGARD-AG-280.

Dibelius, G., Dinger, H., and Jordan, H., 1982, *Turbomaschinenforschung, Orientierungsrahmen für die mittelfristige Forschung und Entwicklung auf einem bedeutendem Gebiet des Deutschen Maschinenbaus*, Springer-Verlag.

Evans, N. A., 1983, "Shock Wave/Boundary Layer Interaction in Dry and Wet Transonic Steam," ASME JOURNAL OF ENGINEERING FOR POWER, Vol. 105, pp. 782–791.

Finke, K., 1977, "Stossschwingungen in Schollnahen Strömungen," VDI-Forschungsheft 580.

Hankey, W. L., and Holden, M. S., 1975, "Two-Dimensional Shock Wave–Boundary Layer Interactions in High Speed Flows," AGARD-AG-203.

Henne, J. M., et al., 1985, "Instationäre Reibungs- und Stossvorgänge bei trans- und supersonischen Strömungen," VDI-Bericht 572.2, Thermische Strömungsmaschinen 85, VDI-Verlag.

Kruse, H., and Quest, J., 1980, "Experimentelle Untersuchungen an Nabendiffusoren hinter Turbinen," VDI-Bericht No. 361.

Lawaczeck, O., and Amecke, J., 1970, "Probleme der transsonischen Strömung durch Turbinenschaufelgitter," VDI-Forschungscheft 540.

Meier, G. E. A., 1974, "Ein instationäres Verhalten transsonischer Strömungen," Mitt. MPI für Strömungsforschung und AVA.

Pfeiffer, R., 1985, "Einfluss unterschiedlicher Paketierungen auf Schwingungsverhalten und Verbundfaktoren von Dampfturbinen-Beschaufelungen," Diss., University Stuttgart.

Sabjen, M., Kroutil, J. C., and Chen, C. P., 1977, "Unsteady Transonic Flow in a Two-Dimensional Diffuser," AGARD Conference on Unsteady Aerodynamics, Proc. No. 227.

Sabjen, M., and Kroutil, J. C., 1981, "Effects of Initial Boundary-Layer Thickness in Transonic Diffuser Flows," *AIAA Journal*, Vol. 19, No. 11.

Thomas, F., 1966, "Die Ermittlung der Schüttelgrenzen von Tragflügeln im transsonischen Geschwindigkeitsbereich," in: *Jahrb. 1966 Wiss. Ges. Luft- u. Raumfahrt* (WGLR), Braunschweig.

Wachter, J., and Jarosch, J., 1980, "Aufgaben und Ziele des Teilprojektes 'Endstufenprüfstand' aus dem Sonderforschungsbereich 'Wärmekraftwerk' der Universität Stuttgart," presented at the conference "Forschung in der Kraftwerkstechnik," Sammelband VGB.

Wachter, J., and Eyb, G., 1982, "The Last Stage Test Stand as a Facility to Investigate the Phenomena in the LP Part of Large Steam Turbines," ASME Paper No. 82-GT-71.

Wachter, J., and Maier, R., 1985, "Diffusoruntersuchungen am Endstufenversuchsstand im Hinblick auf Strömungsverhalten und Wirkungsgrad," presented at the conference "Forschung in der Kraftwerkstechnik," VGB-Tagung.

A Method for Aerodynamic Design of Blades in Quasi-Three-Dimensional Calculation of Turbomachines

Wang Zhengming
Institute of Engineering Thermophysics,
Chinese Academy of Sciences,
Beijing, People's Republic of China

A special inverse problem is formulated in which the shape of the mean streamline and the circumferential thickness distribution of the profile are given. On the basis of the series expansion method on a selected streamline, in quasi-three-dimensional aerodynamic design, the blade profile thickness is automatically fulfilled by computer. Six radial sections of a turbine blade are designed by this method.

Introduction

Based on the general theory of three-dimensional flow [1], the convenient and reliable quasi-three-dimensional design method has been used widely in turbomachines [2–5]. The quasi-three-dimensional calculation is the iteration between a mean S_2 streamsurface (S_{2m}) and several S_1 streamsurfaces of revolution (Fig. 1). In the whole computational process, the first S_{2m} calculation provides the shape and the stream filament thickness of S_1 surfaces. Then according to the data given by S_{2m} the calculation of profile form is done on S_1 surfaces of revolution. After the blade profile is obtained, the computations of the S_1 flow field will start and provide angular momentum $V_\theta r$ distributions on the mean streamline and angular thickness of stream filament for S_{2m} calculation of the second cycle. Therefore the process ($S_{2m} \rightarrow$ forming profile $\rightarrow S_1 \rightarrow S_{2m} \rightarrow \ldots$) is continued until convergence of the iteration, when the aerodynamic parameters on the same points in the computations of the S_{2m} and S_1 surfaces are equal.

In the process of quasi-three-dimensional design, calculation of the blade profile is very important. In practice, engineers are often interested in designing a profile that has excellent aerodynamic performance and satisfies the requirements on structure and strength. Of course, there are a lot of difficulties. In the general design two methods of forming profile may be selected. One is a geometric method, and the other is an aerodynamic method. For the geometric method of forming profile, the flow angle at inlet and exit, the maximum thickness of profile, the position of maximum thickness, and the radii of small circles at leading and trailing edge are given. The blade profile is composed of some analytical curves. The shortcoming of the geometric method is that there are not many varieties of profile and the profile cannot be formed directly on an arbitrary streamsurface of revolution that cannot be expanded to a plane; the calculation of geometric method is often carried out on an approximate conic surface or is completed by a transformation of the coordinates.

On the other hand, there is no obvious connection between geometric method and aerodynamic performance of blade. The stagger angle of profile cannot be obtained directly from the S_2 data. These are inherent problems in the geometric method. In order to overcome the weaknesses of the geometric method, aerodynamic methods of forming a profile have been studied. The series expansion method on selected streamline (i.e., Mean-Stream-Line Method – MSLM) presented in [6, 7] is a simple and effective aerodynamic method of designing profiles. The development of the method in China was mentioned in [8]. The method was utilized in many references

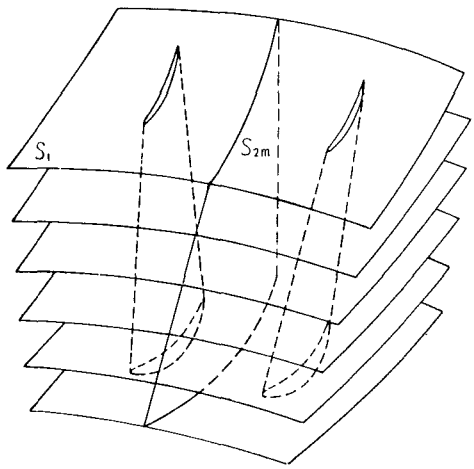

Fig. 1 A mean S_2 streamsurface (S_{2m}) and several S_1 stream surfaces of revolution

Contributed by the Gas Turbine Division of THE AMERICAN SOCIETY OF MECHANICAL ENGINEERS and presented at the 31st International Gas Turbine Conference and Exhibit, Düsseldorf, Federal Republic of Germany, June 8–12, 1986. Manuscript received by the Gas Turbine Division December 24, 1985. Paper No. 86-GT-192.

(e.g., [2, 3]). But in the computation of profiles on the surface of revolution one problem has not been solved so far. The calculation of MSLM depends on the shape of the mean streamline and the aerodynamic parameters on it, which are provided by the calculation on S_{2m}. In the initial cycles of quasi-three-dimensional iteration, the data given by S_{2m} are tentative. Therefore, the thickness distribution obtained according to the data provided by S_{2m} may be unsatisfactory. The local thickness may be either too big or too small, sometimes even negative. In order to solve the practical problem, there are two solutions. The first one is to modify the profile, and the second one is to modify the data given by S_{2m}. However, it is very difficult and troublesome. Therefore, another method must be found with the help of which the requirements of structure, strength, regularity, and aerodynamic performance can be satisfied and the modification work can be automatically completed by the computer.

In this paper, the computational process of a special inverse problem is composed in which the shape of the mean streamline and the circumferential thickness distribution of the profile are given. The profile with reasonable shape may be formed directly on the S_1 surface of revolution. The presented method has been used successfully in practical design.

Basic Equations and Computation Formulae

On the stream surface of revolution (blade to blade), when the flow field at the inlet is uniform, for inviscid adiabatic, and steady relative flow, the following basic equations can be employed:

$$\frac{\partial(\tau\rho w_l r)}{\partial l}+\frac{\partial(\tau\rho w_\phi)}{\partial\phi}=0 \tag{1}$$

$$\frac{1}{r}\frac{\partial w_l}{\partial\phi}-\frac{\partial w_\phi}{\partial l}-\left(\frac{w_\phi}{r}+2\omega\right)\sin\sigma=0 \tag{2}$$

$$\frac{\rho}{\rho_i}=\left(\frac{I+1/2\omega^2r^2-1/2w^2}{h_i}\right)^{\frac{1}{k-1}} \tag{3}$$

Based on the concept of MSLM, if the shape of a selected streamline and the variation of an aerodynamic parameter along the streamline are known, it is possible to derive the expressions of the first-order, the second-order, and even higher order partial derivatives of various aerodynamic parameters. Then, according to the given mass flow, a new streamline or a channel boundary can be obtained with the help of the Taylor series expansion. The main formulae are expressed as follows:

$$\frac{\partial w_\phi}{\partial\phi}=\frac{\cos^2\beta}{\rho}\left[-\frac{1}{\tau}\frac{d(\tau r\rho w_l)}{dl}+\rho r\tan\beta\frac{dw_\phi}{dl}+\rho r\tan\beta\left(\frac{w_\phi}{r}+2\omega\right)\sin\sigma\right] \tag{4}$$

$$\frac{\partial w_l}{\partial\phi}=r\frac{dw_\phi}{dl}-\tan\beta\frac{\partial w_\phi}{\partial\phi}+(w_\phi+2\omega r)\sin\sigma \tag{5}$$

$$\frac{\partial\rho}{\partial\phi}=-\frac{\rho}{(k-1)\,(I+1/2\omega^2r^2-1/2w^2)}\left(w_l\frac{\partial w_l}{\partial\phi}+w_\phi\frac{\partial w_\phi}{\partial\phi}\right) \tag{6}$$

$$\frac{\partial(\rho w_l)}{\partial\phi}=\rho\frac{\partial w_l}{\partial\phi}+w_l\frac{\partial\rho}{\partial\phi} \tag{7}$$

$$\frac{\partial^2w_\phi}{\partial\phi^2}=\frac{\cos^2\beta}{\rho}\left\{2\tan\beta\frac{\partial w_l}{\partial\phi}\frac{\partial\rho}{\partial\phi}-2\frac{\partial\rho}{\partial\phi}\frac{\partial w_\phi}{\partial\phi}-\frac{1}{\tau}\frac{d}{dl}\left(\tau r\frac{\partial(\rho w_l)}{\partial\phi}\right)+r\rho\tan\beta\frac{d}{dl}\left(\frac{\partial w_\phi}{\partial\phi}\right)+\rho\tan\beta\frac{\partial w_\phi}{\partial\phi}\sin\sigma\right\} \tag{8}$$

$$\frac{\partial^2w_l}{\partial\phi^2}=r\frac{d}{dl}\left(\frac{\partial w_\phi}{\partial\phi}\right)-\tan\beta\frac{\partial^2w_\phi}{\partial\phi^2}+\sin\sigma\frac{\partial w_\phi}{\partial\phi} \tag{9}$$

$$\frac{\partial^2\rho}{\partial\phi^2}=\frac{2-k}{\rho}\left(\frac{\partial\rho}{\partial\phi}\right)^2-\frac{\rho}{(k-1)(I+1/2\omega^2r^2-1/2w^2)}\left[w_l\frac{\partial^2w_l}{\partial\phi^2}+\left(\frac{\partial w_l}{\partial\phi}\right)^2+w_\phi\frac{\partial^2w_\phi}{\partial\phi^2}+\left(\frac{\partial w_\phi}{\partial\phi}\right)^2\right] \tag{10}$$

$$\frac{\partial^2(\rho w_l)}{\partial\phi^2}=2\frac{\partial\rho}{\partial\phi}\frac{\partial w_l}{\partial\phi}+\rho\frac{\partial^2w_l}{\partial\phi^2}+w_l\frac{\partial^2\rho}{\partial\phi^2} \tag{11}$$

$$\frac{\partial^3w_\phi}{\partial\phi^3}=\frac{\cos^2\beta}{\rho}\left\{3\tan\beta\left(\frac{\partial^2\rho}{\partial\phi^2}\frac{\partial w_l}{\partial\phi}+\frac{\partial\rho}{\partial\phi}\frac{\partial^2w_l}{\partial\phi^2}\right)-3\left(\frac{\partial^2\rho}{\partial\phi^2}\frac{\partial w_\phi}{\partial\phi}+\frac{\partial\rho}{\partial\phi}\frac{\partial^2w_\phi}{\partial_\phi{}^2}\right)-\frac{1}{\tau}\frac{d}{dl}\left[\tau r\frac{\partial^2}{\partial\phi^2}(\rho w_l)\right]+\rho r\tan\beta\frac{d}{dl}\left(\frac{\partial^2w_\phi}{\partial\phi^2}\right)+\rho\tan\beta\sin\sigma\frac{\partial^2w_\phi}{\partial\phi^2}\right\} \tag{12}$$

$$\frac{\partial^3w_l}{\partial\phi^3}=r\frac{d}{dl}\left(\frac{\partial^2w_\phi}{\partial\phi^2}\right)-\tan\beta\frac{\partial^3w_\phi}{\partial\phi^3}+\sin\sigma\frac{\partial^2w_\phi}{\partial\phi^2} \tag{13}$$

$$\frac{\partial^3\rho}{\partial\phi^3}=(-k^3+5k-6)\frac{1}{\rho^2}\left(\frac{\partial\rho}{\partial\phi}\right)^3$$

Nomenclature

a = speed of sound
B = width of cascade in direction l
F = special function in the paper
h = enthalpy of gas per unit mass
I = relative stagnation rothalpy
k = ratio of specific heat
l, ϕ = orthogonal curvilinear coordinates on S_1 surface of revolution
r = radius
t = cascade spacing
w = relative velocity of gas
β = $\tan^{-1}(W_\phi/W_l)$
ρ = density of gas
σ = $\tan^{-1}(dr/dz)$
τ = normal thickness of stream filament
ψ = stream function
ω = angular velocity of rotor

Superscripts

$\bar{}$ = nondimensional
(n) = nth iteration
(ν) = νth iteration

Subscripts

i = at inlet
j = ordinal number of calculation stations along l direction
l = component on l direction
p = pressure surface
s = suction surface
ϕ = component in ϕ direction
$*$ = critical

$$+(6-3\,k)\,\frac{1}{\rho}\,\frac{\partial\rho}{\partial\phi}\,\frac{\partial^2\rho}{\partial\phi^2}$$

$$-\frac{\rho}{(k-1)\,(I+1/2\omega^2r^2-1/2w^2)}\left[3\,\frac{\partial w_l}{\partial\phi}\,\frac{\partial^2 w_l}{\partial\phi^2}\right.$$

$$\left.+3\,\frac{\partial w_\phi}{\partial\phi}\,\frac{\partial^2 w_\phi}{\partial\phi^2}+w_l\,\frac{\partial^3 w_l}{\partial\phi^3}+w_\phi\,\frac{\partial^3 w_\phi}{\partial\phi^3}\right] \tag{14}$$

$$\frac{\partial^3(\rho w_l)}{\partial\phi^3}=w_l\,\frac{\partial^3\rho}{\partial\phi^3}+3\,\frac{\partial^2\rho}{\partial\phi^2}\,\frac{\partial w_l}{\partial\phi}$$

$$+3\,\frac{\partial\rho}{\partial\phi}\,\frac{\partial^2 w_l}{\partial\phi^2}+\rho\,\frac{\partial^3 w_l}{\partial\phi^3} \tag{15}$$

$$\frac{\partial^4 w_\phi}{\partial\phi^4}=\frac{\cos^2\beta}{\rho}\left\{\tan\beta\,(6\,\frac{\partial^2\rho}{\partial\phi^2}\,\frac{\partial^2 w_l}{\partial\phi^2}+4\,\frac{\partial w_l}{\partial\phi}\,\frac{\partial^3\rho}{\partial\phi^3}\right.$$

$$+4\,\frac{\partial\rho}{\partial\phi}\,\frac{\partial^3 w_l}{\partial\phi^3}\Big)-\Big[6\,\frac{\partial^2\rho}{\partial\phi^2}\,\frac{\partial^2 w_\phi}{\partial\phi^2}+4\,\frac{\partial w_\phi}{\partial\phi}\,\frac{\partial^3\rho}{\partial\phi^3}$$

$$+4\,\frac{\partial\rho}{\partial\phi}\,\frac{\partial^3 w_\phi}{\partial\phi^3}\Big]-\frac{1}{\tau}\,\frac{d}{dl}\left[\tau r\,\frac{\partial^3}{\partial\phi^3}\,(\rho w_l)\right]$$

$$\left.+r\rho\,\tan\beta\,\frac{d}{dl}\left(\frac{\partial^3 w_\phi}{\partial\phi^3}\right)+\rho\,\tan\beta\,\sin\sigma\,\frac{\partial^3 w_\phi}{\partial\phi^3}\right\} \tag{16}$$

$$\frac{\partial^4 w_l}{\partial\phi^4}=r\,\frac{d}{dl}\left(\frac{\partial^3 w_\phi}{\partial\phi^3}\right)-\tan\beta\,\frac{\partial^4 w_\phi}{\partial\phi^4}+\sin\sigma\,\frac{\partial^3 w_\phi}{\partial\phi^3} \tag{17}$$

$$\frac{\partial^4\rho}{\partial\phi^4}=(-k^3+9k^2-26k+24)\,\frac{1}{\rho^3}\left(\frac{\partial\rho}{\partial\phi}\right)^4$$

$$+(-6k^2+30k-36)\,\frac{1}{\rho^2}\left(\frac{\partial\rho}{\partial\phi}\right)^2\,\frac{\partial^2\rho}{\partial\phi^2}$$

$$+(8-4k)\,\frac{1}{\rho}\,\frac{\partial\rho}{\partial\phi}\,\frac{\partial^3\rho}{\partial\phi^3}+(6-3k)\,\frac{1}{\rho}\left(\frac{\partial^2\rho}{\partial\phi^2}\right)^2$$

$$-\frac{\rho}{(k-1)(I+1/2w^2r^2-1/2w^2)}\left[3\left(\frac{\partial^2 w_l}{\partial\phi^2}\right)^2\right.$$

$$+4\,\frac{\partial w_l}{\partial\phi}\,\frac{\partial^3 w_l}{\partial\phi^3}+3\left(\frac{\partial^2 w_\phi}{\partial\phi^2}\right)^2+4\,\frac{\partial w_\phi}{\partial\phi}\,\frac{\partial^3 w_\phi}{\partial\phi^3}$$

$$\left.+w_l\,\frac{\partial^4 w_l}{\partial\phi^4}+w_\phi\,\frac{\partial^4 w_\phi}{\partial\phi^4}\right] \tag{18}$$

$$\frac{\partial^4(\rho w_l)}{\partial\phi^4}=6\,\frac{\partial^2\rho}{\partial\phi^2}\,\frac{\partial^2 w_l}{\partial\phi^2}+4\,\frac{\partial w_l}{\partial\phi}\,\frac{\partial^3\rho}{\partial\phi^3}+4\,\frac{\partial\rho}{\partial\phi}\,\frac{\partial^3 w_l}{\partial\phi^3}$$

$$+\rho\,\frac{\partial^4 w_l}{\partial\phi^4}+w_l\,\frac{\partial^4\rho}{\partial\phi^4} \tag{19}$$

$\partial(\rho w_l)/\partial\phi$, $\partial^2(\rho w_l)/\partial\phi^2$, $\partial^3\,(\rho w_l)/\partial\phi^3$, $\partial^4\,(\rho w_l)/\partial\phi^4$,. . . on the mean streamline are the base of the series solution by stream function algorithm.

In this paper the following nondimensional parameters are employed:

$$\bar r=\frac{r}{B}\qquad \bar\tau=\frac{\tau}{B}$$

$$\overline{\rho w_l}=\frac{\rho w_l}{\rho_{*i}a_{*i}}\qquad \bar\psi=\frac{\psi}{\rho_{*i}a_{*i}B^2}$$

Then the following formulae can be obtained:

$$\frac{\partial\phi}{\partial\bar\psi}=\frac{1}{\bar\tau\bar r}\,\frac{1}{\overline{\rho w_l}} \tag{20}$$

$$\frac{\partial^2\phi}{\partial\bar\psi^2}=-\frac{1}{(\bar\tau r)^2}\,\frac{1}{(\overline{\rho w_l})^3}\,\frac{\partial(\overline{\rho w_l})}{\partial\phi} \tag{21}$$

$$\frac{\partial^3\phi}{\partial\bar\psi^3}=\frac{1}{(\bar\tau\bar r)^3}\left[\frac{3}{(\overline{\rho w_l})^5}\left(\frac{\partial(\overline{\rho w_l})}{\partial\phi}\right)^2\right.$$

$$\left.-\frac{1}{(\overline{\rho w_l})^4}\,\frac{\partial^2(\overline{\rho w_l})}{\partial\phi^2}\right] \tag{22}$$

$$\frac{\partial^4\phi}{\partial\bar\psi^4}=\frac{1}{(\bar\tau\bar r)^4}\left\{-15\,\frac{1}{(\overline{\rho w_l})^7}\left[\frac{\partial(\overline{\rho w_l})}{\partial\phi}\right]^3+10\right.$$

$$\left.\frac{1}{(\overline{\rho w_l})^6}\,\frac{\partial(\overline{\rho w_l})}{\partial\phi}\,\frac{\partial^2(\overline{\rho w_l})}{\partial\phi^2}-\frac{1}{(\overline{\rho w_l})^5}\,\frac{\partial^3(\overline{\rho w_l})}{\partial\phi^3}\right\} \tag{23}$$

$$\frac{\partial^5\phi}{\partial\bar\psi^5}=\frac{1}{(\bar\tau\bar r)^5}\left\{105\,\frac{1}{(\overline{\rho w_l})^9}\left[\frac{(\overline{\rho w_l})}{\partial\phi}\right]^4\right.$$

$$-105\,\frac{1}{(\overline{\rho w_l})^8}\left[\frac{\partial(\overline{\rho w_l})}{\partial\phi}\right]^2\,\frac{\partial^2(\overline{\rho w_l})}{\partial\phi^2}$$

$$+15\,\frac{1}{(\overline{\rho w_l})^7}\,\frac{\partial(\overline{\rho w_l})}{\partial\phi}\,\frac{\partial^3(\overline{\rho w_l})}{\partial\phi^3}$$

$$\left.+10\,\frac{1}{(\overline{\rho w_l})^7}\left[\frac{\partial^2(\overline{\rho w_l})}{\partial\phi^2}\right]^2-\frac{1}{(\overline{\rho w_l})^6}\,\frac{\partial^4(\overline{\rho w_l})}{\partial\phi^4}\right\} \tag{24}$$

$$\phi_p=\phi_m+\left(\frac{\partial\phi}{\partial\bar\psi}\right)_m(\bar\psi_p-\bar\psi_m)+\frac{1}{2!}\left(\frac{\partial^2\phi}{\partial\bar\psi^2}\right)_m(\bar\psi_p-\bar\psi_m)^2$$

$$+\frac{1}{3!}\left(\frac{\partial^3\phi}{\partial\bar\psi^3}\right)_m(\bar\psi_p-\bar\psi_m)^3+\frac{1}{4!}\left(\frac{\partial^4\phi}{\partial\bar\psi^4}\right)_m(\bar\psi_p-\bar\psi_m)^4$$

$$+\frac{1}{5!}\left(\frac{\partial^5\phi}{\partial\bar\psi^5}\right)_m(\bar\psi_p-\bar\psi_m)^5 \tag{25}$$

$$\phi_s=\phi_m+\left(\frac{\partial\phi}{\partial\bar\psi}\right)_m(\bar\psi_s-\bar\psi_m)+\frac{1}{2!}\left(\frac{\partial^2\phi}{\partial\bar\psi^2}\right)_m(\bar\psi_s-\bar\psi_m)^2+$$

$$+\frac{1}{3!}\left(\frac{\partial^3\phi}{\partial\bar\psi^3}\right)_m(\bar\psi_s-\bar\psi_m)^3+\frac{1}{4!}\left(\frac{\partial^4\phi}{\partial\bar\psi^4}\right)_m(\bar\psi_s-\bar\psi_m)^4$$

$$+\frac{1}{5!}\left(\frac{\partial^5\phi}{\partial\bar\psi^5}\right)_m(\bar\psi_s-\bar\psi_m)^5 \tag{26}$$

where ϕ_p and ϕ_s show the ϕ coordinates of channel boundaries obtained in the calculation.

Iterative Procedure and Computed Results

In quasi-three-dimensional design, it is important to consider the aerodynamic performance, structure, strength, and stacking of profiles. In this paper, the automatic adjustment of profiles is achieved in the following iterative manner.

The shape of the mean streamline and the density distribution on it provided by S_{2m} are the basis for obtaining the channel boundary of cascade with series expansion. In former calculations the first three terms of the series were taken. In order to improve calculation accuracy the first five terms of the series may be taken. A method of two-step expansion, in which only the first three terms are taken, is also tried in this paper. Many examples show that either higher order expansion [9, 10] or two-step expansion is beneficial to the accuracy of the calculations. Especially, the method of two-step expansion is more appropriate for cascades of small solidity.

Figure 2 shows schematically the method of two-step expansion. In the first step expansion, according to half of total mass flow, two streamlines 2 and 3 are obtained on the basis

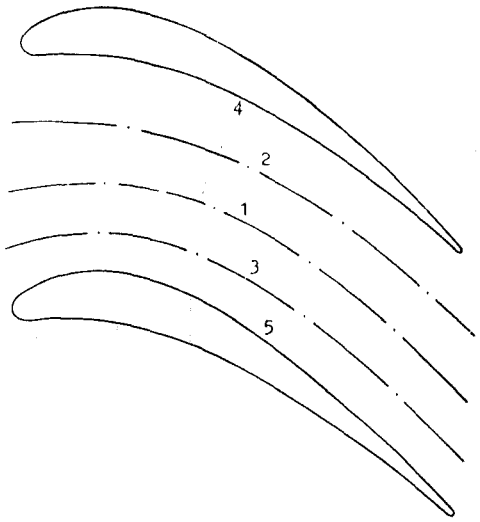

Fig. 2 Schematic drawing of two-step expansion algorithm

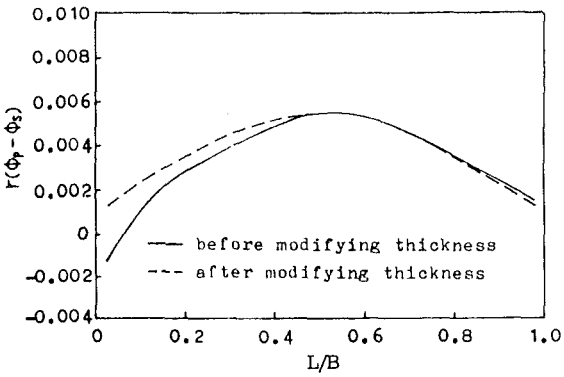

Fig. 3(a) Circumferential thickness distribution curve of profile

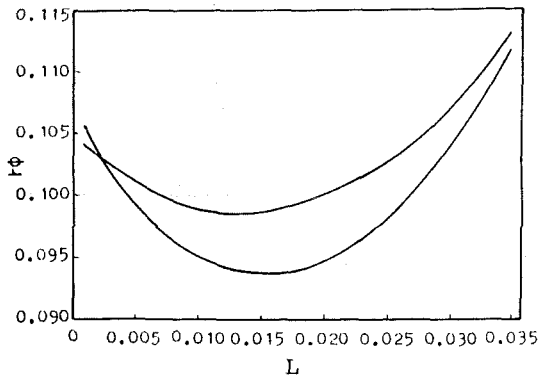

Fig. 3(b) Profile before modifying thickness

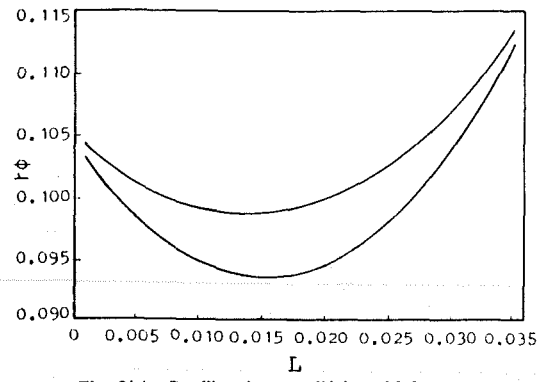

Fig. 3(c) Profile after modifying thickness

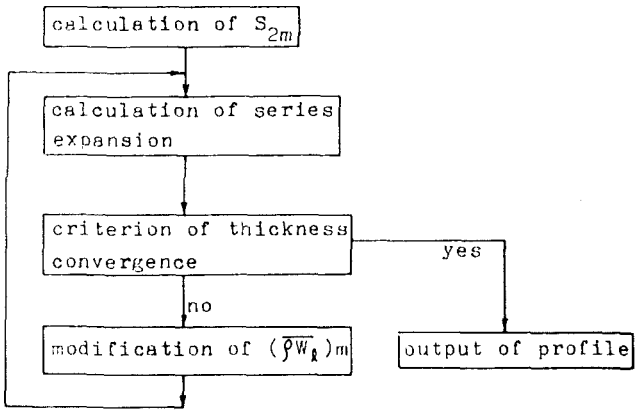

Fig. 4 Flow diagram of the iterative algorithm

of mean streamline 1. Then, in the second step expansion, the channel boundaries 4 and 5 are obtained on the basis of streamlines 2 and 3, respectively. It must be noted that in order to obtain smooth streamlines and smooth channel boundaries, it is very important to smooth the data on selected streamlines.

Usually, the thickness distribution of the profile obtained in the previous calculation is unreasonable. Figure 3(*b*) shows one of the computational examples in which the local thickness of the profile is negative. To obtain a reasonable profile, a selected curve of circumferential thickness distribution is given. For example, the solid line in Fig. 3(*a*) may be changed to the dotted line. Then, the aerodynamic parameters on the mean streamline will be modified according to the new thickness curve and the shape of the mean streamline will not be changed. Therefore a new inverse problem is formed in which the shape of the mean streamline and the circumferential thickness distribution of the profile are given. The problem is different from the standard inverse and various mixed problems in [11–15] and it is especially appropriate to quasi-three-dimensional design in turbine and compressor. In the computational process, the total mass flow through the cascade channel does not change, but the $\overline{\rho w_l}$ on the mean streamline of inner channel of cascade will be modified with the difference between the thickness computed and thickness given. The formula of modification is:

$$(\overline{\rho w_l})_j^{(n+1)} = (\overline{\rho w_l})_j^{(n)} \frac{[t - r(\phi_s - \phi_p)^{(n)}]_j}{(t-\delta)_j} \tag{27}$$

where t is cascade spacing and δ is circumferential thickness given.

Based on new $(\overline{\rho w_l})^{(n+1)}$, the new density $\bar{\rho}^{(n+1)}$ on the mean streamline can be obtained by solving

$$\left(\frac{\rho}{\rho^*}\right)^2 - \frac{2}{k+1}\left(\frac{\rho}{\rho^*}\right)^{k+1} - F = 0 \tag{28}$$

where

$$F = \frac{k-1}{k+1}\frac{1}{\cos^2\beta}(\overline{\rho w_l})^2 \left(\frac{I + 1/2\omega^2 r_i^2}{I + 1/2\omega^2 r^2}\right)^{\frac{k+1}{k-1}} \tag{29}$$

The Newton Iteration Method is one of the methods of solving equation (28). The expression for the iteration is shown as follows:

$$\left(\frac{\rho}{\rho^*}\right)^{(\nu+1)} = \left(\frac{\rho}{\rho^*}\right)^{(\nu)} - \frac{\left[\left(\frac{\rho}{\rho^*}\right)^{(\nu)}\right]^2 - \frac{2}{k+1}\left[\left(\frac{\rho}{\rho^*}\right)^{(\nu)}\right]^{k+1} - F}{2\left\{\left(\frac{\rho}{\rho^*}\right)^{(\nu)} - \left[\left(\frac{\rho}{\rho^*}\right)^{(\nu)}\right]^k\right\}} \tag{30}$$

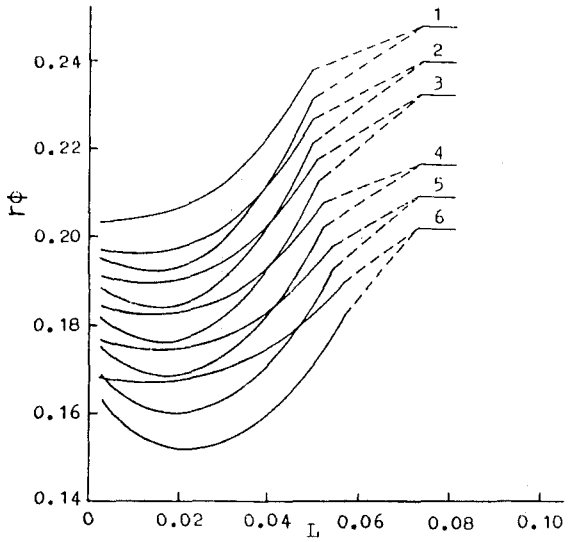

Fig. 5 Profiles on six S_1 surfaces of revolution before modifying thickness

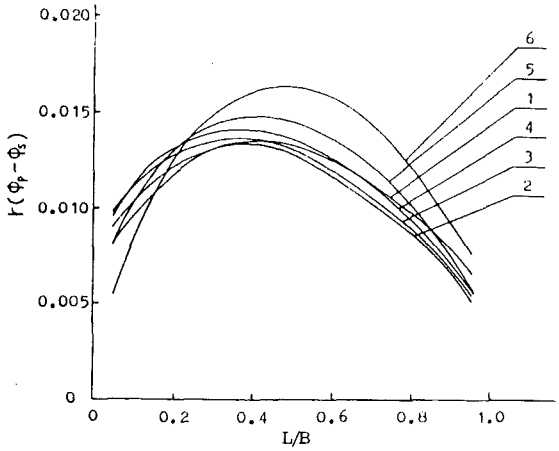

Fig. 6 Thickness distribution of six profiles before modifying thickness

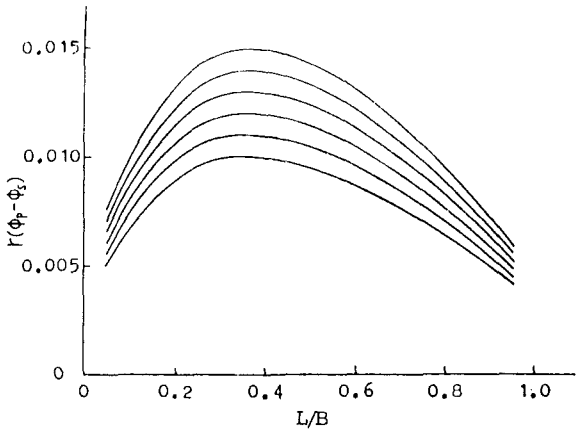

Fig. 7 Thickness distribution of six profiles after modifying thickness (modification plan I)

where (ν) shows the number of iterations, and $\rho*$ is the local critical density.

Then, the series expansion calculations of the second cycle

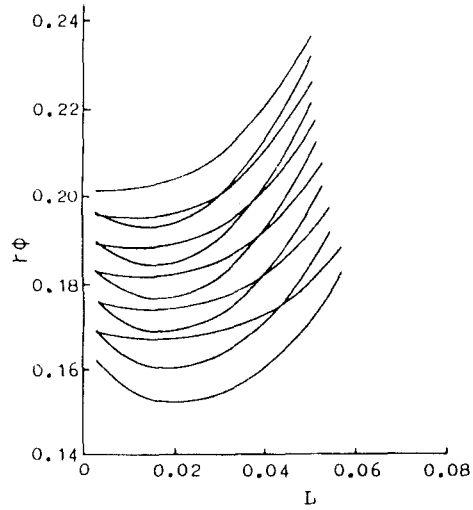

Fig. 8 Profiles on six S_1 surfaces of revolution after modifying thickness (modification plan I)

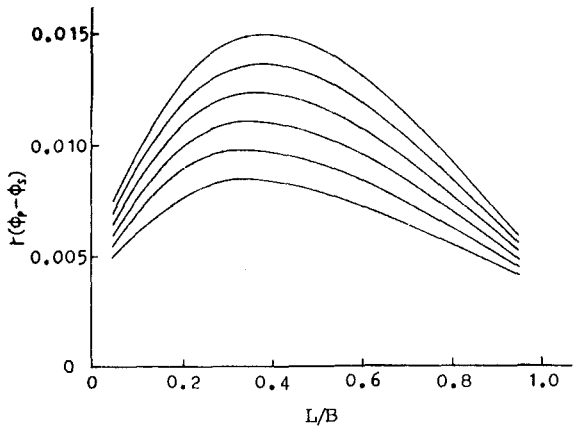

Fig. 9 Thickness distribution of six profiles after modifying thickness (modification plan II)

may be performed on the basis of the original mean streamline and new density distribution. In this way the iterations are continued until the profile thickness obtained in calculations agrees with the given thickness. Figure 3(c) shows the profile after modifying thickness. The simple flow diagram of the iterative algorithm is shown in Fig. 4.

The previous algorithm is used in the quasi-three-dimensional design of a turbine rotor. In design process, the S_{2m} calculation of the first cycle provides the shapes and the stream filament thicknesses of six S_1 surfaces of revolution at different radial positions, and gives the ϕ coordinate values of the mean streamlines of each S_1 surface and ρ distribution on it. Figure 5 shows the six profiles obtained in the case where the profiles have not been adjusted. Figure 6 shows the corresponding curves of thickness distribution. It is easily seen from Figs. 5 and 6 that not all the thickness distributions of these profiles are satisfactory; they cannot satisfy all the requirements of leading edge, trailing edge, and stacking of profiles.

The thickness distribution curves in Fig. 6 are not regular for different radial sections. In order to improve this case the data of the thickness distribution shown in Fig. 7 are specified. The profiles resulting from iterative calculations are shown in Fig. 8. Obviously, the regular variation of profile thickness along radial direction is favorable to the stacking of profiles.

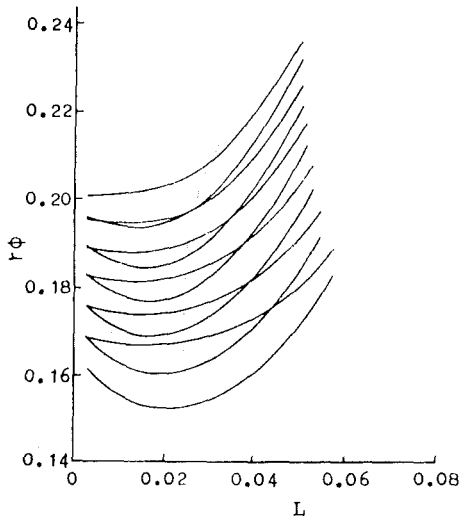

Fig. 10 Profiles on six S_1 surfaces of revolution after modifying thickness (modification plan II)

Figures 9 and 10 show another set of given thickness data and the profiles obtained, respectively. The present method needs very short CPU time on a computer. In the examples the maximum difference of thickness is 0.0001 m.

After several cycles of quasi-three-dimensional design, if the velocity distribution on profile surface is not very satisfactory, the thickness distribution curve may be modified appropriately. In addition, the velocity distribution on the surface of profile obtained by the present method can also be improved by the methods of [12–15].

Concluding Remarks

In this paper, an aerodynamic method of forming profile is presented by which the profile thickness is automatically adjusted. With the help of this method the requirements of aerodynamic performance, structure, strength, and stacking of profiles can be fulfilled. The present method has been successfully used in practical design of quasi-three-dimensional calculations of turbomachines.

Acknowledgments

The author wishes to thank Prof. C. H. Wu for his guidance. Mr. Y. Lou provided the author with the S_{2m} data.

References

1 Wu Chung-Hua, "A General Theory of Three-Dimensional Flow in Subsonic or Supersonic Turbomachines of Axial, Radial and Mixed Flow Types," *Trans. ASME*, Vol. 74, Nov. 1952, Paper No. 50-A-79.

2 Novak, R. A., and Hearsey, R. M., "A Nearly Three-Dimensional Interblade Computing System for Turbomachinery," ASME *Journal of Fluids Engineering*, Vol. 99, Mar. 1977.

3 Academia Sinica, Shenyang Aeroengine Company, "Theory, Method and Application of Three-Dimensional Flow Design of Transonic Axial-Flow Compressors" [in Chinese], *Journal of Engineering Thermophysics*, Vol. 1, No. 1, 1980.

4 Zhu Genxing, Ge Manchu, and Wu Chung-Hua, "Three-Dimensional Subsonic Flow Through a Stator by Use of a Central S_2 Flow Surface and Several S_1 Surfaces of Revolution" [in Chinese], *Journal of Engineering Thermophysics*, Vol. 4, No. 2, 1983.

5 Wang Qinghuan, Zhu Genxing, and Wu Chung-Hua, "Computer Procedure System of Quasi-Three-Dimensional Design and Full-Three-Dimensional Solution in Turbomachines," *Symposium of Chinese Society of Engineering Thermophysics*, 1984.

6 Wu Chung-Hua, and Brown, C. A., "A Theory of the Direct and Inverse Problems of Compressible Flow Past Cascade of Arbitrary Airfoils," *J.A.S.*, Vol. 19, No. 3, 1952.

7 Wu Chung-Hua, Brown, C. A., and Prian, V. D., "An Approximate Method of Determining the Subsonic Flow in an Arbitrary Stream Filament of Revolution Cut by Arbitrary Turbomachine Blades," NACA TN 2702, 1952.

8 Cai, R., "A Summary of Developments of the Mean-Streamline Method in China," ASME JOURNAL OF ENGINEERING FOR GAS TURBINES AND POWER, Vol. 106, 1984, pp. 300–305.

9 Novak, R. A., and Haymann-Haber, G., "A Mixed-Flow Cascade Passage Design Procedure Based on a Power Series Expansion," ASME JOURNAL OF ENGINEERING FOR POWER, Vol. 105, 1983, pp. 231–242.

10 Wang Zhengming, and Cai, R., "Mean-Stream-Line Method With Higher Order Derivatives for Calculating Cascades Lying on Arbitrary Revolution Surface" [in Chinese], *Journal of Engineering Thermophysics*, Vol. 4, No. 4, 1983.

11 Liu Gaolian, "General Theory and Solution (I) of Stream Function Form of Various Hybrid Aerodynamic Problem for Full-Three-Dimensional Compressible Potential Flow in Axial-Flow Rotor," *Symposium of Chinese Society of Engineering Thermophysics*, 1983.

12 Chen Naixing and Li Weihong, "Solution of a Hybrid Aerodynamic Problem on Arbitrary Stream Surface of Revolution Employing Stream Function Equation of Non-orthogonal Curvilinear Coordinates," *Symposium of Chinese Society of Engineering Thermophysics*, 1984.

13 Zhou Xinhai, Zhu Fangyuan, and Zhang Jin, "Finite Volume Method of Solving Inverse Problem For Transonic Cascade," *Symposium of Chinese Society of Engineering Thermophysics*, 1984.

14 Ge Manchu, "A Stream Function Relaxation Method for Solving Blade Coordinates on S_1 Stream Surface," *Symposium of 7th ISABE*.

15 Wang Zhengming, "Inverse Design Calculations for Transonic Cascades," ASME Paper No. 85-GT-6, 1985.

Prediction of Turbulent Source Flow Between Corotating Disks With an Anisotropic Two-Equation Turbulence Model

S. A. Shirazi
Graduate Research Assistant.
Student Mem. ASME

C. R. Truman
Assistant Professor.
Assoc. Mem. ASME

Department of Mechanical Engineering,
University of New Mexico,
Albuquerque, NM 87131

An anisotropic form of a low-Reynolds-number two-equation turbulence model has been implemented in a numerical solution for incompressible turbulent flow between corotating parallel disks. Transport equations for turbulent kinetic energy and dissipation rate were solved simultaneously with the governing equations for the mean-flow variables. Comparisons with earlier mixing-length predictions and with measurements are presented. Good agreement between the present predictions and the measurements of velocity components and turbulent kinetic energy was obtained. The low-Reynolds-number two-equation model was found to model adequately the near-wall region as well as the effects of rotation and streamline divergence, which required ad hoc assumptions in the mixing-length model.

Introduction

Turbulent source flow between corotating disks can serve as a model for several flows which occur in turbomachinery. In axial-flow machines, the coolant flow which enters the rotating cavity formed by corotating turbine or compressor disks (Owen, 1984) can be modeled as a turbulent source flow. The rotating vaneless diffuser of a centrifugal pump (Schumann, 1986) can also be modeled as turbulent source flow between corotating disks. A multiple-disk pump (Köhler, 1971) is composed of many narrowly spaced disks; turbulent source flow occurs between each pair of corotating disks. A more unusual example is the coolant flow in a computer memory disk pack (Bogy et al., 1977).

The design of high-performance turbomachinery requires accurate prediction of heat and momentum transfer in these rotating components. Turbulence models must account for the effects of streamline divergence, adverse pressure gradient, and the interaction between near-wall and outer regions due to the strong influence of rotation. The present work considers the effectiveness of a two-equation turbulence model extended to include anisotropy. The scope was limited to parabolic flows for which comparisons with data could be made. Although not included here, the logical extension to this work would be prediction of heat transfer.

For the present model, the disk spacing was taken to be small, which ensures that shear is important across the entire disk spacing. If the elliptic flow regions which occur at the inlet or exit are small and can be neglected, a parabolic solution procedure can be employed for the resulting thin-shear-layer equations. At high rotation rates and large radius, the radial component of velocity at the centerplane between the disks becomes negative. This flow reversal violates the parabolic assumption, and the flow must be treated with an elliptic procedure for radii beyond this point.

Although the disk spacing considered here is smaller than is typical in gas turbine engines, the present results may provide useful information concerning flow phenomena as disk spacing decreases. For sufficiently narrow disk spacing for example, flow would be pumped outward between corotating disks. This may be relevant to the problem of ingress of hot gases to the rotating cavity.

Previous Predictions. Earlier predictions of turbulent source flow between rotating disks include both integral and finite-difference techniques. Schumann (1986) presents an integral analysis for compressible, turbulent flow in a radial vaneless diffuser using power-law profiles for radial and tangential velocity components. His results showed good agreement with experimental data and with a finite-difference method. Truman and Jankowski (1985) used extended mixing-length models to predict source flow between stationary as well as rotating disks in a thin-shear-layer finite-difference method. Those predictions showed good agreement with experimental data for pressure and tangential velocity. The comparisons with radial velocity profiles were less satisfactory. The predictions correctly displayed increasing radial velocity near the disk surface with increasing radius or rotation rate. This was accomplished by modifying the mixing-length model to include a correction for the extra strain due to the diverging flow (Bradshaw, 1975) and treating the near-wall region as anisotropic through the van Driest damping (Koosinlin and Lockwood, 1974). This anisotropic model was developed to compute swirling boundary layers including flow upon a rotating disk and along a rotating cylinder. The *ad hoc* nature

Contributed by the Gas Turbine Division of THE AMERICAN SOCIETY OF MECHANICAL ENGINEERS and presented at the 32nd International Gas Turbine Conference and Exhibit, Anaheim, California, May 31–June 4, 1987. Manuscript received at ASME Headquarters February 5, 1987. Paper No. 87-GT-73.

of these modifications and the unsatisfactory prediction of radial velocity profiles were the impetus for the present investigation using a two-equation turbulence model.

Chew (1984) used both logarithmic wall function and low-turbulent-Reynolds-number forms of a k–ϵ model in a Navier–Stokes formulation. Source flow between rotating disks, source flow between a stationary disk and a rotating disk, and flow due to a single rotating disk were predicted. The elliptic form was necessary to predict the recirculating flow between disks that occurs for large disk spacing, rapid rotation rate, or small source flow rate. With the integration extended to the wall using the low-Reynolds-number form, the solution failed to converge or the turbulent kinetic energy rapidly decayed and resulted in essentially laminar flow. Predictions using the wall function form gave rather poor agreement with the data. Chew concluded that predictions using his k–ϵ formulation were not very good for any of the three flows considered. Another (elliptic) Navier–Stokes analysis using a k–ϵ turbulence model was recently reported by Kim et al. (1985), but predictions for flow in the cavity formed by a rotating and a stationary disk were not compared with data.

Measurements. Bakke et al. (1973) performed a series of hot-wire measurements which included radial and tangential velocity profiles and turbulent intensities for turbulent source flows between stationary and corotating disks. Unfortunately, the reliability of these measurements near the disks is poor, as discussed below. An experimental study of the rotating cavity with outflow has been reported by Pincombe (1981). These results include cavities with wide spacings in which recirculating flow occurs, so no comparisons with the present model were possible. Hot-wire measurements of radial and tangential velocity profiles for the flow exiting corotating disks have been reported by Köhler (1971). The range of flow parameters of these data is limited. Further, measurements were not taken near the disk surfaces. The limited experimental evidence for turbulent source flow between rotating disks makes the development of a reliable turbulence model more difficult. For the present work comparisons were made with the Bakke (1969) and Köhler (1971) data. Disk parameters and experimental conditions corresponding to data presented herein are listed in Table 1.

Present Analysis. The present work is a numerical investigation of turbulent source flow between corotating disks with a relatively high rotation rate and narrow disk spacing. An anisotropic two-equation k–ϵ model has been used to ex-

Table 1 Experimental flow conditions and disk parameters for data considered

Reference	r_s (mm)	r_o (mm)	h (mm)	ω (rad/s)	Q (m^3/s)	ν (m^2/s)
Bakke (1969)	46	280	7.6	157	0.0405	1.82×10^{-5}
Köhler (1971)	40	200	2	209	0.0139	1.48×10^{-5}
Köhler (1971)	40	200	7	209	0.0287	1.48×10^{-5}
Köhler (1971)	40	200	10	209	0.0329	1.48×10^{-5}

Nomenclature

C_1, C_2, C_μ = constant and parameters in k–ϵ model (Table 2)
E = dimensionless dissipation $=\epsilon/[\mathrm{Re}_Q\mathrm{Re}_\omega^2(\nu r_s/h^2)^3/r_s]$
F = dimensionless stream function, equation (22)
h = spacing between disks
k = turbulent kinetic energy $=\frac{1}{2}[\overline{u'^2}+\overline{v'^2}+\overline{w'^2}]$
K = dimensionless turbulent kinetic energy $=\frac{1}{2}[\overline{U'^2}+\overline{V'^2}+\overline{W'^2}]$
p = time-averaged pressure
P = dimensionless pressure $=p/(\rho\nu Q\mathrm{Re}_\omega/2\pi h^3)$
Q = volume flow rate of source flow between disks
r = radial coordinate
r_o = outer radius of disks
R = dimensionless radial coordinate $=r/(Qh/2\pi\nu\mathrm{Re}_\omega)^{1/2}$
Re_o = overall Reynolds number $=\mathrm{Re}_Q(r_s/h)^2$
Re_Q = throughflow Reynolds number $=Qh/2\pi\nu r_s^2$
Re_t = Reynolds number of turbulence $=k^2/\nu\epsilon$
Re_ω = rotational Reynolds number $=\omega h^2/\nu$
T_R = Rotta anisotropy parameter, equation (21)
u, v, w = time-averaged velocity components in r, θ, z directions
u', v', w' = fluctuating velocity components in r, θ, z directions
$-\overline{u'w'}$, $-\overline{v'w'}$ = Reynolds stresses
U = dimensionless radial velocity component $=u/(Q/2\pi hr)$
V = dimensionless tangential velocity component $=v/r\omega$
W = dimensionless axial velocity component $=w/[(Q\nu/2\pi h)^{1/2}/r]$
U', V', W' = dimensionless fluctuating velocity components $=(u', v', w')/[(Q/2\pi h\nu)^{1/4}\mathrm{Re}_\omega^{1/2}(\nu/h)]$
$-\overline{U'W'}$, $-\overline{V'W'}$ = dimensionless Reynolds stresses
z = axial coordinate
Z = dimensionless axial coordinate $=z/(h/\mathrm{Re}_\omega^{1/2})$
Z^+ = dimensionless wall coordinate $=z(\tau_w/\rho)^{1/2}/\nu$
ϵ = rate of dissipation of turbulent kinetic energy
θ = tangential (azimuthal) coordinate
ν = kinematic viscosity of fluid
ν_t = eddy viscosity
ν_t^+ = dimensionless eddy viscosity $=\nu_t/\nu$
ρ = fluid density
σ_ϵ, σ_k = constants in k–ϵ model (Table 2)
τ_w = wall shear stress
ω = angular speed of the disks

Subscripts

c = centerline (plane of symmetry between disks)
r = radial component
s = starting radius
θ = tangential component

tend the earlier mixing-length results of Truman and Jankowski (1985). The low-Reynolds-number two-equation turbulence model of Jones and Launder (1972) was used to predict the effects due to streamline divergence and the adverse pressure gradient. This k–ϵ turbulence model has been used with success for flows over spinning surfaces (Launder et al., 1977). The low-Reynolds-number version of the k–ϵ model was modified to include the effect of anisotropy caused by disk rotation using Rotta's model (Rotta, 1979). The turbulent transport equations were solved simultaneously with the mean-flow equations using the Keller Box Scheme (Keller and Cebeci, 1972). The results are compared with earlier mixing-length predictions and with available experimental data. The applicability of the k–ϵ turbulence model is discussed along with suggestions for further improvements.

Mean Flow Governing Equations

The time-averaged Navier–Stokes equations for the steady, incompressible flow of a viscous Newtonian fluid in cylindrical coordinates were scaled using the thin-shear-layer approximation (Bradshaw, 1975). The variation of all quantities in the azimuthal coordinate was neglected by assuming rotational symmetry. The approximate governing equations are

$$\frac{\partial u}{\partial r}+\frac{u}{r}+\frac{\partial w}{\partial z}=0 \tag{1}$$

$$u\frac{\partial u}{\partial r}+w\frac{\partial u}{\partial z}-\frac{v^2}{r}=-\frac{1}{\rho}\frac{dp}{dr}+\nu\frac{\partial^2 u}{\partial z^2}-\frac{\partial(\overline{u'w'})}{\partial z} \tag{2}$$

$$u\frac{\partial v}{\partial r}+w\frac{\partial v}{\partial z}+\frac{uv}{r}=\nu\frac{\partial^2 v}{\partial z^2}-\frac{\partial(\overline{v'w'})}{\partial z} \tag{3}$$

The boundary conditions at the disk surface are no-slip and no penetration. Symmetry conditions are used at the centerplane of the disks. For the numerical solution, equations (1)–(3) were expressed in terms of dimensionless variables scaled to be approximately unity in the region of interest (Truman and Jankowski, 1985). Choices for the nondimensionalization were made based on the scaling arguments already used to obtain the approximate equations. The resulting dimensionless reduced equations are

$$\frac{\partial U}{\partial R}+\frac{\partial W}{\partial Z}=0 \tag{4}$$

$$U\frac{\partial U}{\partial R}+W\frac{\partial U}{\partial Z}-\frac{U^2}{R}-R^3V^2 = -R^2\frac{dP}{dR}+R\frac{\partial^2 U}{\partial Z^2}+R^2\frac{\partial(-\overline{U'W'})}{\partial Z} \tag{5}$$

$$U\frac{\partial V}{\partial R}+W\frac{\partial V}{\partial Z}+\frac{2UV}{R}=R\frac{\partial^2 V}{\partial Z^2}+\frac{\partial(-\overline{V'W'})}{\partial Z} \tag{6}$$

The boundary conditions can be written as

$$U(R,0)=0 \tag{7a}$$

$$V(R,0)=1 \tag{7b}$$

$$W(R,0)=0 \tag{7c}$$

$$\partial U(R,Z_c)/\partial Z=0 \tag{7d}$$

$$\partial V(R,Z_c)/\partial Z=0 \tag{7e}$$

Integral conservation of mass, used to determine the unknown pressure gradient dP/dR at each radial station, was written in dimensionless form as

$$\int_0^{Z_c} U(R,Z)dZ=Z_c \tag{8}$$

The above scaled system with appropriate boundary and starting conditions is a system of parabolic partial differential equations which can be solved numerically if a suitable turbulence model is added. Starting conditions must be specified somewhat arbitrarily at $R=R_s$ within the constraints of the parabolic assumption.

Table 2 Constants and parameters used for the k-ϵ model (Launder et al., 1977)

$C_\mu = 0.09\ \exp[-3.4/(1+\mathrm{Re}_t/50)^2]$
$C_1 = 1.44$
$C_2 = 1.92\ [1.0-0.3\ \exp(-\mathrm{Re}_t^2)]$
$\sigma_k = 1.0$
$\sigma_\epsilon = 1.3$

Turbulence Modeling

In previous predictions of turbulent source flow between corotating disks (Truman and Jankowski, 1985), extended forms of the classical mixing-length/eddy-viscosity concept were used to model the two unknown Reynolds stresses, $-\overline{U'W'}$ and $-\overline{V'W'}$. Two eddy viscosities, $(\nu_t)_r$ and $(\nu_t)_\theta$, were defined by

$$-\overline{u'w'}=(\nu_t)_r\frac{\partial u}{\partial z}, \qquad -\overline{v'w'}=(\nu_t)_\theta\frac{\partial v}{\partial z} \tag{9}$$

The isotropic model was obtained when $(\nu_t)_r = (\nu_t)_\theta = \nu_t$. For the anisotropic model, the eddy viscosities were obtained using different van Driest damping in the radial and tangential directions. The Bradshaw (1975) modification to account for extra strain rate associated with the streamline divergence was also incorporated. The strain rate used to compute the mixing length was increased using an *ad hoc* formula.

In the present predictions, the turbulence model was based on the low-Reynolds-number k–ϵ model of Jones and Launder (1972). The eddy viscosity is related to the kinetic energy of turbulent fluctuations k and the rate of dissipation of turbulent kinetic energy ϵ by

$$\nu_t=C_\mu k^2/\epsilon \tag{10}$$

where C_μ is given in Table 2. The transport equations reduced with the thin-shear-layer approximation are similar to those used by Launder et al. (1977) for rotating surfaces; they are:

turbulent kinetic energy equation

$$u\frac{\partial k}{\partial r}+w\frac{\partial k}{\partial z}=-\left[\overline{u'w'}\frac{\partial u}{\partial z}+\overline{v'w'}\frac{\partial v}{\partial z}\right]+\frac{\partial}{\partial z}\left[\left(\nu+\frac{\nu_t}{\sigma_k}\right)\frac{\partial k}{\partial z}\right]-\epsilon-2\nu\left(\frac{\partial k^{1/2}}{\partial z}\right)^2 \tag{11}$$

dissipation equation

$$u\frac{\partial \epsilon}{\partial r}+w\frac{\partial \epsilon}{\partial z}=-C_1\frac{\epsilon}{k}\left[\overline{u'w'}\frac{\partial u}{\partial z}+\overline{v'w'}\frac{\partial v}{\partial z}\right]+\frac{\partial}{\partial z}\left[\left(\nu+\frac{\nu_t}{\sigma_\epsilon}\right)\frac{\partial \epsilon}{\partial z}\right]-C_2\frac{\epsilon^2}{k}+2\nu\nu_t\left\{\frac{\partial}{\partial z}\left[\left(\frac{\partial u}{\partial z}\right)^2+\left(\frac{\partial v}{\partial z}\right)^2\right]^{1/2}\right\}^2 \tag{12}$$

The constants σ_k, σ_ϵ, C_1, and the parameter C_2 are given in Table 2. The parameters C_2 and C_μ are related to a Reynolds number of turbulence defined by

$$\mathrm{Re}_t\equiv k^2/\nu\epsilon \tag{13}$$

The last term in each of equations (11) and (12) and the

viscous diffusion terms do not appear in the high-Reynolds-number form of the k–ϵ model. The last term in equation (11) has been adopted by Jones and Launder (1972) to account for the presence of the solid wall where a nonphysical boundary condition $\epsilon = 0$ is used at the wall. Jones and Launder added the last term in equation (12) to predict the peak of turbulent kinetic energy near the wall shown by experiment. These equations were written in dimensionless form using the scales already used to obtain equations (4)–(6). The scale for dissipation was then chosen so that dissipation approximately balanced production (first and third terms in the right-hand side of equation (11)). The resulting scaled (dimensionless) equations are

$$U\frac{\partial K}{\partial R}+W\frac{\partial K}{\partial Z}=-\mathrm{Re}_o^{1/2}\left[\overline{U'W'}\frac{\partial U}{\partial Z}+\overline{V'W'}R^2\frac{\partial V}{\partial Z}\right]$$
$$+R\frac{\partial}{\partial Z}\left[\left(1+\frac{\nu_t^+}{\sigma_k}\right)\frac{\partial K}{\partial Z}\right]-\mathrm{Re}_o^{1/2}RE-2R\left(\frac{\partial K^{1/2}}{\partial Z}\right)^2 \quad (14)$$

$$U\frac{\partial E}{\partial R}+W\frac{\partial E}{\partial Z}=$$
$$-C_1\mathrm{Re}_o^{1/2}\frac{E}{K}\left[\overline{U'W'}\frac{\partial U}{\partial Z}+\overline{V'W'}R^2\frac{\partial V}{\partial Z}\right]$$
$$+R\frac{\partial}{\partial Z}\left[\left(1+\frac{\nu_t^+}{\sigma_\epsilon}\right)\frac{\partial E}{\partial Z}\right]-C_2\mathrm{Re}_o^{1/2}R\frac{E^2}{K}$$
$$+2\nu_t^+\frac{1}{R}\left\{\frac{\partial}{\partial Z}\left[\left(\frac{\partial U}{\partial Z}\right)^2+\left(R^2\frac{\partial V}{\partial Z}\right)^2\right]^{1/2}\right\}^2 \quad (15)$$

and

$$\nu_t^+ = C_\mu K^2/E \quad (16)$$

The scaled equations contain an overall Reynolds number $\mathrm{Re}_o = \mathrm{Re}_Q(r_s/h)^2$, which characterizes the throughflow between the disks. The boundary conditions for the k–ϵ equations are written in dimensionless form as

$$K(R,0)=0 \quad (17a)$$
$$\partial K(R,Z_c)/\partial Z=0 \quad (17b)$$
$$E(R,0)=0 \quad (17c)$$
$$\partial E(R,Z_c)/\partial Z=0 \quad (17d)$$

Modification of the k–ϵ Model to Include Anisotropy. The usual Boussinesq eddy-viscosity assumption implies that the shear stress tensor is aligned with the rate-of-strain tensor and ν_t is assumed to be a scalar quantity. However, experimental observations such as Johnston (1976) have shown that for three-dimensional turbulent boundary layers, the shear stress vector is not in the same direction as the vector of the mean velocity gradient. To account for this anisotropy in the turbulent stresses, an anisotropic constitutive relation for Reynolds stress was sought. Wilcox and Rubesin (1980) expressed the Reynolds stress tensor in a tensor series to quadratic terms in the mean rates of strain and the vorticity. However, it was found that this model is *isotropic* for Reynolds shear stresses within the thin-shear-layer approximation. Anisotropic effects could appear only through the normal Reynolds stresses. In a similar study, Pouagare and Lakshminarayana (1983) attempted to determine an anisotropic eddy-viscosity by manipulating an algebraic Reynolds stress model. They also found that this model is isotropic within the thin-shear-layer approximation.

Rotta (1979) argued that the nonalignment of the shear stress vector with the mean velocity gradient could be "attributed mainly to the fluctuating pressure term." With a model for the pressure-strain term, nonisotropic eddy viscosity expressions and corresponding forms of the Reynolds shear stresses for three-dimensional flows were derived. Rotta's model for the dimensionless Reynolds shear stresses using the present coordinate system yields

$$-\overline{U'W'}=\frac{1}{R}\left[(\nu_t^+)_{rr}\frac{\partial U}{\partial Z}-(\nu_t^+)_{r\theta}R^2\frac{\partial V}{\partial Z}\right] \quad (18a)$$

and

$$-\overline{V'W'}=\frac{1}{R}\left[-(\nu_t^+)_{\theta r}\frac{\partial U}{\partial Z}+(\nu_t^+)_{\theta\theta}R^2\frac{\partial V}{\partial Z}\right] \quad (18b)$$

The nonisotropic eddy viscosities are

$$(\nu_t^+)_{rr}=\nu_t^+[(U/R)^2+T_R(RV)^2]/U_t^2 \quad (19a)$$
$$(\nu_t^+)_{r\theta}=(\nu_t^+)_{\theta r}=\nu_t^+(1-T_R)UV/U_t^2 \quad (19b)$$
$$(\nu_t^+)_{\theta\theta}=\nu_t^+[T_R(U/R)^2+(RV)^2]/U_t^2 \quad (19c)$$

where

$$U_t^2=(U/R)^2+(RV)^2 \quad (20)$$

The negative signs in the $r\theta$ and θr terms in equation (18) were introduced for the present problem because $\partial v/\partial z$ and $-\overline{v'w'}$ are negative when the disk speed is greater than the tangential velocity of the fluid. The parameter T_R is the ratio of the tangent of the angle between the mean velocity and Reynolds stress vectors ($\gamma_\tau - \gamma$) to the tangent of the angle between the mean velocity and mean rate-of-strain vectors ($\gamma_g - \gamma$)

$$T_R=\frac{\tan(\gamma_\tau-\gamma)}{\tan(\gamma_g-\gamma)} \quad (21)$$

This parameter describes the degree of anisotropy, with $T_R = 1$ yielding the isotropic model where $(\nu_t^+)_{rr} = (\nu_t^+)_{\theta\theta} = \nu_t^+$ and $(\nu_t^+)_{r\theta} = (\nu_t^+)_{\theta r} = 0$. The effect of $T_R < 1$ is to shift the orientation of the Reynolds stress vector toward the mean velocity vector, which changes the magnitudes of the components $-\overline{u'w'}$ and $-\overline{v'w'}$. Rotta suggested a value for the parameter T_R of about 0.5 for boundary-layer calculations.

Cousteix (1982) used this form in a Reynolds-stress model to compute the three-dimensional developing boundary layer on an infinite swept wing. Moderate improvements were obtained using $T_R = 0.7$; anisotropic effects were found to be most significant near separation. Pouagare and Lakshminarayana (1983) used Rotta's idea to modify the anisotropic eddy viscosities $(\nu_t)_r$ and $(\nu_t)_\theta$ in equation (9) to reflect the degree of anisotropy of the solution at the previous marching step. Thus T_R was allowed to vary in the streamwise direction in a heuristic fashion. Slight improvements in the prediction of flow past a rotating cylinder were obtained. As the parameter T_R varied, it evolved to the same value ($T_R \simeq 0.8$) regardless of its initial value. In the present analysis, T_R was assumed to be uniform in both the axial and streamwise directions. Since the Reynolds stresses were computed using equations (18) and (19), there was no obvious way to predict the streamwise variation of T_R.

Solution Method

The coupled system of equations described by equations (4)–(6) and (14)–(15) with the boundary conditions (7) and (17) is a system of parabolic partial differential equations which yields to a marching solution. Equations (16), (18), and (19) provide the link between the mean-flow equations and the turbulent transport equations for the turbulent kinetic energy and the dissipation rate. In addition, integral conservation of mass, equation (8), was used to determine the unknown pressure gradient. The Keller Box Scheme (Keller and Cebeci, 1972) was employed because of its accuracy, generality, efficiency and stability for thin-shear-layer equations.

A stream-function formulation was used to recast the governing equations as a system of first-order equations. The dimensionless stream function $F(R, Z)$ was defined to eliminate conservation of mass equation (4), where

$$U = \partial F/\partial Z \tag{22a}$$

and

$$W = -\partial F/\partial R \tag{22b}$$

Equation (8) then reduces to

$$F(R, Z_c) = Z_c \tag{23}$$

where boundary condition (7*c*) was replaced by

$$F(R, 0) = 0 \tag{24}$$

The stream-function formulation was obtained substituting equation (22*b*) for W. The momentum equations and the K–E equations were then transformed to a system of nine first-order equations with F, U, V, K, E, $\partial U/\partial Z$, $\partial V/\partial Z$, $\partial K/\partial Z$, $\partial E/\partial Z$, and P as unknowns.

A modified version of an efficient block-tridiagonal solution method (Truman et al., 1987) which eliminates the need for "outer" iterations for pressure (Cebeci and Bradshaw, 1977) beyond the "inner" iterations for the nonlinear difference equations was used. In this modified version, equation (23) was used to obtain the unknown pressure gradient at the end of the forward sweep of the block-tridiagonal system in each iteration. Then the unknowns at each grid point were obtained in the backward sweep. Convergence criteria for the iterations were that the wall shear stress and radial pressure gradient change in successive iterations by less than 0.1 and 0.001 percent, respectively.

Starting Conditions. At the first marching step ($R_s + \Delta R_1$), starting conditions must be specified at R_s for all dependent variables. In earlier predictions which employed a mixing-length turbulence model (Truman and Jankowski, 1985), a local-similarity approximation was used to specify the starting conditions at R_s. Several attempts to obtain a local-similarity solution for the set of coupled momentum and k–ϵ equations failed, apparently because the difference equations near the wall are extremely stiff.

The method used to obtain starting conditions was based on a philosophy that the starting solution must at least satisfy approximate governing equations for K and E. To obtain profiles for K and E, a local-similarity solution of the mean-flow governing equations was obtained using the mixing-length model at the starting radius R_s. This solution included approximate profiles for the eddy viscosity ν_t^+ and the Reynolds shear stresses, $-\overline{U'W'}$ and $-\overline{V'W'}$. Production and dissipation in the turbulent kinetic energy equation were equated to obtain an initial profile for E from

$$E = -\left[\overline{U'W'}\,\frac{\partial U}{\partial Z} + \overline{V'W'}R_s^2\,\frac{\partial V}{\partial Z}\right]\Big/R_s \tag{25}$$

This distribution for E was then used to obtain the initial profile for K from equation (16) in the form

$$K = (E\nu_t^+/C_\mu)^{1/2} \tag{26}$$

These profiles for E and K were then modified in the sublayer region where production and dissipation are most significant. This was accomplished by examining the physical behavior of these quantities near the wall. Jones and Launder (1972) assumed that the variation of turbulent kinetic energy near the wall is proportional to the square of axial distance from the wall

$$K = \bar{C}_1 Z^2 \tag{27}$$

The constant $\bar{C}_1$ was then estimated at the outer edge of the viscous sublayer using the profile of K from equation (26); the edge of sublayer was identified as the location of maximum turbulent energy production (Chien, 1982). Dissipation is generally assumed to vary linearly with the axial distance in the near-wall region (Chien, 1982) to ensure that the variation of the eddy viscosity near the wall will be proportional to the cube of axial distance. However, Hanjalic and Launder (1976) have shown that the isotropic part of the dissipation rate varies as the square of axial distance from the wall, so it was assumed that

$$E = \bar{C}_2 Z^2 \tag{28}$$

in the viscous sublayer region. Thus equation (28) was used to correct the E profile in the near-wall region with the constant $\bar{C}_2$ found in the similar manner as $\bar{C}_1$. The initial profiles for K and E obtained with the above procedure provided a satisfactory starting solution at $R = R_s$. The effect of the approximate starting solution upon the subsequent marching steps was investigated by perturbing the initial profiles for turbulent kinetic energy and dissipation. The initial profiles for K and E were taken to be about twice that obtained from the above procedure. This perturbed starting solution at $R/R_s = 1$ significantly affected solutions only near the start. By $R/R_s = 3$ the effects of the starting solution had already damped out. Thus small errors in the approximate starting condition should have negligible effect upon the solution.

Since starting conditions based on the above procedure are only approximate solutions of the governing equations, small oscillations between marching steps appear in the computed solution. To eliminate these oscillations, small marching steps near R_s and a smoothing procedure were employed (Truman and Jankowski, 1985). This smoothing procedure was repeated several times to obtain a "smoothed" profile near R_s. Approximately ten marching steps with small ΔR were taken in the starting region. These initial steps were typically $\Delta R = 0.01\,R_s$, and the step size was then gradually increased. The variable grid spacing of Keller and Cebeci (1972) was employed to give approximately forty axial grid points of which about one third were in the viscous sublayer region. For example, Z^+ corresponding to the first grid point away from the wall was about 0.2 in the prediction of the Bakke case discussed below. Doubling the number of axial grid points changed the wall shear stress less than 0.2 percent.

Results

The k–ϵ model has been employed to predict flow between corotating disks for the following ranges of parameters: $\mathrm{Re}_Q = 180$ to 2211, $\mathrm{Re}_\omega = 57$ to 1415, and $r_s/h = 4$ to 20. Present predictions for several representative cases are compared with the data and with earlier mixing-length predictions. Bakke (1969) made velocity and turbulent intensity profile measurements by inserting a hot-wire probe into the flow region between the two disks. The influence of flow obstruction by the probe is unknown, but is likely significant. Further errors were reported near the wall where large heat transfer effects between the probe and the disk surface occur. With no source flow, a reading of approximately 0.3 m/s (1 ft/s) was recorded by Bakke (1969) near the disk surface. This no-flow reading corresponds to an error as large as 10 percent of the average radial velocity. Thus these data points near the disk surface are ignored in the present discussion and are denoted by solid symbols in the pertinent figures. The limited data presented by Köhler (1971) were also compared to the present predictions. Köhler measured radial and tangential velocity profiles with a hot-wire probe at the outer radius of the disks. These data include the centerline radial velocity, but Bakke's data were normalized by the centerline radial velocity which was not reported. There is insufficient information available to estimate the uncertainties in either set of data.

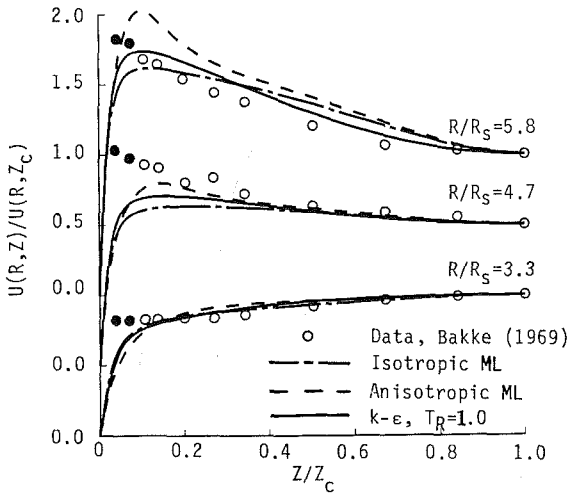

Fig. 1 Predicted and measured radial velocity component versus axial distance (Re_Q = 1276, Re_ω = 501, r_s/h = 6); ML = mixing-length (Truman and Jankowski, 1985)

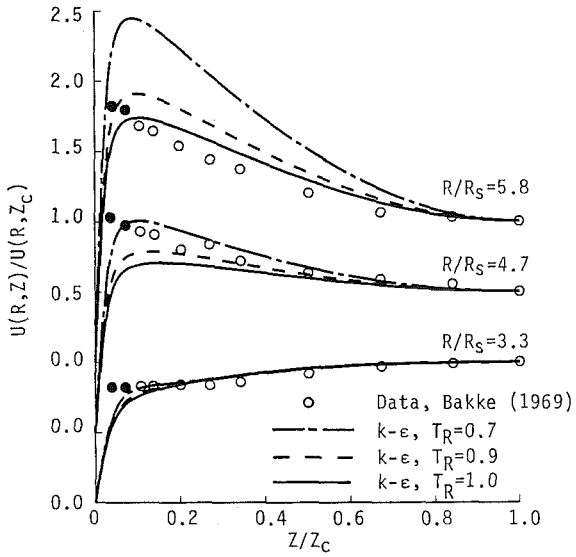

Fig. 2 Predicted and measured radial velocity component versus axial distance (same parameters as Fig. 1)

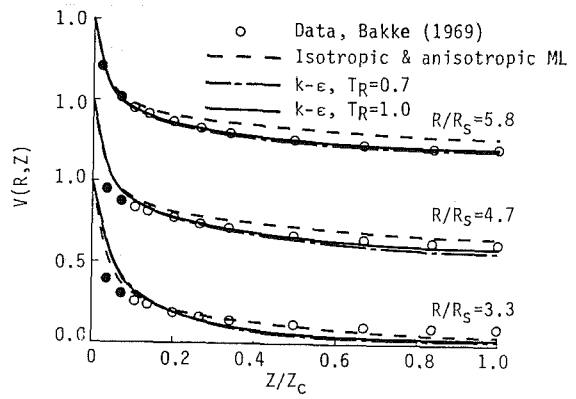

Fig. 3 Predicted and measured tangential velocity component versus axial distance (same parameters as Fig. 1)

Predictions of the radial mean-velocity distribution (normalized by the centerline value) with the isotropic k–ϵ turbulence model and the earlier mixing-length turbulence models are shown in Fig. 1 along with the data of Bakke (1969). The mixing-length model predictions showed that the anisotropic turbulence model was required to produce reasonable agreement with the data shown in Fig. 1. The present prediction with the k–ϵ turbulence model produces good agreement even in its isotropic form. The large peaks in the radial velocity shown by the data at large radii are due to centrifugal forces acting on fluid elements near the rotating disks. At the largest radius (R/R_s = 5.8), the prediction with the k–ϵ model shows good agreement with the data and shows the shape of the (normalized) experimental velocity profile somewhat better than either mixing-length model prediction. The axial locations of the peak in the radial velocity profiles at R/R_s = 5.8 predicted by the k–ϵ model and the mixing-length models are nearly the same.

Anisotropic predictions with the k–ϵ model can be obtained by changing the value of T_R, the Rotta parameter, as shown in Fig. 2. At R/R_s = 4.7, predictions using T_R of 0.7 to 0.9 show good agreement with the peak shown by the experimental data. However, at R/R_s = 5.8 the isotropic model (T_R = 1) shows the best agreement with experimental data. This shows that T_R should not remain constant in the streamwise (R) direction, but no means of predicting its behavior was established. Figure 3 shows predictions of the tangential velocity component with the anisotropic mixing-length model and the k–ϵ turbulence model. The predictions near the wall were not sensitive to the turbulence model. However, the k–ϵ turbulence model predictions show slightly better agreement with experimental data away from the wall. Using different values of T_R had little effect on the predictions of tangential velocity profile. The tangential velocity was shown to be relatively insensitive to anisotropic effects by the mixing-length predictions (Truman and Jankowski, 1985).

Predictions of the radial velocity component for three typical cases which span the range of the Köhler (1971) data are presented in Figs. 4–6; anisotropic mixing-length predictions using the method of Truman and Jankowski (1985) are included for comparison. For the case shown in Fig. 4, both Re_Q and Re_ω are small and the eddy viscosities were extremely small. The prediction of this reverse transition flow by the k–ϵ model is somewhat better than that by the mixing-length model. Figure 5 shows that all the predictions are in good agreement with experimental data. Near the wall, however, no data points were available and thus the effect of anisotropy cannot be carefully examined. The parameters of this case are similar to those of the Bakke case shown in Fig. 2. The results shown in Figs. 2 and 5 suggest a value of T_R between 0.7 and 1.0 for the anisotropic k–ϵ model is appropriate. The case shown in Fig. 6 shows the largest effect of centrifugal acceleration through the largest rate of rotation for Köhler's data. Again the anisotropic k–ϵ prediction with a value of T_R = 0.7 shows good agreement with the experimental data. Predictions of the tangential velocity component also showed good agreement with experimental data.

Figure 7 compares the measured and predicted turbulent kinetic energy for the Bakke case shown in Figs. 1–3 with the isotropic k–ϵ turbulence model. Bakke's results were given in terms of individual turbulent intensities, $\overline{u'^2}$ and $\overline{v'^2}$, with the former normalized by the (unreported) centerline radial velocity. The measured turbulent kinetic energy was computed by multiplying the normalized value of $\overline{u'^2}$ by the square of the *predicted* centerline radial velocity. At R/R_s = 3.3, the predicted and experimental values of K show significant differences, which indicates that the experimental inlet effects (Bakke, 1969) are not being modeled. Farther downstream the agreement with experimental data is good. Predictions of K with the anisotropic k–ϵ model were nearly the same as the isotropic predictions, with only a modest increase in the peak value of K using the anisotropic model. The small change in K with T_R is attributed to the fact that the effect of anisotropy in the Reynolds stresses is limited to the production terms in the K equation.

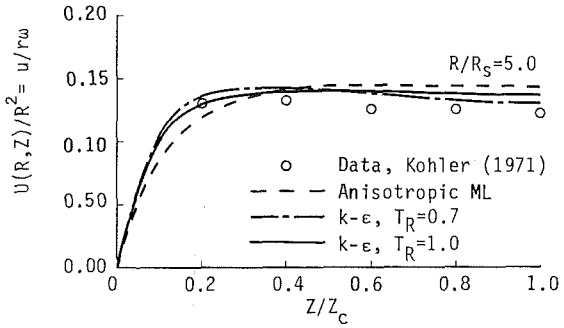

Fig. 4 Predicted and measured radial velocity component versus axial distance (Re_Q = 181, Re_ω = 57, r_s/h = 20)

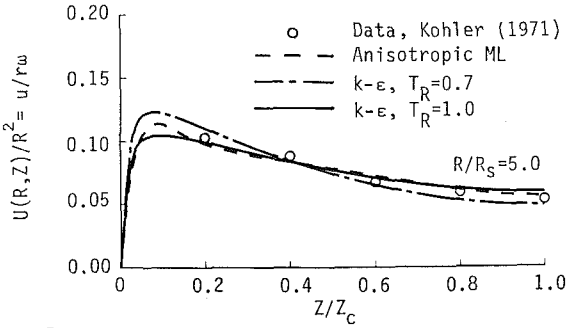

Fig. 5 Predicted and measured radial velocity component versus axial distance (Re_Q = 1350, Re_ω = 693, r_s/h = 5.7)

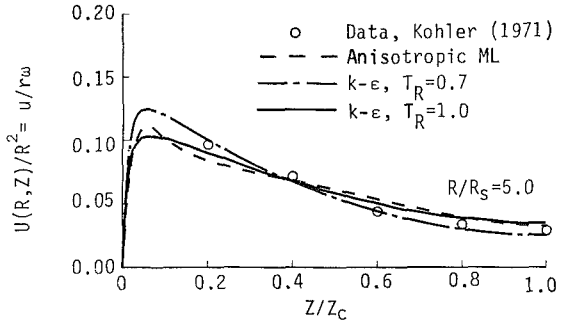

Fig. 6 Predicted and measured radial velocity component versus axial distance (Re_Q = 2211, Re_ω = 1415, r_s/h = 4)

Conclusions

A numerical solution procedure and turbulence model for source flow between corotating disks has been developed. An efficient numerical solution for the radial pressure gradient has been used. Transport equations for turbulent kinetic energy and its rate of dissipation include low-Reynolds-number terms to model the near-wall behavior through which rotation strongly influences the entire flow. This k–ϵ model predicted reverse transition as well as the effects of streamline divergence which required an *ad hoc* correction in the mixing length prediction. An anisotropic Reynolds stress model was implemented; the results indicate that the degree of anisotropy is not large but varies in the streamwise direction. Lack of reliable data near the rotating disk does not allow determination of the variation of anisotropy with radius. Since, as shown in Fig. 2, relatively small anisotropy (e.g., T_R = 0.7) can have significant influence as radius increases, isotropic predictions are recommended at present. Although T_R = 1 may be a conservative choice, the isotropic predictions were quite satisfactory. The shape of the radial velocity distributions predicted by the anisotropic model appear to agree somewhat better with the data, particularly in the vicinity of the peak near the wall. But even in isotropic form, the low-Reynolds-number k–ϵ turbulence model showed significant improvement over earlier anisotropic mixing-length predictions (Truman and Jankowski, 1985). The two-equation turbulence model is robust and, with more extensive and reliable experimental results, can be generalized to predict a variety of flows which include the effects of rotation and streamline divergence. The solution procedure is efficient, requiring about 0.1 s CPU time per radial step per axial grid point on a VAX 8650 using VMS.

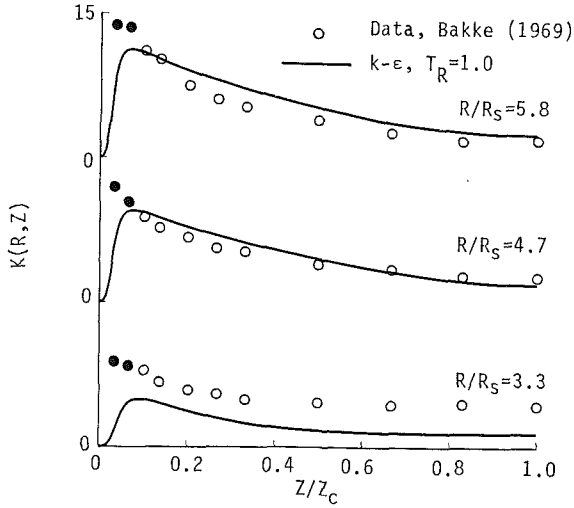

Fig. 7 Predicted and measured turbulent kinetic energy versus axial distance (same parameters as Fig. 1)

Acknowledgments

This work was supported by Sandia National Laboratories, Albuquerque (SNLA), and the Department of Mechanical Engineering, University of New Mexico. The technical assistance of Dr. Frederick G. Blottner (SNLA) is gratefully acknowledged.

References

Bakke, E., 1969, "A Theoretical and Experimental Investigation of the Flow Phenomena Between Two Co-rotating Parallel Disks With Source Flow," Ph.D. Thesis, Univ. of Colorado, Boulder, CO.

Bakke, E., Kreider, J. F., and Kreith, F., 1973, "Turbulent Source Flow Between Parallel Stationary and Co-rotating Discs," *Journal of Fluid Mechanics*, Vol. 58, pp. 209–231.

Bogy, D. B., Fromm, J. E., and Talke, F. E., 1977, "Exit Region Central Source Flow Between Finite Closely Spaced Parallel Corotating Discs," *Physics of Fluids*, Vol. 20, pp. 176–186.

Bradshaw, P., 1975, "Review: Complex Turbulent Flows," *ASME Journal of Fluids Engineering*, Vol. 97, pp. 146–154.

Cebeci, T., and Bradshaw, P., 1977, *Momentum Transfer in Boundary Layers*, Hemisphere, New York, pp. 218–220.

Chew, J. W., 1984, "Prediction of the Flow in Rotating Disc Systems Using the k–ϵ Turbulence Model," ASME Paper No. 84-GT-229.

Chien, K.-Y., 1982, "Prediction of Channel and Boundary-Layer Flows With a Low-Reynolds-Number Turbulence Model," *AIAA Journal*, Vol. 20, pp. 33–38.

Cousteix, J., 1982, "Integral Method and Turbulence Models Applied to Three-Dimensional Boundary Layers," in: *Three-Dimensional Turbulent Boundary Layers*, H. H. Fernholz and E. Krause, eds., Springer-Verlag, New York, pp. 286–297.

Hanjalic, K., and Launder, B. E., 1976, "Contribution Towards a Reynolds-Stress Closure for Low-Reynolds-Number Turbulence," *Journal of Fluid Mechanics*, Vol. 74, pp. 593–610.

Johnston, J. P., 1976, "Experimental Studies in Three Dimensional Turbulent Boundary Layers," Thermosciences Div., Dept. of Mech. Engr. Report MD-34, Stanford Univ., Stanford, CA.

Jones, W. P., and Launder, B. E., 1972, "The Prediction of Laminarization With a Two-Equation Model of Turbulence," *International Journal of Heat and Mass Transfer*, Vol. 15, pp. 301–314.

Keller, H. B., and Cebeci, T., 1972, "Accurate Numerical Methods for Boundary-Layer Flows II: Two-Dimensional Turbulent Flows," *AIAA Journal*, Vol. 10, pp. 1193–1199.

Kim, Y.-N., Buggeln, R. C., and McDonald, H., 1985, "Development of a Navier–Stokes Analysis for Flow in Disk Pumps," AFWAL-TR-85-2039.

Köhler, M., 1971, "The Flow of an Incompressible Viscous Fluid Between Two Parallel Disks" [in German], *Acta Mechanica*, Vol. 12, pp. 33–51.

Koosinlin, M. L., and Lockwood, F. C., 1974, "The Prediction of Axisymmetric Turbulent Swirling Boundary Layers," *AIAA Journal*, Vol. 12, pp. 547–554.

Launder, B. E., Priddin, C. H., and Sharma, B. I., 1977, "The Calculation of Turbulent Boundary Layers on Spinning and Curved Surfaces," ASME *Journal of Fluids Engineering*, Vol. 99, pp. 231–239.

Owen, J. M., 1984, "Fluid Flow and Heat Transfer in Rotating Disc Systems," in: *Heat and Mass Transfer in Rotating Turbomachinery*, D. E. Metzger and N. H. Afgan, eds., Hemisphere, New York, pp. 81–103.

Pincombe, J. R., 1981, "Velocity Measurements in the MK II-Rotating Cavity Rig With a Radial Outflow," Report No. TFMRC/21, Univ. of Sussex, School of Engineering and Applied Sciences.

Pouagare, M., and Lakshminarayana, B., 1983, "Computation and Turbulence Closure Models for Shear Flows in Rotating Curved Bodies," *Proceedings, Fourth Symposium on Turbulent Shear Flows*, L. J. S. Bradbury et al., eds., pp. 6.6-6.13; also *Journal of Propulsion and Power*, Vol. 2, 1986, pp. 289–290.

Rotta, J. C., 1979, "A Family of Turbulence Models for Three-Dimensional Boundary Layers," *Turbulent Shear Flows 1*, L. J. S. Bradbury et al., eds., Springer-Verlag, New York, pp. 267–278.

Schumann, L. F., 1986, "A Three-Dimensional Axisymmetric Calculation Procedure for Turbulent Flows in a Radial Vaneless Diffuser," ASME JOURNAL OF ENGINEERING FOR GAS TURBINES AND POWER, Vol. 108, pp. 118–124.

Truman, C. R., and Jankowski, D. F., 1985, "Prediction of Turbulent Source Flow Between Stationary and Rotating Discs," *International Journal of Heat and Fluid Flow*, Vol. 6, pp. 69–78.

Truman, C. R., Shirazi, S. A., and Blottner, F. G., 1988, "Noniterative Solution for Pressure in Parabolic Flows," in preparation.

Wilcox, D. C., and Rubesin, M. W., 1980, "Progress in Turbulent Modelling for Complex Flow Fields Including Effects of Compressibility," NASA Tech. Paper 1517.

O. K. Kwon
Senior Project Engineer,
Allison Gas Turbine Division,
General Motors Corporation,
Indianapolis, IN
Assoc. Mem. ASME

R. H. Pletcher
Professor,
Department of Mechanical Engineering and
Computational Fluid Dynamics Center,
Iowa State University,
Ames, IA
Fellow ASME

R. A. Delaney
Chief, Computational Fluid Dynamics,
Allison Gas Turbine Division,
General Motors Corporation,
Indianapolis, IN
Mem. ASME

Calculation of Unsteady Turbulent Boundary Layers

An unsteady, two-dimensional boundary-layer solution procedure is used to predict two different types of incompressible turbulent mean flows, the Blasius and Howarth flows, with superimposed time-dependent harmonic oscillations. A simple algebraic mixing length model that includes a minor modification for unsteadiness in the inner part of the boundary layer was used. Computed results for the two different mean flows over a wide range of unsteady conditions are presented and compared with measured data and other numerical solutions. The overall agreement of the present solutions with measurements is very good, although details of unsteady characteristics are not completely resolved due to shortcomings in the closure model.

Introduction

An increased level of both experimental and analytical research activity on unsteady turbulent flows has been observed in recent years. This is due in part to the increasing importance of these flows in determining the performance of rotating machinery. Although the phenomena are too complicated for a full understanding at present, reliable computational procedures that should allow the evaluation of turbulence models for unsteady flows without great concern for the numerical formulation have been developed (see Kwon et al., 1986) and validated for laminar flows. In an earlier paper (Kwon et al.), the authors presented a finite-difference solution procedure for solving the compressible, unsteady boundary-layer equations. The comparisons in that paper were predominantly for laminar flows to establish the accuracy of the numerical scheme. Only a sample of turbulent flow results was included to show how the numerical procedure deals with turbulent flows. In this paper, the application of the solution scheme to a fairly wide range of unsteady turbulent flows is considered.

As in steady flows, establishing closure of the governing equations by evaluating the Reynolds stress term in an appropriate manner is necessary. Although numerous efforts on developing closure models for unsteady turbulent boundary layers have been made recently, none of the models can be identified as completely satisfactory over a wide range of unsteady conditions (see Telionis, 1975; McCroskey, 1976; Telionis, 1979). Difficulties in developing accurate closure models are due to a poor understanding of the phenomena as well as a lack of reliable, complementary experimental data according to the review by Carr (1981). Closure models developed for steady flows have often been used to predict unsteady flows. These models have often performed rather poorly in strong pressure gradients with relatively high fluctuating amplitudes and frequencies (see Cebeci, 1977; Orlandi, 1981).

Among these turbulence models, the most popular at present for unsteady flows are the models based on the mixing-length concept. This is because of their simplicity and ability to predict mean flows with reasonable accuracy under near-equilibrium flow conditions (Telionis, 1975). However, higher-order models that can accurately resolve details are generally in demand (McCroskey, 1976; Cousteix, 1981). To date no evidence has shown that existing higher order models can predict unsteady flow details with consistently greater accuracy than algebraic models. On the order hand, algebraic models are expected to have limitations in unsteady flows. One of the objectives of this study is to identify some of these shortcomings. Once this has been done, the development of improved models can proceed on a rational basis. The algebraic model used in the present study is of the mixing length type and incorporates a suggestion due to Cebeci (Cebeci, 1977; Murphy and Prenter, 1981; Cebeci and Carr, 1982) for modifying a steady flow model in the inner region to account partially for the effects of unsteadiness. Further details on the turbulence model will be given in the next section.

Using the mixing length model, the unsteady boundary layer solution procedure described in Kwon et al. (1986) was applied to two different types of flows: an unsteady flow over a flat

Contributed by the Gas Turbine Division of THE AMERICAN SOCIETY OF MECHANICAL ENGINEERS and presented at the 32nd International Gas Turbine Conference and Exhibit, Anaheim, California, May 31–June 4, 1987. Manuscript received at ASME Headquarters February 4, 1987. Paper No. 87-GT-53.

plate measured by Karlsson (1959) and an oscillatory decelerating flow measured by Parikh et al. (1981). Computed solutions are compared with measured data and other numerical results. Overall, the results agreed well with measurements. In particular, for the oscillatory decelerating flow, the present solutions are significantly better than the results obtained using a higher-order model in Orlandi (1981). However, some flow details, especially near the solid wall, are not well resolved with the present mixing length model. Further work in developing more complete models for unsteady flows is required.

Analysis

The boundary layer solution procedure described in Kwon et al. (1986) is for unsteady, two-dimensional, compressible flows. Since the same numerical solution procedure has been used in the present work for predicting unsteady incompressible turbulent boundary layers, the solution procedure is only briefly discussed here. Following the earlier work, the governing unsteady, two-dimensional, compressible boundary layer equations with the equation of state for an ideal gas can be written in Cartesian coordinates as

$$\frac{\partial \rho}{\partial t}+\frac{\partial}{\partial x}(\rho u)+\frac{\partial}{\partial y}(\rho v)=0 \tag{1}$$

$$\rho\frac{\partial u}{\partial t}+\rho u\frac{\partial u}{\partial x}+\rho v\frac{\partial u}{\partial y}=-\frac{\partial p}{\partial x}+\frac{\partial}{\partial y}\left(\mu_{\text{eff}}\frac{\partial u}{\partial y}\right) \tag{2}$$

$$C_p\ \rho\frac{\partial T}{\partial t}+C_p\ \rho u\frac{\partial T}{\partial x}+C_p\ \rho v\frac{\partial T}{\partial y}=\frac{\partial}{\partial y}\left(k_{\text{eff}}\frac{\partial T}{\partial y}\right)+\mu_{\text{eff}}\left(\frac{\partial u}{\partial y}\right)^2+\frac{\partial p}{\partial t}+u\frac{\partial p}{\partial x} \tag{3}$$

$$p=\rho RT \tag{4}$$

with

$$\mu_{\text{eff}}=\mu+\mu_t$$

$$k_{\text{eff}}=k+k_t=C_p\left(\frac{\mu}{\text{Pr}}+\frac{\mu_t}{\text{Pr}_t}\right)$$

where x and y are coordinates along and normal to the streamwise direction, respectively; t, the time; u and v, the velocity components in the x and y directions; p, the pressure; T, the temperature; ρ, C_p, μ, and k, the density, specific heat, viscosity, and thermal conductivity of the fluid, respectively; R, the gas constant; and Pr, the Prandtl number. The subscripts eff and t refer to the effective and turbulent quantities, respectively.

The boundary conditions are

$$\text{at } y=0, \qquad u(x,\ 0,\ t)\ =\ u_w(x,\ t),$$

$$v(x,\ 0,\ t)\ =\ 0.0,$$

$$T(x,\ 0,\ t)\ =\ T_w(x,\ t) \tag{5}$$

$$\text{as } y\to\infty, \qquad u(x,\ y,\ t)\ =\ u_e(x,\ t) \tag{6}$$

and in the free stream where the normal gradients of velocity and temperature are zero, pressure, velocity, density, and temperature must satisfy the following relations and the equation of state, equation (4),

$$\partial p/\partial x=-\rho_e(\partial u_e/\partial t+u_e\partial u_e/\partial x) \tag{7}$$

$$\partial p/\partial t=C_p\rho_e(\partial/\partial t+u_e\partial/\partial x)(T_e+u_e^2/2\ C_p) \tag{8}$$

Here it is clear that, for compressible flows, one of the free-stream variables of pressure, velocity, density, or temperature can be fixed by boundary conditions and the other three quantities should be determined using equations (4), (7), and (8). That is, with the prescribed free-stream velocity u_e, pressure, density, and temperature in the free-stream are, therefore, evaluated from equations (4), (7), and (8). It should be noted that equation (8) indicates that, for unsteady compressible flow, the total enthalpy is no longer constant but varies with time if the pressure varies with time. For incompressible flows, equation (4) and (8) are not used. Instead, the free-stream temperature T_e should be specified as a boundary condition for the energy equation.

The governing partial differential equations (1)–(4) written in the primitive variables, u, v, T, and ρ, were solved using a fully coupled solution procedure that overcomes the difficulties associated with the time integration for the normal velocity component. With the solution procedure, the governing equations were discretized using a fully implicit numerical scheme. These discretized equations are algebraically nonlinear in the unknown dependent variables of u, v, T, and ρ. The linear representation of these finite-difference equations is obtained through iterative application of the Newton linearization scheme to the nonlinear terms. The linearized finite-difference equations are then rearranged to obtain a block tridiagonal system for the unknown vector of $[u, v, T]^T$ after eliminating the unknown density ρ in the discretized equations using the equation of state. Finally, the linearized tridiagonal system of equations is solved using a block tridiagonal matrix solver. The density is then calculated separately from the equation of state. It should be noted that since a linearization scheme has been used for the nonlinear terms during the solution procedure, local iterations are necessary to obtain the solution that satisfies the governing

Nomenclature

A^+ = function defined in equation (11)
a_0 = constant
C_p = specific heat
c_f = skin friction coefficient
f = frequency $=\omega/2\pi$
k = thermal conductivity
L = reference length
l = mixing length
Pr = Prandtl number
p = pressure
p_x^+ p_t^+ = function defined in equation (11)
R = gas constant
T = temperature
t = time
u, v = velocity component in x and y directions, respectively
u_τ = friction velocity
Δu = velocity amplitude
x, y = Cartesian coordinates
δ = boundary layer thickness
δ^* = displacement thickness
μ = viscosity
ν = kinematic viscosity
ρ = density
τ = shear stress
ϕ = phase angle
ω = frequency

Subscripts and Superscripts

e = boundary layer edge condition
eff = effective condition
0 = reference condition or leading edge condition
t = turbulent flow
w = wall condition
$(\ )'$ = fluctuating quantity
$\overline{(\ )}$ = time-averaged quantity

equations simultaneously at each streamwise station. The local iterative procedure at a streamwise station starts with the solution of u, v, T, and ρ at the previous time level as the initial value. The fluid properties are updated after each local iteration. For air, a standard property table such as in Eckert and Drake (1972) is used to evaluate the properties.

Since the flow of interest in this study is incompressible and does not include heat transfer, neither the energy equation nor the equation of state are required. Further, no property update is necessary. Only the continuity and momentum equations are solved for the unknown u and v, as discussed by Kwon et al. This simplification makes the solution procedure converge fast in the local Newton iteration loop. Typically two-three iterations are required to achieve the convergence criteria that the maximum variation of u between two successive iterations be less than 0.01 percent of the u obtained at the latest iteration across the computation domain. As to the numerical stability, the present scheme is not constrained by the size of the time step since the fully implicit algorithm is used for the discretization of the governing equations. However, relatively fine time steps were used for the solution to ensure computation accuracy. Further details of the present solution procedure can be found elsewhere (Kwon et al., 1986).

The turbulence closure model used for evaluating the turbulent viscosity μ_t in the Reynolds-averaged unsteady boundary layer equations is a simple mixing length model incorporating a minor modification for unsteadiness as suggested by Cebeci (1977). According to this model, the turbulent viscosity μ_t is expressed by

$$\mu_t = \rho l^2 \left| \frac{\partial u}{\partial y} \right| \tag{9}$$

where l is the mixing length.

In the inner layer region of the boundary layer, the mixing length is defined by the following formula:

$$l = 0.41y(1.0 - \exp[-y/A^+]) \tag{10}$$

where

$$A^+ = 26\nu/u_\tau \sqrt{1 - 11.8(p_t^+ + p_x^+)}$$

$$\mu_\tau = \sqrt{\tau_w/\rho} \tag{11}$$

$$p_t^+ = (\nu/u_\tau^3)\partial u_e/\partial t$$

$$p_x^+ = (\nu u_e/u_\tau^3)\partial u_e/\partial x$$

Here y is the normal coordinate; ν, the kinematic viscosity; τ_w, the wall shear stress; u_e, the local free-stream velocity; t, the time; and x, the streamwise coordinate. The correction for A^+ was suggested by Cebeci (1977) and has been used by several investigators with the Cebeci–Smith eddy viscosity model (see Cebeci, 1977; Murphy and Prenter, 1981; Cebeci and Carr, 1982).

In the outer region, the mixing length is defined by

$$l = 0.085\,\delta \tag{12}$$

Here δ is the boundary layer thickness defined as the y location where the streamwise velocity component reaches 99 percent of the local free-stream velocity. The switch from the inner to the outer model is made at the y location where the mixing length l obtained from equation (10) becomes equal to or greater than l from equation (12).

Results and Discussion

With the turbulence model discussed previously, the unsteady boundary layer solution procedure described by Kwon et al. was applied to two different types of two-dimensional turbulent unsteady incompressible flows: a uniform mean flow with a harmonic oscillation measured by Karlsson (1959) and an oscillatory decelerating turbulent flow measured by Parikh et al. (1981). These cases provide a common basis for comparisons with other numerical methods such as Cebeci (1977), Orlandi (1981), Murphy and Prenter (1981), Lam (1983), and Telionis and Lomaniuk (1979). The present calculations were started with steady-state solutions that were generated by solving the governing equations in the steady mode with the free-stream velocity at $t = 0$, and continued until the periodic solutions were established. Details of the results are discussed below.

Flow Measured by Karlsson (1959). Karlsson measured the turbulent boundary layer on a flat wall of a wind tunnel with a rectangular cross section. The harmonic oscillation was introduced by four parallel rotating shutters located at the tunnel exit. With the facility, Karlsson was able to obtain the free-stream velocity approximately in the form of

$$u_e(t) = u_0\left(1 + \frac{\Delta u_e}{u_0}\cos\ \omega t\right) \tag{13}$$

where u_e is the instantaneous edge velocity; u_0, the mean free-stream velocity; Δu_e, the amplitude of the free-stream velocity; ω, the frequency; and t, the time. The measured mean free-stream velocity varied from 15 ft/sec to 17.5 ft/sec. The ranges of amplitude and frequency were 8–34 percent of the mean free-stream velocity and 0–48 Hz, respectively.

The present predictions were made for the six different frequencies of 0.33, 1.0, 2.0, 4.0, 7.65, and 48 Hz. The flow was assumed fully turbulent throughout the domain. The amplitude of the free-stream oscillation for these frequencies was set to 14.7, 10.7, 28.6, 26.4, 7.3, and 34.0 percent of the mean free-stream velocity, respectively. The mean free-stream velocities were set to 5.33 m/s for all cases except for the case with the frequency of 0.33 Hz, for which 4.57 m/s was specified in accordance with the measurements of Karlsson.

Figure 1 shows the computed mean velocity profiles for frequencies of 0.33, 2.0, and 7.65 Hz compared with measurements. These velocity profiles indicate that the mean flow is affected very little by the free-stream fluctuations. For the flows with oscillation frequencies up to 7.65 Hz, no temporal flow reversal was observed inside the boundary layer.

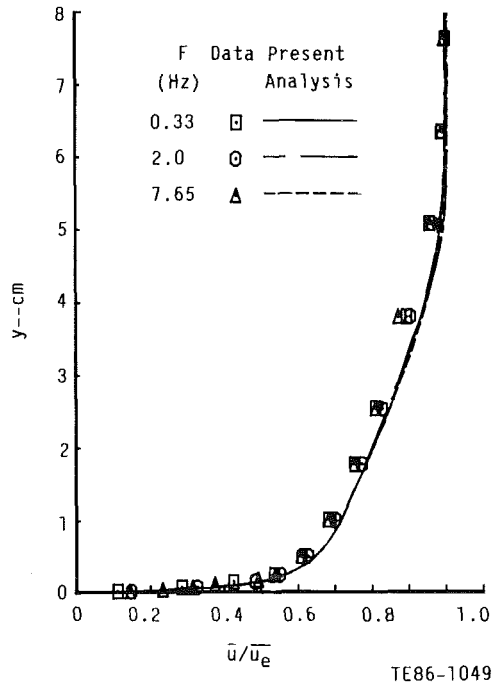

Fig. 1 Mean velocity profiles for oscillating turbulent boundary layers with zero-streamwise mean pressure gradient

However, for 48 Hz, a small flow reversal occurred near the solid wall during part of the period, as shown in Fig. 2. At this frequency, Karlsson's measurements indicate that the higher harmonics (primarily secondary) were relatively large (approximately 15 percent of the total root-mean-square amplitude). To take account of these higher harmonics, modifying equation (13) would be required. However, Karlsson did not provide an appropriate expression. The maximum height of the calculated reversed flow was 0.783 mm. This prediction of flow reversal agrees with Karlsson's observations in his experiments. It should be noted that the present predictions did not account for the effect of the secondary harmonics.

Figures 3 and 4 present the calculated amplitude profiles for oscillation frequencies and amplitudes of 0.33 Hz and 14.7 percent and 7.65 Hz and 7.3 percent, respectively. The present solutions compare well with the measurements of Karlsson and with the numerical results obtained by Lam (1983) for 0.33 Hz, and Murphy and Prenter (1981) for 7.65 Hz. The solutions obtained by Telionis and Romaniuk (1979) agree well with Karlsson's data for the in-phase component of the amplitude defined as $(\Delta u/\Delta u_e)\cos\phi$. However, the out-phase amplitude, $(\Delta u/\Delta u_e)\sin\phi$, compares poorly with other solutions, as shown in Fig. 3. The discrepancies between their solutions and measurements become more pronounced at higher frequencies, e.g., at 1 Hz (see Telionis, 1979). The prediction of the in-phase component of amplitude by Cebeci (1977) does not agree well with the measured and the other computed solutions for 0.33 Hz. The reason for this is unclear since all the analyses shown in the figures except for that by Telionis and Romaniuk used basically the same turbulence model.

The present predictions for various frequencies show that increasing the frequency causes the peak amplitude to occur closer to the wall and the amplitude profile to be more uniform. At the highest frequency of 48 Hz, except for the near-wall region, the computed amplitude profiles were nearly uniform across the boundary layer with the value of 1.0 for the in-phase component and 0.0 for the out-phase components, as observed by Karlsson (see Fig. 5).

As for the local wall skin-friction coefficient, c_f $(=\tau_w/2\rho u_e^2)$, its amplitude of oscillation increased as both the frequency and amplitude of the free-stream oscillation increased, as shown in Figs. 6 and 7. At the highest frequency and amplitude, the deviation of the skin-friction coefficient from the harmonic pattern is noticeable. At 48 Hz, as discussed previously, a temporal flow reversal with a large wall shear is shown in Fig. 7. The amplitude of oscillation of the boundary-layer displacement thickness becomes larger as the amplitude of free-stream oscillation increases, as shown in Fig. 8. Further, the oscillation of the displacement thickness becomes gradually symmetric at the higher frequencies.

These solutions were obtained using a 141 × 85 grid spanning a region from $x=0.00$–3.38 m and $y=0.00$–0.2595 m.

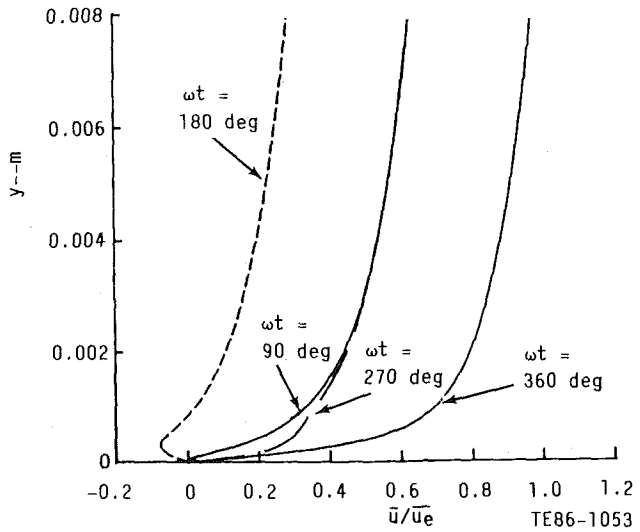

Fig. 2 Mean velocity profiles for oscillating turbulent boundary layers in the near wall region at 90-deg increments from $\omega t = 90$ deg: $f = 48$ Hz; $\Delta u_e/u_0 = 0.34$

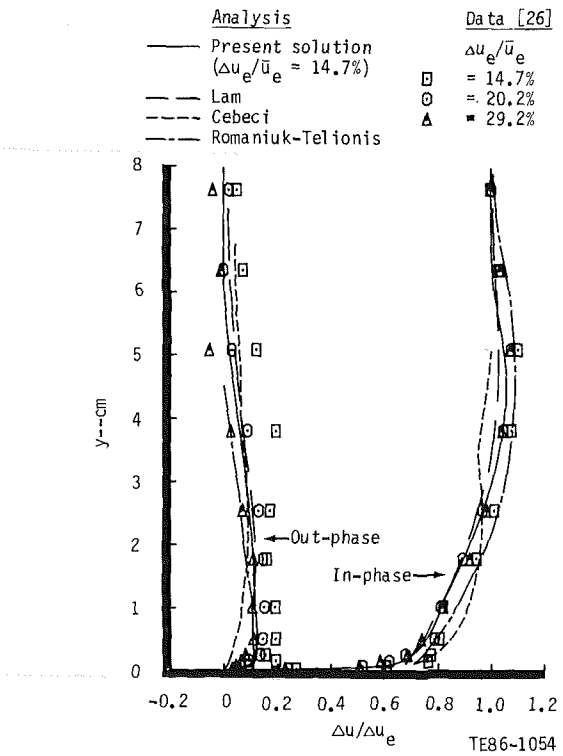

Fig. 3 Amplitude profiles for oscillating turbulent boundary layers with zero-streamwise mean pressure gradient: $f = 0.33$ Hz; $\Delta u_e/u_0 = 0.147$

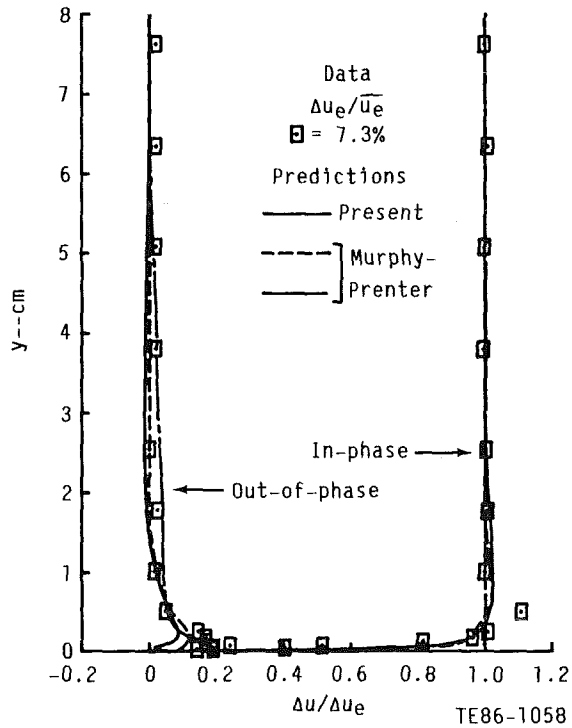

Fig. 4 Amplitude profiles for oscillating turbulent boundary layers with zero-streamwise mean pressure gradient: $f = 7.65$ Hz; $\Delta u_e/u_0 = 0.073$

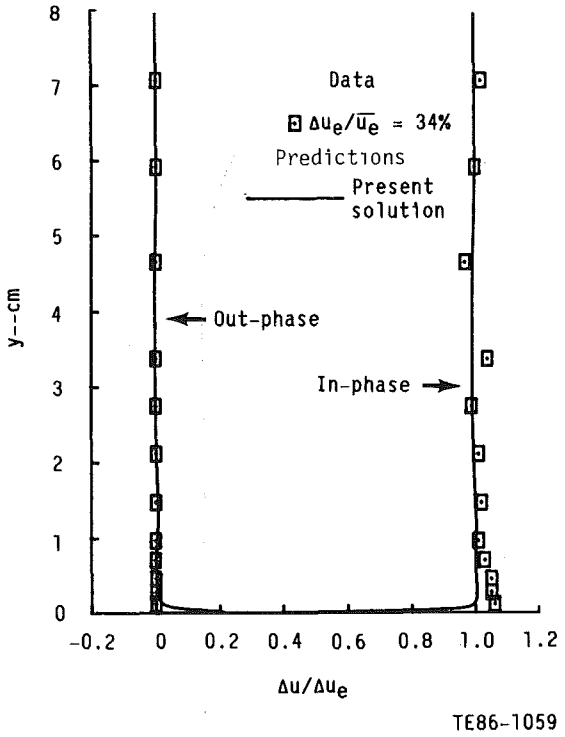

Fig. 5 Amplitude profiles for oscillating turbulent boundary layers with zero-streamwise mean pressure gradient: $f = 48.0$ Hz; $\Delta u_e/u_0 = 0.34$

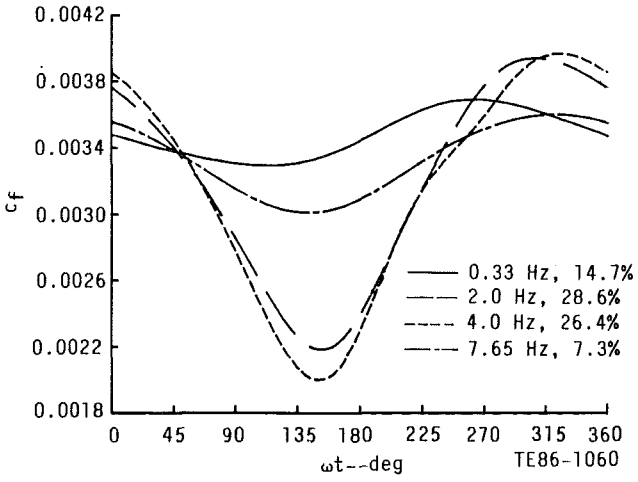

Fig. 6 Time variation of the wall shear stress for oscillating turbulent boundary layers with zero-streamwise mean pressure gradient: $f = 0.33$, 2.0, 4.0, and 7.65 Hz

The time-periodic solutions were achieved in 4–6 cycles of oscillation. Each cycle was computed with 128 time steps.

Flow Measured by Parikh et al. (1981). Parikh et al. measured a linearly retarded flow with a harmonic oscillation using a water channel. The free-stream velocity was constant upstream of the zone of deceleration. The free-stream velocity, $u(x, t)$, in the deceleration zone is expressed in the following form:

$$u_e(x, t) = u_0 - (a_0/L)(x - x_0)(1.0 - \cos \omega t) \qquad (14)$$

where u_0 is the free-stream mean velocity at the leading edge of the plate; x, the distance along the plate; x_0, the distance from the leading edge to the point where the flow starts to decelerate; a_0, the maximum amplitude of imposed free-stream oscillations; L, the extent of flow deceleration zone; ω, the frequency; and t, the time. The measurements were made

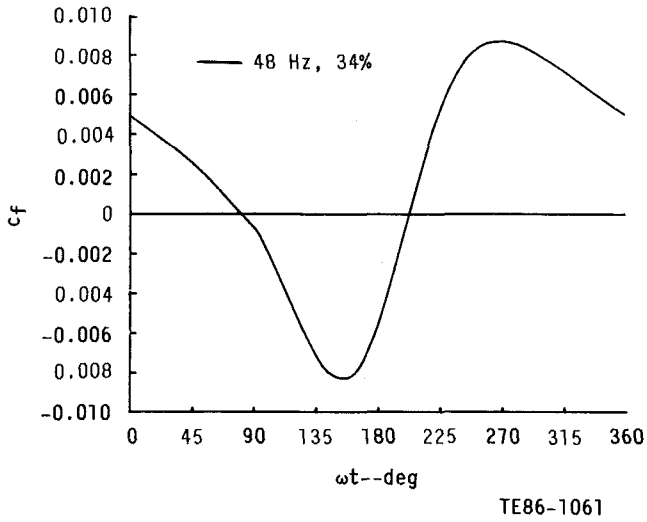

Fig. 7 Time variation of the wall shear stress for oscillating turbulent boundary layers with zero-streamwise mean pressure gradient: $f = 48.0$ Hz

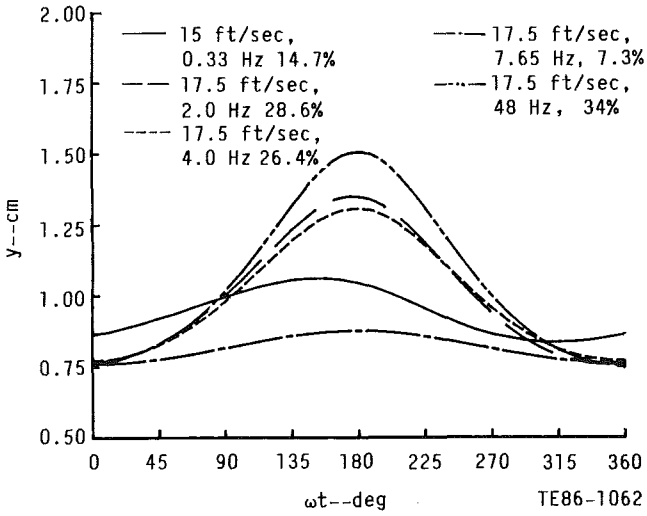

Fig. 8 Time variation of the displacement thickness for oscillating turbulent boundary layers with zero-streamwise mean pressure gradient: $f = 0.33$, 2.0, 4.0, 7.65, and 48.0 Hz

for the amplitude parameter $a_0/u_0 = 0.05$ and for frequencies of 0, 0.25, 0.5, and 2.0 Hz. The flow deceleration point x_0 and the extent of the deceleration zone L were 2.0 m and 0.6 m, respectively.

The calculation was performed over $x = 1.88$–2.6 m after the initial profiles were established at $x = 1.88$ m by solving the steady two-dimensional incompressible boundary layer equations from the leading edge ($x = 0$ m). A 41 × 85 grid was used for the unsteady solutions. In the computations, the time-periodic solutions were established quickly in two or three cycles. This is due to the low frequencies of the oscillation. Each cycle was divided into 96 time steps.

Figure 9 presents the calculated velocity profile at the x location where the flow deceleration starts. The present results agree well with the measurements by Parikh et al. Similar velocity profile comparisons are shown in Fig. 10. These velocity profiles are for $x = 2.568$ m and zero frequency, i.e., a quasi-steady condition. The computed profiles of amplitudes inside the boundary layer normalized by the free-stream amplitude are shown in Fig. 11 along the measured data by Parikh et al. and the numerical results obtained by Orlandi (1981). The present results compare well with measurements

considering the uncertainties in the measurements and are noticeably better than Orlandi's solutions that were obtained using a one-equation (turbulence kinetic energy) turbulence model. The calculated maximum amplitude was obtained for the quasi-steady condition, i.e., 0 Hz, with the value of 1.608 that is a little smaller than the measured value of 1.676. The amplitude profiles become uniform as the frequencies of the free-stream oscillation increase. At the highest frequency of 2 Hz, the amplitude profile was nearly uniform inside the boundary layer except for the near-wall region where a rapid drop to zero followed by a slight overshoot occurred. Interestingly, the present computed amplitudes for 0.5 Hz are smaller than those for the 2 Hz case, as was also observed by Parikh et al. (see Fig. 11).

Figure 12 shows the computed and measured phase differences between the boundary layer oscillations and free-stream oscillations. Overall agreement between the present calculated results and measurements by Parikh et al. is good, although in the near-wall region the present solutions are generally underpredicted. The effect of increasing the frequency is to reduce the phase lag in the region away from the wall and to cause phase lead in the region close to the wall. The computed solutions for the wall shear, however, do not compare well with measurements. The computed wall skin-friction coefficient, c_f $(=\tau_w/2\ \rho u_e^2)$, gradually deviates from measurements as the frequencies increase, as shown in Fig. 13. Orlandi obtained the same type of deviation. In general, as the frequencies increase, the amplitude of the periodic skin-friction coefficient seems to be reduced initially (until the frequency reaches around 2 Hz) and then to start increasing at higher frequencies.

The predicted integral parameters, however, such as the displacement thickness, agree well with measurements. Figure 14 shows a comparison between the time variation of the calculated displacement thickness and the measured data. As shown, the amplitude of the displacement thickness oscillation seems to be reduced as the frequency increases. The phase shift of the displacement thickness is 180 deg with respect to the free-stream oscillation at the quasi-steady state (0 Hz) and decreases with increasing frequency until it reaches a minimum value. Further increases in the free-stream frequency cause an increase in the phase shift. The present displacement thickness variation in time compares favorably with the solution obtained by Orlandi, although a direct comparison between the two solutions is not presented in this paper.

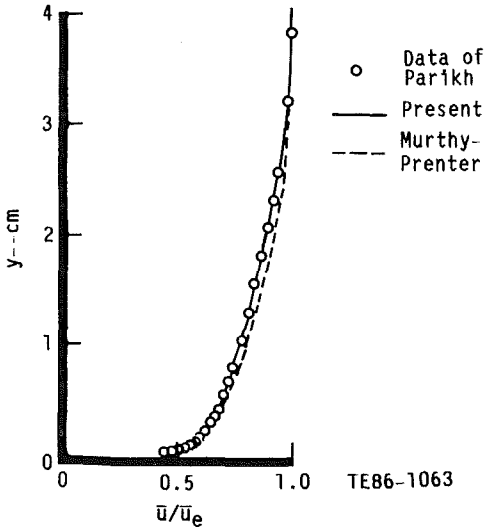

Fig. 9 *Mean velocity profile at the start of the flow deceleration for the measurements of Parikh et al. (1981)*

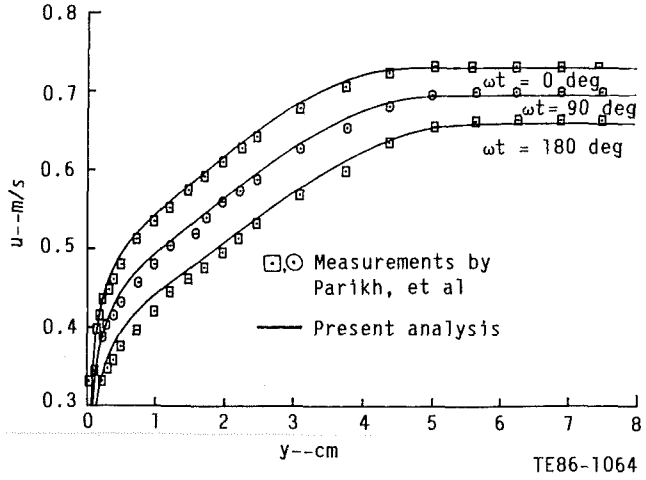

Fig. 10 **Mean velocity profiles for oscillating turbulent boundary layers with adverse streamwise pressure gradient at $\omega t = 0$, 90, and 180 deg: $f = 0.0$ Hz; $a_0/u_0 = 0.05$; $x - x_0 = 5.568$ m; $L = 0.6$ m; $x_0 = 2$ m**

Conclusions

The unsteady two-dimensional boundary-layer solution procedure described in Kwon et al. (1986) has been successful-

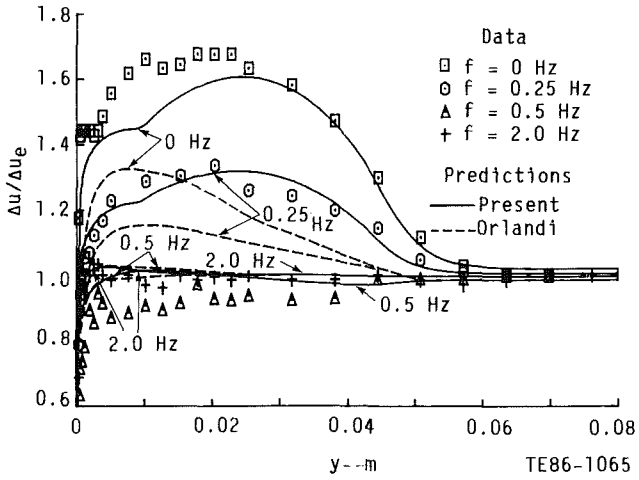

Fig. 11 **Amplitude profiles for oscillating turbulent boundary layers with adverse streamwise pressure gradient: $a_0/u_0 = 0.05$; $x - x_0 = 0.568$ m; $L = 0.6$ m; $x_0 = 2$ m**

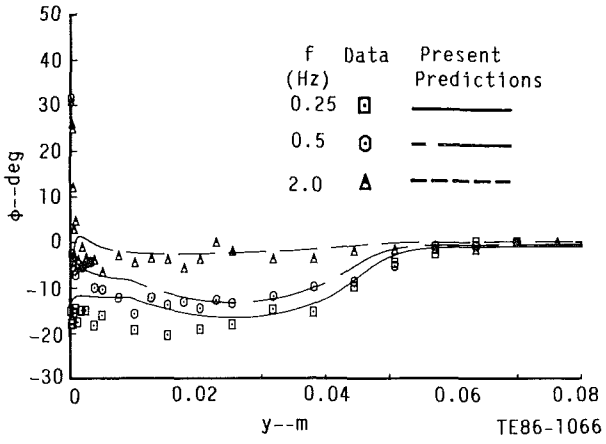

Fig. 12 **Phase angle profiles for oscillating turbulent boundary layers with adverse streamwise pressure gradient: $a_0/u_0 = 0.05$; $x - x_0 = 0.568$ m; $L = 0.6$ m; $x_0 = 2$ m**

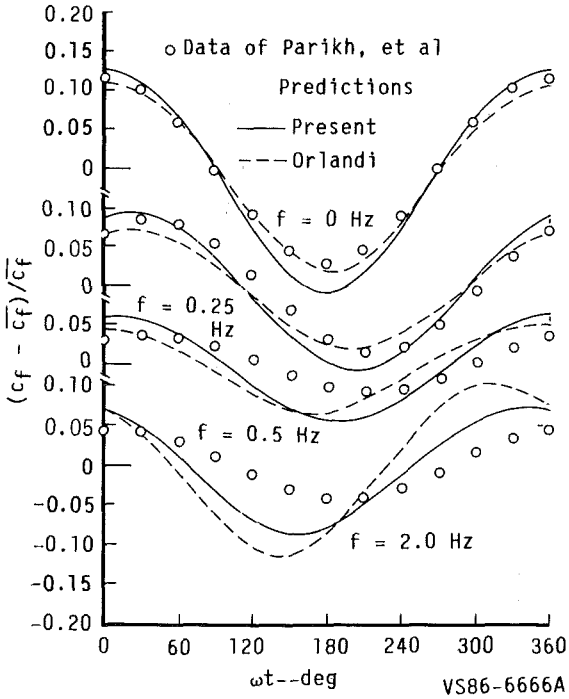

Fig. 13 Wall shear stress variations for oscillating turbulent boundary layers with adverse streamwise pressure gradient: $a_0/u_0 = 0.05$; $x - x_0 = 0.568$ m; $L = 0.6$ m; $x_0 = 2$ m

ly used for computing unsteady turbulent boundary layers with zero and adverse mean streamwise pressure gradients. A simple algebraic mixing length model provides reasonable mean flow characteristics of the oscillating flows and even better solutions than a more complicated higher-order model. The agreement between computed solutions and measured data is good even for high amplitudes and frequencies of oscillation.

Although the present study has demonstrated that the mixing length model can be useful for simulating unsteady flow phenomena with reasonable accuracy over a relatively wide range of unsteady oscillatory conditions, additional work on turbulence modeling seems to be required to resolve details more accurately, especially in the near-wall region. In this region, the amplitudes and phase shifts of velocities are often underpredicted and the wall shear stresses do not often compare well with measured data.

Acknowledgments

This research is sponsored by the Air Force Wright Aeronautical Laboratories (AFWAL)/POTC under contract F33615-83-C-2339. The authors wish to express their gratitude to Dr. Charles MacAuthur and Lt. Michael Stanek (AFWAL/POTC), and Messrs. Donald Tipton and Stacy Thompson for their continued support and cooperation. The authors also wish to acknowledge the assistance given by Dr. Lawrence Carr (NASA-Ames) in supplying the digitized data for both Karlsson's (1959) and Parikh, Reynolds, and Jayaraman's (1981) experiments.

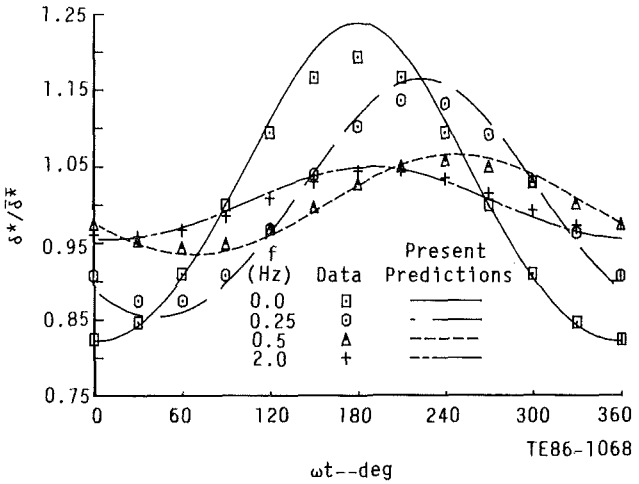

Fig. 14 Displacement thickness variations for oscillating turbulent boundary layers with adverse streamwise pressure gradient: $a_0/u_0 = 0.05$; $x - x_0 = 0.568$ m; $L = 0.6$ m; $x_0 = 2$ m

References

Carr, L. W., 1981, "A Review of Unsteady Turbulent Boundary Layer Experiments," *Unsteady Turbulent Shear Flows*, R. Richel, J. Cousteix, and R. Houdeville, eds., IUTAM Symposium, Toulouse, France, Springer-Verlag, Berlin, pp. 3–34.

Cebeci, T., 1977, "Calculation of Unsteady Two-Dimensional Laminar Turbulent Boundary Layers With Fluctuations in External Velocity," *Proceedings of the Royal Society of London*, Vol. A355, pp. 225–238.

Cebeci, T., and Carr, L. W., 1982, "Computation of Steady Turbulent Boundary Layers With Flow Reversal and Evaluation of Two Separated Turbulence Models," *Proceedings of the Royal Society of London*, Vol. A380, pp. 291–304.

Cousteix, J., 1981, "Turbulence Modeling and Boundary Layer Calculation Methods," *Separated Flows in Turbomachinery Components*, Vol. 2, Lecture Series 1981-1, von Karman Institute for Fluid Dynamics.

Eckert, E. R. G., and Drake, R. M., 1972, *Analysis of Heat and Mass Transfer*, McGraw-Hill, New York.

Karlsson, S. K. F., 1959, "An Unsteady Turbulent Boundary Layer," *Journal of Fluid Mechanics*, Vol. 5, pp. 622–636.

Kwon, O. K., Pletcher, R. H., and Delaney, R. A., 1986, "Solution Procedure for Unsteady Two-Dimensional Boundary Layers," presented at the American Institute of Aeronautics & Astronautics/American Society of Mechanical Engineers (AIAA/ASME) 4th Joint Fluid Mechanics, Plasma Dynamics, and Laser Conference, Atlanta, GA, May 12–14.

Lam, C. Y., 1983, "Unsteady Laminar and Turbulent Boundary Layer Computations Using a Difference Method," Ph.D. Thesis, University of London, London, England.

McCroskey, W. J., 1977, "Some Current Research in Unsteady Fluid Dynamics—the 1976 Freeman Scholar Lecture," ASME *Journal of Fluids Engineering*, Vol. 99, pp. 8–38.

Murphy, J. D., and Prenter, P. M., 1981, "A Hybrid Computing Scheme for Unsteady Turbulent Boundary Layers," presented at Third Symposium on Turbulence Shear Flows, held at Davis, CA, Sept. 9–11.

Orlandi, P., 1981, "Unsteady Adverse Pressure Gradient Turbulent Boundary Layers," *Unsteady Turbulent Shear Flows*, R. Michel, J. Cousteix, and R. Houdeville, eds., Springer-Verlag, New York, pp. 159–170.

Parikh, P. G., Reynolds, W. C., and Jayaraman, R., 1981, "On the Behavior of an Unsteady Turbulent Boundary Layer," presented at the Symposium on Numerical and Physical Aspects of Aerodynamic Flows, Long Beach, CA, Jan. 19–21.

Telionis, D. P., 1975, "Calculations of Time-Dependent Boundary Layers," *Unsteady Aerodynamics*, R. B. Kinney, ed., Vol. 1, pp. 155–190.

Telionis, D. P., 1979, "REVIEW—Unsteady Boundary Layers Separated and Attached," ASME *Journal of Fluids Engineering*, Vol. 101, pp. 29–43.

Telionis, D. P., and Romaniuk, M. S., 1979, "Turbulence Models for Oscillating Boundary Layers," AIAA Paper No. 79-0069.

Numerical Prediction of Turbulent Flow in Rotating Cavities

A. P. Morse

Thermo-Fluid Mechanics Research Centre,
School of Engineering and Applied Sciences,
University of Sussex,
Brighton, Sussex, United Kingdom

Predictions of the isothermal, incompressible flow in the cavity formed between two corotating plane disks and a peripheral shroud have been obtained using an elliptic calculation procedure and a low turbulence Reynolds number k–ϵ model for the estimation of turbulent transport. Both radial inflow and outflow are investigated for a wide range of flow conditions involving rotational Reynolds numbers up to $\sim 10^6$. Although predictive accuracy is generally good, the computed flow in the Ekman layers for radial outflow often displays a retarded spreading rate and a tendency to laminarize under conditions that are known from experiment to produce turbulent flow.

1 Introduction

Understanding of the flow and heat transfer processes occurring in rotating cavity geometries is of considerable importance to current design efforts to achieve efficient cooling of the disk components of gas turbine engines. The annular cavity formed between two corotating plane disks and a peripheral shroud provides a simple model geometry to facilitate such understanding. However, before a reliable design procedure can be established for predicting the drag and heat transfer in the high-speed geometries of practical interest, a necessary prerequisite is the validation of the procedure for flows under isothermal, low-speed conditions, where compressibility and buoyancy effects are negligible. Such a study forms the focus of the present work.

Figure 1 shows predicted streamline contours for the flows of interest, which were obtained using the low turbulence Reynolds number k–ϵ model of Section 2.1 and which conform fairly well in essential detail to the flow structures observed experimentally [1–5]. The values associated with the streamlines denote mass flow rates normalized with the total mass flow rate through the cavity, with a datum corresponding to the surface of the left-hand disk. Figure 1(*a*) refers to the radial outflow case, where the "coolant" air enters the cavity axially through a central hole in one of the disks, forms a source region, characterized by a recirculation zone adjacent to the upstream disk, and is then entrained into two symmetric Ekman layers before leaving the cavity through a sink layer near the perforated outer shroud. Bounded by the source and sink regions and the Ekman layers is an interior core of rotating fluid in which the axial and radial velocity components are essentially zero. The flow conditions may be characterized by a flow rate parameter $C_w = Q/\nu b$, and a rotational Reynolds number $\mathrm{Re}_\theta = \omega b^2/\nu$. The relative sizes of the individual flow regions vary in a systematic way with both parameters [3]; in particular the radial extent of the source region increases with either an increase in C_w or a reduction of Re_θ, while the Ekman layer thickness varies in roughly inverse proportion to $\mathrm{Re}_\theta^{1/2}$. Typically, the vortex in the source region is predicted to recirculate about 25 percent of the mass flow rate through the cavity.

For reasons of computational economy, the flow structure may be approximated by the assumption of a uniform source-sink flow with a radial entry as shown in Fig. 1(*b*). This enables computation of the flow in the Ekman layers (the main object of concern here) with attention confined to one half of the cavity, based on assumed symmetry about the mid-axial plane, $z = s/2$. Computations for both the axial and radial inlet geometries have borne out the validity of this assumption provided that the flow conditions are such that the source region does not encroach upon the radial location at which the comparison with data is required (in this case, at $r/b = 0.833$). In the interior core region of the flow, a complicated system of counterrotating vortices is predicted, which was not observed in the flow visualization experiments of [1, 3], but is in any case weak, recirculating approximately 3 percent of the mass flow rate. This system of vortices is difficult to resolve accurately due to the low flow velocities predicted in this region coupled with the effects of truncation error resulting from the use of a fairly coarse finite-difference grid outside the Ekman layers. A stronger and more definable vortex is, however, predicted adjacent to the sink layer.

Figure 1(*c*) shows the situation for radial inflow which is essentially the reverse of that discussed above. The flow enters the cavity through a slot arrangement or a series of discrete holes in the center of the peripheral shroud and, in so doing, attains some degree of initial angular momentum denoted by the swirl fraction, $c = V/\omega b$. The value of c would be expected to depend on the actual geometry of the shroud, the mass flow rate and rotational speed, and whether the flow is laminar or turbulent. For the discrete hole arrangement, the Ekman layer theory [3] is correlated fairly well by a value of $c = 0.54$ for laminar flow and $c = 0.59$ for turbulent flow, largely irrespective of the values of C_w and Re_θ. Between the central source region and the disk lies a strong vortex which is predicted to

Contributed by the Gas Turbine Division of THE AMERICAN SOCIETY OF MECHANICAL ENGINEERS and presented at the 32nd International Gas Turbine Conference and Exhibit, Anaheim, California, May 31–June 4, 1987. Manuscript received at ASME Headquarters February 5, 1987. Paper No. 87-GT-74.

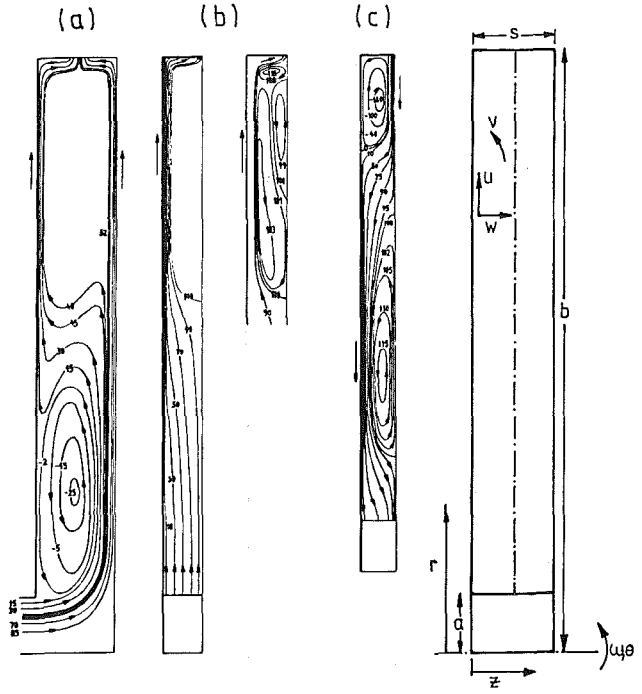

Fig. 1 Predicted streamlines for flows in rotating cavities: (a) radial outflow with axial entry: $C_W = 2184$, $Re_\theta = 4 \times 10^5$; (b) radial outflow with uniform source and sink, showing detail in "potential core": $C_W = 2184$, $Re_\theta = 4 \times 10^5$; (c) radial inflow with uniform source and sink: $C_W = -1415$, $Re_\theta = 1.97 \times 10^5$; for outflow geometry, $b = 442.5$ mm, for inflow geometry, $b = 381.0$ mm; in each case, $a/b = 0.1$, $s/b = 0.133$

recirculate approximately 1.6 times the incoming mass flow rate under the conditions shown. This vortex convects angular momentum from the disk and the shroud into the source flow and the values quoted for c denoted the *effective* swirl fraction for the limitations of the theory, i.e., taking into account the combined effects of this action and the true initial degree of swirl. According to [3] the vortex extends from the shroud to the radial location where $r/b = c^{1/2}$; the prediction shown (based on a *true* value of $c = 0.59$ at inlet) reveals the recirculation zone to be approximately 20 percent shorter than this.

Adjacent to the Ekman layer another vortex is predicted, which is impressive in size but weaker than the corner vortex, recirculating about 15 percent of the mass flow rate. The strength of this vortex has, however, been found to vary with the value chosen for the initial swirl fraction. For $c = 0$, the vortex disappears completely, leaving a truly irrotational core (in accordance with the experimental evidence), while the same is generally true for laminar flow computations, whatever the value of c. The reasons for this behavior are not immediately clear, but the predicted presence of this vortex for nonzero values of c may again be due, at least in part, to the effects of truncation error in the computations. Although in the experiment the flow left the cavity through a central hole in one of the disks, the simplifying assumption of a uniform sink and symmetry about $z = s/2$ is again appropriate.

Source-sink flows in rotating cavities have been treated analytically using integral momentum techniques by, e.g., Owen et al. [3], who obtained solutions of the linear and nonlinear forms of the Ekman layer equations. These portray many aspects of the flows satisfactorily at modest computational expense. However, detailed investigation of the flow structure in the whole of the cavity space demands use of a more elaborate finite-difference elliptic solver. Chew [6] developed a computer program for this purpose based on the familiar TEACH code of Gosman and Ideriah [7] and successfully applied it to the calculation of laminar radial outflow. In later papers [8, 9], predictions of turbulent flow were obtained based on energy-dissipation (k–ϵ) and mixing length models, respectively, for the estimation of turbulent transport. In the former, the parent or "high turbulence Reynolds number" form of the model using the traditional logarithmic wall function approach [10] proved clearly unsuitable for prediction of the data listed in [2], while a low Reynolds number version, essentially that used by Launder and Sharma [11], produced a tendency for the computed flow in the Ekman layers to revert to laminar under conditions that are known experimentally to result in turbulent flow. Better agreement with data was claimed using the mixing length model of Koosinlin et al. [12], although the spreading of the Ekman layers remained less than revealed experimentally, particularly at high rotational speeds.

It is however clear that the k–ϵ model, which avoids any troublesome specification for a length-scale variable, offers a greater scope for improvement than does a mixing length model and, in this context, it was decided to conduct a reassessment of its performance in the present work. A particular motivation for this approach was that some of the findings reported in [8] appear inconclusive, most probably due to convergence difficulties with the iterative finite-difference procedure of TEACH. For the current investigation, improvements to the TEACH code have largely removed convergence problems, which hitherto became serious at high rotational speeds, and solutions have become feasible at rotational Reynolds numbers in excess of 10^7, albeit assuming incompressible flow. Predictions based on a slightly modified form of the Launder-Sharma k–ϵ model are presented for radial outflow over the full range of flow conditions detailed

Nomenclature

a = internal flow radius
b = outer cavity radius
c = initial swirl fraction for radial inflow
C_w = flow rate parameter $= Q/\nu b$
G = production rate of turbulent kinetic energy
k = turbulent kinetic energy
P = static pressure
p' = pressure correction
Q = volumetric flow rate through cavity
r = radial coordinate
Re_θ = rotational Reynolds number $= \omega b^2/\nu$
Re_T = turbulence Reynolds number $= k^2/\epsilon\nu$
s = disk spacing
U = time-averaged *radial* velocity component
V = time-averaged *circumferential* velocity component
W = time-averaged *axial* velocity component
z = axial coordinate
α = underrelaxation factor
Γ = diffusivity
ϵ = dissipation rate of turbulent kinetic energy
θ = circumferential coordinate
μ = viscosity (without suffix = molecular viscosity)
ν = kinematic viscosity $= \mu/\rho$
ρ = fluid density
ϕ = generalized variable in transport equation
ω = angular velocity of cavity

Subscripts

eff = effective (= laminar + turbulent)
i, j, l = Cartesian tensor coordinates
in = value at cavity inlet
T = turbulent

in [2] and, in order to provide a definitive assessment of the model's performance, are compared to the high turbulence Reynolds number and laminar flow solutions. Additionally, predictions are shown for a broad spectrum of the data in [5] for radial inflow.

2 Mathematical Solution

The turbulence model closure problem involves the approximation of the Reynolds stresses ($-\rho\overline{u_i u_j}$) that appear in the time-averaged Navier–Stokes equations. Ideally, these should form the dependent variables of modeled transport equations, but, in the current approach, the concept of an isotropic "turbulent viscosity" is employed, whereby, for axisymmetric flow in cylindrical-polar (r, θ, z) coordinates,

$$\rho\overline{u^2} = 2/3\rho k - 2\mu_T \frac{\partial U}{\partial r}, \qquad \rho\overline{uv} = -\mu_T r \frac{\partial}{\partial r}\left(\frac{V}{r}\right),$$

$$\rho\overline{v^2} = 2/3\rho k - 2\mu_T \frac{U}{r}, \qquad \rho\overline{uw} = -\mu_T\left(\frac{\partial U}{\partial z} + \frac{\partial W}{\partial r}\right),$$

$$\rho\overline{w^2} = 2/3\rho k - 2\mu_T \frac{\partial W}{\partial z}, \qquad \rho\overline{vw} = -\mu_T \frac{\partial V}{\partial z} \tag{1}$$

where μ_T denotes the turbulent viscosity and k the turbulent kinetic energy ($=\frac{1}{2}\overline{u_i^2}$). Substitution into the momentum equations then enables these latter to be recast into the conveniently common form

$$\frac{\partial}{\partial z}(\rho W\phi) + \frac{1}{r}\frac{\partial}{\partial r}(\rho r U\phi) =$$

(convection)

$$\frac{\partial}{\partial z}\left(\Gamma_{\phi,z}\frac{\partial\phi}{\partial z}\right) + \frac{1}{r}\frac{\partial}{\partial r}\left(r\Gamma_{\phi,r}\frac{\partial\phi}{\partial r}\right) + S_\phi \tag{2}$$

(diffusion) (source)

where ϕ represents the generalized momentum variable and the net source term S_ϕ is different for each component of momentum. $\Gamma_{\phi,z}$ and $\Gamma_{\phi,r}$ are the effective diffusivities for the axial and radial directions and comprise laminar and turbulent components according to

$$\phi = W\text{(axial)}: \Gamma_{\phi,z} = 2\mu_{eff} - \mu;\ \Gamma_{\phi,r} = \mu_{eff},$$

$$\phi = U\text{(radial)}: \Gamma_{\phi,z} = \mu_{eff};\ \Gamma_{\phi,r} = 2\mu_{eff} - \mu$$

$$\phi = rV\text{(circumferential)}:$$

$$\Gamma_{\phi,z} = \mu_{eff};\ \Gamma_{\phi,r} = \mu_{eff} \tag{3}$$

where μ_{eff} ($=\mu+\mu_T$) denotes the effective viscosity. The net source terms can be written as

$$\phi = W: S_\phi = -\frac{\partial}{\partial z}(P + \underline{2/3\rho k}) + \underline{\frac{1}{r}\frac{\partial}{\partial r}\left(r\mu_T\frac{\partial U}{\partial z}\right)},$$

$$\phi = U: S_\phi = -\frac{\partial}{\partial r}\left(P + \underline{2/3\rho k}\right) + \frac{\rho V^2}{r}$$

$$-(2\mu_{eff} - \mu)\frac{U}{r^2} + \underline{\frac{\partial}{\partial z}\left(\mu_T\frac{\partial W}{\partial r}\right)},$$

$$\phi = rV: S_\phi = -\frac{2}{r}\frac{\partial}{\partial r}(\mu_{eff} r V) \tag{4}$$

in which P denotes the static pressure and the underlined terms vanish for laminar flow (where $\mu_{eff} = \mu$).

2.1 The Turbulence Model. The turbulent viscosity required to close equations (2) and (3) is obtained from the Prandtl–Kolmogorov equation

$$\mu_T = c_\mu \frac{\rho k^2}{\epsilon} \tag{5}$$

where c_μ is a numerical coefficient. Exact transport equations for turbulent kinetic energy and dissipation rate ϵ [$=\nu(\overline{\partial u_i/\partial x_j})^2$] can be derived from the Navier–Stokes equations but contain intractable terms which have to be modeled in terms of calculable flow properties. Using gradient diffusion assumptions for turbulent transport, the conventional modeled equations may be represented in the common form of equation (2) with

$$\phi = k:\ \Gamma_{\phi,z} = \Gamma_{\phi,r} = \mu + \frac{\mu_T}{\sigma_k};\quad S_\phi = G - \rho\epsilon - D \tag{6}$$

$$\phi = \epsilon:\ \Gamma_{\phi,z} = \Gamma_{\phi,r} = \mu + \frac{\mu_T}{\sigma_\epsilon};$$

$$S_\phi = \frac{\epsilon}{k}(c_{\epsilon 1}G - c_{\epsilon 2}\rho\epsilon) + E - F \tag{7}$$

where G denotes the rate of production of turbulent kinetic energy and, with the modeling of equation (1), is expressible as

$$G = \mu_T\left[2\left\{\left(\frac{\partial W}{\partial z}\right)^2 + \left(\frac{\partial U}{\partial r}\right)^2 + \left(\frac{U}{r}\right)^2\right\} + \left(\frac{\partial W}{\partial r} + \frac{\partial U}{\partial z}\right)^2 + \left(\frac{\partial V}{\partial z}\right)^2 + \left\{r\frac{\partial}{\partial r}\left(\frac{V}{r}\right)\right\}^2\right] \tag{8}$$

Under conditions of high turbulence Reynolds number Re_T ($=k^2/\epsilon\nu$), molecular diffusion is neglected, the terms represented by D, E, and F are set to zero, and the numerical coefficients of the model are assigned constant values: Those used by Chew [8] are listed in Table 1. This form of the model (hereafter designated $k\epsilon 1$) has been used successfully to predict a wide range of both free and wall-bounded shear flows [10, 13]. For the latter, the wall-function approach [14], based on a logarithmic velocity distribution in the turbulent core, has traditionally been used to determine turbulence properties close to a wall and the associated values of the wall fluxes. In the current work, the use of a compressed finite-difference grid in near-wall regions has, however, ensured that the first off-wall grid node has been situated well within the viscous sublayer, so that the effective viscosity is essentially equal to the laminar value and hence no profile assumptions are necessary.

Table 1 Details of k–ϵ turbulence models

Item	High Re_T model	Low Re_T model
	($k\epsilon 1$)	($k\epsilon 2$)
c_μ	0.09	($\mathrm{Re}_T < 10$): $0.0027\,\mathrm{Re}_T^{1/2}$
		($\mathrm{Re} \geq 10$): $0.09\exp\left[\frac{-3.4}{(1+0.02\mathrm{Re}_T)^2}\right]$
$c_{\epsilon 1}$	1.44	1.44
$c_{\epsilon 2}$	1.92	$1.92 - 0.43\exp(-\mathrm{Re}_T^2/36)$
σ_k	1.0	1.0
σ_ϵ	1.3	1.3
D	0	$2\mu\left[\left(\frac{\partial k^{1/2}}{\partial z}\right)^2 + \left(\frac{\partial k^{1/2}}{\partial r}\right)^2\right]$
E	0	$\frac{2\mu\mu_T}{\rho}\left[\left(\frac{\partial^2 U}{\partial z^2}\right)^2 + \left(\frac{\partial^2 V}{\partial z^2}\right)^2 + \left(\frac{\partial^2 W}{\partial r^2}\right)^2 + \left(\frac{\partial^2 V}{\partial r^2}\right)^2\right]$
F	0	$2\mu\left[\left(\frac{\partial \tilde{\epsilon}^{1/2}}{\partial z}\right)^2 + \left(\frac{\partial \tilde{\epsilon}^{1/2}}{\partial r}\right)^2\right]$

The form of the model necessarily becomes more complex for the calculation of flows where the viscous sublayer is of appreciable extent and the direct effects of molecular viscosity on the turbulence structure have to be taken into account. A modified version of the k–ϵ model capable of predicting such "low turbulence Reynolds number" flows was first proposed by Jones and Launder [15] and applied, with minor changes, to the calculation of rotating flows by Launder and Sharma [11]. In a recent paper, Patel et al. [16] present a critical assessment of various alternative models proposed since and conclude that no significant improvement in all-round predictive capability has been achieved. Accordingly, the Launder–Sharma form of the model (designated $k\epsilon 2$) was chosen as the subject of the present work, although with minor alteration to improve its internal consistency.

In the Launder–Sharma approach, the terms D and E appearing in equations (6) and (7) are represented (in Cartesian tensor notation) as

$$D = 2\mu\left(\frac{\partial k^{1/2}}{\partial x_j}\right)^2 \tag{9}$$

and

$$E = \frac{2\mu\mu_T}{\rho}\left(\frac{\partial^2 U_i}{\partial x_j \partial x_l}\right)^2 \tag{10}$$

where D is identically equal to the value of the dissipation rate (times the density) at a wall. The dissipation rate ϵ is then replaced throughout the system of model equations by a "dissipation variable" $\tilde{\epsilon}$ $(=\epsilon - D/\rho)$ which becomes the operand of the transport equation with the boundary condition that $\tilde{\epsilon}=0$ at a wall. Formal transformation of the E term into cylindrical-polar coordinates yields 13 terms involving (mainly) second derivatives of the flow field; of these, only the four most important have been retained in the present computations. The current model differs from that used in [11, 15] by the inclusion of the F term in equation (7), where

$$F = 2\mu\left(\frac{\partial \tilde{\epsilon}^{1/2}}{\partial x_j}\right)^2 \tag{11}$$

At the wall, this term balances the viscous diffusion, $\mu(\partial^2\tilde{\epsilon}/\partial x_j^2)$ which, in keeping with the analysis of Hanjalic and Launder [16], ensures a quadratic variation of $\tilde{\epsilon}$ in the near-wall region. The forms of the D, E, and F terms appropriate to axisymmetric flow in cylindrical-polar coordinates are listed in Table 1. Additionally, it can be seen that, for the $k\epsilon 2$ model, the model coefficients c_μ and $c_{\epsilon 2}$ become functions of the turbulence Reynolds number $\mathrm{Re}_T (= k^2/\tilde{\epsilon}\nu)$. The slight amendment to the Launder–Sharma c_μ function for $\mathrm{Re}_T < 10$ has been introduced to give a cubic variation of turbulent shear stress in the near-wall region [16], while the function for $c_{\epsilon 2}$ is that suggested in [17] as providing the best empirical fit to the data for the far-field decay of homogeneous turbulence behind a grid. The nature of this function is, however, largely irrelevant as the inclusion of the F term in equation (7) nullifies the effect of any departure of $c_{\epsilon 2}$ from its asymptotic value of 1.92. It should be emphasized that the modifications made to the Launder–Sharma model in this work are largely cosmetic and produce only slightly beneficial effects as far as predictive accuracy is concerned.

2.2 Computational Procedure. TEACH is a finite-difference computational technique for elliptic flows in which discretized forms of the transport equations are assembled for each node of a staggered orthogonal grid network and solved by a line-by-line procedure based on the tridiagonal matrix algorithm. In the present work, the convection and diffusion terms of each equation have been treated in accordance with the power-law hybrid differencing scheme of Patankar [18]. The discretized equations are solved iteratively with the use of underrelaxation until each equation is satisfied at all the grid nodes to within a small aggregate amount. All the predictions shown here represent solutions which were converged to the extent that each residual, when normalized with the product of the mass flow rate through the cavity and the value of the relevant variable at entry, was less than 10^{-4}. In no case tested did it appear worthwhile to drive the solution to tighter convergence as further changes in the dependent variables were minute and largely confined to the central regions of weak vortices.

In order to obtain the degree of grid refinement necessary to resolve the flow detail in the Ekman layers, particularly at high rotational speeds, multiple step changes in mesh spacing were employed. Details of this technique, which requires modification of the finite difference coefficients for compatibility with the solution algorithm, are available in [6]. Typically, three or four step changes, with an expansion/contraction ratio of 3, were employed in both the axial and radial directions for computation of the flow in a half-cavity: With a grid mesh of 45 × 70 (axial-radial) nodes, this resulted in a closest off-wall node distance of approximately 0.05 mm. The increase in CPU time necessary to implement this feature was a modest 20 percent for a system of six step changes.

TEACH also solves an equation for the pressure correction p' which is used both to update the pressure field during each iteration and to correct the axial and radial velocities in order to satisfy mass continuity for each control volume. This is a most important aspect of the program as the particular treatment given to the pressure corrections is likely to affect substantially the convergence properties and hence cost of the computation. In the present work, the SIMPLEC algorithm of Van Doormal and Raithby [19] has been used. This has the main advantage over the basic SIMPLE technique used in [6] that the terms neglected in the formulation of the p' equation are much smaller; accordingly, fewer line-by-line sweeps are required to obtain the same level of accuracy and the value of the underrelaxation parameter α_p can be close to unity. Using this algorithm, ten double sweeps were considered to be the optimum with α_p set equal to 0.7 in the early stages of the computations, increasing to 0.95 as convergence was neared. As noted in [18], the pressure corrections are much more effective in reducing the mass residual than in correcting the pressure field, which is manifest here as a persistently high residual in the radial momentum equation. Use of the SIMPLER algorithm, which updates the pressure field via solution of a separate pressure correction equation, produced material advantages in this respect for rotational Reynolds numbers higher than about 10^6, but was not generally needed for the computations shown here. For calculations of laminar flow at $\mathrm{Re}_\theta > 10^5$, it was found expedient to introduce a stabilizing term in the radial momentum equation [6]; the value of the associated damping factor was initially set to 100 but was reduced automatically as convergence was neared.

For all the flows considered here, the incompressibility assumption was valid as pressure differences across the cavity (which increase approximately quadratically with rotational speed) never exceed 1 percent. However, since global pressure differences increase with rotational speed and the pressure corrections must necessarily approach zero as convergence is neared, use of double-precision FORTRAN was sometimes needed on the VAX VMS 11/70 machine (which only has seven-figure accuracy) in order to update the pressure field and thus drive the solution to convergence in the final stages. This was particularly the case for computation of radial inflow, where the pressure differences across the cavity are significantly larger than for radial outflow under the same flow conditions.

Cost savings of the order of 50 percent in obtaining fine-grid solutions were made by first performing the calculations on a coarse mesh with typically 15 × 20 nodes. A special

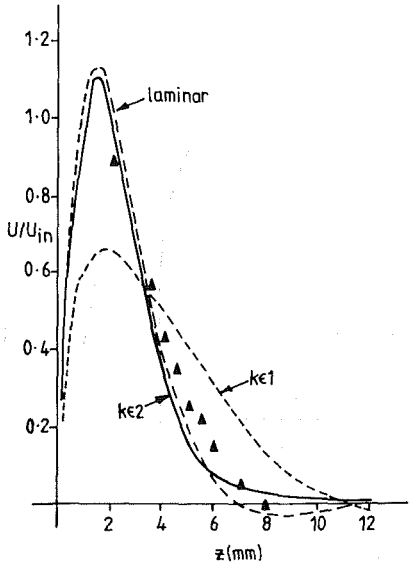

Fig. 2(*a*) Predicted profiles of radial velocity component at $r/b = 0.833$; radial outflow: $C_w = 1092$, $Re_\theta = 10^5$; data of [2]

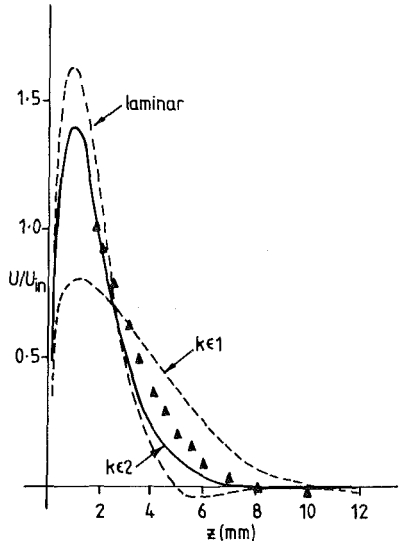

Fig. 2(*b*) Predicted profiles of radial velocity component at $r/b = 0.833$; radial outflow: $C_w = 1544$, $Re_\theta = 2 \times 10^5$; data of [2]

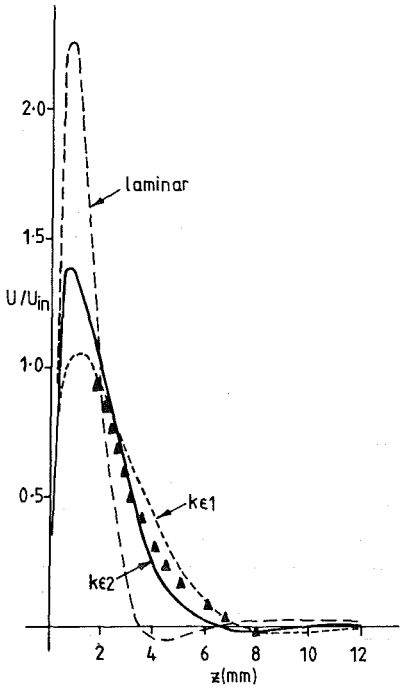

Fig. 2(*c*) Predicted profiles of radial velocity component at $r/b = 0.833$; radial outflow: $C_w = 2184$, $Re_\theta = 4 \times 10^5$; data of [2]

overlay program was then used to expand the grid arbitrarily, interpolating values from the original grid to use as starting profiles for the fine-grid calculation. Convergence becomes more difficult to achieve as the rotational Reynolds number Re_θ increases, which usually requires the use of severe underrelaxation in the early stages of the computation. At rotational Reynolds numbers of order 10^7, the underrelaxation factors had initially to be set to values as low as 0.2 to avoid divergence, whereas, for Re_θ up to about 5×10^5, values of $\alpha = 0.5$ for U and W and 0.8 for rV, k, and ϵ could safely be used. Starting from a coarse-grid solution, computations on a grid of 45×70 nodes required about 250 iterations to reach convergence with a CPU time requirement of approximately 1½ h for turbulent flow at $Re_\theta = 10^5$. This increased to 600 iterations and 4 h CPU time at $Re_\theta = 10^6$ and 1000 iterations (10 h) at $Re_\theta = 10^7$. CPU time requirements for inflow calculations were roughly 30 percent higher at equivalent flow conditions due to the frequent necessity to use double-precision FORTRAN.

2.3 Boundary Conditions. Boundary conditions for the axial and radial velocity components were obtained from the mass-continuity equation with the assumption of uniform flow profiles and the no-slip condition at a wall. In this context, the discrete hole geometry of the outer shroud was modeled as a slot of equivalent flow area. The boundary conditions for angular momentum were based on solid-body rotation of the flow at the rotational speed of the cavity, except at the internal flow boundary for radial inflow, where the parabolic exit condition of [18] provided a sufficient prescription. At axes of symmetry, the gradients of all dependent variables were set to zero, apart from the cross-axis velocity component which itself has a boundary condition of $\phi = 0$.

For each geometry investigated, the turbulent kinetic energy at entry to the cavity was taken as 10^{-4} times the square of the local resultant mean velocity and the dissipation rate then obtained by inversion of the definition of the turbulence Reynolds number using a value of $Re_T = 100$. As noted in [8], the initial values chosen for the turbulence properties exert negligible effect on the calculated flow in the Ekman layers and indeed little effect even in the source region. At a solid boundary, $k = 0$ and, for the low turbulence Reynolds number model, $\tilde{\epsilon} = 0$. For the $k\epsilon1$ model, the dissipation rate at the near-wall nodes was evaluated from

$$\epsilon = c_D^{3/4} k^{3/2} / \kappa y$$

where c_D is numerically equal to the coefficient c_μ, κ is the von Karman constant ($= 0.42$), and y denotes the normal distance to the wall.

3 Numerical Results

Predictions for radial outflow are presented in Figs. 2–7 and for radial inflow in Figs. 8–10. All the calculations were performed on grids of 35×60 or 45×70 nodes. These represent sensibly "grid-independent" solutions since predictions obtained with a mesh as fine as 100×150 nodes would be indistinguishable on the scales of the graphs shown.

Figure 2 shows computed profiles of the radial velocity component in the Ekman layer at $r/b = 0.833$ for values of C_w

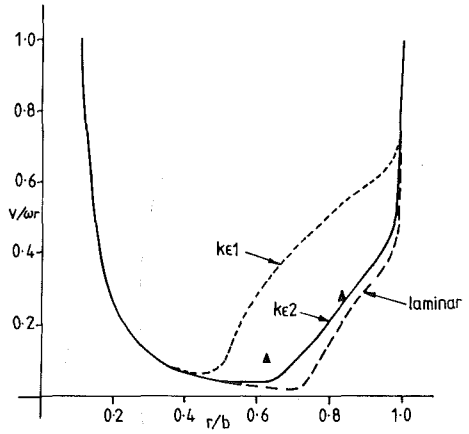

Fig. 3(a) Predicted profiles of circumferential velocity component at midaxis; radial outflow: $C_w = 1092$, $Re_\theta = 10^5$; data of [2]

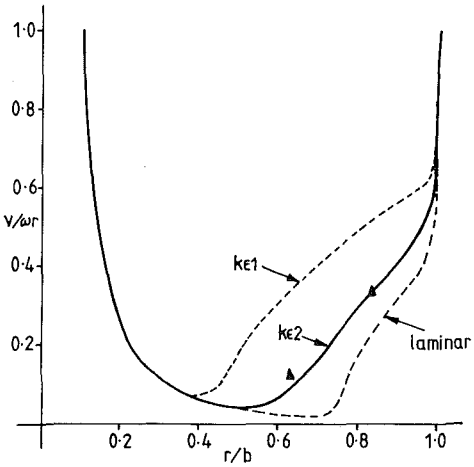

Fig. 3(b) Predicted profiles of circumferential velocity component at midaxis; radial outflow: $C_w = 1544$, $Re_\theta = 2 \times 10^5$; data of [2]

and Re_θ covering a wide range of the conditions investigated for outflow. The profiles are normalized with the values of the radial velocity at the cavity inlet ($r/b = 0.1$) assuming a uniform source flow. A value of $Re_\theta = 10^5$ corresponds to a rotational speed of approximately 70 rev/min. In each figure, comparison is drawn between the high and low turbulence Reynolds number predictions and the laminar flow solution. As would be expected due to the low prevailing values of Re_T, profiles calculated with the $k\epsilon1$ model, which may be regarded as representing a "fully turbulent" solution, reveal a considerable overestimate of turbulent transport, resulting in low values of the peak velocity and exaggerated spreading of the Ekman layer in the outer regions. In contrast, laminar flow is characterized by a high peak velocity and a slower spreading rate than is evident from the experimental data. Although the accuracy of the $k\epsilon1$ predictions improves steadily as C_w and Re_θ increase, i.e., as the turbulence Reynolds number increases, it is clear that a model capable of predicting the onset of turbulent Ekman layer flow has to tread a fine middle ground between these two solutions.

At $C_w = 1092$, $Re_\theta = 10^5$ (Fig. 2*a*), the $k\epsilon2$ predictions do reveal a slight reduction in the peak velocity compared to the laminar flow solution but, in contrast to the data, the velocity magnitudes continue to fall below those for laminar flow until $z \sim 6$ mm; also, there is no predicted region of reverse flow in the Ekman layer. These defects are largely removed at $C_w = 1544$, $Re_\theta = 2 \times 10^5$ (Fig. 2*b*), although the predicted

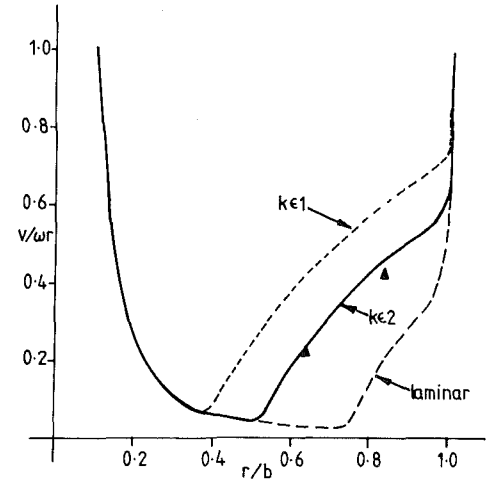

Fig. 3(c) Predicted profiles of circumferential velocity component at midaxis; radial outflow: $C_w = 2184$, $Re_\theta = 4 \times 10^5$; data of [2]

spreading rate of the Ekman layer remains sluggish. The calculations do, however, reveal a marked departure from laminar flow and this trend continues at $C_w = 2184$, $Re_\theta = 4 \times 10^5$ (Fig. 2*c*). For this last case, the predictions are just about within the positional uncertainty of the measurements, estimated as ± 0.45 mm [2], although some distortion of the profile is evident. For the computations of Fig. 2(*a*), the turbulent kinetic energy decreases continuously with development of the Ekman layer and turbulent flow is never established (i.e., the effective viscosity across the Ekman layer does not differ significantly from the laminar value). In contrast, at the higher values of C_w and Re_θ, turbulent flow is established at lower radii, but the predictions at $r/b = 0.833$ then reveal a fairly rapid reduction in the thickness of the Ekman layer, indicative of a tendency toward premature laminarization.

Corresponding predictions for the circumferential velocity component at the midaxial plane are shown in Fig. 3. Here, the profiles are normalized with the local disk velocity ωr, so that the imposed boundary conditions are $V/\omega r = 1.0$ at $r/b = 0.1$ and 1.0. Irrespective of the flow conditions, a free vortex (constant angular momentum) occurs in the source region, so that $V \propto 1/r$. Although there are only two data points for each test case, these provide a reasonably clear indication of predictive accuracy. Again, the $k\epsilon1$ model considerably overestimates the velocities in the core region beyond the Ekman layers, while the laminar flow predictions indicate low velocities due to insufficient diffusion of angular momentum from the disk. The $k\epsilon2$ model results in a significant difference from laminar flow behavior that is roughly in accordance with the data, although it is evident that the predicted onset of turbulent flow in the Ekman layers is somewhat retarded for the conditions of Figs. 3(*a*) and 3(*b*). This retardation is overcome at higher flow rates and rotational speeds (Fig. 3*c*), although it is noticeable that a slight overestimate of the velocity magnitude then occurs at $r/b = 0.833$.

Further insight into the performance of the $k\epsilon2$ model in differentiating between laminar and turbulent Ekman layer flow may be gained from Fig. 4. At very low flow rates, corresponding to $C_w = 386$, there is little difference between the $k\epsilon2$ and laminar solutions, so that the flow may be regarded as essentially laminar throughout the cavity. As C_w is increased, the $k\epsilon2$ model at first mirrors accurately the increase in velocities resulting from the first stages of turbulence, but then falls increasingly wide of the mark at $r/b = 0.633$ as the turbulence in reality becomes more established. As can be seen from Fig. 5, for $C_w = 1092$, increase of Re_θ to 2×10^5 and 4×10^5 brings the computations back into line in this respect.

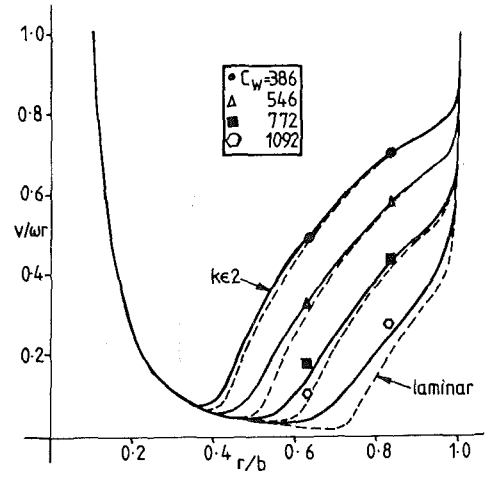

Fig. 4 Predicted profiles of circumferential velocity component at midaxis; radial outflow: $Re_\theta = 10^5$; data of [2]

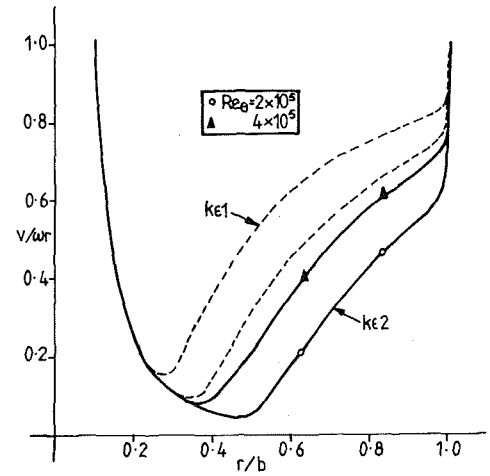

Fig. 5 Predicted profiles of circumferential velocity component at midaxis; radial outflow: $C_w = 1092$; data of [2]

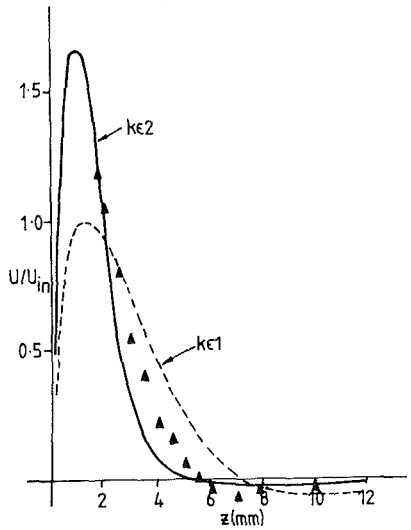

Fig. 6(a) Predicted profiles of radial velocity component at $r/b = 0.833$; radial outflow: $C_w = 1092$, $Re_\theta = 2 \times 10^5$; data of [2]

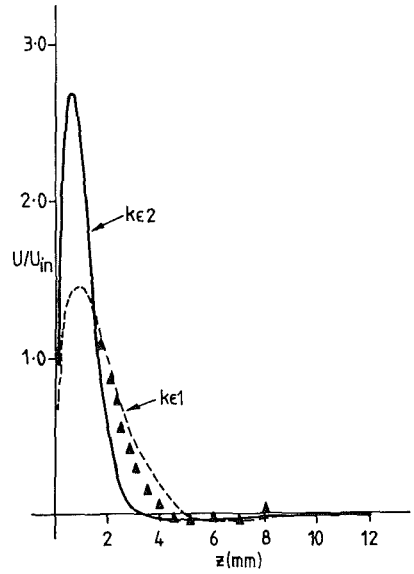

Fig. 6(b) Predicted profiles of radial velocity component at $r/b = 0.833$; radial outflow: $C_w = 1092$, $Re_\theta = 4 \times 10^5$; data of [2]

Also noticeable from this figure is the fact that the $k\epsilon1$ model predicts higher velocity values at $Re_\theta = 2 \times 10^5$ than does the $k\epsilon2$ model at $Re_\theta = 4 \times 10^5$, which clearly invalidates use of the former for prediction of these flows. With the $k\epsilon2$ model, however, the spreading rate of the Ekman layer continues to be underestimated at these intermediate flow conditions (Fig. 6).

Finally, for radial outflow, Fig. 7 shows computed profiles of the circumferential velocity at midaxis for $C_w = 2500$ and values of Re_θ up to 1.1×10^6. In contrast to all other predictions in this section, these utilized the full cavity solution with a uniform axial inlet flow. Although the predictive accuracy is clearly good, there does appear to be a tendency to overestimate the velocity values at high rotational speeds, which is perhaps also evident in the computation of Fig. 3(*c*). Measurements of the radial velocity component are not available for these test cases but it seems reasonable to assume that the calculations would be of at least comparable accuracy to those shown in Fig. 2(*c*), where the general level of turbulence Reynolds number is similar.

Computed profiles for radial inflow are shown in Figs. 8–10. Unfortunately, these again refer only to the circumferential velocity distribution at the midaxial plane. An unknown factor in these computations is the value of the initial swirl fraction c, which determines the angular momentum of the incoming flow (see Section 1). Predictions using the value of $c = 0.59$, recommended for turbulent flow in [4], are compared for the $k\epsilon1$ and $k\epsilon2$ models in Fig. 8. For the flow conditions $C_w = -1415$, $Re_\theta = 1.97 \times 10^5$ (C_w is assigned negative values for inflow), both models result in slightly high velocity values in the source region ($r/b > 0.8$), although the degree of overprediction is noticeably less with the $k\epsilon2$ model. In this region, the $k\epsilon1$ solution, in which turbulence is necessarily overestimated, represents an excess of transfer of angular momentum from the disk. As can be seen, outside the source region, the angular velocity of the flow becomes greater than that of the disk at the same radial location. At low radii, the $k\epsilon1$ model therefore predicts too high a transfer of angular momentum back toward the disk, resulting in low values of the circumferential velocity at midaxis. Although the laminar flow solution conforms quite well to the experimental data in the source region, the predictions are characterized by a tendency to overestimate the velocity values as the radius decreases. In contrast, the $k\epsilon2$ model mirrors fairly accurately the interchange of angular momentum between the disk and the central regions of the flow.

The above predictions refer to the shroud A geometry of [4, 5], which consisted of a series of equally spaced discrete holes located at the midaxial plane. For such a geometry, the initial swirl fraction cannot be determined analytically, and, as shown in Fig. 6, the predictions are indeed sensitive to the value chosen. Values of $c=0$ and 1.0 are clearly inappropriate for the data obtained with shroud A, while $c=0.42$ gives a slightly better prediction in the source region. This last value was that recommended in [4] as best correlating the data for the shroud E geometry, which consisted of a continuous peripheral slot at midaxis, corresponding approximately to the same inlet flow area as given by shroud A. In view of the three dimensionality of the mixing region behind the shroud, it is not immediately possible to distinguish deficiencies of the turbulence model from errors associated with modeling the shroud geometry adequately or in prescribing the value of the initial swirl fraction. However, as comparison of Figs. 8 and 9 shows, the predictions in the source region are far more sensitive to the value chosen for c than to the form of the model employed, which suggests that the major uncertainty lies in prescription of the initial swirl fraction. Furthermore, in this context, it is interesting to note that the predictions based on $c=1.0$ correspond very well to the data obtained using the shroud F geometry. In this case, the central peripheral slot was filled with plastic foam of sufficient thickness to promote solid-body rotation at the flow inlet; with the doubt about the value of c removed, the predictive accuracy of the $k\epsilon2$ model is obviously good.

It is also of interest to note the variation with initial swirl fraction of the size of the vortex formed between the shroud and the disk (see Fig. 1*c*). According to the linear Ekman layer theory of [4], the stagnation point on the disk corresponding to the extremity of this vortex lies at the radial location where $r/b=c^{1/2}$. The present predictions bear out this correlation qualitatively, in that the vortex grows larger as the value of c is reduced, but not quantitatively. For $c=0.42$ and 0.59, the vortex region is approximately 20 percent shorter than estimated by the simplified theory, and extends only as far as $r/b=0.61$ for $c=0$; however, for $c=1.0$, the vortex is indeed absent from the calculations.

Predictions for a fairly wide range of flow conditions are shown in Fig. 10, which also serves to illustrate the effect of the flow rate on the angular momentum distribution within the cavity. Again, a value of $c=0.59$ was used for the *true* initial swirl fraction although this indicates the *effective* swirl fraction for the theory of [4]. According to the criterion established in [3], the transition from laminar to turbulent flow in the Ekman layer occurs at a value of the radial Reynolds number, $\mathrm{Re}_r=(|C_w|/2\pi r/b)$, of about 180. On this basis, the flow would be expected to be essentially laminar for $r/b>0.27$ at $C_w=-309$ and turbulent for $r/b<0.83$ at $C_w=-946$. Clearly, the $k\epsilon2$ model performs well in predicting the circumferential velocity distribution for the transition between these two flow regimes without any empirical prescription for the radius at which transition actually occurs. One reason for the good predictive accuracy is that there is considerably less difference between the $k\epsilon1$, $k\epsilon2$, and laminar solutions for radial inflow than there is for radial outflow under similar conditions (compare Figs. 3*b* and 8), and thus less margin for error. However, a more fundamental reason is that radial inflow results in higher shearing rates in the Ekman layers which generate considerable turbulence with the effect that the $k\epsilon2$ model experiences little difficulty in establishing turbulent flow under appropriate conditions. Again, according to the above criterion, radial outflow has a tendency to reverse transition, so that laminar Ekman layer flow may result at large radii if the value of C_w is insufficiently high. In contrast, for radial inflow, the turbulence becomes continuously more established as the Ekman layer develops, and the exaggerated laminarization effect that is found in some of the outflow predictions ceases to be a problem.

4 Discussion

From the foregoing, it is evident that the low turbulence Reynolds number k–ϵ model produces solutions for both radial inflow and outflow in rotating cavity geometries which are of sufficient accuracy for normal engineering design pur-

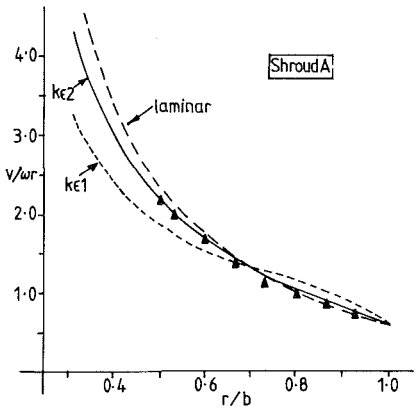

Fig. 8 Predicted profiles of circumferential velocity component at midaxis; radial inflow: $C_w=-1415$, $\mathrm{Re}_\theta=1.97\times10^5$; data of [5]

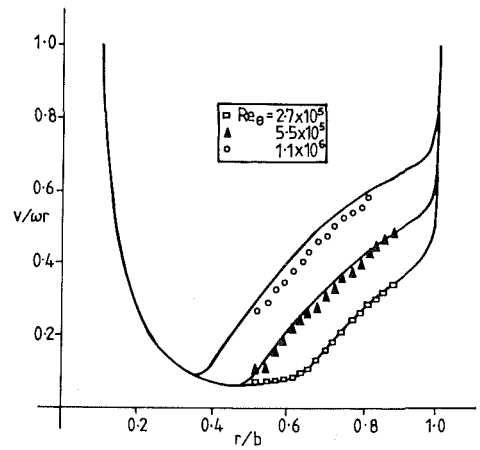

Fig. 7 Predicted profiles of circumferential velocity component at midaxis; radial outflow: $C_w=2500$; $k\epsilon2$ model; data of [2]

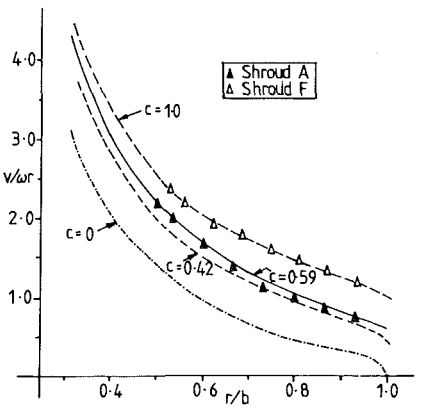

Fig. 9 Predicted profiles of circumferential velocity component at midaxis; radial inflow: $C_w=-1415$, $\mathrm{Re}_\theta=1.97\times10^5$; $k\epsilon2$ model; data of [5]

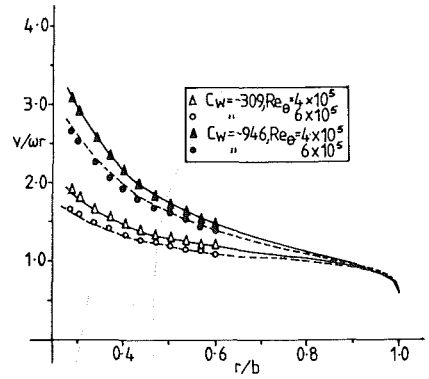

Fig. 10 Predicted profiles of circumferential velocity component at midaxis; radial inflow; $k\epsilon 2$ model; data of [5]

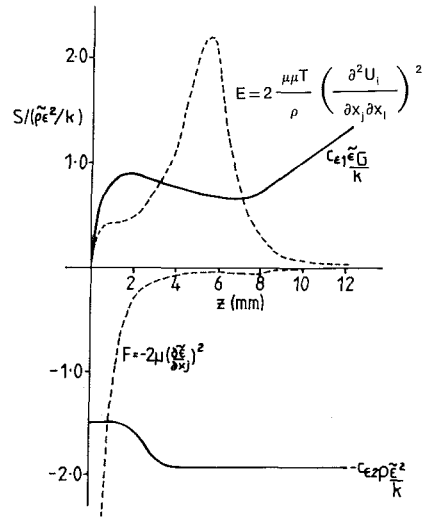

Fig. 11 Comparison of source terms in the $\tilde{\epsilon}$ equation at $r/b = 0.833$; radial outflow: $C_w = 1092$, $Re_\theta = 10^5$

poses. Regarding the shortcomings of the model, the most salient conclusion that can be drawn is that although it provides an adequate description of near-wall flow for fully turbulent conditions beyond the viscous sublayer, it does not portray, at least with desirable accuracy, the onset and persistence of turbulent flow in the Ekman layers for radial outflow. This latter aspect perhaps contains echoes of the fact that the model was originally developed [15] to predict laminarization, the transition from turbulent to laminar flow. Although apparently successful in this respect, transition in the reverse direction, resulting in turbulent flow from quasi-laminar conditions, is often more difficult to achieve.

Turbulent flow in the Ekman layers is established by the influx of energy from the source region combining with the high shearing rates of the radial and circumferential velocity components to give the necessary upsurge in energy level. At the low flow rates and rotational speeds typified by the computations of Fig. 2(*a*), this upsurge does not occur and the near-wall energy levels decay continuously as the Ekman layer develops. There are two main reasons for this behavior—energy levels have already dropped appreciably in the source region preceding formation of the Ekman layer and any increase in production rate which occurs is immediately nullified by a corresponding effect in the dissipation rate equation. The lack of any time-lag effect between the input of energy at the low wave number (production) end of the energy spectrum and the appropriate response at high (dissipation) wave numbers has long been recognized as an inherent fault in the k–ϵ model, although attempts to remedy the situation [20] have met with little success. With a positive dissipation source modeled as proportional to the energy production rate [see equation (4)], turbulent Ekman layer flow can only be brought about if the strain rates are sufficiently large, as caused by high values of C_w and Re_θ. In this respect, the predicted onset of turbulent flow in the Ekman layers lags somewhat behind that observed experimentally.

Another important consideration regarding the performance of the model in predicting transitional flows is the effect of the E term in the modeled $\tilde{\epsilon}$ equation (see Table 1). A term of this type is essential, for without it, the solutions tend to those for the parent high turbulence Reynolds number model. However, the gradient-diffusion assumption used in modeling the exact term, $2\mu\overline{u_i \partial u_i/\partial x_j}(\partial^2 U_i/\partial x_j \partial x_l)$, has to be recognized as the major fault of the model, especially in light of the fact that this term can often dominate the ϵ equation at low turbulence Reynolds numbers. This is clearly shown in Fig. 11 where the four source terms in the $\tilde{\epsilon}$ equation are compared at $r/b = 0.833$ for the *outflow* conditions $C_w = 1092$, $Re_\theta = 10^5$. Comparison with Fig. 2(*a*) shows that it is essentially in the region of the Ekman layer where the E term dominates the conventional positive source term that the radial velocity is underestimated due to the resulting low turbulence levels. As Re_T increases, the E term decreases steadily in importance, although, as the outflow predictions at intermediate conditions show, the term remains effective either in inhibiting the growth of turbulence in the Ekman layer or in promoting a partial laminarization effect once turbulent flow has been established. Reducing the value of the coefficient of the E term gives some improvement in prediction but no consistency as to the value required. If a rational alternative to this term could be formulated, it is anticipated that the performance of the model in predicting transitional flows could be much improved.

Attempts have been made to improve the predictions of radial outflow by (*a*) modification of the turbulence model and (*b*) artificial injections of turbulence in the near-wall region. Precise details of the methods used are not important here but it is sufficient to note that, although the desired effect of improved Ekman layer growth was achieved, this was at the expense of overestimated values of the angular momentum distribution within the cavity at high rotational speeds. Since the radial and circumferential velocity components cannot in general *both* be predicted accurately with the $k\epsilon 2$ model, this immediately calls into question the validity of an isotropic turbulent viscosity hypothesis. However, the Reynolds stress closures of Launder et al. [21] imply that the degree of anisotropy is indeed small for the present flows, at least regarding the shear stresses $\overline{uw}$ and $\overline{uw}$, which govern the dominant axial diffusion of momentum. Although it is apparent that the shear stress $\overline{uv}$ governing radial diffusion of angular momentum is underpredicted by an order of magnitude using an isotropic viscosity formulation, this is not important here as the flow in the Ekman layers is closely parabolic. Reynolds stress closures have been used successfully for the computation of rotating free thin shear layer flows [22] but their use is not advocated in the present context as models of this type are unlikely to yield the degree of anisotropy needed for all-round predictive accuracy and, in any case, are subject to the same shortcomings in the $\tilde{\epsilon}$ equation as encountered here.

5 Conclusions

A low turbuence Reynolds number k–ϵ model has been used to predict radial inflow and outflow in a rotating cavity for a wide range of flow conditions. Although predictions for the former are satisfactory in most respects, the model performs

less well for radial outflow, particularly at low flow rates and rotational speeds. This shortcoming is in keeping with the findings of Chew [8], although the accuracy of the predictions improves significantly as either of the flow parameters C_w or Re_θ is increased.

The solutions represent a slight but definite improvement over those of [9] based on a mixing length approach. In this context, the present model clearly presents the greater scope for refinement and it is envisaged that an alternative formulation for the extra source term required in the $\tilde{\epsilon}$ equation will considerably improve its performance. Lam and Bremhorst [23] have proposed an equation for the dissipation rate which bypasses the troublesome E term by increasing the value of the source coefficient $c_{\epsilon 1}$ near a wall. The author has used this model, which solves a transport equation for the dissipation rate itself rather than for a variable which is set to zero as a convenient wall boundary condition, but has been unable to obtain grid-independent solutions because of the nature of the function chosen for $c_{\epsilon 1}$. However, careful examination of the common ground between the two models may produce a satisfactory alternative formulation for the dissipation rate equation. Adapting the model to include anisotropic effects and thereby validating its use for the high-speed geometries of practical interest appears to be a more difficult task.

Acknowledgments

The author is glad to acknowledge the interest shown in this work by Dr. J. M. Owen, Ms. C. L. Ong, and Dr. C. Vaughan, colleagues at the Thermo-Fluid Mechanics Research Centre of the University of Sussex, and by Dr. J. W. Chew of Rolls-Royce plc, Derby, United Kingdom.

References

1 Owen, J. M., and Pincombe, J. R., 1980, "Velocity Measurements Inside a Rotating Cylindrical Cavity With a Radial Outflow of Fluid," *J. Fluid Mech.*, Vol. 99, p. 111.

2 Pincombe, J. R., 1981, "Velocity Measurements in the Mk II-Rotating Cavity Rig With a Radial Outflow," Report 81/TFMRC/21, School of Engineering and Applied Sciences, University of Sussex, Brighton, Sussex, United Kingdom.

3 Owen, J. M., Pincombe, J. R., and Rogers, R. H., 1985, "Source-Sink Flow Inside a Rotating Cylindrical Cavity," *J. Fluid Mech.*, Vol. 155, p. 233.

4 Firouzian, M., Owen, J. M., Pincombe, J. R., and Rogers, R. H., 1985, "Flow and Heat Transfer in a Rotating Cavity With a Radial Inflow of Fluid. Part I: The Flow Structure," *Int. J. Heat and Fluid Flow*, Vol. 6, No. 4, p. 228.

5 Firouzian, M., Owen, J. M., Pincombe, J. R., and Rogers, R. H., 1986, "Flow and Heat Transfer in a Rotating Cylindrical Cavity With a Radial Inflow of Fluid. Part II: Velocity, Pressure and Heat Transfer Measurements," *Int. J. Heat and Fluid Flow*, Vol. 7, No. 1, p. 21.

6 Chew, J. W., 1984, "Development of a Computer Program for the Prediction of Flow and Heat Transfer in a Rotating Cavity," *Int. J. Num. Methods in Fluids*, Vol. 4, p. 667.

7 Gosman, A. D., and Ideriah, F. J. K., 1976, "Teach-T: a General Computer Program for Two-Dimensional Turbulent Recirculating Flows," in: *Calculation of Recirculating Flows*, Mech. Eng. Dept., Imperial College, Univ. of London, London, United Kingdom.

8 Chew, J. W., 1984, "Prediction of Flow in Rotating Disc Systems Using the k–ϵ Turbulence Model," ASME Paper No. 84-GT-229.

9 Chew, J. W., 1985, "Prediction of Flow in a Rotating Cavity With Radial Outflow Using a Mixing Length Turbulence Model," *Proc. 4th Int. Conf. on Numerical Methods in Laminar and Turbulent Flow*, Swansea, United Kingdom.

10 Launder, B. E., and Spalding, D. B., 1972, *Mathematical Models of Turbulence*, Academic Press, London–New York.

11 Launder, B. E., and Sharma, B. I., 1974, "Application of the Energy-Dissipation Model of Turbulence to the Calculation of Flow Near a Spinning Disc," *Letters in Heat and Mass Transfer*, Vol. 1, p. 131.

12 Koosinlin, M. L., Launder, B. E., and Sharma, B. I., 1974, "Prediction of Momentum, Heat and Mass Transfer in Swirling Turbulent Boundary Layers," ASME *Journal of Heat Transfer*, Vol. 96, p. 204.

13 Launder, B. E., Morse, A. P., Rodi, W., and Spalding, D. B., 1973, "The Prediction of Free Shear Flows—a Comparison of the Performance of Six Turbulence Models," *Proc. NASA Free Turbulent Shear Flows Conf.*, Vol. 1, NASA SP320.

14 Patankar, S. V., and Spalding, D. B., 1970, *Heat and Mass Transfer in Boundary Layers*, Intertext Books, London.

15 Jones, W. P., and Launder, B. E., 1972, "The Prediction of Laminarization With a Two-Equation Model of Turbulence," *Int. J. Heat and Mass Transf.*, Vol. 15, p. 301.

16 Patel, V. C., Rodi, W., and Scheuerer, G., 1985, "Turbulence Models for Near-Wall and Low Reynolds Number Flows: a Review," *AIAA J.*, Vol. 23, No. 9, p. 1308.

17 Hanjalic, K., and Launder, B. E., 1976, "Contribution Towards a Reynolds-Stress Closure for Low-Reynolds Number Turbulence," *J. Fluid Mech.*, Vol. 74, p. 593.

18 Patankar, S. V., 1980, *Numerical Heat Transfer and Fluid Flow*, Hemisphere, Washington, DC.

19 Van Doormal, J. P., and Raithby, G. D., 1984, "Enhancements of the SIMPLE Method for Predicting Incompressible Fluid Flows," *J. Num. Heat Trans.*, Vol. 7, p. 147.

20 Morse, A. P., 1980, "Axisymmetric Free Shear Flows, With and Without Swirl," Ph.D. Thesis, Univ. of London, London, United Kingdom.

21 Launder, B. E., Reece, G. J., and Rodi, W., 1975, "Progress in the Development of a Reynolds Stress Turbulence Closure," *J. Fluid Mech.*, Vol. 68, p. 537.

22 Launder, B. E., and Morse, A. P., 1979, "Numerical Prediction of Axisymmetric Free Shear Flows With a Second-Order Reynolds Stress Closure," in: *Turbulent Shear Flows*, Vol. I, Springer-Verlag, New York, p. 279.

23 Lam, C. K. G., and Bremhorst, K. A., 1981, "Modified Form of the k–ϵ Model for Predicting Wall Turbulence," ASME *Journal of Fluids Engineering*, Vol. 103, p. 456.

less well for radial outflow, particularly at low flow rates and rotational speeds. This shortcoming is in keeping with the findings of Chew [8], although the accuracy of the predictions improves significantly as either of the flow parameters C_w or Re_θ is increased.

The solutions represent a slight but definite improvement over those of [9] based on a mixing length approach. In this context, the present model clearly presents the greater scope for refinement and it is envisaged that an alternative formulation for the extra source term required in the $\tilde{\epsilon}$ equation will considerably improve its performance. Lam and Bremhorst [23] have proposed an equation for the dissipation rate which bypasses the troublesome E term by increasing the value of the source coefficient $c_{\epsilon 1}$ near a wall. The author has used this model, which solves a transport equation for the dissipation rate itself rather than for a variable which is set to zero as a convenient wall boundary condition, but has been unable to obtain grid-independent solutions because of the nature of the function chosen for $c_{\epsilon 1}$. However, careful examination of the common ground between the two models may produce a satisfactory alternative formulation for the dissipation rate equation. Adapting the model to include anisotropic effects and thereby validating its use for the high-speed geometries of practical interest appears to be a more difficult task.

Acknowledgments

The author is glad to acknowledge the interest shown in this work by Dr. J. M. Owen, Ms. C. L. Ong, and Dr. C. Vaughan, colleagues at the Thermo-Fluid Mechanics Research Centre of the University of Sussex, and by Dr. J. W. Chew of Rolls-Royce plc, Derby, United Kingdom.

References

1 Owen, J. M., and Pincombe, J. R., 1980, "Velocity Measurements Inside a Rotating Cylindrical Cavity With a Radial Outflow of Fluid," *J. Fluid Mech.*, Vol. 99, p. 111.

2 Pincombe, J. R., 1981, "Velocity Measurements in the Mk II-Rotating Cavity Rig With a Radial Outflow," Report 81/TFMRC/21, School of Engineering and Applied Sciences, University of Sussex, Brighton, Sussex, United Kingdom.

3 Owen, J. M., Pincombe, J. R., and Rogers, R. H., 1985, "Source-Sink Flow Inside a Rotating Cylindrical Cavity," *J. Fluid Mech.*, Vol. 155, p. 233.

4 Firouzian, M., Owen, J. M., Pincombe, J. R., and Rogers, R. H., 1985, "Flow and Heat Transfer in a Rotating Cavity With a Radial Inflow of Fluid. Part I: The Flow Structure," *Int. J. Heat and Fluid Flow*, Vol. 6, No. 4, p. 228.

5 Firouzian, M., Owen, J. M., Pincombe, J. R., and Rogers, R. H., 1986, "Flow and Heat Transfer in a Rotating Cylindrical Cavity With a Radial Inflow of Fluid. Part II: Velocity, Pressure and Heat Transfer Measurements," *Int. J. Heat and Fluid Flow*, Vol. 7, No. 1, p. 21.

6 Chew, J. W., 1984, "Development of a Computer Program for the Prediction of Flow and Heat Transfer in a Rotating Cavity," *Int. J. Num. Methods in Fluids*, Vol. 4, p. 667.

7 Gosman, A. D., and Ideriah, F. J. K., 1976, "Teach-T: a General Computer Program for Two-Dimensional Turbulent Recirculating Flows," in: *Calculation of Recirculating Flows*, Mech. Eng. Dept., Imperial College, Univ. of London, London, United Kingdom.

8 Chew, J. W., 1984, "Prediction of Flow in Rotating Disc Systems Using the k–ϵ Turbulence Model," ASME Paper No. 84-GT-229.

9 Chew, J. W., 1985, "Prediction of Flow in a Rotating Cavity With Radial Outflow Using a Mixing Length Turbulence Model," *Proc. 4th Int. Conf. on Numerical Methods in Laminar and Turbulent Flow*, Swansea, United Kingdom.

10 Launder, B. E., and Spalding, D. B., 1972, *Mathematical Models of Turbulence*, Academic Press, London–New York.

11 Launder, B. E., and Sharma, B. I., 1974, "Application of the Energy-Dissipation Model of Turbulence to the Calculation of Flow Near a Spinning Disc," *Letters in Heat and Mass Transfer*, Vol. 1, p. 131.

12 Koosinlin, M. L., Launder, B. E., and Sharma, B. I., 1974, "Prediction of Momentum, Heat and Mass Transfer in Swirling Turbulent Boundary Layers," ASME *Journal of Heat Transfer*, Vol. 96, p. 204.

13 Launder, B. E., Morse, A. P., Rodi, W., and Spalding, D. B., 1973, "The Prediction of Free Shear Flows—a Comparison of the Performance of Six Turbulence Models," *Proc. NASA Free Turbulent Shear Flows Conf.*, Vol. 1, NASA SP320.

14 Patankar, S. V., and Spalding, D. B., 1970, *Heat and Mass Transfer in Boundary Layers*, Intertext Books, London.

15 Jones, W. P., and Launder, B. E., 1972, "The Prediction of Laminarization With a Two-Equation Model of Turbulence," *Int. J. Heat and Mass Transf.*, Vol. 15, p. 301.

16 Patel, V. C., Rodi, W., and Scheuerer, G., 1985, "Turbulence Models for Near-Wall and Low Reynolds Number Flows: a Review," *AIAA J.*, Vol. 23, No. 9, p. 1308.

17 Hanjalic, K., and Launder, B. E., 1976, "Contribution Towards a Reynolds-Stress Closure for Low-Reynolds Number Turbulence," *J. Fluid Mech.*, Vol. 74, p. 593.

18 Patankar, S. V., 1980, *Numerical Heat Transfer and Fluid Flow*, Hemisphere, Washington, DC.

19 Van Doormal, J. P., and Raithby, G. D., 1984, "Enhancements of the SIMPLE Method for Predicting Incompressible Fluid Flows," *J. Num. Heat Trans.*, Vol. 7, p. 147.

20 Morse, A. P., 1980, "Axisymmetric Free Shear Flows, With and Without Swirl," Ph.D. Thesis, Univ. of London, London, United Kingdom.

21 Launder, B. E., Reece, G. J., and Rodi, W., 1975, "Progress in the Development of a Reynolds Stress Turbulence Closure," *J. Fluid Mech.*, Vol. 68, p. 537.

22 Launder, B. E., and Morse, A. P., 1979, "Numerical Prediction of Axisymmetric Free Shear Flows With a Second-Order Reynolds Stress Closure," in: *Turbulent Shear Flows*, Vol. I, Springer-Verlag, New York, p. 279.

23 Lam, C. K. G., and Bremhorst, K. A., 1981, "Modified Form of the k–ϵ Model for Predicting Wall Turbulence," ASME *Journal of Fluids Engineering*, Vol. 103, p. 456.

DISCUSSION

J. W. Chew[1]

The author is to be congratulated on clarifying the performance of the low-turbulence Reynolds number k–ϵ model in rotating disk flows. The tendency for early laminarization in radial outflow is certainly consistent with the results of Chew (1984). In this earlier study the laminarization effect was more severe. Perhaps the different formulations of the model used in the two studies could explain this. Hopefully, at the higher Reynolds numbers appropriate to gas turbine engines this shortcoming will not be so important. A significant advantage of the k–ϵ model over mixing length models (Chew, 1985, 1987) is the comparative ease of coding and extension to general geometries. Obviously further evaluation and comparison of different models would be useful. In addition to the accuracy of the turbulence models, computing and mesh requirements should also be considered.

In their experimental study of radial inflow, Firouzian et al. (1985) obtained the surprising result that for a variety of shroud designs with open inlet holes, flow rates, and rotational speeds, the "effective inlet swirl fraction" (c_e) did not vary much. These workers concluded that flow entered the cavity with a swirl fraction of just over 1/2. Morse has correctly indicated that this swirl fraction could be partly due to transfer of angular momentum within the cavity and Fig. 9 suggests that the "true inlet swirl fraction" (c) will be between 0.42 and 0.59. Laminar flow computations (Chew, 1982) for $C_w = -396$, $\mathrm{Re}_\theta = 5 \times 10^4$ suggest that a true inlet swirl fraction of 0 could give a value for c_e of about 0.6. Turbulent flow calculations with a mixing length model with $C_w = -3.7 \times 10^4$, $\mathrm{Re}_\theta = 7.6 \times 10^6$ indicate that with $c = 0.225$, c_e is about 0.5 (Chew, 1987).

An integral calculation method has also been developed for radial inflow (Chew, 1987). This model employs von Karman's (1921) integral technique and includes a calculation of c_e from c. Results from the integral method and mixing length

[1]Theoretical Science Group, Rolls-Royce plc, Derby, United Kingdom.

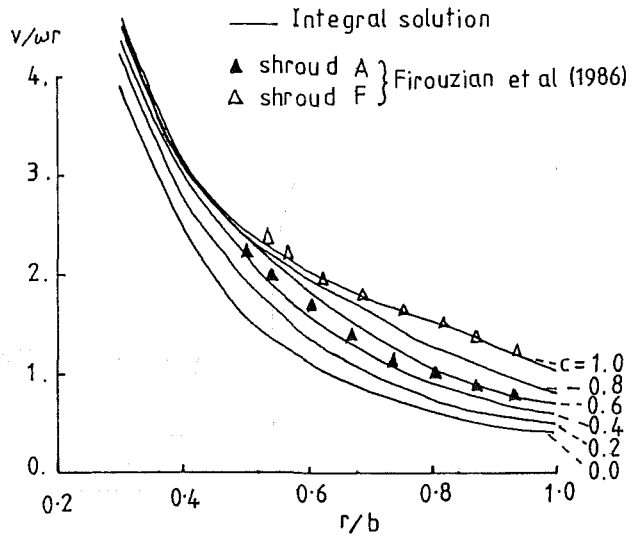

Fig. 12 Tangential velocity at $z/s = 0.5$; radial inflow, $C_w = -1415$, $Re_\theta = 1.97 \times 10^5$

calculations show reasonably good agreement. Figure 12 gives predictions from the integral method for different values of c for the conditions shown in Morse's Fig. 9. The integral solutions are in reasonable agreement with Morse's results, $c = 0.4$ giving $c_e = 0.58$, which is close to the experimental value. Further integral calculations show that for $c = 0.4$, doubling the flow rate to $C_w = -2840$ gives $c_e = 0.52$. For fixed c the integral solution for c_e will depend on C_w and Re_θ only through the group $C_w\ Re_\theta^{-0.8}$. Thus, considering all the theoretical work, it seems that within certain parameter ranges the value of c_e is not unduly sensitive to c, C_w, and Re_θ. This might account for Firouzian et al.'s observations regarding c_e. Of course, it should be remembered that there may be effects in the experiment, such as unsteadiness, nonaxisymmetry, and loss of fluid through the "inlet" holes, that have not been considered in the theoretical work.

I would like to thank Dr. Morse for providing a preprint of his paper.

References

Chew, J. W., 1982, "Computation of Flow and Heat Transfer in Rotating Cavities," D. Phil. Thesis, School of Engineering and Applied Science, University of Sussex, United Kingdom.

Chew, J. W., 1987, "Computation of Flow and Heat Transfer in Rotating Disc Systems," *Proc. of the 2nd ASME–JSME Thermal Engineering Joint Conference*, Vol. 3, pp. 361–367.

von Karman, T., 1921, "Uber laminare und turbulente reibung," *Z. angew. Math. Mech.*, Vol. 1, pp. 233–252.

Flow Characteristics of Long Orifices With Rotation and Corner Radiusing

W. F. McGreehan

M. J. Schotsch

GE Aircraft Engines,
Cincinnati, OH

The discharge coefficient of an orifice is a function of both geometric and flow effects, such as inlet corner radius, orifice length, inlet velocity orientation, and Reynolds number. Loss characteristics are available for each of these effects; however, a need exists for a reasonable method of predicting the discharge coefficient with an arbitrary combination of the above effects. Presented is a technique for calculating the discharge coefficient for arbitrary geometry with results compared to test data.

Introduction

The flow characteristics of sharp-edged orifice plates as metering/restricting devices are well understood. Calculation procedures and supporting data have been summarized for many standard orifice types by Miller [1], Cusick [2], Bean [3], and others. The general theory of orifice flows, with varying amounts of orifice coefficient data, is presented by Blevins [4], Ward-Smith [5], and Benedict [6]. In addition, there have been a number of excellent studies on specific orifice types, especially Alvi et al. [7]. However, in aircraft gas turbine engines there are many applications where an orifice is used as a flow restricting device without the benefit of ASME standard orifice construction and installation. In such situations the operating environment of an orifice is usually dictated by hardware constraints, which complicate the prediction of the discharge coefficient.

Designers need to be able to predict the orifice discharge coefficient reliably for arbitrary conditions of inlet corner radius, length, and inlet velocity orientation (Fig. 1). Data exist for each of these effects separately, and to a limited degree, in various combinations, but a comprehensive technique for quickly calculating the discharge coefficient for specific geometry and flow conditions does not exist. A reliable technique is of particular value for incorporation into network flow analysis software.

The original method used for obtaining the discharge coefficient for a combination of effects was to normalize each separate discharge coefficient value to a baseline C_d and take the product. For the effects of corner radius and long orifice, for example, the net discharge coefficient would be

$$C_d = (C_{d:r}/0.60)(C_{d:r,L}/0.60) \times 0.60 \tag{1}$$

A baseline C_d of 0.60 for a sharp-edged orifice is used as a reference point at Re = 3.2×10^4 and was chosen for convenience. This calculation is relatively simple and generally gives reasonable results if the net C_d is not greater than 0.80. Certain combinations of r/d, L/d, and U_1/V_i however can result in discharge coefficients greater than 1.0, which are illogical under these circumstances. Thus, there exists a need for accurate empirical C_d representations for each of the separate effects and a reliable procedure for combining them.

Basic Orifice Equation. The basic equation for flow through an orifice or nozzle is

$$W = C_d\ Y\ A_a \sqrt{2g_c\ P_{t1}/(R\ T_{t1})(P_{t1} - P_{s2})} \tag{2}$$

Note that for flow in a pipe the normal velocity of approach correction

$$k = 1/\sqrt{1 - (d/D)^4} \tag{3}$$

is accounted for in the total pressure P_{t1} and total temperature T_{t1}. The adiabatic gas expansion factor Y for an orifice is

$$Y_o = 1 - 0.41\ (P_{t1} - P_{s2})/(\gamma\ P_{t1}) \tag{4}$$

For a nozzle, Y is derived from the isentropic flow equations as

$$Y_n = \left[S^{2/\gamma} \left(\frac{\gamma}{\gamma - 1}\right) \left(\frac{1 - S^{(\gamma-1)/\gamma}}{1 - S}\right)\right]^{1/2} \tag{5}$$

where Y accounts for the drop in fluid density with the lowering of static pressure and temperature during flow acceleration. Also, S is the pressure ratio P_{s2}/P_{t1}. The value of Y for a

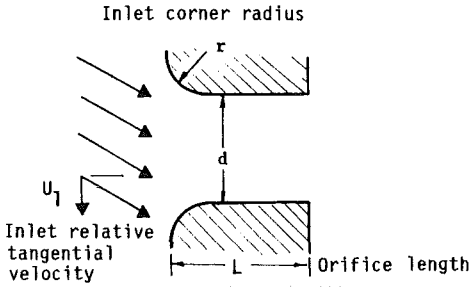

Fig. 1 Conditions affecting discharge coefficient

Contributed by the Gas Turbine Division of THE AMERICAN SOCIETY OF MECHANICAL ENGINEERS and presented at the 32nd International Gas Turbine Conference and Exhibit, Anaheim, California, May 31–June 4, 1987. Manuscript received at ASME Headquarters February 17, 1987. Paper No. 87-GT-162.

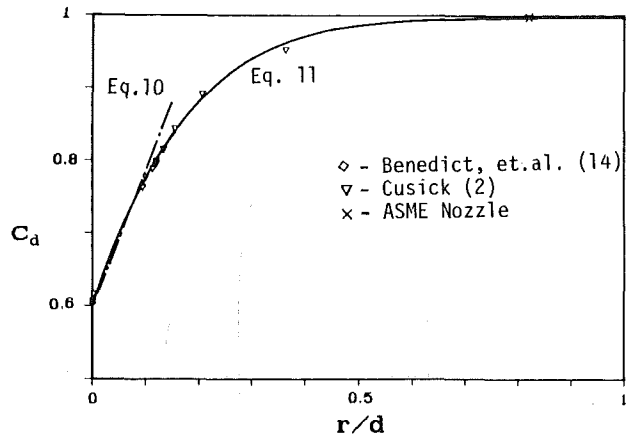

Fig. 2 Effect of orifice *r/d* on C_d

particular geometry is determined primarily by the manner in which the expansion process takes place between upstream conditions and the throat. The use of this factor to handle compressibility effects is important to the incorporation of data taken from incompressible flow tests. The net C_d in equation (2), when determined for a particular device, will be a function only of Reynolds number.

When the orifice inlet radius and/or length result in a net discharge coefficient that approaches a nozzle C_d, Y_o will approach Y_n. For a nozzle, the expansion process to the throat is essentially isentropic with the throat established by a physical boundary. The sharp-edged orifice expansion process is not isentropic and the throat (vena contracta) can be in the discharge free stream, or for long orifices, within the orifice length. An additional complication is that the vena contracta is not necessarily the location where the local static pressure equals discharge static pressure. An example is a long orifice with inlet separation.

Generally, the exact nature of flow in an orifice is not known and therefore the following approximation can be used to calculate the value of Y based on the calculated value of the discharge coefficient. The expansion will generally be controlled by a physical boundary when the net C_d is greater than 0.82. As the discharge coefficient increases toward 1.0, the abiabatic gas expansion factor will approach that of the nozzle. The net value of Y is then

$$Y=(1-X)Y_o+X\,Y_n \qquad (C_d > 0.82) \tag{6}$$

where

$$X=8.333\,(C_d-0.82) \tag{7}$$

Reynolds Number Effects. The effect of Reynolds number on discharge coefficient for an orifice and nozzle has been determined by Miller and Kneisel [8]. The discharge coefficient for an orifice, for plenum-to-plenum flow ($\beta=0$), is

$$C_{d:\mathrm{Re}}=0.5885+372/\mathrm{Re} \tag{8}$$

and for a nozzle

$$C_{d:\mathrm{Re}}=0.9981-4.73/\sqrt{\mathrm{Re}} \tag{9}$$

where equations (8) and (9) are valid for Re $\geq$ 10,000. For very large Re, equations (8) and (9) reduce to 0.5885 for an orifice and 0.9961 for a nozzle. The discharge coefficient corrected for Reynolds number is used as the baseline C_d in the equations to correct for geometry and configuration effects.

Corner Radius Effects. An orifice with inlet corner radiusing will have a higher discharge coefficient as a result of reduced flow separation at the inlet. The influence of orifice corner radius on the discharge coefficient has been studied by Benedict et al. [14] for $r/d < 0.0035$. Also, data presented by Cusick [3] for quadrant-edge orifices covers a range of $0.1 < r/d < 0.36$. An equation in common use to correct C_d for corner radiusing is published by Schoder and Dawson [13]

$$\Delta C_d/C_d=3.10\,(r/d) \tag{10}$$

which is a good approximation for $0 < r/d < 0.1$. An ASME nozzle C_d is the limiting condition at $r/d = 0.82$; that is, beyond this r/d ratio no further benefit for inlet radiusing is achieved. The above referenced corner radiusing data are plotted on Fig. 2 assuming a basic $C_d = 0.60$, and have been curve-fit to an exponential equation. This equation should give a good prediction of corner radius effects for the full range of r/d. The curve-fit equation is

$$C_{d:r}=1-f\,(1-C_{d:\mathrm{Re}}) \tag{11}$$

where $C_{d:\mathrm{Re}}$ is the basic Reynolds number adjusted discharge coefficient and the f factor equation is

$$f=0.008+0.992\,e^{-5.5\,(r/d)-3.5\,(r/d)^2} \tag{12}$$

Long Orifice Effects. A long orifice has a higher discharge coefficient than a thin orifice due to the controlled expansion

Nomenclature

A_a = actual area
C_d = net discharge coefficient = W_a/W_i
$C_{d:r}$ = C_d with r/d correction
$C_{d:r,L}$ = C_d with r/d, L/d corrections
$C_{d:r,L,U}$ = C_d with r/d, L/d, U_1/V_i corrections
$C_{d:Re}$ = C_d with Reynolds number correction
C_1 = term in the $C_{d:r,\,L,\,U}$ equation
C_2 = term in the $C_{d:r,\,L,\,U}$ equation
C_3 = term in the $C_{d:r,\,L,\,U}$ equation
d = orifice diameter
D = pipe diameter
f = r/d effects function
g = L/d effects function
g_c = gravitational constant
k = normal velocity of approach factor
L = orifice flat length
P_{s2} = exit static pressure
P_{t1} = inlet total pressure
r = inlet corner radius
R = gas constant
Re = Reynolds number = $V_i d/\nu$
R_v = velocity ratio parameter
S = pressure ratio = P_{s2}/P_{t1}
T_{t1} = inlet total temperature
U_1 = inlet relative tangential velocity
V_i = orifice ideal through flow velocity
W = orifice flow
W_a = actual flow
W_i = ideal incompressible flow
X = coefficient for adiabatic gas expansion factor
Y = net adiabatic gas expansion factor
Y_o = orifice adiabatic gas expansion factor
Y_n = nozzle adiabatic gas expansion factor
β = orifice diameter ratio = d/D
γ = ratio of specific heats
ν = kinematic viscosity

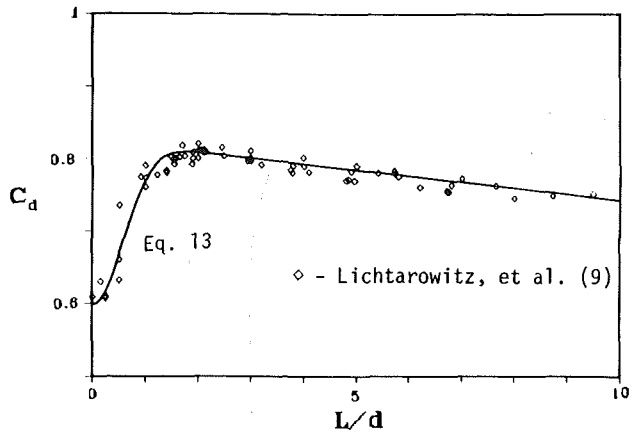

Fig. 3 Effect of orifice *L/d* on C_d

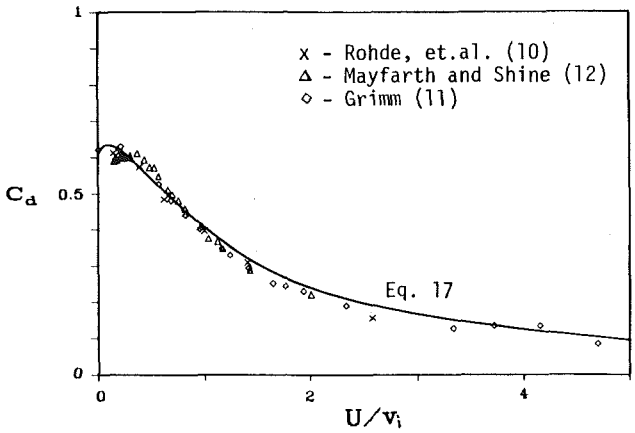

Fig. 4 Orifice U/v_i effect on C_d

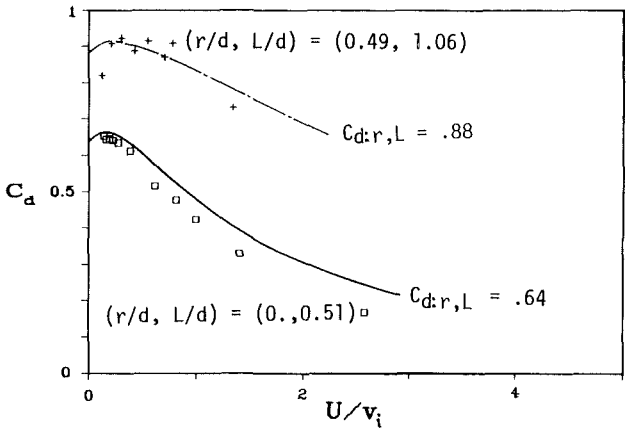

Fig. 5 Predicted *r/d* effect with Rohde data [10]

and recovery of excess dynamic pressure downstream of the vena contracta. Long orifice data have been presented by Lichtarowitz et al. [9] and are plotted in Fig. 3 for a basic $C_{d:r}$ of 0.60. The curve is represented by

$$C_{d:r,L} = 1 - g\,(1 - C_{d:r}) \tag{13}$$

where, in general, the basic discharge coefficient is adjusted for corner radius effects. The g factor in equation (13) is

$$g = [1 + 1.3e^{-1.606\,(L/d)^2}](0.435 + 0.021\,L/d) \tag{14}$$

Special caution should be taken when r/d and L/d effects occur together. The corner radius reduces the tendency for separation at the inlet and hence decreases the dynamic pressure recovery benefit of the long orifice. Consequently, the inlet radius should be subtracted from the total length and a revised basic C_d calculated from the g factor equation using the r/d. This revised basic C_d is

$$(C_{d:r})' = 1 - g\,(1 - C_{d:r}) \tag{15}$$

where g is calculated by substituting r/d for L/d in equation (14). The final L/d effect is then obtained by calculating g using

$$(L/d)' = L/D - r/d \tag{16}$$

and $(C_d)'$ from equation (15) substituted into equation (13).

Relative Tangential Velocity Effects. The normal velocity of approach to an orifice or nozzle contributes to the inlet total pressure and temperature but does not influence the discharge coefficient. The relative tangential velocity, however, does change the discharge coefficient due to the increased separation at the inlet. Typically the discharge coefficient is viewed as a function of the velocity ratio U_1/V_i, where U_1 is the relative tangential velocity and V_i is the ideal orifice throughflow velocity. Higher ratios result in lower discharge coefficients.

A relative tangential velocity can be created by a rotating orifice with stationary inlet air or by an orifice in the side of a duct. The ideal orifice velocity is based on the static pressures and temperature consistent with flow through a rotating orifice. Caution must be taken not to use the total pressure based on the tangential velocity when calculating ideal orifice velocity with inlet crossflow (orifice in the side of a duct). This will significantly alter the resulting C_d.

The effect of relative tangential velocity on C_d has been studied by a number of investigators, including Rohde [10], who studied an orifice in the side of a duct with orifice velocity calculated from the duct total conditions. Rohde's results have been adjusted using static parameters. Grimm [11] and Meyfarth and Shine (12) determined discharge coefficients for rotating orifices. The data from the above sources have been compiled and plotted for comparison on Fig. 4 in order to correct the basic C_d for relative tangential velocity. An expression generated to represent this data is

$$C_{d:r,\,L,\,U} = C_{d:r,\,L}\,(C_1 + C_2\,C_3) \tag{17}$$

where

$C_1 = e^{-R_v^{1.2}}$

$C_2 = 0.5\,R_v^{0.6}\,(C_{d:r,L}/0.6)^{-0.5}$

$C_3 = e^{-0.5\,R_v^{0.9}}$

Here the velocity ratio parameter is

$R_v = (U_1/V_i)\,(C_{d:r,\,L}/0.6)^{-3}$

and $C_{d:r,L}$ is obtained from equation (13).

Equation (17) expresses the final discharge coefficient and corrects the orifice C_d for Reynolds number, inlet corner radius, orifice length, and relative tangential velocity.

Various Combinations of *r/d*, *L/d*, and U_1/V_i. When corner radius, length, and relative tangential inlet velocity effects are combined, the net C_d can be calculated following the procedure outlined in equations (8)-(17). The experimental data associated with the combination of effects are limited and not in a form that readily facilitates comparison with predictions. Rhode [10] presents various configurations with these variables for small orifices in the side of a duct. The data scatter is significant due in part to the use of small orifices, compressibility effects, and the dynamic pressure ratio correlation method.

A limited comparison can be made between the predictions of equation (17) and data from Rohde. The results of Rohde generally show trends that are consistent with the C_d versus r/d and L/d data from other authors, although his basic values are lower for r/d and $L/d > 0$. The trends with U_1/V_i

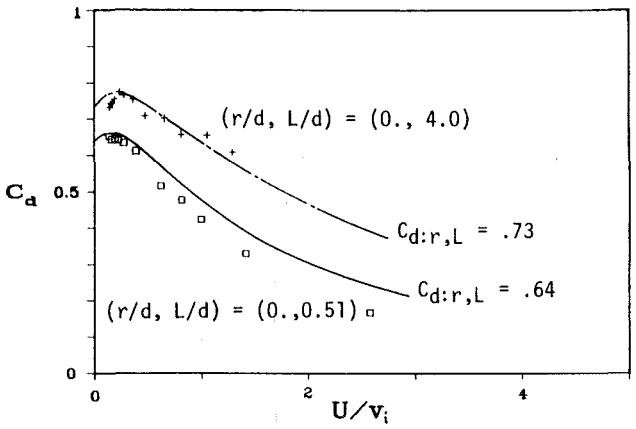

Fig. 6 Predicted *L/d* effect with Rohde data [10]

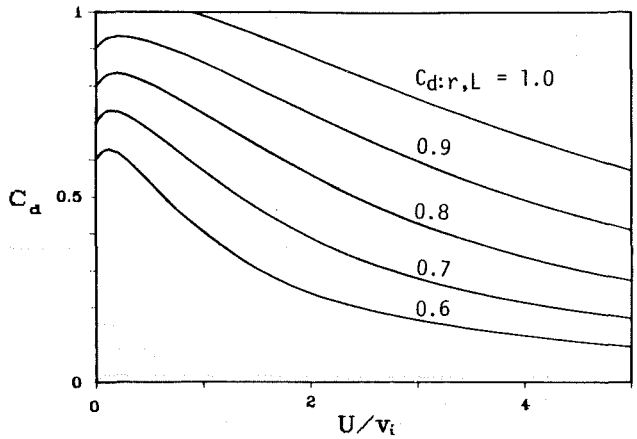

Fig. 7 Predicted effect of U/V_i for various values of $C_{d:r,L}$

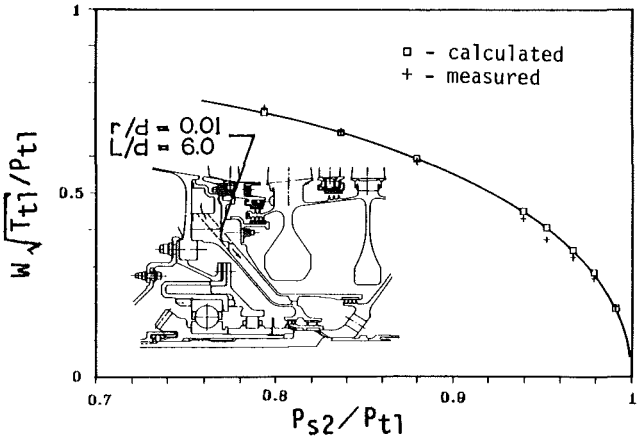

Fig. 8 Flow function predicted and measured for a long slot

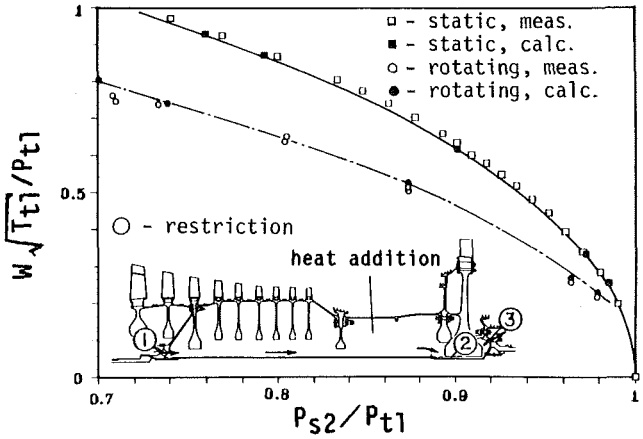

Fig. 9 Flow function predicted and measured for both static and rotating assemblies

are shown in Figs. 5 and 6 for the discharge coefficient compared with calculated C_d from a set baseline point at $U_1/V_i = 0$. Figure 5 illustrates the variation of the C_d with velocity ratio for a sharp-edge orifice ($r/d = 0$) and a generous corner radius ($r/d = 0.49$).

The effect of L/D on discharge coefficient is shown in Fig. 6 for L/D values of 0.51 and 4.0. The results shown on Figs. 5 and 6 traverse most of the range of variation expected for r/d and L/d showing a reasonable degree of correlation. The trend with varying U_1/V_i and $C_{d:r,L}$ is illustrated on Fig. 7.

Experience with the method in predicting flow characteristics of complex orifices in aircraft engine systems has shown excellent agreement with test data. Figure 8 illustrates a typical flow function–pressure ratio curve showing predicted and measured flow function for a long orifice slot with inlet corner radius. The flow function is given by

$$W\sqrt{T_{t1}}/P_{t1} = C_d\ Y\ A_a\sqrt{2g_c/R\ (1-P_{s2}/P_{t1})} \qquad (18)$$

The agreement is excellent over the range of pressure ratios tested.

Additional testing has been done on a compressor-turbine rotor assembly where a series of complex restrictions are numbered 1 through 3 as shown in Fig. 8. The flow characteristics of the rotor assembly were measured on a static rig test and during engine testing. The flow function of the rotor is reduced during engine test by the relative tangential velocity of approach at rotating orifice 1 and the rotor internal heat addition between 1 and 2. Predicted and measured flow functions are shown on Fig. 9 for both tests. The net C_d of each orifice is calculated based on the effects of inlet corner radiusing and length. For the rotating assembly, the relative inlet swirl and heat addition are added with a resulting drop in the flow function. In both cases the agreement between test results and predictions is excellent.

Summary and Conclusions

The accurate prediction of loss characteristics in orifices for many flow systems is complicated by complex hardware and installation conditions. As a result of Reynolds number, corner radiusing, length, and relative tangential velocity of approach effects, the discharge coefficient cannot be determined from standard metering orifice tables.

A technique has been presented to calculate the net C_d based on empirical data from various investigators. The discharge coefficient $C_{d:r,L,U}$ is a function of U_1/V_i and basic $C_{d:r,L}$ as represented by equation (17). This equation can be used to account for any combination of the effects of r/d, L/d, or U_1/V_i.

The method outlined is somewhat tedious for hand calculations but easily coded for solution on computer. Use of the technique has proven to be beneficial to the accurate estimation of flow characteristics in complex restrictions. The discharge coefficient technique presented here has been incorporated in a comprehensive air system design program for compressible flow network analysis, and has been valuable to cooling system design.

Based on the work done to date, it is apparent that new test data are required to study and verify combinations of r/d, L/d, and U_1/V_i effects. For angled orifices, the present method of solution is to assume that the C_d is influenced the same way as an orifice with a relative tangential velocity of approach. This is based on the consideration that in both cases

the air approach velocity vector has a component normal to the orifice orientation axis, and therefore must experience a turn in order to enter the orifice. Additional work is required to check this assumption against available data and to perform appropriate testing where necessary.

Acknowledgments

The authors would like to thank the General Electric Aircraft Engine Business Group for funding and facilities to complete the analysis and testing associated with this effort. Special thanks are also in order to F. G. Haaser, Manager of Air Systems Design, for his support of this project and valuable input to all phases of the effort.

References

1 Miller, R. W., *Flow Measurement Engineering Handbook*, McGraw-Hill, New York, 1983.

2 Cusick, C. F., *Flow Meter Engineering Handbook*, Honeywell Inc., 1977.

3 Bean, H. S., *Fluid Meters*, 6th ed., ASME New York, 1971.

4 Blevins, R. D., *Applied Fluid Dynamics Handbook*, Van Nostrand, New York, 1984.

5 Ward-Smith, A. J., *International Fluid Flow*, Clarendon Press, Oxford, 1980.

6 Benedict, R. P., *Fundamentals of Pipe Flow*, McGraw-Hill, New York, 1980.

7 Alvi, S. H., Sridharan, K., and Lakshmana Rao, N. S., "Loss Characteristics of Orifices and Nozzles," ASME *Journal of Fluids Engineering*, Vol. 100, 1978, pp. 299–307.

8 Miller, R. W., and Kneisel, O., "A Comparison Between Orifice and Flow Nozzle Laboratory Data and Published Coefficients," ASME Paper No. 73-WA/FM-5, 1973.

9 Lichtarowitz, A., Duggins, R. K., and Markland, E., "Discharge Coefficients for Incompressible Noncavitating Flow Through Long Orifices," *Journal of Mechanical Engineering Science*, Vol. 7, No. 2, 1965, pp. 210–219.

10 Rohde, J. E., Richards, H. T., and Metger, G. W., "Discharge Coefficients for Thick Plate Orifices With Approach Flow Perpendicular and Inclined to the Orifice Axis," NASA TN D-5467, 1969.

11 Grimm, R. E., "Fluid Flow Characteristics Through Orifices in Enclosed Rotating Disks," M. S. Thesis, AFIT, 1967.

12 Meyfarth, P. F., and Shine, A. J., "Experimental Study Of Flow Through Moving Orifices," *Journal of Basic Engineering*, Dec. 1965, pp. 1082–1083.

13 Schoder, E. W., and Dawson, F. M., *Hydraulics*, McGraw-Hill, New York, 1934, p. 408.

14 Benedict, R. F., Wyler, J. S., and Brandt, G. B., "The Effect of Edge Sharpness on the Discharge Coefficient of an Orifice," ASME Paper No. 74-WA/FM-4, 1974.

Sealing of a Shrouded Rotor-Stator System With Preswirl Coolant

Z. B. El-Oun

P. H. Neller

A. B. Turner

School of Engineering and Applied Sciences,
University of Sussex, Brighton,
E. Sussex, United Kingdom

This paper describes an experimental study of a modeled gas turbine rotor-stator system using both preswirled blade coolant and radially outward flowing disk coolant. A double mitered rim seal was used together with, for some tests, an inner seal below the preswirl nozzles and blade feed holes in the rotor which were situated at the same radius. Some flow visualization results are presented together with measurements of pressure distribution, internal flow distribution, and the minimum seal flow necessary to prevent "mainstream" gas ingress into the wheelspace. The experiments are described for a range of rotational speeds up to $Re_\theta = 1.8 \times 10^6$ for various combinations of preswirl flow, disk coolant flow, and "blade" coolant flow. The preswirled coolant flow is shown to have little effect on the pressure distribution below the preswirl nozzles but a gas concentration sampling technique showed that considerable contamination of the preswirled coolant by the frictionally heated disk coolant can occur. A clear pressure inversion effect was observed when coolant was provided by the preswirl nozzles only, whereby the pressure under the rim seal increased with increasing rotational speed. Except for the lowest flow rates, blade coolant flow is shown to increase the sealing flow requirement, but to a very much reduced extent when disk coolant flow is used simultaneously. A nonlinear relationship between minimum sealing flow and Re_θ is produced when the blade cooling system is in operation.

1 Introduction

As gas turbine pressure ratios and turbine entry temperatures (TET) continue to increase, the problem of cooling the disks and blades becomes more severe. The prevention of mainstream gas ingress into the rotor-stator wheelspace with the economical minimum of coolant flow is also necessary if the thermodynamic advantages of increased TET are not to be lost. One now established method of introducing blade cooling air into the rotor-stator wheelspace is by accelerating it through preswirl nozzles at an acute angle to the rotating blade feed holes in the rotor. While the stagnation temperature of the air is unchanged relative to the stator, its total temperature relative to the rotor is reduced with consequent benefit to the blade cooling system. If disk cooling air is also used, either with radial outflow or radial inflow, then unless the two flows are physically separated there can be a complex interaction between them. The nature of this interaction affects the radial pressure distribution and thus the rim sealing flow requirement.

Although little work has been published on preswirled coolant flow systems [1], several experiments have been reported on the sealing of rotor-stator cavities. Bayley and Owen [2] modeled the turbine wheelspace with a plane rotor and stator using a simple axial clearance shroud fitted to the stator to form the rim seal. Coolant was admitted centrally through the stator and exhausted through the shroud to a quiescent environment. They carried out tests for rotational Reynolds numbers up to $\mathrm{Re}_\theta = 4 \times 10^6$ with two shroud clearance ratios, $G_{ca} = 0.0033$ and 0.0067, and suggested the relationship

$$C_{wmin} = 0.61 G_{ca} \mathrm{Re}_\theta$$

where $G_{ca} = S_{ca}/r_o$, $\mathrm{Re}_\theta = \rho\omega r_o^2/\mu$, $C_w = \dot{m}/\mu r_o$ and C_{wmin} is the minimum dimensionless flow rate necessary to prevent ingress of surrounding air into the cavity between rotor and stator.

The simple axial clearance seal was further investigated by Owen and Phadke [3], in a quiescent environment, who correlated their results with the relationship

$$C_{wmin} = 0.14 G_{ca}^{0.66} \mathrm{Re}_\theta$$

based on a range of rotational Reynolds numbers up to $\mathrm{Re}_\theta = 10^6$ and five values of seal clearance ratio with $0.0025 \leq G_{ca} \leq 0.04$.

Abe et al. [4] tested a model turbine rotor-stator cavity with a form of radial clearance seal in the presence of an external axial flow with swirl. They did not report specifically on the seal flows required to prevent ingress, but examined the level of ingress, i.e., the amount of external flow drawn into the

Contributed by the Gas Turbine Division of THE AMERICAN SOCIETY OF MECHANICAL ENGINEERS and presented at the 32nd International Gas Turbine Conference and Exhibit, Anaheim, California, May 31-June 4, 1987. Manuscript received at ASME Headquarters February 5, 1987. Paper No. 87-GT-72.

wheelspace, and its subsequent distribution. For the range of values tested, $3 \times 10^5 \leq \mathrm{Re}_\theta \leq 10^6$, they found the rotational speed of the disk to have little influence on ingress—a somewhat surprising result at the time in view of Owen and Phadke's linear relationship between the minimum seal flow required to prevent ingress and rotational speed.

Phadke and Owen [5] studied a variety of rim seals, again without external flow. They observed that some seals with a radial clearance could, unlike axial clearance seals, exhibit a pressure inversion effect so that the cavity pressures at the outer radii were seen to increase rather than decrease with rotational speed. It must be noted, however, that this was only observed with seal flows that were more than double the minimum flow required to prevent ingress and the relationship between this minimum flow C_{wmin}, and rotational speed Re_θ, was still found to be linear for all seals examined.

Kobayashi et al. [6] tested a model turbine with radial clearance seals in an axial external flow without swirl, at rotational Reynolds numbers up to 6.5×10^6. Using the pressure differential across the seals as a criterion to indicate the onset of ingress they obtained a near-linear relationship between C_{wmin} and Re_θ which was in good agreement with Phadke and Owen's [5] results and extended to the much higher Reynolds number. However, when Kobayashi et al. monitored temperatures inside the cavity (their external air flow was heated) they detected temperature fluctuations with seal flows well above those predicted to prevent ingress according to the pressure differential criterion. The seal flows required to prevent these temperature fluctuations were almost double that predicted by the pressure criterion at the highest speed, and sensibly independent of rotational speed, lending some support to the work by Abe et al.

Phadke and Owen [7] offered an explanation for the difference between tests in a quiescent environment and turbine-like tests with a swirling external flow. A comprehensive series of experiments was conducted on a simple model rotor–stator system with an external axial flow over the rim seal both "near axisymmetric" and with various degrees of circumferential asymmetry in both velocity and pressure. These experiments, briefly reported in [7], used flow visualization, pressure measurement, and gas concentration techniques to study the performance of several rim seals. It was concluded that the difference between tests in a quiescent environment and tests with an external flow could be accounted for by induced circumferential pressure variations—the pressure ripple—which increase with increasing external flow. Indeed these experiments showed that by increasing the external flow velocity (and thus the circumferential pressure variation) the minimum sealing flow moved from a linear dependence on rotational speed to complete independence of it at the higher external flow velocities.

Sambo [8] studied the sealing performance of rotor–stator cavities fitted with single and double-mitered shrouds. Flow visualization and pressure measurements showed the single-mitered shrouds to be better than axial clearance shrouds but not as effective as radial clearance shrouds. His experiments with the 15 deg double-mitered system indicated it to be superior to the 15 deg single-mitered shroud.

The purpose of this paper is to present the results of sealing experiments on a 15 deg double-mitered rim seal, shown in Fig. 1, for one seal clearance ratio, $G_{cm} = 0.0072$, and for various combinations of preswirl flow, centrally introduced disk coolant flow, and blade cooling flow. Brief mention is made of the sealing of an inner radial seal situated below the preswirl nozzles so that the preswirl flow acts in much the same manner as the external mainstream flow in Phadke and

Nomenclature

$C_w \equiv \dot{m}/\mu r_o$ = dimensionless mass flow coefficient
C_{wb} = dimensionless blade coolant flow
C_{wd} = dimensionless disk coolant flow
C_{wdb} = dimensionless disk coolant flow drawn into the blade feed holes (calculated from the gas concentration measurements)
C_{we} = dimensionless flow entrained by rotor from core flow
C_{wmin} = minimum dimensionless mass flow required to prevent ingress
C_{wo} = dimensionless mass flow up the rotor
C_{wp} = dimensionless preswirl coolant flow
C_{ws} = dimensionless flow through the rim seals
$F^*_{db} \equiv C_{wdb}/C_{wb}$ = proportion of blade flow composed of disk coolant flow
$F^*_{dd} \equiv C_{wdb}/C_{wd}$ = proportion of disk coolant flow taken into blade feed holes
$G \equiv S/r_o$ = rotor/stator axial gap ratio
$G_{ca} \equiv S_{ca}/r_o$ = clearance ratio for the simple axial shroud
$G_{cm} \equiv S_{cm}/r_o$ = clearance ratio for the 15 deg mitered shrouds
$G_{cr} \equiv S_{cr}/r_o$ = clearance ratio for the radial shrouds
$\dot{m}$ = coolant mass flow rate
p = static pressure
$p^* = 10^3(p-p_a)/p_a$ = dimensionless pressure difference
r = radial distance from disk center line
r_b = radius of central axis of blade feed holes = radius of central axis of preswirl nozzles
$\mathrm{Re}_w \equiv \rho V_p r_o/\mu$ = preswirl flow Reynolds number
$\mathrm{Re}_\theta \equiv \rho\omega r_o^2/\mu$ = rotational Reynolds number
S = axial gap between rotor and stator
S_{ca} = axial clearance in rotor/stator rim seal
S_{cm} = mitered clearance in rotor/stator rim seal
S_{cr} = radial clearance in rotor/stator rim seal
$S_r \equiv V_{\phi p}/\omega r_b$ = swirl ratio of preswirl flow
V_p = the preswirl average velocity
$V_{\phi p} \equiv V_p \sin\theta$ tangential component of preswirl flow velocity
θ = angle of preswirl nozzle to axial direction = 70 deg
μ = fluid dynamic viscosity
$\nu = \mu/\rho$ = fluid kinematic viscosity
ρ = fluid density
ω = disk angular velocity

Subscripts

a = refers to ambient conditions
b = refers to blade coolant flow[1]
ca = refers to seal axial clearance
cm = refers to seal mitered clearance
cr = refers to seal radial clearance
d = refers to disk coolant flow
i = refers to conditions at inner radius $r = r_i$
o = refers to conditions at outer radius
p = refers to preswirl coolant flow
s = refers to seal flow
min = minimum value

[1]There are no blades on the rotor, but air can be drawn into the rotor at the points corresponding to the blade cooling inlet orifices in the real engine. This flow is referred to as blade flow.

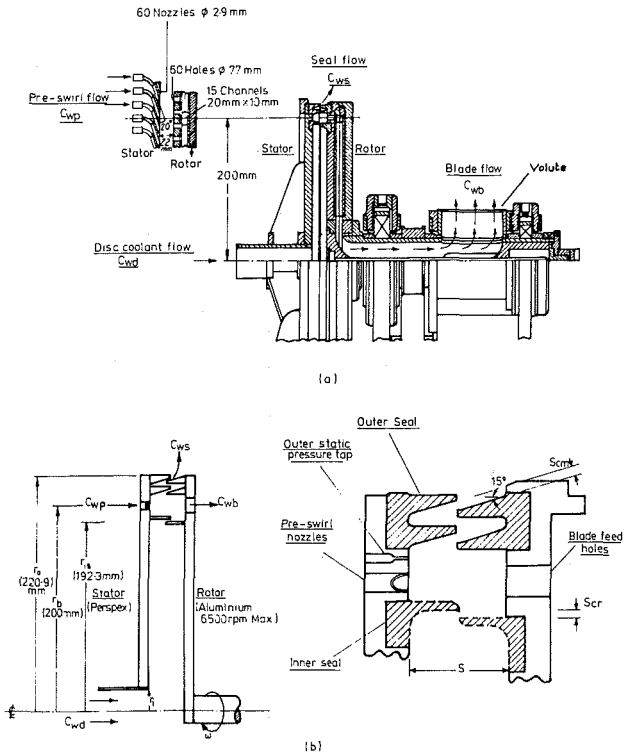

Fig. 1 (*a*) General arrangement of the preswirl rotor-stator rig; (*b*) schematic diagram of the rotor-stator cavity and details of the rim and inner seals

Owen's [7] work, but with considerable swirl. The experimental apparatus is described in section 2, some flow visualization tests are discussed in section 3, and the measured pressure distributions are presented in section 4. The gas concentration experiments, showing the extent of the mixing between the preswirl and the disk coolant flows, are discussed in section 5 and the minimum flows required to seal the cavity for the various combinations of preswirl flow, disk coolant flow, and blade coolant flow are presented in section 6.

2 Experimental Apparatus

The rotor–stator general arrangement is shown in Fig. 1(*a*) and details of the cavity, rim, and inner seals are shown in Fig. 1(*b*). The apparatus essentially consists of a plane stationary disk (stator) with preswirl nozzles adjacent to a plane rotating disk (rotor) containing blade feed holes at the same radius as the preswirl nozzles. The various flows into, and out of, the cavity are also indicated (nondimensionally) in Fig. 1(*b*): C_{wd} is the centrally admitted disk coolant flow, C_{wp} is the preswirled flow, C_{wb} is the blade coolant flow drawn into the rotor, and C_{ws} is the flow through the rim seal. The stator was made from perspex, 10 mm thick, to allow flow visualization and laser-Doppler anemometry, and contained 60 preswirl nozzles, 2.9 mm diameter, inclined at 20 deg to the face at a radius of 200 mm. The rotor was made from two aluminum alloy disks with two disks of "rohacell" insulation sandwiched between. The insulation contained 15 radial passages connected at the outer edge of the cavity to 60 blade feed holes, each 7.7 mm in diameter, to allow the blade coolant flow C_{wb} to be drawn radially down through the rotor and then out via the rotating shaft and flow volute (see Fig. 1*a*) through a flow meter and the exhauster. Although the rotor–stator gap and the rim seal clearance were adjustable, they were constant for the tests reported below. The gap ratio was maintained at $G = 0.10$ and the rim shroud clearance ratio $G_{cm} = 0.0072$ with the seal edges positioned as shown in Fig. 1(*b*). Brief mention is made in section 6 of the effect of inner seals of radial clearance ratio $G_{cr} = 0.0033$, based on the outer radius of the rotor. The rotor was driven by a Tasc motor system affording precise speed control up to 5400 rpm ($Re_\theta = 1.8 \times 10^6$). Air, at flow rates up to $C_{wp} = 2 \times 10^4$, was supplied to the preswirl nozzles via a manifold system at pressures up to 1.28 bar and 35°C upstream of the nozzles. For rotational Reynolds number $Re_\theta = 1 \times 10^6$ and preswirl flows over the range $4000 < C_{wp} < 18{,}000$, the swirl ratio S_r varies in the range $0.46 < S_r < 2.07$. The disk air coolant flow, up to $C_{wd} = 1.2 \times 10^4$, was supplied at essentially atmospheric pressure and 25°C to the center of the stator via a pipe of 38 mm diameter. All mass flow rates were measured, with an accuracy of ± 3 percent, by Annubar flow meters. The flow out through the seals was not measured directly but determined from the other flow rates, thus the nondimensional seal flow is found from

$$C_{ws} = C_{wp} + C_{wd} - C_{wb}$$

The stator was instrumented with static pressure taps (0.5 mm diameter) on three orthogonal radii. On the test radius, taps were located at radial positions of 50, 82, 105, 124, 140, 155, 168, 181, and 204.8 mm; the outer pressure tap above the preswirl nozzles and below the rim seal (Fig. 1*b*) was used for measuring the pressure difference across the seal for one of the ingress criteria. The other ingress criteria used were flow visualization (smoke), gas concentration (N_2O), and temperature measurements. The pressure measurements were made using a 36-way multichannel manually controlled switching unit and a single transducer.

The system consisted of a pressure switching unit coupled to two different M10 electromanometers, one with a maximum range of 30 mm W. G. and the other fitted with a capsule which measured up to 1000 mm W. G.

Air temperatures were measured inside the cavity at $r/r_o = 0.93$ (just under the stator rim seal) and in the blade feed holes. The rotating thermocouples in the blade feed holes were connected to a slip-ring assembly mounted on the far end of the rotating shaft. The output signals from the thermocouples and the electromanometers were fed to a Solartron IMS 3512 data logger, which was controlled by a PDP 11/44 minicomputer.

The flow visualization photographs were achieved with oil smoke introduced into the central disk flow (C_{wd}) and an argon-ion laser operating in the all-line mode providing "slit" illumination, with the scattered light viewed at approximately 45 deg to an r–z plane across the cavity below the position of the inner seal.

The flow distribution, i.e., the eventual destinations of the disk coolant flow C_{wd} and the preswirl flow C_{wp}, were determined by seeding the preswirl flow with nitrous oxide gas (N_2O) and measuring the concentration level of N_2O in both the preswirl flow C_{wp} upstream of the cavity and in the blade flow C_{wb} with a GP Instrumentation IRGA 120 Infrared gas analyzer.

3 Flow Visualization

For tests where estimates of the minimum mass flow rate C_{wmin} necessary to seal the cavity and prevent ingress of the external fluid into the cavity were required, smoke was injected around the periphery of the rim seals, and by setting the disk rotation at a fixed value, it was possible to obtain C_{wmin} by reducing C_{ws} until smoke was observed to enter the cavity. It should be noted that no photographs of the flow structure were taken with ingress present.

By injecting smoke into the disk coolant flow, it was possible to determine the flow structure inside the cavity with and without preswirl coolant flow. Owing to the rapid dispersion

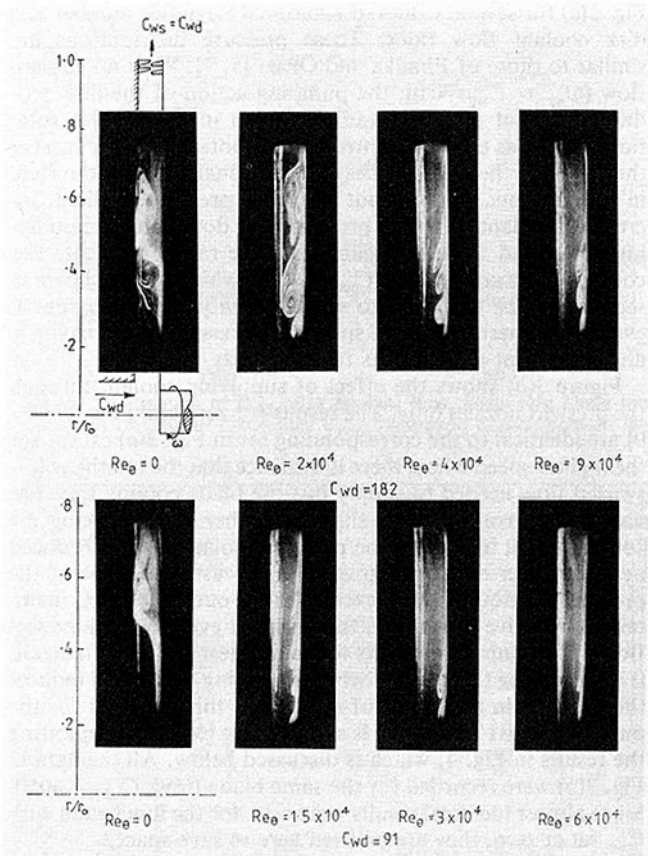

Fig. 2(a) The flow structure inside the cavity with disk coolant flow only

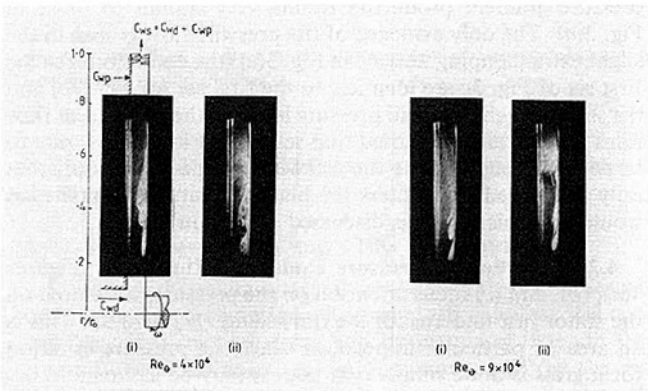

Fig. 2(b) Flow structure inside the cavity with and without preswirl coolant flow: (*i*) no preswirl flow, $C_{wd} = 182$; (*ii*) with preswirl flow, $C_{wp} = 2000$ and $C_{wd} = 182$

of oil smoke in high shear flows, the flow visualization photographs in Figs. 2(*a*) and 2(*b*) are only for laminar flows, i.e., at low rotational Reynolds numbers and low values of disk and preswirl coolant flows. Nevertheless, the results for these values do provide useful additional insight into the nature of the flow in a rotor–stator cavity. In all the photographs presented, the disk coolant flow C_{wd} enters near the bottom left-hand side; the preswirl coolant flow C_{wp} enters near the top left-hand side; and the outflow leaves near the top of the photograph. It should be noted that the field of view was limited to the range $0.24 < r/r_o < 0.75$ and that reflections caused mirror images near the stator side.

With no preswirl coolant flow, Fig. 2(*a*) shows the effects of the disk coolant flow rate and rotational Reynolds number on

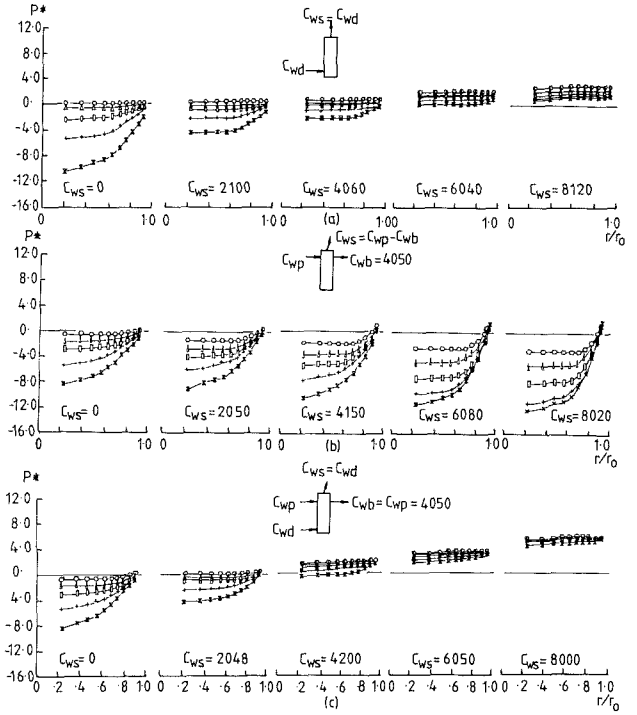

Fig. 3 The effect of rotational Reynolds number Re_θ, and seal flow C_{ws}, on the radial distribution of pressure:

Symbol	○	△	□	+	X
$Re_\theta/10^6$	0	0.4	0.8	1.2	1.8

the flow structure in the wheelspace between the rotor and stator. For $C_{wd} = 182$ and zero rotational speed, the flow is laminar and behaves as a normal jet impinging on the stationary rotor surface and "re-attaches" itself to the stator wall at around $r/r_o = 0.45$ to 0.50. For the same C_{wd} and $Re_\theta = 2 \times 10^4$, the coolant flow attaches to the rotor, forming a laminar boundary layer with large vortexlike instabilities propagating on the rotor surface and spreading toward the core of the cavity and stator wall. Due to the fact that all these photographs were taken at about 45 deg to the r–z plane across the cavity it was not possible to visualize the reverse flow boundary layer near the stator. When the rotational Reynolds number is increased to $Re_\theta = 4 \times 10^4$, the rotor side vortices are reduced in size, and in number, and break away from the center of the cavity. As Re_θ is increased further to 9×10^4, the latter effect increases with the rotor vortices diminishing as the rotor boundary layer entrains all the disk coolant supplied. For $C_{wd} = 91$ and over the range $0 < Re_\theta < 6 \times 10^4$, Fig. 2(*a*) shows that, although behavior similar to that before was obtained, the rotor instabilities are reduced with all the coolant flow being entrained into the rotor boundary layer at a lower rotational speed than that for $C_{wd} = 182$. For disk coolant flows above $C_{wd} = 300$ and rotational Reynolds numbers above $Re_\theta = 10^5$ it was more difficult to visualize the flow patterns, and no useful information could be obtained.

Figure 2(*b*) shows the effect of introducing the preswirl coolant flow C_{wp} on the behavior of the flow in the cavity. The investigation was conducted for one set of values of $C_{wp} = 2000$ and $C_{wd} = 182$ and two rotational Reynolds numbers, $Re_\theta = 4 \times 10^4$ and 9×10^4. In general, it is clear that the disk coolant flow has interacted with the incoming preswirl flow to divide the cavity into two zones separated by a "mixing" region starting at around $r/r_o = 0.57$. The structure of the flow below this region is similar to the classical flow structure in a simple shrouded rotor–stator cavity. Unfortunately it was not possible to visualize the zone above the mixing region

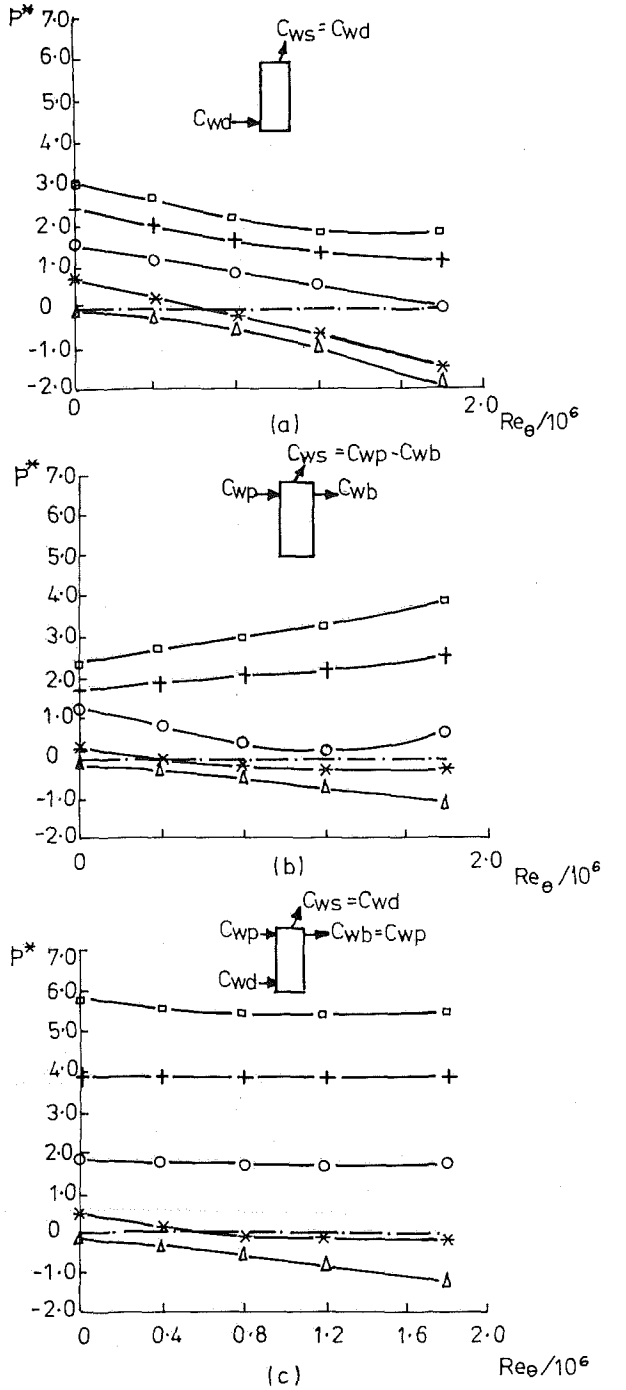

Fig. 4 The effect of variation of C_{ws} on P^* at r/r_o = 0.93 with $Re_\theta \cdot C_{wb} = 4050$ for (*b*) and (*c*):

Symbol	△	*	○	+	□
$C_{ws}/10^4$	0	0.2	0.4	0.6	0.8

where the preswirl flow may be crossing the cavity and impinging on the rotor surface.

4 Pressure Measurements

4.1 Radial Pressure Distribution. While all the pressure distribution measurements presented below were obtained from the test row, the pressure measurements on all three sets of radial pressure taps showed that the flow was axisymmetric to within 1 percent. For a simple rotor–stator system with centrally admitted coolant and no blade flow (i.e., all coolant leaves via the seals) the pressure distributions are shown in Fig. 3(*a*) for several values of rotational Reynolds number and disk coolant flow rates. These pressure distributions are similar to those of Phadke and Owen [5, 7]. With no coolant flow ($C_{ws} = C_{wd} = 0$), the pumping action of the disk produces a radial pressure gradient which increases with rotational speed as expected. Introducing coolant without swirl at the center of the disk reduces the rotational speed of the fluid in the core thus damping out the radial pressure gradient. Increasing coolant flow C_{wd} progressively dominates the pumping effect and ultimately eliminates the radial gradient. For coolant flows greater than $C_{ws} = 4060$ (which will be shown in section 6 to be sufficient to seal the cavity against ingress at even the highest rotational speed) the pressure in the cavity is above ambient at all points for all speeds.

Figure 3(*b*) shows the effect of supplying coolant through the preswirl nozzles only. The results for zero seal flow ($C_{ws} = 0$) are identical to the corresponding set in Fig. 3(*a*) except for the highest speed where there is evidence that the relatively low swirled flow needed to supply just the blade cooling flow has damped the core rotation slightly. Rather than reducing the core rotation, increasing the preswirl coolant flow introduced near the outer radius progressively increases the slope of the pressure distribution and, except for the outer tappings, maintains a negative pressure in the cavity at even the highest seal flows. Examining the results for the highest seal flow in detail, it is interesting to note that while increasing disk speed reduces the pressure in the center of the cavity, this is not so for the outer tappings. This effect is shown more clearly by replotting the results in Fig. 4, which is discussed below. All the data in Fig. 3(*b*) were recorded for the same blade flow, $C_{wb} = 4050$. Since almost identical results were seen for the inner radii with C_{wb} set at zero, they are omitted here to save space.

The result of setting the preswirl flow and the blade flow constant and equal to each other ($C_{wp} = C_{wb} = 4050$) is seen in Fig. 3(*c*). Once again increasing the central nonswirled flow progressively slows the core rotation and eliminates the radial pressure gradient producing results very similar to those in Fig. 3(*a*). The only evidence of the preswirl flow is seen in the slight extra damping noticed in Fig. 3(*c*) (the conditions for the first set of Fig. 3*c* are identical to the first set for Fig. 3*b*) and the slightly higher overall pressure levels at the higher seal flow rates. It should be be noted that setting the blade flow rate to be equal in magnitude to the preswirl flow does not imply that only preswirled flow enters the blades, desirable though that would be. This aspect is discussed further in section 5.

4.2 Variation of Pressure Under the Rim Seal. Figures 4(*a*), (*b*), and (*c*) focus attention on the pressures measured on the stator just underneath the rim seal at $r/r_o = 0.93$. This is an area of particular importance since the pressure criterion for ingress is quite simply that ingress may be assumed to occur if the static pressure at this point falls below ambient, i.e, if $p^* < 0$. In Fig. 4(*a*), the blade flow was zero and coolant was supplied only at the center. With $C_{ws} = C_{wd} = 0$, the pressure at $r/r_o = 0.93$ falls almost linearly with rotational speed. At high seal flow rates ($C_{ws} = 4000$ is sufficient to seal the cavity even at the highest rotational speed), the damping effect of introducing the nonswirled coolant at the center of the cavity is apparent even at the rim. The pressures at $r/r_o = 0.93$ depend much more on the flow through the seal than on the rotational speed. Supplying seal flow, but no blade flow, using only the preswirl nozzles produced almost identical results (not shown) at the rim tapping. This is anyway a rather academic arrangement since the whole purpose of the preswirl nozzles is to supply the blades.

Comparing Fig. 4(*c*) with 4(*a*) shows the effect of superimposing both preswirl flow and blade flow on the system. Apart from the lowest curve, obtained with no disk flow, the pressures show almost no dependence on rotational speed. The most interesting aspect of Fig. 4(*b*) is that it does show the

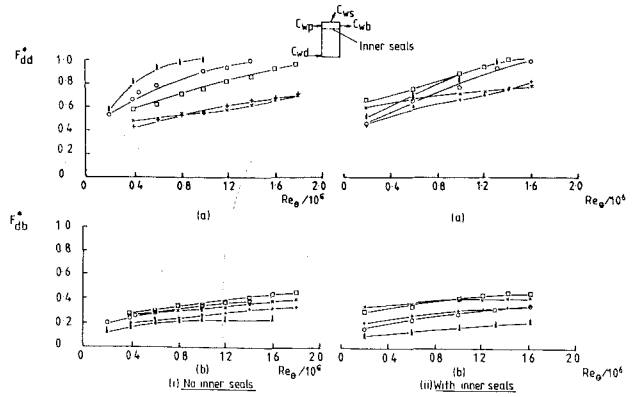

Fig. 5 (a) Fraction of C_{wd}, disk coolant flow, taken into blade feed holes; (b) fraction of blade flow C_{wb}, composed of disk coolant flow C_{wd}:

Symbol	△	○	□	+	×
$C_{wp}/10^4$	1.2	1.2	1.2	1.8	1.8
$C_{wb}/10^4$	0.52	0.64	0.78	0.76	0.94
$C_{wd}/10^4$	0.12	0.24	0.36	0.36	0.54

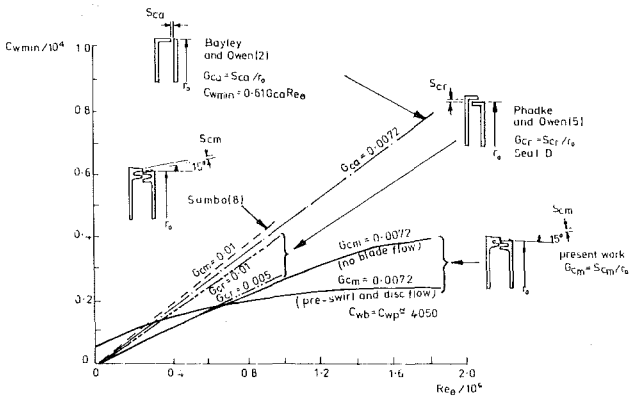

Fig. 6 Minimum sealing flow relationships of various workers for various seal configurations

pressure inversion effect, i.e., pressure increases rather than decreases with Reynolds number for high flow rates through the seals.

5 Gas Concentration and Flow Distributions

If a preswirl cooling system is used to supply the blades of a real engine, in combination with a centrally supplied disk cooling flow, it is inevitable (though unfortunate) that the flow entering the blade holes will be "contaminated" by the disk flow which will be hotter than the preswirl flow. Seeding the preswirl flow with nitrous oxide, N_2O, and monitoring concentrations in both preswirl and blade flows allows this contamination to be assessed.

Figures 5(*a*) and 5(*b*) show in two different ways the extent of the mixing of the disk coolant flow C_{wd}, with the preswirl flow C_{wp}, both with and without the inner seals (Fig. 1*b*) fitted. Figures 5(*a*) show the fraction of disk coolant flow C_{wd} taken into the blade feed holes at different rotational Reynolds numbers for various combinations of preswirl flow C_{wp}, and blade flow C_{wb}. Figure 5(*ia*) shows that all the disk flow of $C_{wd} = 1200$ ($=0.1 \times C_{wp}$) is drawn into the blade feed holes when the Reynolds number reaches 10^6 and that even when C_{wd} is increased to 3600 ($= 0.3 \times C_{wp}$) and C_{wb} increased by 50 percent, over 90 percent of C_{wd} is still taken in at a Reynolds number of 1.8×10^6. At most Reynolds numbers increasing the preswirl flow C_{wp} above 12,000 had a marked effect in reducing the proportion of disk coolant in the blade flow.

It is clear that with this particular experimental arrangement considerable contamination of the preswirl flow occurs and that the blade coolant holes draw the disk coolant flow in preference to the preswirl flow. Except for low flows and low speeds, Figs. 5(*iia*) and (*b*) show that the particular forms of inner seals used do little to reduce the proportion of disk flow in the blade flow and even aggravate the situation.

For the simple rotor–stator system used with no inner seals, the results shown in Fig. 5 can be predicted using the theory of Owen [10]. This momentum integral theory calculates the "rotor flow" C_{wo}, say, which comprises the disk coolant C_{wd}, and a flow entrained from the rotating core C_{we}. It is assumed that all the rotor flow is taken into the blade holes when the blade flow C_{wb} is equal to the calculated rotor flow C_{wo}. For example, in Fig. 5(*ia*) for $C_{wd} = 1200$ at $\mathrm{Re}_\theta = 10^6$ the predicted C_{wo} is 4500 and it can be seen that all the disk flow is eventually taken into the blade feed holes at about $C_{wb} = 5200$. For $C_{wd} = 2400$ at $\mathrm{Re}_\theta = 1.6 \times 10^6$ the corresponding values are $C_{wo} = 6500$ and $C_{wb} = 6400$.

To measure the minimum mass flow rate C_{wmin} necessary to prevent ingress with both C_{wp} and C_{wd} present, nitrous oxide was injected around the periphery of the cavity and C_{wmin} was taken as the value of the seal flow C_{ws} required to ensure that no N_2O was present in the blade flow, i.e., no gas ingestion.

With the preswirl flow system used alone however, N_2O was injected into the preswirl coolant upstream of the cavity, and when the concentration level of N_2O in the blade flow was equal to that in the preswirl flow, C_{wmin} was taken to be equal to the seal flow C_{ws}.

6 Minimum Sealing Flow Requirements C_{wmin}

This section shows that the relative proportions of the three controllable flows – C_{wd}, C_{wp}, and C_{wb} – have a considerable effect on C_{wmin}, the minimum seal flow required to prevent ingress. Figure 6 compares the different relationships for C_{wmin} obtained by other workers for a selection of seals and seal clearance ratios. The present results show a nonlinear relationship between C_{wmin} and Re_θ, especially with the preswirl flow, which indicates perhaps the role of the pressure inversion effect.

Although not always used together, in general agreement to within 15 percent was obtained between four different methods of detecting ingress: pressure difference across the rim seal, concentration sampling, flow visualization, and cavity temperature measurements. For flow configurations where either the disk coolant flow C_{wd}, or the preswirl coolant flow C_{wp}, was supplied with no blade coolant flow present, the estimates of C_{wmin} were determined using the pressure difference criterion, the flow visualization technique, or both. However, for flow configurations which included blade coolant flow, values of C_{wmin} were obtained using the pressure difference criterion, the gas concentration technique, or temperature measurement method, or all three. In using the temperature measurement method with no disk flow (C_{wd}) present, three hot air blowers, each of 1.6 kW, were mounted around the periphery of the cavity, and the temperatures of the air flow just under the stator rim seal and in the blade feed holes were recorded with the blowers on and off. By setting the disk rotation and C_{wb} flow to fixed values, C_{wmin} was taken to be equal to the seal flow C_{ws}, when the temperatures recorded became insensitive to changes in the surrounding air temperature. A detailed theoretical and experimental investigation of the effect of superimposed flows, C_{wp} and C_{wd}, on the temperature of blade coolant flow was carried out for various geometries and flow configurations and these results will be reported later.

In Fig. 7 it is shown that if there is no blade flow an almost identical relationship between C_{wmin} and Re_θ is obtained irrespective of where the coolant is admitted into the cavity.

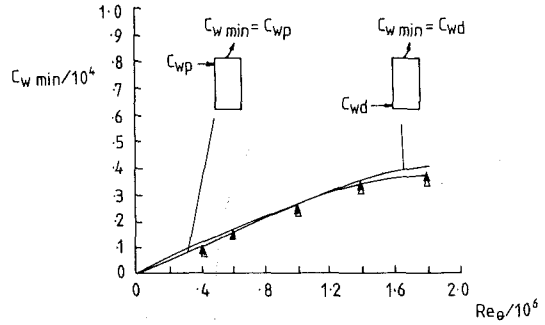

Fig. 7 Variation of C_{wmin} with Re_θ with no blade flow present: ___ from pressure difference criterion at $r/r_o = 0.93$; △ from flow visualization with C_{wp} present only; ▲ from flow visualization with C_{wd} present only

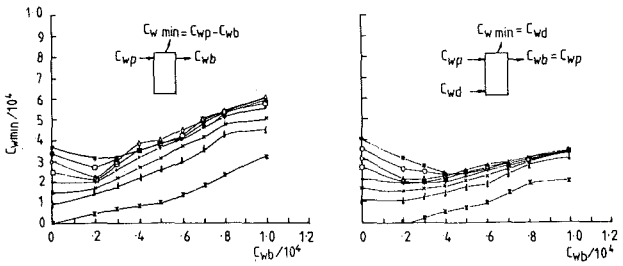

Fig. 8 Variation of C_{wmin} with C_{wb} and Re_θ using the pressure difference criterion at $r/r_o = 0.93$:

Symbol	⧖	△	×	+	□	◇	○	*
$Re_\theta/10^6$	0	0.4	0.6	0.8	1.0	1.2	1.4	1.8

This confirms the statement made in section 4 with respect to pressures measured at $r/r_o = 0.93$ with zero blade flow.

Both sets of curves in Fig. 8 show that increasing blade flow from zero to a small value reduces the minimum seal flow at high Reynolds numbers. Further increasing C_{wb} increases C_{wmin} however, although the effect is less pronounced when disk and preswirl flows are used simultaneously. In both cases C_{wb} is provided by preswirl flow so this result fits with the observations in section 4. For midrange values of C_{wb}, C_{wmin} actually falls with Re_θ as Re_θ is increased beyond 1.2×10^6, presumably due to the pressure inversion effect. This effect continues for the highest C_{wb} when coolant is supplied solely by preswirl, but for the combined arrangement C_{wmin} is independent of Re_θ for high blade flow rates. Minimum seal flow is significantly lower for the combined supply than for the preswirl-only configuration for all but the very lowest blade flows.

The minimum sealing flow requirement for the inner cavity when inner seals were fitted is shown in Figs. 9(*a*) and (*b*), using the pressure difference criterion across the stator inner seal. The inner seal, illustrated in Fig. 1, is similar to seal D of Phadke and Owen [5] and can be viewed as a rim seal with the preswirl nozzles providing a high-speed swirling flow much as the turbine nozzle guide vanes do for the conventional rim seal. Figure 9(*a*) shows that the rotational speed Re_θ continues to affect the minimum sealing flow required to prevent preswirl inflow into the inner cavity up to the highest value of $Re_\theta = 1.8 \times 10^6$. (This value of rotational Reynolds number is based on the radius of the complete disk; however, the equivalent value based on the radius of the inner cavity would be 1.36×10^6.) This is shown in a different way in Fig. 9(*b*) where increasing Re_w represents increasing swirl velocity above the seal. This result, for a very symmetric preswirl flow, confirms in many respects the supposition of Phadke and Owen [7] that the differences between turbine tests and model rig tests in a quiescent environment are due to differences in circumferential pressure asymmetry. A result very similar to

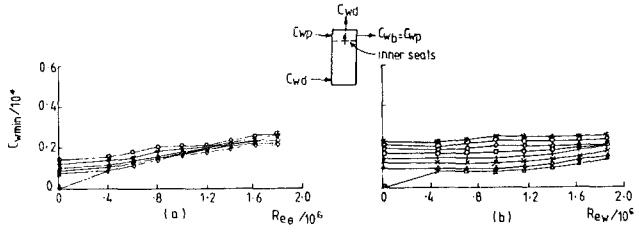

Fig. 9(*a*)

Symbol	◇	×	□	+	△	*	○
$C_{wb}/10^4$	0	0.4	0.8	1.0	1.2	1.4	1.6
Equivalent $Re_w/10^6$	0	0.46	0.93	1.16	1.4	1.62	1.85

Fig. 9(*b*)

Symbol	⧖	△	×	+	□	◇	○	*
$Re_\theta/10^6$	0	0.4	0.6	0.8	1.0	1.2	1.4	1.8

Fig. 1 Variation of C_{wmin} (required to seal the inner cavity from the outer one) with Re_θ and Re_w

Fig. 9(*b*) has been obtained by Dadkhah and Turner [9], for a "near-axisymmetric" external flow over a simple axial seal, with increased rotational speed continuing to increase the sealing flow requirement at high external flow speeds.

7 Conclusions

This paper has described a series of experiments on the sealing performance of a rotor–stator system with a 15 deg double mitered rim seal, with and without an inner radial seal, using various combinations of preswirled coolant flow and centrally admitted disk coolant flow to supply the seals and blade holes. The tests, conducted in the absence of an external gas flow, have determined radial pressure distributions, internal flow distributions, and the minimum dimensionless coolant flow rate C_{wmin} necessary to prevent the ingress of external "mainstream gas." One seal clearance ratio, $G_{cm} = 0.0072$, was used at rotational Reynolds numbers up to 1.8×10^6.

It was found that the use of preswirl coolant alone did not affect the classical parabolic radial pressure distribution below the preswirl nozzles in contrast to the effect of centrally admitted disk coolant. However, with both preswirl coolant and central disk coolant used together, the pressure distribution was very similar to that with disk coolant alone with a pressure level constant with radius being eventually produced. When coolant flow was supplied solely via the preswirl nozzles, a pressure inversion effect was observed at the higher rotational speeds with the pressure under the rim seal increasing rather than decreasing with increasing speed. Some flow visualization photographs have been presented for essentially laminar flow. The action of the preswirl coolant was effectively to divide the flow field into two zones separated by a "mixing" region.

Flow distribution results, obtained by a gas concentration technique, showed that the disk coolant flow is entirely drawn into the blade feed holes for moderate disk coolant flow rates but at the higher flow rates only about 70 percent is entrained. The radial type of inner seal used is shown to make matters worse with respect to this "contamination" of the blade coolant to high disk flow rates.

The minimum sealing flow results show that with no blade flow the minimum dimensionless sealing requirement C_{wmin} is independent of where the coolant is admitted into the cavity. When flow was taken off to feed the blade holes the effect was to increase C_{wmin} but this effect was reduced when preswirl and disk coolant were employed together. The pressure inversion effect at the higher rotational Reynolds numbers is shown to produce a nonlinear relationship between C_{wmin} and Re_θ

with much less coolant being required. With the inner seals fitted the sealing flow results for the inner cavity alone showed that C_{wmin} remained dependent on Re_θ throughout the entire range tested. This suggested that model turbine tests, which find that C_{wmin} is independent of Re_θ, may have some degree of asymmetry in the external flow over the rim seal and that this asymmetry dominates the sealing requirements.

It is intended to extend the present investigation and test experimental arrangements designed to separate the disk coolant flow C_{wd}, which feeds the rim seals, from the preswirl flow, which feeds the blades. There is also a need to extend the range of Reynolds numbers, particularly for the minimum sealing flow relations, to provide greater confidence in the extrapolation of data.

Acknowledgments

The authors are grateful to Dr. J. R. Pincombe for his assistance in obtaining the flow visualization results, and Dr. J. M. Owen for his valuable advice and interest throughout the course of the work. They should like to thank SERC, Rolls-Royce plc, U.K., and GEC-Ruston Gas Turbines plc, U.K., for supporting the work described in this paper.

References

1 Meierhofer, B., and Franklin, C. J., "An Investigation of a Pre-swirled Cooling Airflow to a Turbine Disc by Measuring the Air Temperature in the Rotating Channels," ASME Gas Turbine Conf., Paper No. 81-GT-132, 1981.

2 Bayley, F. J., and Owen, J. M., "The Fluid Dynamics of a Shrouded Disc System With a Radial Outflow of Coolant," ASME *Journal of Engineering Power*, Vol. 92, 1970, p. 335.

3 Owen, J. M., and Phadke, U. P., "An Investigation of Ingress for a Simple Shrouded Rotating Disk System With a Radial Outflow of Coolant," ASME Paper No. 80-GT-49, 1980.

4 Abe, T., Kikuchi, J., and Takeuchi, H., "An Investigation of Turbine Disc Cooling (Experimental Investigation and Observation of Hot Gas Flow Into a Wheelspace)," 13th CIMAC Conf., Vienna, 1979, Paper No. GT-30.

5 Phadke, U. P., and Owen, J. M., "An Investigation of Ingress for an 'Air-Cooled' Shrouded Rotating Disc System With Radial-Clearance Seals," ASME *Journal of Engineering Power*, Vol. 105, 1983, p. 178.

6 Kobayashi, N., Matsumato, M., and Shizuya, M., "An Experimental Investigation of a Gas Turbine Disk Cooling System," ASME *Journal of Engineering for Gas Turbines and Power*, Vol. 106, 1984, pp. 136–141.

7 Phadke, U. P., and Owen, J. M., "The Effect of Geometry on the Performance of 'Air-Cooled' Rotor–Stator Seals," Int. Council on Combustion Engines (CIMAC) 15th Congress, Paris, France, 1983.

8 Sambo, A. S., "A Theoretical and Experimental Study of the Flow Between a Rotating and a Stationary Disc," D. Phil. Thesis, University of Sussex, United Kingdom, 1983.

9 Dadkhah, S., and Turner, A. B., "Rotor–Stator Cavity With External Flow: Pressure and Temperature Measurements With Ingress," University of Sussex, Report No. 86/TFMRC/TN7, 1986.

10 Owen, J. M., "An Approximate Solution for the Flow Between a Rotating and a Stationary Disc," University of Sussex, Report No. 86/TFMRC/86, Aug. 1986.

Experimental Simulation of Turbine Airfoil Leading Edge Film Cooling

A. R. Wadia[1]

D. A. Nealy

Allison Gas Turbine Division,
General Motors Corporation,
Indianapolis, IN 45215

Leading edge showerhead cooling designs represent an important feature of certain classes of high-temperature turbine airfoils. This paper outlines a methodology for predicting the surface temperatures of showerhead designs with spanwise injection through an array of discrete holes. The paper describes a series of experiments and analyses on scaled cylinder models with injection through holes inclined at 20, 30, 45, and 90 deg for typical radial and circumferential spacing-to-diameter ratios of 10 and 4, respectively. The experiments were conducted in a wind tunnel on several stainless steel test specimens in which flow and heat transfer parameters were measured over the simulated airfoil leading edge surfaces. Based on the experiments, an engineering design model is proposed that treats the gas-to-surface heat transfer coefficient with film cooling in a manner suggested by a recent Purdue–NASA investigation and includes the important contribution of upstream (coolant inlet face) heat transfer. The experiments suggest that the averaged film cooling effectiveness in the showerhead region is primarily influenced by the inclination of the injection holes. The effectiveness parameter is not strongly affected by variations in coolant-to-gas stream pressure ratio, free-stream Mach number, gas-to-coolant temperature ratio, and gas stream Reynolds number. The model is employed to determine (inferentially) the average Stanton number reduction parameter for a series of pressure ratios varying from 1.004 to 1.3, Mach numbers ranging from 0.1 to 0.2, temperature ratios between 1.6 and 2.0, and Reynolds numbers ranging from 3.5×10^4 to 9.0×10^4.

Introduction

The continuing trend toward higher turbine inlet temperatures in gas turbine engines has historically demanded increasingly effective turbine airfoil cooling approaches in order to realize more fully the performance gains accruing from higher temperature operation. At the operational temperature levels characterizing most state-of-the-art (and next generation) gas turbines, surface film cooling, in combination with one or more variants of internal forced convection cooling, represents one of the more practical and effective approaches to this problem. A typical impingement/convection/film-cooled airfoil is shown in Fig. 1, which illustrates the large number of cooling system design variables which ultimately must be characterized and organized into some rational design procedure.

The focus of the present paper is restricted to design procedures applicable to the airfoil leading edge region, which is typically characterized by a closely spaced array of angled "showerhead" film cooling holes, as shown in Fig. 1. While this highly effective approach to leading edge cooling has found wide acceptance in practice, surprisingly little basic design information regarding "showerhead" film cooling arrays seems to have been published. Most of the representative archival literature on the subject of film cooling relates to single slot injection (Goldstein, 1971; Stollery, 1965), isolated rows of inclined film holes (Pedersen, 1972; Ericksen, 1971; Liess, 1973; Kadotani and Goldstein, 1979; Sasaki et al., 1978) or discrete (isolated) film holes (Ericksen et al., 1971; LeGrives, 1977; Ramette, 1983) interacting with a developed

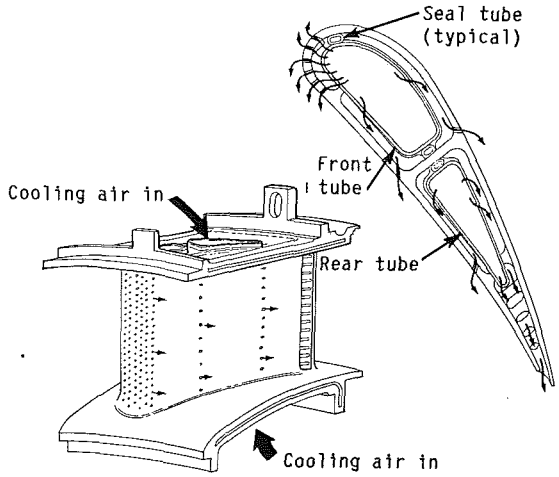

Fig. 1 Typical impingement/convection/film-cooled airfoil

[1]Present address: General Electric Company, Commercial Fan and Compressor Aero Design, Evendale, OH 45215.

Contributed by the Gas Turbine Division of THE AMERICAN SOCIETY OF MECHANICAL ENGINEERS and presented at the 30th International Gas Turbine Conference and Exhibit, Houston, Texas, March 18–21, 1985. Manuscript received at ASME Headquarters May 26, 1987. Paper No. 85-GT-120.

flat plate turbulent boundary layer at zero or moderate mainstream pressure gradient. The limited multihole array data (Mayle, 1974; Choe, 1976; Crawford, 1980) are similarly restricted to the equilibrium turbulent flat plate situation, which differs rather fundamentally from the strongly accelerated, nominally laminar, thin boundary layer developing around the cylinder-like airfoil leading edge. Some limited insight regarding the airfoil leading edge film cooling problem is provided by the work of Sasaki et al. (1976) and Luckey and L'Ecuyer (1981), where heat transfer measurements were made downstream and within arrays of film holes in scaled cylindrical model simulations of the airfoil leading edge. While the experiments of Sasaki et al. (1976) included multiple combinations of film hole pitch-to-diameter ratio and injection angle, the experimental results were largely confined to recovery temperature data *downstream* of the film hole array. The work of Luckey and L'Ecuyer (1981) included the more interesting measurements of surface heat transfer *within* the film hole (showerhead) array, but was restricted to a single geometry. Neither investigation included consideration of the important contribution of active cooling within the hole array.

Recognizing the need for a rational, cost-effective engineering approach to the showerhead film cooling design problem, a program was initiated to (1) extend the limited cylindrical surface "showerhead" data base to include the important components of *active* heat transfer within the showerhead array and (2) to develop a first-order engineering design model which could provide a realistic mechanism for extrapolating limited cylindrical specimen heat transfer (rig) data to airfoil leading edge configurations of practical interest. The purpose of the present paper is to highlight the key experimental and analytical aspects of that program. To place the work in somewhat better perspective for the reader, it might be noted that the analytical modeling approach considered here was a conscious attempt to provide direct, array-averaged prediction of leading edge "showerhead" cooling effectiveness—including active heat transfer within and upstream of the film hole array. The influence of "showerhead" surface injection on external (gas-to-wall) heat transfer was (inferentially) derived from the cylindrical specimen heat transfer rig data using the design model, which was first correlated with the limited experimental results of Luckey and L'Ecuyer (1981). As such, the approach was intentionally structured as a simplified engineering design tool, but one which would provide a means of accomplishing thermal/structural design tradeoffs of sufficient (first-order) validity at least to reduce the number of costly high-temperature rig or engine tests required to qualify a design.

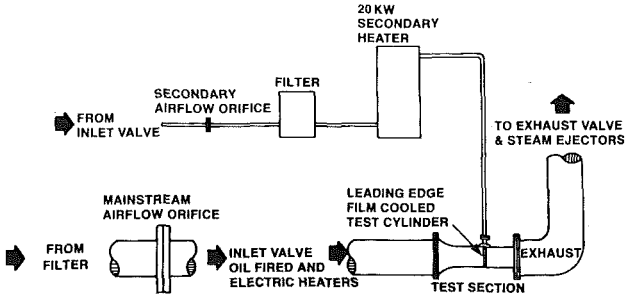

Fig. 2 Schematic of cylinder model installed in the test section

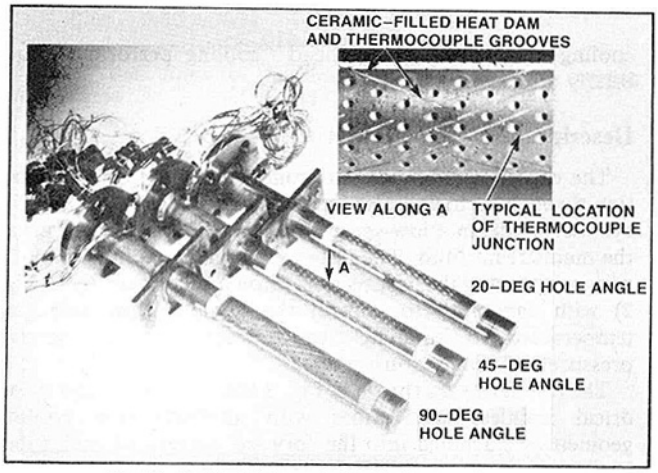

Fig. 3 Typical film-cooled cylinder specimens

In the following sections, the experimental heat transfer tunnel test facilities are briefly described and the cylindrical model test results are summarized. Next, the basis for the engineering design model is described. Finally, implications of the present results regarding the relative importance of active

Nomenclature

d = coolant hole diameter
D = leading edge cylinder diameter
G_c = coolant airflow rate per unit surface area $= W_c/A_s$
h_c = mean coolant film coefficient within the holes with entrance correction
h_{FC} = external heat transfer coefficient with film cooling
h_{NFC} = external heat transfer coefficient without film cooling
h_{cu} = upstream coolant inlet cylindrical surface film coefficient
h_C = mean internal film hole coefficient
k = thermal conductivity of gas
k_c = coolant thermal conductivity
ℓ = length of coolant holes $= t/\sin\alpha$
M = blowing ratio $= \rho_c V_c/\rho_g V_g$
P_c = coolant pressure (total)
P_g = gas pressure (total)
Pr = Prandtl number based on freestream conditions
Pr_c = Prandtl number of coolant
Re_d = hole Reynolds number based on coolant conditions
Re_D^* = freestream Reynolds number based on mean conditions
SNR = Stanton number reduction parameter $= 1 - h_{FC}/h_{NFC}$
t = wall thickness
T_c = average coolant temperature
T_g = gas temperature
T_w, T_1 = hot-side wall temperature
T_2 = cold-side wall temperature
T_{cu} = coolant inlet temperature (reservoir)
T_{c1} = coolant temperature at hole exit
T_{c2} = coolant temperature at hole inlet
V_c = coolant injection velocity
V_g = free-stream velocity
W_c = coolant flow rate
α = coolant injection angle (plunge angle)
η = thermal effectiveness $= (T_g - T_1)(T_g - T_{cu})$
θ = angular extent of film cooling array
ρ_c = density of coolant
ρ_g = free-strean density

Table 1 Film cooling geometries and range of test variables

Outside leading edge radius	= 1.56464 cm
Inside leading edge radius	= 1.12014 cm
Hole diameter	= 0.13335 cm
Radial spacing	= 1.3335 cm
Circumferential spacing	= 0.5334 cm
Injection angle	= 20, 30, 45, and 90 deg
Number of holes per row	= 10
Total number of holes	= 90
Gas stream inlet Mach number	= 0.089 to 0.210
Leading edge Reynolds number	= 35,000 to 90,000
Coolant-to-gas stream pressure ratio	= 1.005 to 1.30
Gas-to-coolant temperature ratio	= 1.726 to 2.763
Wind tunnel turbulence level	= less than 1 percent

cooling on overall "showerhead" cooling performance are briefly discussed.

Description of Experiment

The experimental study was conducted with coolant injection through inclined holes located near the leading edge of a cylinder model in a low-speed wind tunnel using heated air as the mainstream fluid. The tests were conducted in a specially designed rectangular test section (shown schematically in Fig. 2) with capability to control the coolant flow rate and temperature to simulate realistic coolant-to-gas stream pressure and temperature ratios.

The test hardware shown in Fig. 3 consisted of hollow cylindrical stainless steel tubes with alternate film cooling geometries machined into the forward portion of each tube. The four tubes tested to date differ only in the film cooling hole angle. The staggered array of film cooling holes was oriented in the spanwise direction at angles of 20, 30, 45, and 90 deg measured from the surface of the tubes. The film cooling geometries tested are summarized in Table 1. The geometries and operating conditions shown in Table 1 were tentatively selected as representative of scaled core turbine designs in the 1644 K–1922 K RIT regime.

Metal temperatures were measured by thermocouples (placed in filled grooves in the cylinder surface) aligned to provide independent radial and circumferential measurements. To minimize circumferential and radial conduction effects from the non-film-cooled portions of the tube, approximately 75 percent of the cylinder wall thickness at the periphery of the hole matrix was machined and filled with a ceramic filler of extremely high thermal resistance, effectively forming a "heat barrier" (Fig. 3). In addition, the metal temperature thermocouples were concentrated near the radial center of the film cooling hole array in an attempt to further minimize the influence of radial conduction. All metal temperatures were measured using 0.0508 cm sheathed, open tip C-A thermocouples. Inasmuch as the principal objective of the experimental program was to establish average showerhead array cooling effectiveness as a function of film hole array geometry and aerothermodynamic operating condition, the following measurements were made in addition to surface metal temperature:

- Upstream (undisturbed) gas stream total pressure, static pressure, and total temperature
- Mainstream mass flow rate
- Test cylinder surface circumferential static pressure distribution
- Coolant total pressure and temperature (in cylinder, upstream of film hole array)
- Coolant mass flow rate

The foregoing measurements were sufficiently complete to characterize local and average showerhead array cooling effectiveness as a function of both upstream and local (cylinder surface) Mach number/Reynolds number level, as well as coolant-to-mainstream pressure ratio and temperature ratio.

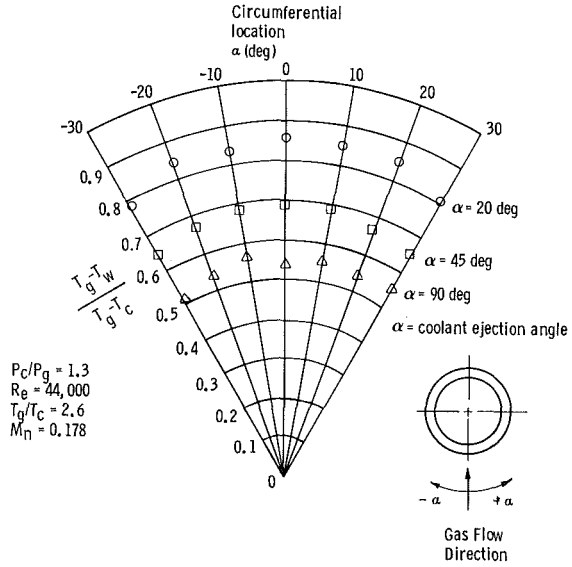

Fig. 4 Typical circumferential effectiveness distribution

The tubes were tested over the range of Mach numbers, Reynolds numbers, coolant-to-gas stream pressure ratios, and gas-to-coolant temperature ratios shown in Table 1. These ranges are representative of those encountered in first-stage vanes with the exception of the coolant-to-gas stream pressure ratio, which was varied over a much larger range than is normally available to more completely define the effect of the pressure ratio variable.

Experimental Results and Discussion

Typical effectiveness results for the centrally located thermocouples are shown in Fig. 4. An average of the cooling effectiveness over the circumferential and radial directions in the midsection of the film cooling hole array was made and the trends of the averaged effectiveness with the various operating parameters are presented in Figs. 5 and 6. Again, it should be emphasized that all "effectiveness" data discussed herein represent "cooled wall effectiveness" and thus reflect active cooling within the film hole array.

An increase in the pressure ratio across the holes increases the coolant flow through the holes and should produce an increase in cooling effectiveness provided the increase in injected fluid does not have the adverse effect of simultaneously increasing the external (gas-to-wall) heat transfer coefficient. As shown in Fig. 5, the effectiveness does indeed increase with pressure ratio over the range of pressure ratio and hole angles. However, the moderate increase in effectiveness at the higher blowing ratios implies that the increase in the coolant side heat transfer coefficient (due to increased coolant flow rate) may be at least partially offset by a simultaneous increase in the gas side film coefficient at higher blowing ratios. This is consistent with current observations of film liftoff and local separation in the vicinity of the injection site based on flat plate film cooling viscous analysis (Wadia, 1983) and experiments (Lander, 1972) at high blowing ratios.

The significant differences in cooling effectiveness level for the different hole inclinations shown in Fig. 5 suggest the importance of including active cooling and conduction effects within the holes in the development of a film cooling design model. Shallower angles may not only aid in restricting coolant "liftoff" (with improved downstream film coverage), but may also provide significantly increased hole length-to-diameter ratios with corresponding increases in *active* heat

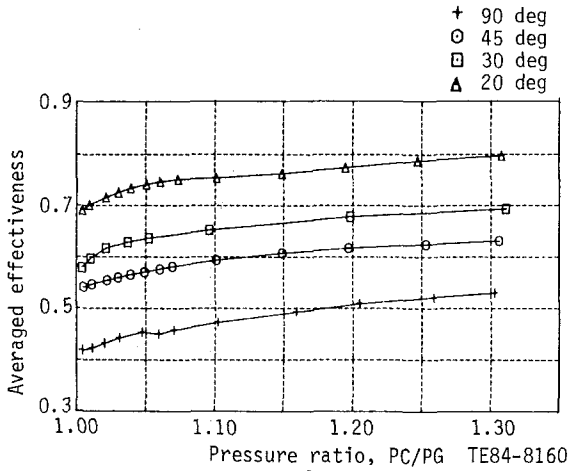

Fig. 5(*a*) The effect of coolant-to-gas stream pressure ratio on average cooling effectiveness

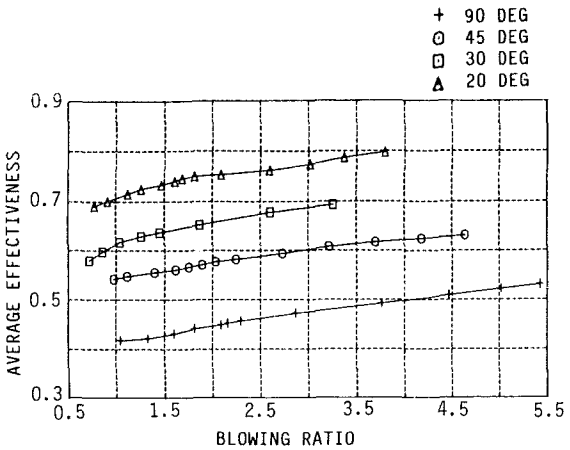

Fig. 5(*b*) The effect of blowing ratio on average cooling effectiveness

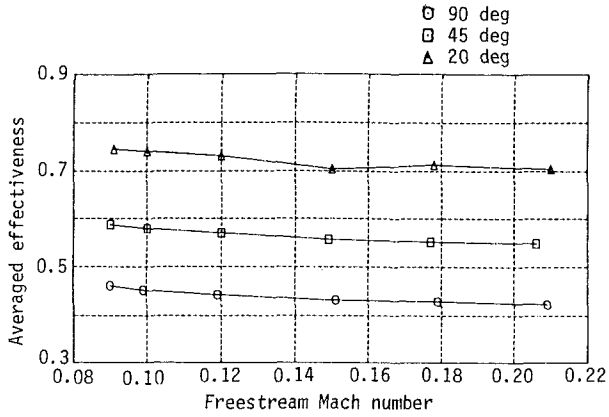

Fig. 6(*a*) The effect of freestream Mach number on cooling effectiveness

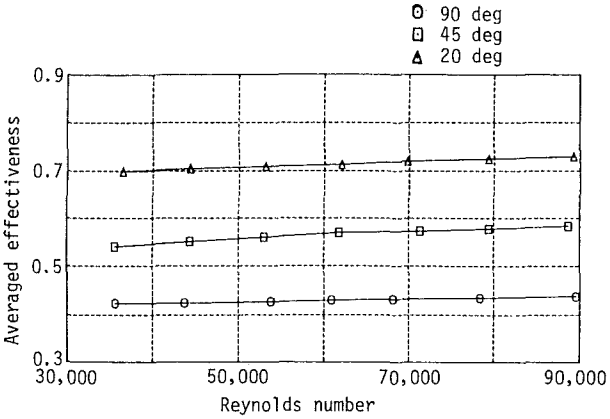

Fig. 6(*b*) The effect of leading edge Reynolds number on cooling effectiveness

transfer surface area within any array of given hole spacing and diameter.

Figure 6 shows the effects of free-stream Mach number and leading edge Reynolds number on cooling effectiveness for a typical coolant-to-gas stream pressure ratio of 1.02. The cooling effectiveness is observed to decrease slightly with increasing Mach number at a constant Reynolds number and pressure ratio. This trend essentially reflects the fact that the gas stream total pressure was reduced with increasing Mach number to maintain a constant value of mainstream mass velocity (and hence, Reynolds number). The coolant pressure was decreased simultaneously to maintain a constant pressure ratio, resulting in an effective decrease in the coolant-flow rate and a corresponding reduction in active cooling within the hole array. The external gas-to-wall heat transfer coefficient would not be expected to change significantly (constant Reynolds number) although the reduced coolant flow (blowing ratio) may have had a slightly favorable effect on this parameter (see following sections).

In contrast, the cooling effectiveness is observed to increase slightly with increasing Reynolds number, as illustrated in Fig. 6(*b*). An increase in leading edge Reynolds number at constant Mach number reflects an increase in both the gas side flow rate and pressure level. Operating at fixed coolant-to-gas stream pressure ratio would then produce an equal (percent) increase in *coolant side* pressure, flow, and Reynolds number. Under these operating conditions, the observed cooling effectiveness improvements (with increasing Reynolds number) could be reconciled by an elementary argument, which suggests that coolant side heat transfer coefficients would increase more rapidly with Reynolds number than would gas side heat transfer coefficients. In other words, at fixed system Mach number, pressure ratio, and temperature ratio, the characteristic Reynolds number (on either coolant or gas side) would simply be proportional to $P_g/\sqrt{T_g}$. Arguing that (to first order) the coolant side heat transfer coefficients increase with Reynolds number to the 4/5 power, while the "nominally laminar" gas side heat transfer coefficients exhibit an $(\mathrm{Re})^{1/2}$ power law dependence, the *ratio* of coolant-to-gas side heat transfer coefficients might be expected to vary as $h_c/h_g \sim (P_g/\sqrt{T_g})^{0.3}$. Thus, h_c/h_g, an intrinsic measure of *active* cooling effectiveness, might be expected to *increase* with pressure level (Reynolds number).

The systematic nature of the experimental trends observed herein suggested that it might be possible to construct a simplified analytical framework to (1) predict the important measured trends characterizing the specific experimental test hardware in this program, and (2) provide a mechanism for extension of these limited experimental results to alternate geometric configurations and generalized aerothermodynamic operating conditions of practical interest. To that end, the simplified engineering design model described in the following section was developed.

Synthesis of Internal/External Heat Transfer Trends

In developing a predictive model, an overriding consideration was to evolve an approach of first-order engineering utility, namely one which would simply, but realistically, accommodate the following key design and operational variables:

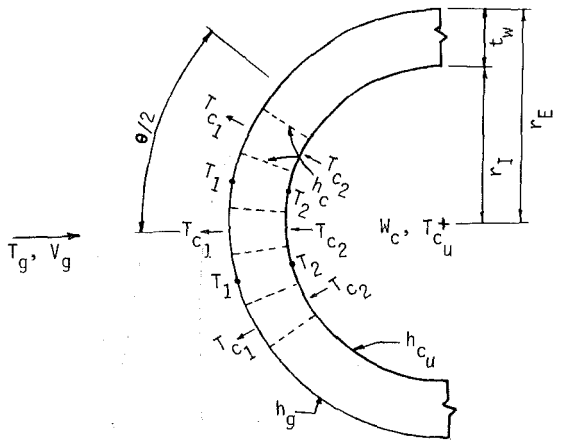

Fig. 7 Leading edge film cooling cylinder model

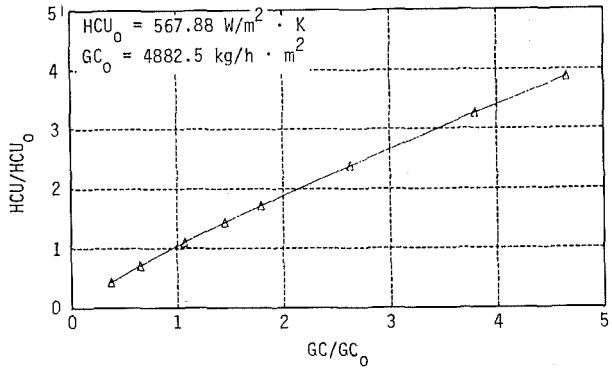

Fig. 8 Coolant-to-wall upstream heat transfer coefficients

- Film hole diameter, spacing (radial and circumferential), and plunge angle
- Leading edge radius and wall thickness
- Mainstream Mach number and Reynolds number level (upstream or locally)
- Coolant-to-mainstream pressure ratio (local or global average basis).
- Simply specified (or predicted) film cooling adjustments to independent predictions of nonblown gas-to-wall heat transfer coefficients.

The approach was specifically structured to predict the engineering parameter of most interest, namely overall, *nonadiabatic*, showerhead array cooling effectiveness. The thermal analysis model was, therefore, formulated in terms of four coupled, linear heat balance equations which describe the steady-state heat transfer process within the physical model shown in Fig. 7.

Before this system could be solved for the four unknown temperatures of interest (T_1, T_2, T_{c1}, T_{c2}), several key boundary conditions and thermal resistance parameters had to be specified or calculated. These included:

- the gas-to-wall heat transfer coefficient h_{FC} with film cooling
- the driving temperature T_g along the leading edge surface
- the wall-to-coolant heat transfer coefficient h_{cu} along the upstream surface of the film hole array
- the internal heat transfer coefficient h_c within the coolant hole array
- the cooling air supply temperature T_c

The critically important gas-to-wall heat transfer coefficient predictions for the cylinder models were based on the widely accepted correlation for a cylinder in cross-flow (laminar flow) without film cooling

$$h_{NFC} = 1.14\,(\mathrm{Re}_D^*)^{0.5}(\mathrm{Pr})^{1/3}[1-(\theta/90)^3]k/d \qquad (1)$$

modified for film cooling using the averaged Stanton number reduction parameter obtained in the Purdue–NASA experiments (Luckey and L'Ecuyer, 1981) as

$$h_{FC} = (1-\mathrm{SNR}_{av})h_{NFC} \qquad (2)$$

The array-averaged dry wall heat transfer coefficient h_{NFC} was evaluated at a value of θ corresponding to an average circumferential extent between the stagnation point and the last row of film cooling holes.

A mean internal film hole coefficient h_c was computed using the turbulent pipe flow correlation

$$h_{c_\infty} = 0.023\,k_c/d(\mathrm{Re}_d)^{0.8}(\mathrm{Pr})^{1/3} \qquad (3)$$

corrected for entrance effects such that

$$h_c = h_{c_\infty}[1+(d/\ell)^{0.7}] \qquad (4)$$

Specification of the upstream face heat transfer coefficient h_{cu} proved to be rather troublesome and deserves some discussion. Initially, this component of heat transfer was ignored in the development of the predictive model. However, it became readily apparent that, unless the coefficients established by equations (1)–(4) were in gross error, the experimental cooling performance trends represented by Figs. 5 and 6 could be (analytically) reconciled only by inclusion of a *significant* upstream or backface heat transfer component in the model. It remained to define systematically the backface heat transfer coefficient h_{cu}. Lacking any relevant archival data for heat transfer to coolant entering a "perforated" cylindrical wall, the coefficient h_{cu} was derived from earlier in-house heat transfer data on laminated porous walls (Nealy, 1968) whose upstream perforated surfaces were at least nominally representative of the hole spacings and diameters in the showerhead film hole arrays. Based on a representative "mean" trend for the earlier porous wall data, the upstream face film coefficient trend shown in Fig. 8 was established and employed in the model. It is perhaps worth noting that more recently, some attention has been given to the upstream (inlet face) heat transfer problem (Sparrow, 1982; Andrews, 1984). The results reported by these investigators confirm the significance of the upstream face heat transfer component, but suggest heat transfer trends of somewhat lower level and slope than the results shown in Fig. 8. While the trend given by Fig. 8 produces acceptable prediction of our showerhead cooling effectiveness results, it is recognized that more research work is clearly warranted to characterize heat transfer to the inlet side of perforated plates (and cylinders) better.

Having established the key heat transfer coefficient parameters via equations (1)–(4) and Fig. 8, the heat balance equations are then readily solved to yield the metal and fluid (coolant) temperatures of interest.

The analytical model is largely based on experimentally derived correlations, the most critical boundary conditions being those that describe the external (equation (2)) and upstream (Fig. 8) heat transfer coefficients. For the purpose of initial verification of the analytical method described above, it was decided to base equation (2) on the laterally and radially averaged Stanton number reduction data for multiple row injection from the Purdue investigation (Table A-13 of Luckey and L'Ecuyer, 1981). With the (SNR) average parameter established as indicated, the model was then used to analyze (predict) the present 30-deg film-cooled cylinder effectiveness trends and was found to predict slightly higher effectiveness than measured levels. This may in fact be reasonable inasmuch as the Stanton number reduction parameter was derived from the *25-deg* Purdue cylinder experiment, which might be expected to produce somewhat more favorable external film

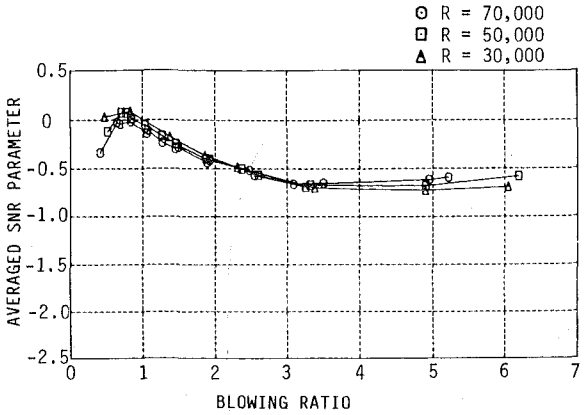

Fig. 9 Averaged Stanton number reduction for the 30-deg array

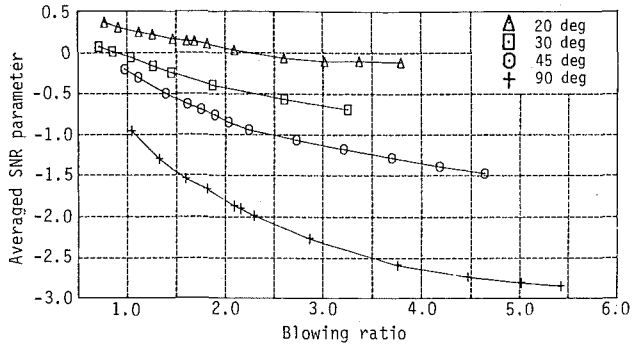

Fig. 10 Inferred Stanton number reduction from leading edge showerhead experiments

coverage than injection from 30 deg holes. A more detailed description of the analytical model and its validation is provided in an earlier publication by the authors (Wadia and Nealy, 1985).

Having established a reasonably validated "baseline" for the 30 deg cylinder data, the model was then exercised in a manner to extract "apparent" external heat transfer trends from the present cylinder effectiveness data at hole angles and/or aerothermodynamic operating conditions other than those reported by Luckey and L'Ecuyer (1981). More specifically, the SNR_{av} parameter in equation (2) was adjusted until the measured effectiveness trends shown in Fig. 5 were essentially matched by the model predictions. No other adjustments to the boundary condition parameters in equations (1)–(4) or Fig. 8 were made.

Figure 9 shows typical "derived" Stanton number reduction trends for the 30-deg tube at three different Reynolds numbers. The results were found to collapse to essentially one curve when the external film coefficient effects were examined versus blowing ratio. The trends in the 30-deg data show remarkable similarity to multiple row injection flat plate heat flux data where the Stanton number reduction peaks at blowing ratios in the vicinity of 0.9. Similar trends were observed in the leading edge heat flux data of Luckey and L'Ecuyer (1981).

The derived distribution of the Stanton number reduction with blowing ratio for the full series of showerhead arrays is illustrated in Fig. 10. In all cases the external film coefficient with blowing was enhanced (increased) at blowing ratios greater than 2. For the normal injection ($\alpha = 90$ deg) case, the heat transfer coefficient with film cooling appears to be significantly higher than the dry wall heat transfer coefficient, probably due to strong recirculation within the surface boundary layer immediately downstream of the injection sites, with consequent increases in near-wall turbulence production.

While the data of Luckey and L'Ecuyer (1981) have been represented in significantly more detail for a 25-deg circular cylinder model, the additional averaged heat flux data for the 20, 30, 45, and 90-deg tubes presented in this paper will, it is hoped, aid the designer with an expanded basic heat transfer data base for the design of leading edge showerhead configurations. The average Stanton number reduction results, shown in Fig. 10, are, of course, strictly valid for the hole array spacing-to-diameter ratios of our specific cylinder configurations, and reflect the assumption that the upstream heat transfer coefficients (Fig. 8) are invariant with hole angle. Thus, extrapolation of these trends to other spacing-to-diameter ratios and hole angles should be made with caution. The results themselves, however, are quite interesting and clearly demonstrate the strong adverse effect of higher blowing rates on external heat transfer, especially at more nearly normal injection angles. These results at least appear to reinforce the often expressed view that the real merit of showerhead cooling lies in the active cooling within the array and not in the external "film protection" afforded by the injected coolant.

Summary

Results of an experimental investigation of heat transfer to four leading edge full-coverage film-cooled cylinder models have been presented. The hole geometry details were representative of typical high-temperature turbine vanes with hole plunge angles selected to emphasize the strong influence of length-to-diameter ratio on showerhead cooling performance. The experimental measurements were made at moderate gas temperatures (811 K) under steady-state conditions. The cylinders were tested over a range of inlet Mach number/Reynolds number conditions representative of engine environment, and were actively cooled to produce wall-to-gas temperature ratios in the 0.6–0.8 range. The test matrix was structured to provide an assessment of the independent influence of free-stream Mach number, Reynolds number, temperature ratio, and pressure ratio on leading edge film cooling heat transfer.

The principal observations regarding the cylinder test program described herein can be summarized as follows:

1 The averaged effectiveness was found to decrease slightly with increasing free-stream Mach number, while the reverse was true of the leading edge Reynolds number. However, no strong Reynolds number/Mach number dependency was observed over the test range of these parameters.

2 The independent effect of gas-to-coolant temperature ratio on the average leading edge film cooling effectiveness was negligible over the range of test conditions.

3 The effectiveness levels showed significant dependency on the hole spanwise inclination (plunge) angle.

The experimental results served as the basis for development of an analytical model for engineering design. The model was structured as a first-order approach to array-averaged prediction of leading edge showerhead cooling effectiveness, including active heat transfer both within and upstream of the film hole array. Reinforced by empirical external surface heat transfer data from recent Purdue–NASA work, the model was shown to provide adequate prediction of relevant cylinder cooling effectiveness trends. The principal observations regarding the analytically predicted (or derived) showerhead cooling behavior trends may be summarized as follows:

- The active cooling mechanisms within and upstream of the film hole array produce the principal beneficial effects of showerhead cooling.

- The influence of film discharge on external (gas-to-wall) Stanton number becomes increasingly negative at all combinations of higher blowing rates and more nearly normal injection angles.
- At leading edge coolant/gas pressure ratios of practical interest, showerhead cooling performance is systematically enhanced by progressively lower values of hole diameter, hole spacing, and hole plunge angles.

In conclusion, the experimental/analytical program provided results that are both operationally realistic and computationally interesting. The results provide some insight into the fundamental nature of the leading edge showerhead cooling problem, and the analytical model appears suitable for preliminary design applications. However, further validation of the design methodology is clearly required, with special emphasis on determination of the upstream face film coefficients, and expansion of the data base to alternate hole spacings.

Acknowledgments

The authors would like to acknowledge the help of Dr. J. Custer, Mr. F. Ames, and Mr. L. Hylton for the fabrication and assembly of the experimental setup and assistance in data reduction.

References

Andrews, G. E., Gupta, M. L., and Mkpadi, M. C., 1984, "Full Coverage Discrete Hole Wall Cooling: Cooling Effectiveness," ASME Paper No. 84-GT-212.

Choe, H., Kays, W. M., and Moffat, R. J., 1976, "Turbulent Boundary Layer on a Full-Coverage Film-Cooled Surface—An Experimental Heat Transfer Study With Normal Injections," NASA CR-2642.

Crawford, M. E., Kays, W. M., and Moffat, R. J., 1980, "Full Coverage Film Cooling on Flat, Isothermal Surfaces: A Summary Report on Data and Predictions," NASA CR 3219.

Ericksen, V. L., 1971, "Film Cooling Effectiveness and Heat Transfer Injection Through Holes," Ph.D. Thesis, University of Minnesota.

Ericksen, V. L., Eckert, E. R. G., and Goldstein, R. J., 1971, "A Model for the Analysis of the Temperature Field Downstream of a Heated Jet Injected Into an Isothermal Crossflow at an Angle of 90°," NASA CR 72990.

Goldstein, R. J., 1971, "Film Cooling," in: *Advances in Heat Transfer*, Academic Press, New York–London, Vol. 7, p 321.

Kadotani, K., and Goldstein, R. J., 1979, "Effect of Mainstream Variables on Jets Issuing From a Row of Inclined Round Holes," ASME *Journal of Engineering for Power*, Vol. 101, pp. 298–304.

Lander, R. D., Fish, R. W., and Suo, M., 1972, "The External Heat Transfer Distribution on Film Cooled Turbine Vanes," AIAA Paper No. 72–9.

LeGrives, E., and Nicolas, J. J., 1977, "A New Computation Method of Turbine Blade Film Cooling Efficiency," AGARD Conference, Ankara.

Liess, C., 1973, "Film Cooling with Ejection From a Row of Inclined Circular Holes," Von Karman Institute for Fluid Dynamics, Technical Note 97.

Luckey, D. W., and L'Ecuyer, M. R., 1981, "Stagnation Region Gas Film Cooling—Spanwise Angled Injection From Multiple Rows of Holes," NASA CR 165333.

Mayle, R. E., and Camarata, F. J., 1974, "Multihole Cooling Film Effectiveness and Heat Transfer," AIAA/ASME 1974 Thermophysics and Heat Transfer Conference, AIAA Paper No. 74–675 (ASME Paper No. 74-HT-9).

Nealy, D. A., and Anderson, R. D., 1968, "Heat Transfer Characteristics of Laminated Porous Materials," AFAPL-TR-68-95, Air Force Systems Command.

Pedersen, D., 1972, "Effect of Density Ratio on Film Cooling Effectiveness for Injection Through a Row of Holes and for a Porous Slot," Ph.D. Thesis, University of Minnesota.

Ramette, P. H., and Louis, J. F., 1983, "Analytical Study of the Thermal and Fluid Mechanical Evolution of a Cooling Film Injected From a Single Line of Inclined Round Holes," *International Journal of Turbo and Jet Engines*, Vol. 1, No. 1, pp. 1–28.

Sasaki, M., Takahara, K., Sakata, K., and Kumagai, T., 1976, "Study on Film Cooling of Turbine Blades—Experiments on Film Cooling With Injection Through Holes Near the Leading Edge," *Bulletin of the JSME*, Vol. 19, No. 137, pp. 1344–1352.

Sasaki, M., Takahara, K., Kumagi, T., and Hamano, M., 1978, "Film Cooling Effectiveness for Injection From Multirow Holes," ASME Paper No. 78-GT-32.

Sparrow, E. M., and Carranco Ortiz, M., 1982, "Heat Transfer Coefficients for the Upstream Face of a Perforated Plate Positioned Normal to an Oncoming Flow," *International Journal of Heat and Mass Transfer*, Vol. 25, No. 1, pp. 127–135.

Stollery, J. L., and El-Ehwany, A. A. M., 1965, "A Note on the Use of a Boundary-Layer Model for Correlating Film-Cooling Data," *International Journal of Heat and Mass Transfer*, Vol. 8, pp. 55–65.

Wadia, A. R., 1983, "Comment on Influence of Finite Slot Size on Boundary Layer With Suction or Injection," *AIAA Journal*, Vol. 21, No. 12, pp. 1777–1778.

Wadia, A. R., and Nealy, D. A., 1985, "Development of a Design Model for Airfoil Leading Edge Film Cooling," ASME Paper No. 85-GT-120.

Effect of Rib Angle on Local Heat/Mass Transfer Distribution in a Two-Pass Rib-Roughened Channel

P. R. Chandra
Graduate Assistant.

J. C. Han
Associate Professor.

S. C. Lau
Assistant Professor.

Turbomachinery Laboratories,
Department of Mechanical Engineering,
Texas A&M University,
College Station, TX 77843

The heat transfer characteristics of turbulent air flow in a two-pass channel were studied via the naphthalene sublimation technique. The test section, which consisted of two straight, square channels joined by a sharp 180 deg turn, resembled the internal cooling passages of gas turbine airfoils. The top and bottom surfaces of the test channel were roughened by rib turbulators. The rib height-to-hydraulic diameter ratio (e/D) *was 0.063 and the rib pitch-to-height ratio* (P/e) *was 10. The local heat/mass transfer coefficients on the roughened top wall, and on the smooth divider and side walls of the test channel, were determined for three Reynolds numbers of 15,000, 30,000, and 60,000, and for three angles of attack* (α) *of 90, 60, and 45 deg. The results showed that the local Sherwood numbers on the ribbed walls were 1.5 to 6.5 times those for a fully developed flow in a smooth square duct. The average ribbed-wall Sherwood numbers were 2.5 to 3.5 times higher than the fully developed values, depending on the rib angle-of-attack and the Reynolds number. The results also indicated that, before the turn, the heat/mass transfer coefficients in the cases of $\alpha = 60$ and 45 deg were higher than those in the case of $\alpha = 90$ deg. However, after the turn, the heat/mass transfer coefficients in the oblique-rib cases were lower than those in the traverse-rib case. Correlations for the average Sherwood number ratios for individual channel surfaces and for the overall Sherwood number ratios are reported.*

Introduction

In advanced gas turbine airfoils, rib turbulators are cast onto two opposite walls of internal cooling passeges to enhance the heat transfer to the cooling air, as shown in Fig. 1. A typical cooling passage can be modeled as a straight or a multipass rectangular channel with two opposite rib-roughened walls. Han et al. (1984, 1985) investigated systematically the effects of the rib pitch, the rib height, and the rib angle of attack on the average heat transfer and the pressure drop in a fully developed air flow in a uniformly heated, straight, square channel with two opposite ribbed walls. The results showed that ribs with oblique angles of attack (α) of 30 and 45 deg provided higher heat transfer enhancement than ribs with an angle of attack of 90 deg for the same pumping power consumption.

In a multipass rectangular channel, in addition to the rib turbulators, the flow separation and recirculation in the turnaround regions and the flow redevelopment downstream of the turns are expected to have significant effects on the distribution of the local heat transfer coefficient and on the overall channel heat transfer. Boyle (1984) studied the heat transfer in a two-pass square channel with four smooth walls and in a similar two-pass square channel with two smooth walls and two opposite ribbed walls ($\alpha = 90$ deg). The top and bottom walls of the test channels were heated uniformly by passing current through thin foils and were instrumented with thermocouples, while the other two walls were unheated. The results showed that the heat transfer coefficients at the turn in the smooth channel and in the rib-roughened channel were about 2 to 3 and 3 to 4 times the fully developed values, respectively. In both cases, the heat transfer decreased in the main flow direction after the turn.

It is well known that the naphthalene sublimation technique has many advantages over the conventional heat transfer technique in determining the detailed distribution of the local heat transfer coefficients in complex flow fields. The naphthalene sublimation technique was employed by Han et al. (1988) to obtain the highly detailed heat/mass transfer distributions in a two-pass square channel with smooth walls and in the same channel with two opposite ribbed walls. The rib angle of attack was kept at 90 deg. In addition to the smooth channel data, the effects of the rib pitch and the rib height on the detailed distributions of the heat/mass transfer

Contributed by the Gas Turbine Division of THE AMERICAN SOCIETY OF MECHANICAL ENGINEERS and presented at the 32nd International Gas Turbine Conference and Exhibit, Anaheim, California, May 31–June 4, 1987. Manuscript received at ASME Headquarters February 6, 1987. Paper No. 87-GT-94.

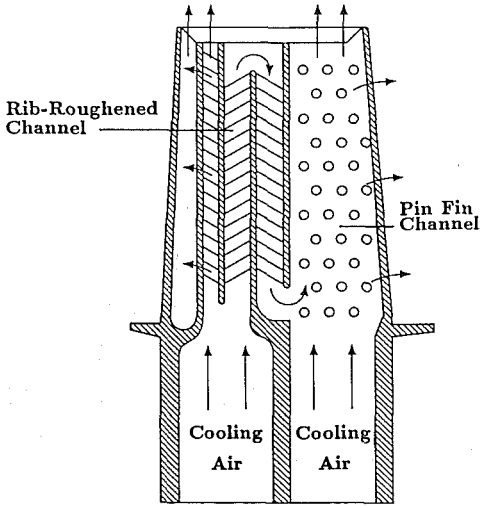

Fig. 1 Cooling concept of a modern turbine blade

coefficient on the rib-roughened top wall and on the smooth side walls were reported. The local heat/mass transfer coefficients were measured at up to 600 points in each of the test runs. However, the highly localized measurements were made around the sharp turn only. Therefore, the effects of the rib angle of attack and of the sharp turn on the distribution of the heat transfer coefficient in the entire two-pass channel are yet to be investigated.

In the present investigation, the detailed distribution of the heat/mass transfer coefficient in a two-pass square channel with rib turbulators was studied via the naphthalene sublimation technique. Emphasis was placed on determining the effects of the rib angle and of the turn on the detailed heat transfer coefficients along the two straight sections of the channel and around the sharp 180 deg turn. All the inner surfaces of the walls of the two-pass test channel were coated with naphthalene. The rib turbulators were attached to the top and bottom walls of the two straight sections of the test channel such that the rib turbulators on opposite walls were all parallel with an angle of attack of 90, 60, or 45 deg. The rib height-to-hydraulic diameter ratio (e/D) was 0.063. The rib pitch-to-height ratio (P/e) was 10. Highly detailed local measurements on the top wall (rib-roughened), the outer wall between the channel entrance and far downstream of the second straight channel, for three Reynolds numbers of 15,000, 30,000 and 60,000. Furthermore, the heat transfer coefficients before the turn, in the turn, and after the turn on each wall of the test channel were averaged and correlated.

Additional information on the present investigation can be found in works by Chandra (1987) and Han and Chandra (1987).

Experimental Apparatus and Instrumentation

Apparatus. The test apparatus, which was an open air flow loop, consisted of the test section, a settling chamber, a calibrated orifice flow meter, a gate valve, and a centrifugal blower. The entire test rig and the instrumentation were located in an air-conditioned laboratory, which was maintained at a constant temperature over the entire period of the investigation.

A schematic diagram of the test section is shown in Fig. 2. The test section, which was constructed of aluminum, was a three-pass channel with a 2.54-cm (1-in.) square flow cross section. The gap at the tip of each divider wall (inner wall) also measured 2.54 cm (1 in.). The length of each of the three straight sections of the test channel was 13 times the channel hydraulic diameter. Also, the thickness of the divider walls was 0.25 times the hydraulic diameter. All the dimensions were selected so that the test channel modeled the actual internal passages of turbine airfoils.

The test section was designed and constructed of a top plate, a bottom plate, and 2.54 cm (1 in.) by 0.64 cm (0.25 in.) spacer bars (divider walls and side walls) so that it could be assembled and disassembled in a relatively short period of time. All of the inside surfaces of the first two straight sections of the test channel, as well as those at the 180 deg turn between them, were coated with naphthalene in a casting process against a highly polished, flat, stainless steel surface. Rib turbulators, which were standard 1.59-mm (0.063-in.) square brass rods, were glued onto the naphthalene-coated top and bottom surfaces of the two straight sections of the test channel. The ribs were aligned such that all the ribs on opposite surfaces were parallel with $P/e = 10$, and that the rib angle of attack was 90, 60, or 45 deg. No ribs were installed in the turn region.

A large baffle was attached to the inlet of the test section to provide an abrupt contraction entrance condition. During test runs, air was drawn through the test section from the naphthalene-free laboratory. Upon exiting the test section, the air was ducted to the outside of the building.

Procedure and Instrumentation. Before each test run, all of the freshly prepared naphthalene-coated plates (active walls of the test section), tightly sealed in plastic bags to prevent sublimation, were left in the laboratory for 6–8 h to attain thermal equilibrium. Immediately before the test run, the surface contour of each of the naphthalene plates was measured with a Starrett electronic depth gage, which has an accuracy of 0.00001 in./0.0001 mm. The measured data were recorded

Nomenclature

D = channel width; also hydraulic diameter
e = rib height
h_m = local mass transfer coefficient, equation (1)
$\dot{m}''$ = local mass transfer rate per unit area, equation (2)
M = cumulative mass transfer
Nu = Nusselt number
P = rib pitch
P_w = naphthalene vapor pressure at the wall, equation (4)
Pr = Prandtl number of air
$\dot{Q}$ = volumetric flow rate of air
Re = Reynolds number based on channel hydraulic diameter
Sc = Schmidt number for naphthalene
Sh = local Sherwood number, equation (6)
Sh_o = Sherwood number of fully developed turbulent flow in square duct
$\overline{\mathrm{Sh}}$ = average Sherwood number on each of the channel surfaces
$\overline{\overline{\mathrm{Sh}}}$ = overall average Sherwood number on all surfaces
t = thickness of the inner (divider) wall
Δt = duration of the test run
T_w = naphthalene wall temperature, equations (3) and (4)
X = axial distance from channel entrance
$\tilde{D}$ = diffusion coefficient, equation (6)
α = rib angle of attack
ν = kinematic viscosity of pure air
ρ_b = bulk naphthalene vapor density, equation (5)
ρ_s = density of solid naphthalene
ρ_w = local naphthalene vapor density at wall, equation (3)

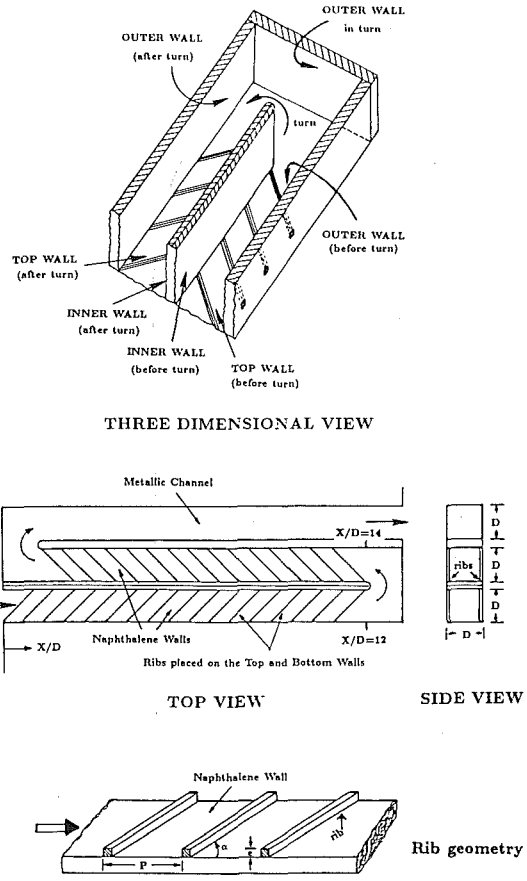

Fig. 2 Sketch of the test section

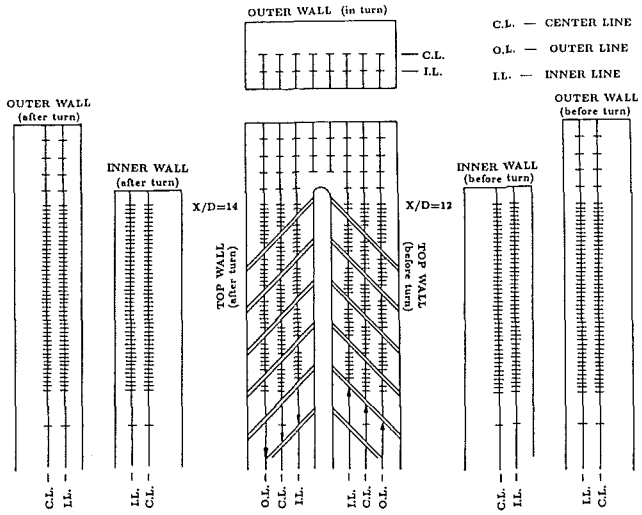

Fig. 3 Measurement points before, in, and after the turn for a typical test run

with an A/D converter, which was connected to the depth gage. The measurement points on the top wall, the outer wall, and the inner wall for a typical test run are shown in Fig. 3. It can be seen that measurements were made along three axial lines (centerline, inner line, and outer line) on the ribbed top wall, and along two axial lines (centerline and inner line) on both the smooth outer and inner walls. The inner line and outer line were halfway between the centerline and the respective walls. Measurements were made at seven (or, in some cases, eight) points along an axial line between adjacent ribs in selected regions on the ribbed top wall. In other regions, measurements were made along an axial line in one rib-pitch intervals.

The procedure for measuring the surface contour of a naphthalene plate was described in detail by Han et al. (1988) and will not be repeated here.

After the completion of the contour measurements, the test section was assembled and installed on the flow loop. The blower was then switched on to allow air to flow through the test section. During the test run, the air temperature, several temperatures on the naphthalene surfaces, the pressure drop across the orifice, the static pressure immediately upstream of the orifice, and the atmospheric pressure were recorded periodically. The naphthalene surface temperatures were measured at four locations, two in each of the two straight sections, with small-gage copper-constantan thermocouples, whose junctions were carefully positioned beneath the naphthalene surfaces. The naphthalene surface temperatures were needed in the mass transfer coefficient calculations.

At the completion of the test run, the duration of which was about 30 min, the contours of all the naphthalene surfaces were measured and recorded again. From the before-run and after-run contour measurements, the rates of mass transfer at the measurement points on all the naphthalene surfaces were calculated.

Supplementary experiments were conducted to determine the mass losses from the naphthalene surfaces by natural convection when the contours of the naphthalene surfaces were measured. It was found that the total mass losses by natural convection were on the order of 1-4 percent of the total mass transfer during the test run. The mass losses were subtracted from the mass transfer at the measurement points in the local mass transfer coefficient calculations.

Data Reduction

The local mass transfer coefficient at any measurement point was determined from the rate of mass transfer per unit surface area and the local naphthalene vapor density at the measurement point, and the local bulk naphthalene vapor density

$$h_m = \dot{m}''/(\rho_w - \rho_b) \tag{1}$$

The rate of mass transfer per unit surface area at the measurement point was evaluated from the density of solid naphthalene, the measured change of elevation at the measurement point ΔZ, and the duration of the test run Δt

$$\dot{m}'' = \rho_s \cdot \Delta Z/\Delta t \tag{2}$$

The local naphthalene vapor density was calculated from the ideal gas law in conjunction with the measured naphthalene surface temperature and with the vapor pressure-temperature relationship for naphthalene developed by Sogin (1958)

$$\rho_w = P_w/(R_v T_w) \tag{3}$$

$$\log_{10} P_w = A - B/T_w \tag{4}$$

where R_v, A, and B were given by Sogin (1958).

The local bulk naphthalene vapor density was evaluated by the equation

$$\rho_b = M/\dot{Q} \tag{5}$$

The cumulative mass M was the total mass entering the airstream from the four channel walls between the entrance and the measurement station over the duration of the test.

Based on the definition of the local Sherwood number

$$\mathrm{Sh} = h_m \cdot D/\tilde{D} = h_m \cdot D/(\nu/\mathrm{Sc}) \tag{6}$$

where the Schmidt number for naphthalene was 2.5, according to Sogin (1958). The local Sherwood number was normalized

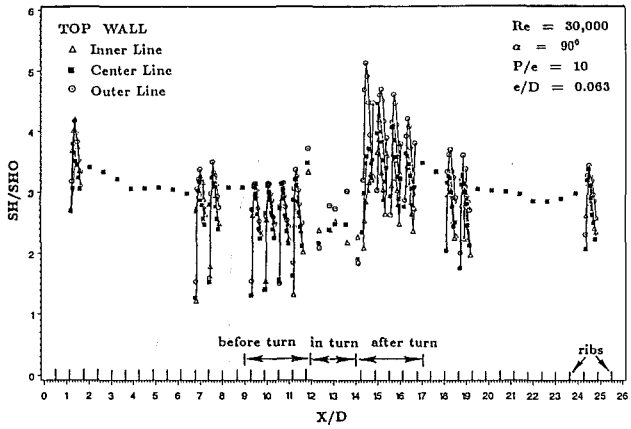

Fig. 4 Local Sherwood number ratio with $\alpha = 90$ deg and Re = 30,000

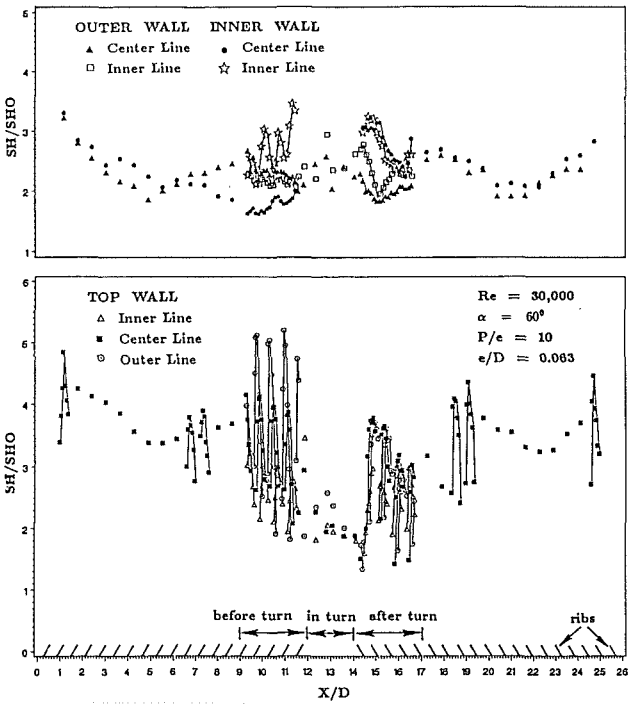

Fig. 5 Local Sherwood number ratio with $\alpha = 60$ deg and Re = 30,000

by the Sherwood number for fully developed turbulent flow in a smooth square channel.

$$\frac{\mathrm{Sh}}{\mathrm{Sh}_o} = \frac{h_m D/\tilde{D}}{0.023\mathrm{Re}^{0.8}\mathrm{Pr}^{0.4}(\mathrm{Sc}/\mathrm{Pr})^{0.4}} \tag{7}$$

where the correlation of Dittus and Boelter and the heat/mass transfer analogy, $\mathrm{Nu}/\mathrm{Sh} = (\mathrm{Pr}/\mathrm{Sc})^{0.4}$, were used.

It should be noted that, by using equations (3) and (4), the local naphthalene vapor density at a measurement point can be found to change by 6 percent for a 0.56°C (1°F) variation in the naphthalene surface temperature. Therefore, it is necessary that the surface temperature at any measurement point be measured accurately. In the present investigation, the naphthalene surface temperatures were measured at only four stations in the test section. However, the variation of the four readings was never more than 0.28°C (0.5°F) for any run. Therefore, the errors in the local vapor density calculations were relatively small.

Errors were also introduced into the bulk vapor density calculations due to the fact that elevations were measured only at discrete points along one, two, or three axial lines on each

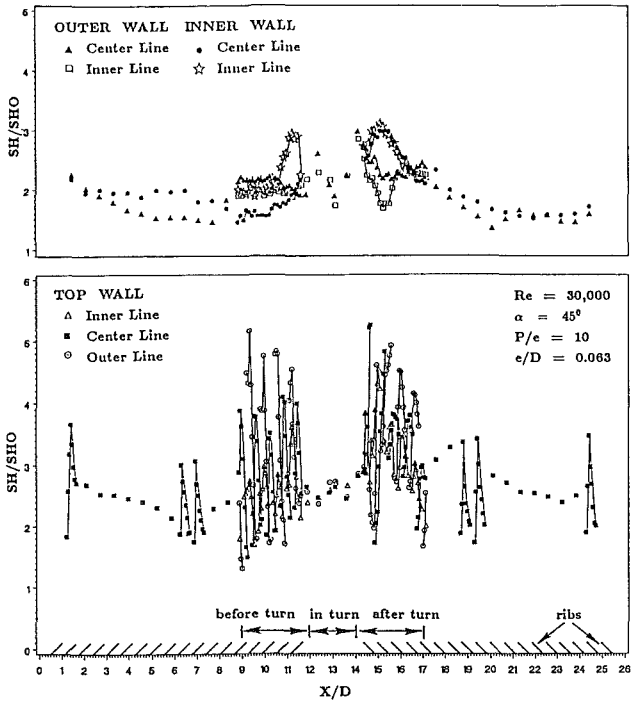

Fig. 6 Local Sherwood number ratio with $\alpha = 45$ deg and Re = 30,000

naphthalene surface. In some regions on the naphthalene surfaces, elevation measurements were made at every rib pitch. Fortunately, the values of the bulk vapor density were small, with a maximum of about 10 percent, compared with those of the local naphthalene vapor density.

The maximum uncertainty in the calculation of $(\rho_w - \rho_b)$ was estimated to be 6 percent. The uncertainties in the calculations of the density of solid naphthalene (ρ_s), the elevation measurement (ΔZ), and the duration of the test run, (Δt) were estimated to be 2, 4, and 3 percent, respectively. By using the uncertainty estimation method of Kline and McClintock (1953), the maximum uncertainty of the local Sherwood number was found to be slightly less than 8 percent.

Presentation and Discussion of Results

The experimental results will now be presented. Seven sets of local mass transfer data were obtained. The axial distributions of the ribbed-wall Sherwood number ratio, as well as those of the inner-wall and the outer-wall Sherwood number ratios, are given in Figs. 4–6, and Figs. 8–11. The effect of the rib angle of attack on the distribution of the local Sherwood number will be examined first with the results for Re = 30,000 and for the three angles of attack 90, 60 and 45 deg. In the ensuing section, the Reynolds number effect will be discussed. The averages of the local mass transfer data over individual segments of the channel walls and the overall mass transfer data will then presented, and correlations for the average results will be given. Finally, the present mass transfer data will be compared with previous heat transfer data to show the reliability of the present data.

It should be noted that the regions in the test channel between $X/D = 9$ and $X/D = 12$, and between $X/D = 14$ and $X/D = 17$ ($3D$ upstream and $3D$ downstream of the turn) are referred to herein as "before the turn" and "after the turn," respectively. It should also be pointed out that, in regions of interest, such as before and after the turn, the local Sherwood number was determined at up to eight stations every rib pitch along axial lines. However, in other regions, the local Sherwood number was determined at only one station every rib pitch.

Effect of Rib Angle on Local Sherwood Number Ratio. The distributions of the ribbed-wall Sherwood number ratio along three axial lines for $\alpha = 90$ deg and for Re = 30,000 are shown in Fig. 4. The periodic nature of the distributions in the entrance duct is evident. The Sherwood number ratios attain their maximum values at the points of flow reattachment, which occur slightly upstream of the midpoints between adjacent ribs. The variations of the Sherwood number ratio in the spanwise direction are very small compared with the axial variations.

In the turn region, where there are no ribs on either the top wall or the bottom wall, the Sherwood number ratios along the outer line are higher than those along the inner line. The trend carries onto the after-turn region, where the ribbed-wall Sherwood number ratios near the outer wall are higher than those near the inner wall. The low ribbed-wall Sherwood number ratios near the inner wall are the results of the flow separation at the tip of the inner wall. The strong lateral pressure gradient due to the sharp turn forces the main flow to impinge onto the outer wall. The flow then gets pushed back toward the inner wall, resulting in the large values of the ribbed-wall Sh/Sh_o near the outer wall. In general, the Sherwood number ratios after the turn are greater than those before the turn.

Farther downstream of the turn, as the effect of the turn on the flow field vanishes gradually, both the peak Sherwood number ratio and the spanwise Sh/Sh_o variation decrease with increasing axial distance, until the axial Sh/Sh_o distributions become periodic again.

The axial distributions of the ribbed-wall, inner-wall, and outer-wall Sherwood number ratios for angles of attack of 60 and 45 deg are shown in Figs. 5 and 6, respectively. The Reynolds number is 30,000 in both cases. Selected segments of the axial distributions before and after the turn from Figs. 5 and 6 are replotted on an enlarged scale in Figs. 7(*a*) and 7(*b*). These figures facilitate the close examination of the ef-

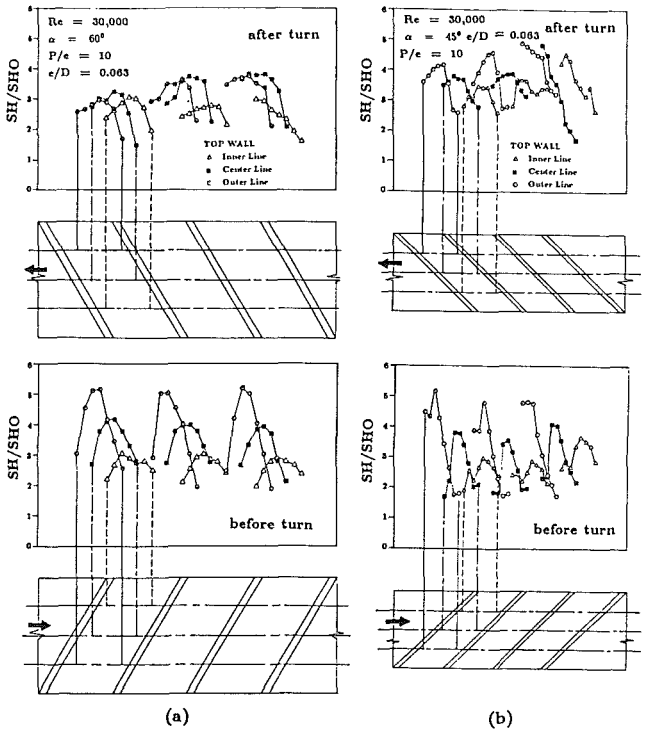

Fig. 7 Detailed Sherwood number ratios on the top wall with Re = 30,000: (*a*) $\alpha = 60$ deg; (*b*) $\alpha = 45$ deg

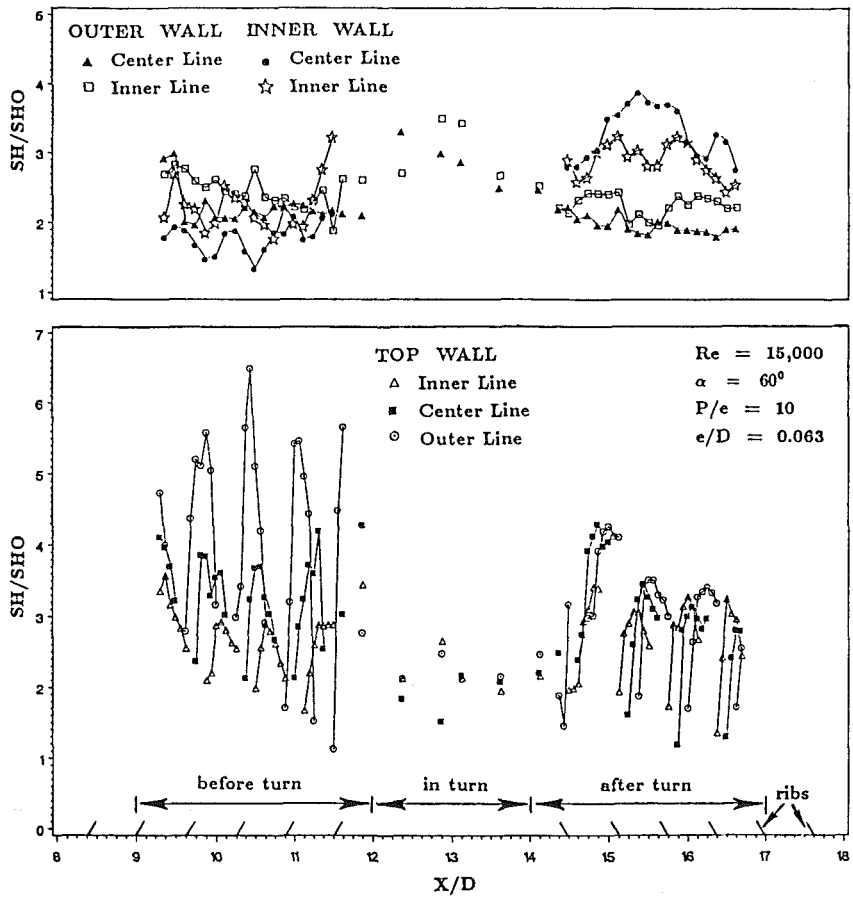

Fig. 8 Local Sherwood number ratio with $\alpha = 60$ deg and Re = 15,000

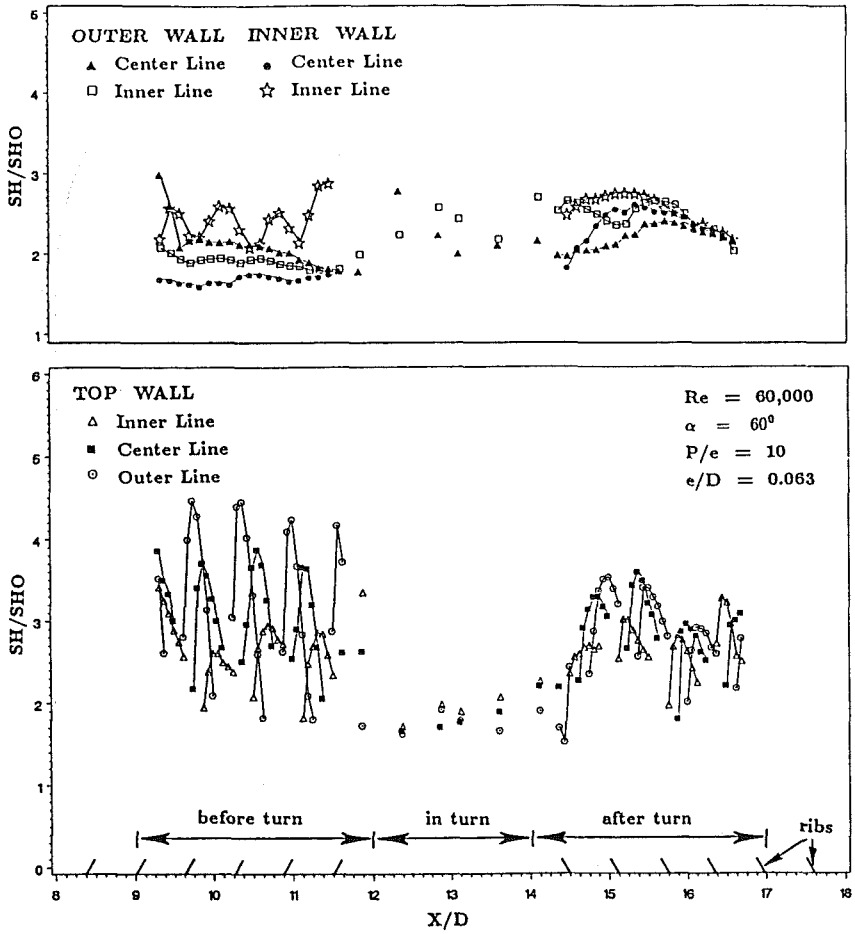

Fig. 9 Local Sherwood number ratio with $\alpha = 60$ deg and Re = 60,000

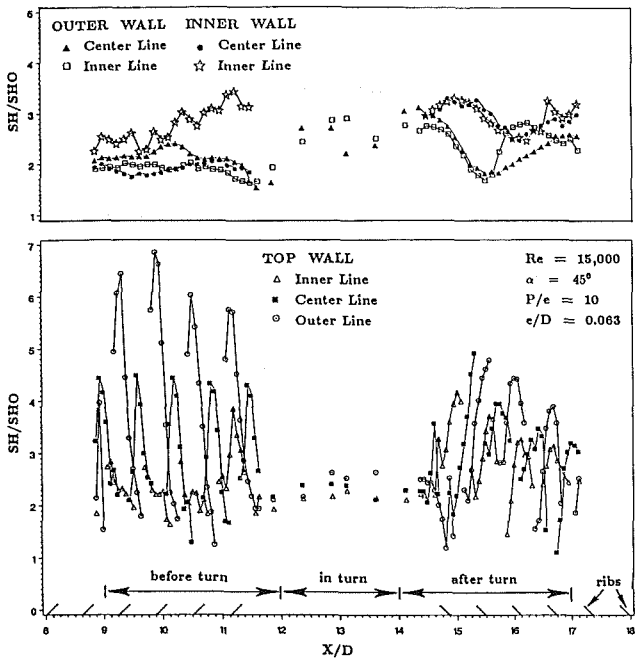

Fig. 10 Local Sherwood number ratio with $\alpha = 45$ deg and Re = 15,000

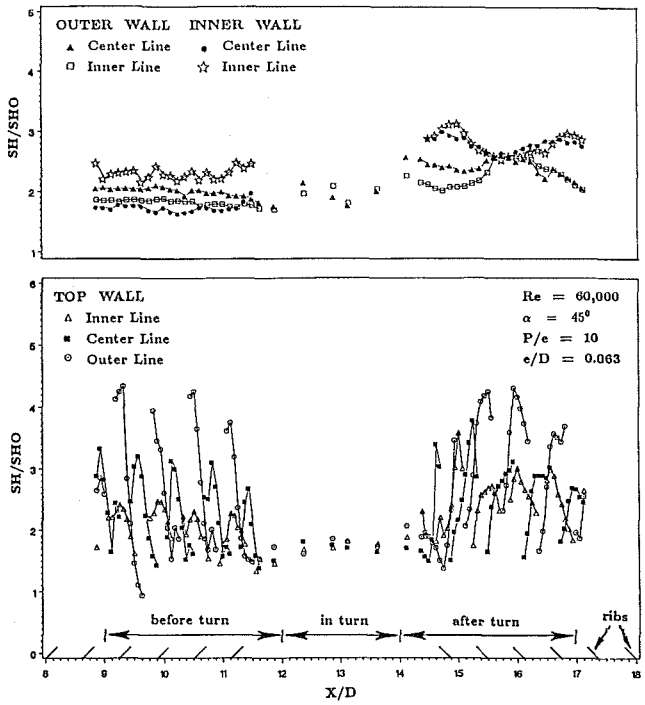

Fig. 11 Local Sherwood number ratio with $\alpha = 45$ deg and Re = 60,000

fects of the rib angle and the sharp turn on the local ribbed-wall Sh/Sh_o in the before-turn and after-turn regions. In Figs. 7(*a*) and 7(*b*), the axial locations of the measurement stations relative to the ribs are also illustrated.

For $\alpha = 60$ deg, the magnitude of the variations of the before-turn top-wall Sh/Sh_o in the spanwise direction is comparable to those of the axial periodic Sh/Sh_o distributions. The values of the before-turn Sh/Sh_o along the outer line are always greater than the corresponding values along the inner

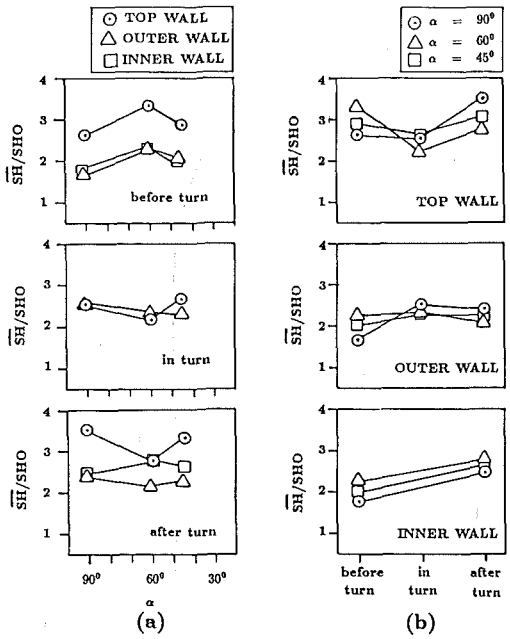

Fig. 12 Average Sherwood number ratio on each of the channel surfaces with Re = 30,000

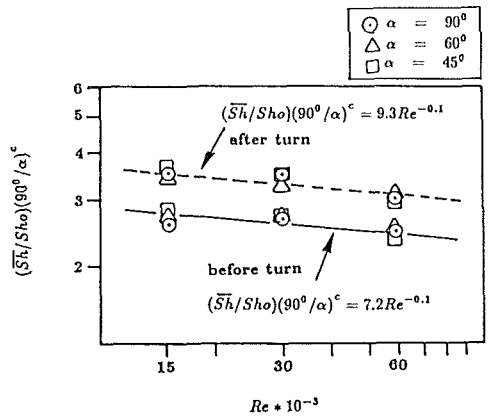

Fig. 13(a) Correlations of the average Sherwood number ratio on the top wall with rib angles

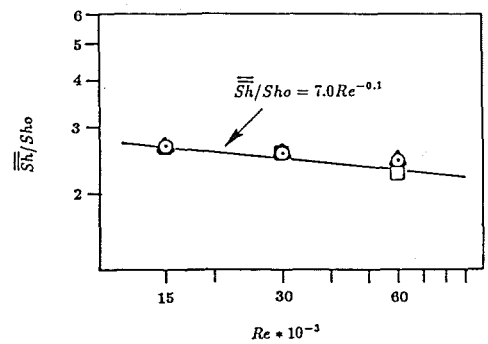

Fig. 13(b) Correlations of the overall average Sherwood number ratio on all surfaces with rib angles

line. These lateral variations of the ribbed-wall Sh/Sh_o in the before-turn region are due to the secondary flow along the rib axes toward the inner wall.

In the turn, the Sherwood number ratios are smaller than those before the turn with the values of Sh/Sh_o along the

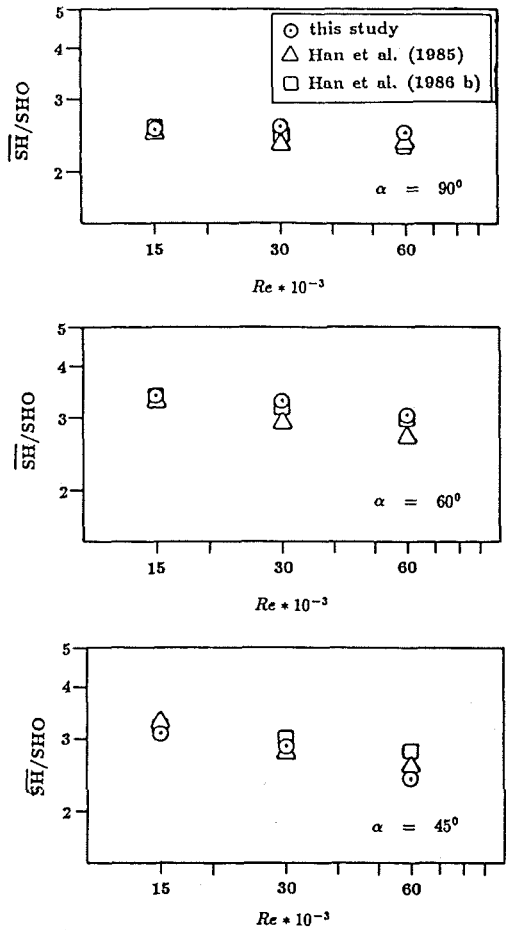

Fig. 14 Comparison between the present results on the top wall (before the turn) and the published heat transfer data

outer line generally higher than those along the centerline and the inner line.

After the turn, the peak Sherwood number ratios along the outer line decrease significantly from the before-turn values; meanwhile, the decreases (from the before-turn values) of the peak values of Sh/Sh_o along the centerline and along the inner line are successively lower than those along the outer line. The spanwise variations of Sh/Sh_o are relatively small after the turn. This may be caused by the complicated interaction between the main flow, which is forced toward the inner wall due to the turn (as described earlier), and the secondary flow along the rib axes toward the outer wall.

For $\alpha = 45$ deg, the top-wall Sh/Sh_o distributions before the turn are similar to those for $\alpha = 60$ deg. Again, the Sherwood number ratios along the outer line are higher than those along the centerline, which, in turn, are higher than those along the inner line. The Sherwood number ratio is relatively uniform in the turn. The after-turn values of Sh/Sh_o are about the same as those in the before-turn region.

Attention will now be turned to the top of Figs. 5 and 6, where the axial inner-wall and the outer-wall Sherwood number distributions are given. For $\alpha = 60$ deg, the spanwise variations of the before-turn Sh/Sh_o on the inner (divider) wall are much larger than those on the outer wall. The before-turn Sherwood number ratios along the inner line on the inner wall are much greater than those along the centerline on the inner wall, while the outer wall, the values of the centerline Sh/Sh_o are only slightly higher than those of the inner-line Sh/Sh_o. The secondary flow created by the oblique ribs impinges on the inner wall, resulting in the high Sherwood number ratios on the inner wall near the ribbed walls. For

Table 1 Coefficients, *a*, *b*, and c in equation (8)

Region	Surface	a	b	c if $\alpha \geq 60^o$	c if $\alpha < 60^o$
before turn	top wall	7.2	-0.1	-0.58	-0.059
	outer wall	4.6	-0.1	-0.74	-0.26
	inner wall	4.8	-0.1	-0.63	-0.3
in turn	top wall	6.7	-0.1	0.24	0.02
	outer wall	7.0	-0.1	0.11	0.18
after turn	top wall	9.3	-0.1	0.4	0.15
	outer wall	6.7	-0.1	0	0.066
	inner wall	7.3	-0.1	-0.099	-0.077

$\alpha = 45$ deg, the before-turn Sherwood number ratios exhibit the same trends, except that the spanwise Sh/Sh_o variations on the inner wall are not as large as those for $\alpha = 60$ deg.

After the turn, the values of the inner-wall Sh/Sh_o for both $\alpha = 60$ deg and $\alpha = 45$ deg are large compared to the corresponding values of the outer-wall Sh/Sh_o. The high Sherwood number ratios on the inner wall are believed to be caused by flow reattachment and by the main flow being forced toward the inner wall due to the turn. On the outer wall, the values of the after-turn Sh/Sh_o along the inner line are higher than those along the centerline for $\alpha = 60$ deg. However, the reverse is true in the case of $\alpha = 45$ deg.

Effect of Reynolds Number. The effect on the Reynolds number on the local Sherwood number will now be examined. Experimental data for $\alpha = 60$ and 45 deg and for Re = 15,000 and 60,000 are presented in Figs. 8–11.

Attention is focused first on Figs. 8 and 9, along with Fig. 5. The top-wall Sherwood number ratios in all three cases are very similar. The spanwise top-wall Sh/Sh_o variations decrease with increasing Reynolds number. Before the turn, there are much larger spanwise Sh/Sh_o variations on the inner wall than on the outer wall in the two high Reynolds number cases. However, the inner-wall and the outer-wall spanwise variations are comparable in the case of Re = 15,000. After the turn, the inner-wall Sherwood number ratios are always higher than the corresponding outer-wall values and the differences are smaller at Re = 60,000.

Comparing Figs. 10 and 11 with Fig. 6, it can be seem that the spanwise variations of the before-turn, top-wall Sh/Sh_o are again larger at lower Reynolds numbers. The differences between the before-turn Sh/Sh_o variations on the inner wall and those on the outer wall are most pronounced at Re = 15,000.

In general, the flow Reynolds number has only a modest effect on the local Sherwood number ratio.

Average Sherwood Number and Correlations. For all the cases studied, the local Sherwood number ratios for individual segments of the channel walls before the turn, in the turn, and after the turn were averaged. Typical average Sherwood number ratios, those for Re = 30,000, are shown in Figs. 12(*a*) and 12(*b*). In Fig. 12(*a*), the average Sherwood number ratios ($\overline{Sh}/Sh_o$) are plotted as functions of the rib angle. Before the turn, the values of the top-wall $\overline{Sh}/Sh_o$ are much greater than those of the outer-wall $\overline{Sh}/Sh_o$ and of the inner-wall $\overline{Sh}/Sh_o$ for all three angles of attack of 90, 60, and 45 deg. The top-wall $\overline{Sh}/Sh_o$, the outer-wall $\overline{Sh}/Sh_o$, and the inner-wall $\overline{Sh}/Sh_o$ for $\alpha = 60$ deg are all higher than their counterparts for $\alpha = 90$ deg and $\alpha = 45$ deg.

After the turn, the average inner-wall Sherwood number ratios are higher than the average outer-wall Sherwood number ratios for all three rib angles. Also, the top-wall $\overline{Sh}/Sh_o$ for $\alpha = 60$ deg decreases significantly after the turn from its before-turn value while those for $\alpha = 90$ and 45 deg increase after the turn from their corresponding before-turn values. These trends are also evident in Fig. 12(*b*), where the $\overline{Sh}/Sh_o$ results are replotted to show the effect of the sharp 180 deg turn on the average Sherwood number ratios for the three rib angles of attack studied.

The average Sherwood number ratios for the various segments of the channel walls were found to correlate well with the Reynolds number and the rib angle by the following equation:

$$\overline{Sh}/Sh_o = a\mathrm{Re}^b\,(\alpha/90\ \mathrm{deg})^c \tag{8}$$

where *a*, *b*, and *c* are constant coefficients. The numerical values of these coefficients are listed in Table 1. Equation (8) correlates the experimental data of the present study to within ±6 percent. It should be noted that equation (8) applies to $e/D = 0.063$ and $P/e = 10$ only. Correlations for the cases of other e/D and P/e ratios can be found in Chandra (1987) and Han et al. (1988).

Figure 13(*a*) shows $(\overline{Sh}/Sh_o)\ (90\ \mathrm{deg}/\alpha)^c$ as a function of the flow Reynolds number. The experimental data shown in the figure are the average top-wall Sherwood number ratios obtained in the present study. Four of the data points (for $\alpha = 90$ deg, Re = 15,000 and 60,000) are from Chandra (1987). The figure shows that the present experimental before-turn and after-turn results are well represented by the equations.

The Sherwood number ratios for all of the surfaces in and around the 180 deg turn were averaged. The overall average Sherwood number ratios ($\overline{\overline{Sh}}/Sh_o$) for the three rib angles studied are plotted versus the flow Reynolds number in Fig. 13(*b*). The overall Sherwood number ratio is independent of the rib angle but decreases slightly with increasing Reynolds number. It was found that the following equation

$$\overline{\overline{Sh}}/Sh_o = 7.0\mathrm{Re}^{-0.1} \tag{9}$$

correlates the data to within ±4 percent.

Comparison With Heat Transfer Data. In Fig. 14, the average before-turn ribbed-wall Sherwood number ratios for all the cases studied were compared with the fully developed average heat transfer data reported by Han et al. (1985, 1986). The average heat transfer data are those for the fully developed flow of air in a uniformly heated, straight, square channel with two opposite ribbed walls, and with the same values of e/D, P/e, α, and Re as those of the present study. In the heat transfer studies, the Nusselt numbers were normalized by their corresponding Nusselt numbers for fully developed turbulent flow in a smooth square channel.

Since $\overline{Nu}/\overline{Sh} = (Pr/Sc)^{0.4}$ and $Nu_o/Sh_o = (Pr/Sc)^{0.4}$, it follows that

$$\overline{Nu}/Nu_o = \overline{Sh}/Sh_o \tag{10}$$

Therefore, the heat/mass transfer analogy enables the direct comparison of the Nusselt number ratios from Han et al. (1985, 1986b) and the Sherwood number ratios of the present study.

It can be seen from Fig. 14 that the present mass transfer results compare very well with the published heat transfer data in most cases. The deviations between the heat transfer and mass transfer data are less than 10 percent, except for the case of $\alpha = 45$ deg and Re = 60,000, the deviation of which is 14 percent. The good agreement between the heat and mass transfer data reaffirms that the naphthalene sublimation technique is a reliable tool for the determination of highly localized distributions of the heat transfer coefficient in complicated channel flows, such as those encountered in the present study.

Concluding Remarks

The experimental investigation reported here has provided

local heat/mass transfer coefficient data for turbulent flow in a two-pass square channel with two opposite ribbed walls. The main findings of the investigation are as follows:

1 Before the turn, the axial distributions of the ribbed-wall Sherwood number are periodic for all three rib angles of attack studied. The local ribbed-wall Sherwood numbers for $\alpha = 60$ and 45 deg, near the outer wall, are higher than those near the inner wall. The spanwise Sherwood number variations decrease as the Reynolds number increases. The spanwise variations of the local ribbed-wall Sherwood number for $\alpha = 90$ deg are very small.

2 After the turn, the ribbed-wall Sherwood numbers near the outer wall are higher than those near the inner wall for all three rib angles studied. For $\alpha = 60$ and 45 deg, the spanwise variations of the ribbed-wall Sherwood numbers after the turn are smaller than those before the turn.

3 Before the turn, the average ribbed-wall Sherwood number for $\alpha = 60$ deg is higher than that for $\alpha = 45$ deg, which, in turn, is higher than that for $\alpha = 90$ deg. However, after the turn, the average ribbed-wall Sherwood number for $\alpha = 90$ deg is higher than those for $\alpha = 45$ and 60 deg.

4 For any rib angle of attack, the average inner-wall Sherwood number after the turn is always higher than both the average inner-wall Sherwood number before the turn and the average outer-wall Sherwood number after the turn.

5 The average Sherwood number ratios for individual channel surfaces could be correlated with equations in the form of $\overline{\mathrm{Sh}}/\mathrm{Sh}_o = a\mathrm{Re}^b\,(\alpha/90\ \mathrm{deg})^c$.

6 The overall average Sherwood number ratio in the region around the sharp turn is independent of the rib angle, but decreases slightly as the Reynolds number increases.

7 The published heat transfer results for straight ribroughened channels can be applied to the design of the straight channel before the first sharp turn in a multipass ribbed cooling passage in a turbine airfoil.

Acknowledgments

This work was funded in part by the NASA-Lewis Research Center under Contract NAS 3-24227. Their support is gratefully appreciated.

References

Boyle, R. J., 1984, "Heat Transfer in Serpentine Passages With Turbulence Promoters," ASME Paper No. 84-HT-24.

Chandra, P. R., 1987, "A Study of Local Heat/Mass Transfer Distribution in Multipass Channels for Turbine Blade Cooling," Ph.D. Thesis, Texas A&M University, College Station, TX.

Han, J. C., 1984, "Heat Transfer and Friction in Channels With Two Opposite Rib-Roughened Walls," ASME *Journal of Heat Transfer*, Vol. 106, pp. 774–781.

Han, J. C., Park, J. S., and Lei, C. K., 1985, "Heat Transfer Enhancement in Channels With Turbulence Promoters," ASME JOURNAL OF ENGINEERING FOR GAS TURBINES AND POWER, Vol. 107, pp. 628–635.

Han, J. C., Park, J. S., and Ibrahim, M. Y., 1986, "Measurement of Heat Transfer and Pressure Drop in Rectangular Channels With Turbulence Promoters," NASA CR-4015; USAAVSCOM-TR-86-C-25.

Han, J. C., and Chandra, P. R., 1987, "Local Heat/Mass Transfer and Pressure Drop in a Two-Pass Rib-Roughened Channel for Turbine Airfoil Cooling," NASA CR-179635; AVSCOM-TR-87-C-14.

Han, J. C., Chandra, P. R., and Lau, S. C., 1988, "Local Heat/Mass Transfer Distribution Around Sharp 180 Degree Turn in Multipass Rib-Roughenend Channels," ASME *Journal of Heat Transfer*, Vol. 110, No. 1, pp. 91–98.

Kline, S. J., and McClintock, F. A., 1953, "Describing Uncertainties in Single-Sample Experiments," *Mechanical Engineering*, Vol. 75, pp. 3–8.

Sogin, H. H., 1958, "Sublimation From Disks to Air Streams Flowing Normal to Their Surfaces," *Transactions of ASME*, Vol. 80, pp. 61–69.

Procedures for Determining Surface Heat Flux Using Thin Film Gages on a Coated Metal Model in a Transient Test Facility

J. E. Doorly
Department of Engineering Science,
University of Oxford,
Oxford, United Kingdom

The paper describes how thin film surface heat flux gages may be used to measure surface heat transfer rate to enamel-coated metal turbine blades. Flexible methods, which are also computationally efficient, for obtaining the heat transfer rate are described. Experimental results, using the new coated metal turbine blades and processing techniques, in a stationary transient cascade facility are given, and are shown to agree well with results using the existing method for gages on single-layer substrate blades. The application of the gages for measuring highly unsteady heat transfer is also discussed.

1 Introduction

The use of thin film gages to measure surface heat flux on a single substrate model turbine blade (in particular machinable glass ceramic) in stationary short-duration wind tunnel tests is well established (Schultz and Jones, 1973; Oldfield et al., 1978; Jones et al., 1979). There is, however, increasing interest in measuring unsteady heat transfer in rotating turbine test rigs, as shown by the work of Dunn et al. (1986) and Epstein et al. (1985). The use of machinable glass ceramic models for new test facilities under consideration is not considered by the author to be feasible for high-speed rotating components, for structural reasons. (In fact, even for the stationary nozzle guide vanes, experience at Oxford has shown that producing complex, film-cooled models from machinable glass is costly and difficult, and furthermore, structural strength limits the model blade thickness when simulating high-pressure vane operating conditions.)

The present developments in heat flux gages designed for application in rotating environments include the use of isolated miniature quartz inserts in metal blades, with deposited thin film gages as described by Dunn et al. (1986). Epstein et al. (1985) describe the use of two-sided heat flux gages on a thin Kapton sandwich, which is bonded to the blade surface. These techniques have been used successfully, but both present some handicaps.

In the former, these include difficulty in flush mounting and temperature discontinuities. Flush mounting of isolated inserts requires the use of a microscope, as described by Dunn et al. (1986). Temperature discontinuities arise owing to the mismatch between the thermal properties of an isolated insert, and the blade in which it is mounted. The resulting problems are well known, and flat plate laminar and turbulent boundary layer corrections are given by Kays (1966), Rubesin (1951), Reynolds et al. (1958), Chapman and Rubesin (1949), Schultz and Jones (1973), and Ainsworth (1976). Suitable compensating corrections have not, to the author's knowledge, been developed for transitional boundary layers, as discussed by Daniels (1978).

A bonded Kapton covering, similar to that described by Epstein et al. (1985), but used as a single-sided heat flux gage, was evaluated by the author in wind tunnel tests (Doorly, 1985). It was found that accurate heat flux measurements could be obtained. For this alternative, however, the maximum allowable temperature (about 300°C) was considerably less than is possible with a vitreous enamel coating. Although this is not significant for the present application, it was also observed that the lack of robustness of the gages posed problems when wrapping the Kapton around a highly curved model.

Recently, an alternative instrumentation technique has been developed, whereby thin film gages are painted and fired onto two-layered substrate models (Doorly, 1985; Doorly and Oldfield, 1986a). The model is comprised of a metal base, which is coated with an electrically insulating vitreous enamel layer. These gages, together with the models, are robust enough to withstand rotation and high pressures, and furthermore, do not introduce discontinuities in surface temperature or height. Instrumented blades are easily fabricated from standard turbine blades; the method of gage calibration and one technique for the processing of the heat flux signals obtained from them were described by Doorly (1985) and Doorly and Oldfield (1986a, b). The results of wind tunnel testing, using gages on two-layered circular cylinder models to measure stagnation point heat transfer, demonstrated that very accurate surface heat flux measurements could be obtained using the gages.

Contributed by the Gas Turbine Division of THE AMERICAN SOCIETY OF MECHANICAL ENGINEERS and presented at the 32nd International Gas Turbine Conference and Exhibit, Anaheim, California, May 31–June 4, 1987. Manuscript received at ASME Headquarters February 6, 1987. Paper No. 87-GT-95.

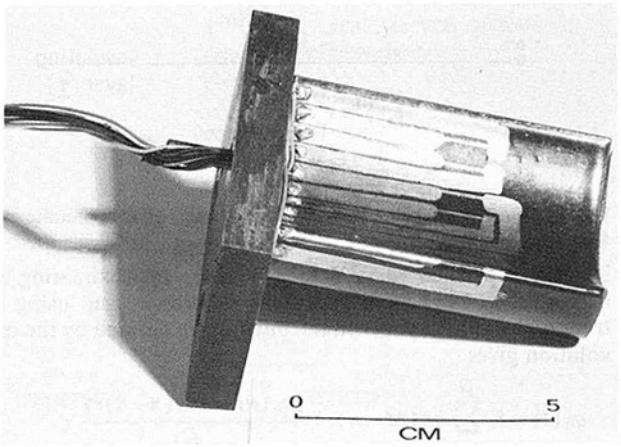

Fig. 1 Instrumented enamel-coated metal blade

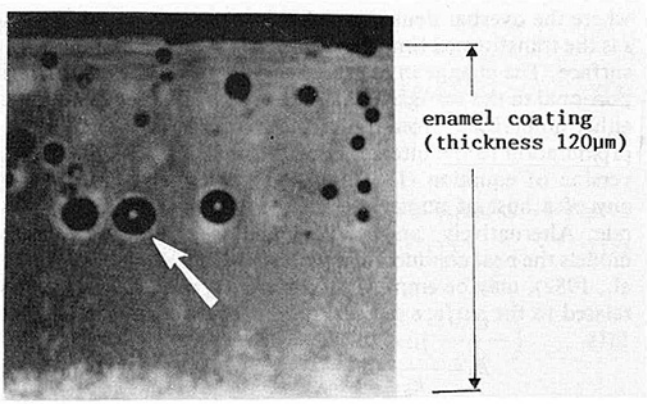

Fig. 2 Acoustic micrograph at 500 × magnification of section through enamel-coated sample; arrow shows typical void (approximately 10 μm diameter)

This paper describes the application of these new heat flux gages on two-layered model turbine blades in a cascade wind tunnel. Section 2 describes the gage construction, section 3 summarizes previous techniques, and the subsequent sections 4 and 5 detail new processing procedures coupled with experimental evaluations of both the multilayered gage and data processing in steady and highly unsteady flow, using a short-duration wind tunnel facility.

2 Gage Construction

The model turbine blade used in this work is shown in Fig. 1. The basic metal profile was coated with a vitreous enamel layer, by spraying and firing. This produces an electrically insulating layer which is non-porous to the platinum paint used in painting the gages on the surfaces.

An acoustic micrograph (magnification of 500) of a section through an enamel-coated test surface is shown in Fig. 2. This illustrates both the maximum size of the spherical voids that form during the firing of the enamel, and also the order of magnitude of the coating thickness (that illustrated is approximately 120 μm; the coating on the blade model was approximately 200 μm). The dimensions of the thin film gages used for this work are typically 0.5 mm wide by 10 mm long so that the width of the section contained in the photograph corresponds to approximately one quarter of the gage width. The porosity is small compared to the gage width, and because it consists of isolated bubbles, nowhere provides a conducting path to the blade surface. Consequently no electrical shorts were found to occur in painting on the gages prior to firing.

The assumption is not made that the thermal properties of the coating are uniform all around the surface of the blade. Instead, each gage is calibrated in situ, and the preferred calibration technique uses a radiant heat pulse, as described by Doorly (1985) and Doorly and Oldfield (1986a). The advantage of this is that the calibration procedure closely duplicates the actual conditions of experimental application, and local values of the thermal property and the thermal thickness parameter a/k are calculated. This avoids the errors that could be introduced if only the bulk properties of the enamel were used, corrected by a statistical estimate of the void distribution, using the theory of diffusion in heterogeneous media (Crank, 1979). The presence of the voids may, however, place some limitation on the absolute minimum gage dimensions; this question has yet to be considered.

3 Brief Theory of Thin Film Gage Use

(a) Gages on Single-Layer Substrate. This method is described more fully by Schultz and Jones (1973), Jones et al. (1979), and Oldfield et al. (1978). Painted platinum surface gages on machinable glass models are used to measure the heat flux. Solution of the one-dimensional constant property heat conduction equation by the Laplace transform method gives

$$\bar{\dot{q}}_0(s) = (s\rho ck)^{1/2}\bar{T}_0 \tag{1}$$

Nomenclature

a/k = thermal thickness parameter = thickness of enamel/thermal conductivity

$A = \dfrac{\sqrt{(\rho_1 c_1 k_1)} - \sqrt{(\rho_2 c_2 k_2)}}{\sqrt{(\rho_1 c_1 k_1)} + \sqrt{(\rho_2 c_2 k_2)}}$

A/D = analog to digital
c = specific heat capacity
$c(s)$ = digital filter
DFT = Discrete Fourier Transform
erfc = complimentary error function
f = frequency
FFT = Fast Fourier Transform
$h(t)$ = gage step calibration function
IDFT = Inverse Discrete Fourier Transform
$i(t)$ = impulse train
j = $\sqrt{-1}$
k = thermal conductivity
k_a = analog calibration constant
mgc = machinable glass ceramic
Nu = Nusselt number
pde = partial differential equation
$\dot{q}_0$ = surface heat transfer rate
Re = Reynolds number
s = Laplace transform variable
T = temperature
T_∞ = free-stream total temperature
t = time
Tu = overall turbulence intensity, percent
$U(t)$ = unit step function
v = voltage
v_a = analog output voltage
v_0 = film set voltage
w = angular frequency
x = vertical coordinate
$(\bar{\ })$ = transformed variable
α = temperature coefficient of resistance
$\delta(t)$ = unit impulse
$\hat{\delta}(t)$ = Dirac delta function
ρ = density
σ = $(\rho_2 c_2 k_2/\rho_1 c_1 k_1)^{1/2}$
τ = sampling interval

Subscripts

0 = surface
init = initial

where the overbar denotes the Laplace transformed function, s is the transformed time variable, and $\dot{q}_0$ is the heat flux at the surface. The change in resistance of the thin film gage is proportional to the surface temperature, so $\dot{q}_0$ may be determined either numerically from the surface temperature, using an approximation to the integral equation that results from the inversion of equation (1) (Cook and Felderman, 1966), or by any of a host of numerical methods that tackle the original pde. Alternatively, an electrical analog circuit that exactly models the heat conduction equation (Meyer, 1960; Oldfield et al., 1982), may be employed. The analog output voltage v_a is related to the surface temperature in transform space by

$$\bar{v}_a = \frac{s^{1/2}}{k_a}\,\bar{v} = \frac{v_0}{k_a}\,s^{1/2}\alpha\,\bar{T}_0 \tag{2}$$

(k_a is an analog calibration constant for the analog gain, v is the voltage across the film, v_0 is the pre-set film voltage, α is the film temperature coefficient of resistance).

(b) Gage on Two-Layered Semi-infinite Substrate. A brief account of the previously developed processing technique follows, although the derivation is different from that presented by Doorly and Oldfield (1986a), so as to facilitate a comparison with the new techniques.

Solution of the one-dimensional constant property heat conduction equation (1) through two layers (Fig. 3) leads to the relationship

$$\bar{\dot{q}}_0(s) = (\rho_1 c_1 k_1 s)^{1/2}\,\frac{(1 - A\,\exp\{-2a\sqrt{(s/\alpha_1)}\})\bar{T}_0}{(1 + A\,\exp\{-2a\sqrt{(s/\alpha_1)}\})} \tag{3}$$

where a is the thickness of the insulating layer, $A = (1-\sigma)/(1+\sigma)$, and $\sigma = (\rho_2 c_2 k_2/\rho_1 c_1 k_1)^{1/2}$.

The electrical analog no longer models the heat conduction through the two-layered substrate. It was shown by Doorly (1985) and Doorly and Oldfield (1986a), however, that the electrical analog may still be used to obtain the heat transfer rate. Essentially, the analog serves as an exact model for high frequency heat conduction in the top layer (which appears semi-infinite for short time scales), whereas a numerical correction is applied to the low-frequency signal component, to account for the second layer.

By substituting for $\bar{T}_0$ from equation (2) into equation (3), we obtain

$$\bar{\dot{q}}_0(s) = \sqrt{(\rho_1 c_1 k_1)}\,\frac{(1 - A\,\exp\{-2a\sqrt{(s/\alpha_1)}\})}{(1 + A\,\exp\{-2a\sqrt{(s/\alpha_1)}\})}\,\bar{v}_a(s)\,\frac{k_a}{\alpha v_0} \tag{4}$$

If we define

$$\bar{h}(s) = \frac{1}{s}\,\frac{(1 - A\,\exp\{-2a\sqrt{(s/\alpha_1)}\})}{(1 + A\,\exp\{-2a\sqrt{(s/\alpha_1)}\})} \tag{5}$$

and let the constant $K = \sqrt{(\rho_1 c_1 k_1)}\,\dfrac{k_a}{\alpha v_0}$

then

$$\bar{\dot{q}}_0(s) = K \cdot s \cdot \bar{h}(s) \cdot \bar{v}_a(s) \tag{6}$$

where v_a is the analog output voltage.

The s in equation (6) may be associated either with $v_a(s)$ or $h(s)$. In the former case, inversion gives

$$\dot{q}_0(t) = K \cdot \frac{d}{dt}(h(t)) * v_a(t) \tag{7a}$$

Choosing the latter, however, yields

$$\dot{q}_0(t) = K \cdot h(t) * \frac{d}{dt}(v_a(t)) \tag{7b}$$

where $*$ denotes convolution.

Assuming the analog output to be sampled with a sampling

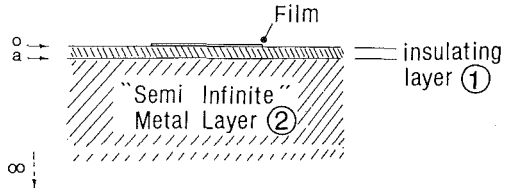

Fig. 3 Thin film gage on two-layered substrate with semi-infinite metal layer

interval τ s, then at a time $t = M\tau$, approximating the derivative in 7(b) by a backward difference, and using the trapezoidal rule to perform the integration defined by the convolution gives

$$\dot{q}_0(t) = K \sum_{n=1}^{M} h((M-n)\tau)\,\frac{(v_a(n\tau) - v_a(n-1)\tau)}{\tau}\,\tau \tag{8}$$

The inverse Laplace transform of the function $h(s)$ in (5) is given by

$$h(t) = 1 + 2\sum_{m=1}^{\infty}(-A)^m \operatorname{erfc}\frac{ma}{\sqrt{(\alpha_1 t)}} \tag{9}$$

for a gage on a two-layered substrate.

The calibration of the parameters $(\rho_1 c_1 k_1)$, $(\rho_2 c_2 k_2)$, a/k_1 required to obtain $\dot{q}$ from the analog voltage was described in Doorly (1985) and Doorly and Oldfield (1986a).

This method of obtaining $\dot{q}$ is accurate, but for large numbers of sampled data, is computationally quite time consuming, since it involves evaluating erfc, the complementary error function, by a sum of series, followed by a time convolution. An approximate operation count indicates that for an N point record, $N(N + 100)$ multiplications are required, where N^2 comes from the convolution and $100N$ from the evaluation of $h(t)$.

New Procedures to Obtain the Surface Heat Flux Using Multilayered Gages. The main thrust of the subsequent work is the description and evaluation of alternative procedures for obtaining the heat flux using multilayered gages. It is clear from the preceding that the use of a standard electrical analog by itself is not sufficient to derive the surface heat flux from the gage output signal, but that a further digital processing must be employed. As an alternative, therefore, one could consider numerically calculating the heat flux directly from the digitally recorded temperature signal. The problem with this, however, is that the amplitude of the fluctuating surface temperature signal, which is produced by a fluctuating surface heat flux, decreases in proportion to $\sqrt{f}$, where f is the frequency of the applied, time-varying heat flux. As is well known (Oldfield et al., 1982; Dunn et al., 1986), the consequence of this is that the high-frequency components of the imposed heat flux signal tend to disappear in the quantization error of the digitally recorded temperature signal. To overcome this, it is necessary either to boost the high-frequency component of the temperature signal prior to digital recording, or to use very high-precision A/D converters in a low-noise environment.

The analog boosts the signal by exactly matching the attenuation of the temperature fluctuations with a $\sqrt{f}$ frequency-dependent gain, over a broad working bandwidth, and in doing so, effectively also calculates the single-layer heat flux. An alternative procedure employed for the single-layered substrate case, from Dunn et al. (1986), is to record separately both the temperature and its derivative (using a wide band differentiator). The differentiator introduces a gain proportional to f, more than compensating for the attenuation of the high-frequency temperature signal. However, this has the disadvantage that the number of recording channels required is doubled. This technique has only been applied to gages on single-layered substrates.

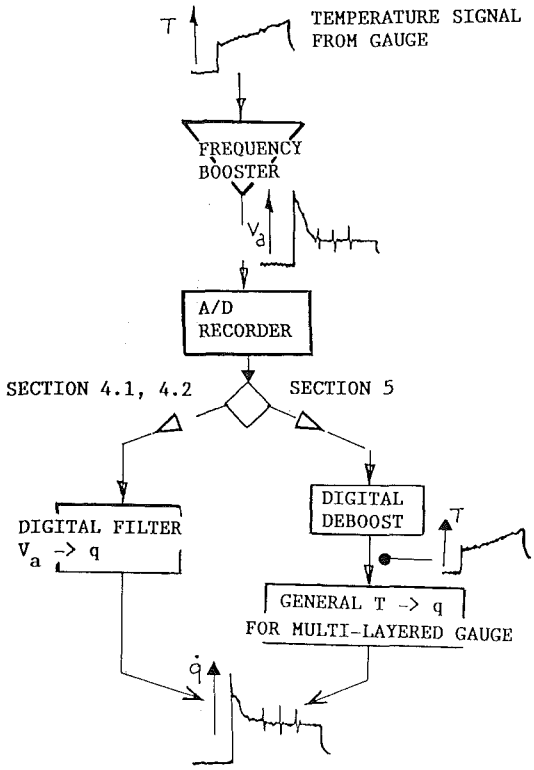

Fig. 4 Schematic of T to q processes

For the general case of processing the low or high-frequency signals from a single or multilayered gage, the subsequent procedures of sections 4.1 and 4.2 have been developed. In each case, the processing reduces to recovering the heat flux from a digitally recorded, frequency boosted temperature signal. Since the analog is, at present, the only circuit used for single-channel frequency boosting of temperature signals, the procedures have in each case been evaluated using this circuit as the booster. It is to be stressed, however, that the subsequent mathematical framework is equally valid for any general frequency boosting circuit. It is assumed that the frequency gain characteristic of the circuit is such that the amplitude of each spectral component of the signal is raised well above the quantization threshold, across the frequency band of interest.

Finally, in section 5, a technique is described that splits the boosting and temperature-to-heat flux calculations into separate procedures. This allows maximum flexibility (particularly in the incorporation of techniques to handle nonlinearities in the T to q conversion). A general schematic of these processes is given in Fig. 4.

4 Determining Heat Flux Using Digital Filters to Process Recorded Boosted Temperature Signals

4.1 Impulse Response of Processing Filter Obtained by Laplace Inversion. Using the analog as a frequency booster, the heat flux for a multilayered gage is given in transformed variables by

$$\bar{\dot{q}}_0(s) = \bar{K} \cdot \bar{c}(s) \cdot \bar{v}_a(s) \tag{10}$$

where $\bar{c}(s)$ is a digital filter to convert the boosted signal to the heat flux, and here

$$\bar{c}(s) = \frac{(1 - A\ \exp\{-2a(s/\alpha_1)^{1/2}\})}{(1 + A\ \exp\{-2a(s/\alpha_1)^{1/2}\})} \tag{11}$$

$\bar{c}(s)$ can be expanded as

$$\left(1 + 2\sum_{m=1}^{\infty} (-A^m)\exp(-2ma\sqrt{(s/\alpha_1)})\right) \tag{12}$$

Put

$$\bar{g}(s) = 2\sum_{m=1}^{\infty} (-A^m)\exp(-2ma\sqrt{(s/\alpha_1)}) \tag{13}$$

then $$\bar{\dot{q}}_0(s) = K \cdot \bar{v}_a(s) \cdot (1 + \bar{g}(s)). \tag{14}$$

Taking the inverse Laplace transform of equation (14) gives

$$\dot{q}_0(t) = K \cdot (v_a(t) + v_a(t) * g(t)) \tag{15}$$

where

$$g(t) = 2\sum_{m=1}^{\infty} \frac{ma}{\sqrt{(\alpha_1 \pi t^3)}} (-A)^m \exp - \left(\frac{m^2 a^2}{\alpha_1 t}\right) \tag{16}$$

For the combination of enamel/metal used, A is approximately -0.8, so that 20 terms in the above series reduce $(-A)^m$ to less than 1.0E−9.

Comparing equations (15) and (7*a*), it is clear that

$$(1 + g(t)) * v_a(t) = \frac{d}{dt}(h(t)) * v_a(t) \tag{17}$$

hence

$$1 + g(t) = \frac{d}{dt}(h(t)) \tag{18}$$

The evaluation of $g(t)$ is more computationally efficient than the evaluation of erfc in equation (7). For a straight time convolution, from equation (15), $N(N + 10)$ multiplications are required for an N point record, which is slightly faster than the equivalent evaluation in equation (8).

A Fast Fourier Transform algorithm may be used to accelerate the convolution operation in equation (15), by extending both $g(t)$ and $v_a(t)$ to length $2N$ with extra zeros ("zero padding"), as discussed by Brigham (1974), Rabiner and Gold (1975), and Burrus and Parks (1985). The infinite convolution is then replaced by a circular convolution, which gives an identical result over the original interval consisting of samples in $[0, N-1]$. Using the trapezoidal rule to approximate the convolution integral in equation (15) gives

$$g(m\tau) * v_a(m\tau) = \left[\sum_{r=0}^{m} g((m-r)\tau) \cdot v_a(r\tau) - \left\{\frac{1}{2} \cdot g(0) \cdot v_a(m\tau) + \frac{1}{2} \cdot g(m\tau) \cdot v_a(0)\right\}\right]\tau \tag{19}$$

The summation term is, in fact, both most accurately and rapidly evaluated using the identity

$$\sum_{r=0}^{m} g((m-r)\tau) \cdot v_a(r\tau) = \mathrm{FAC} * \mathrm{IDFT}\left[(\mathrm{DFT}(g) \cdot \mathrm{DFT}(v_a))\right] \tag{20}$$

where FAC is a factor equal to either $\sqrt{(2N)}$ or $2N$ depending on the FFT routine used. The particular routine used for this work was the NAG library routine C06EKF, which makes full use of the symmetry property of the discrete Fourier transform of real signals, and allows the signal length to be composed of up to 20 prime factors, so that there is no 2^N type restriction. The computational requirements are thus reduced to 3 times $2N\log N + 10N$ operations. The accuracy of the process was tested using the exact predicted analog output signal from a gage on a two-layered substrate, subject to a step in heat transfer rate, shown in Fig. 5. (Note that for a conventional gage on a single-layer substrate, the analog output would be a step.)

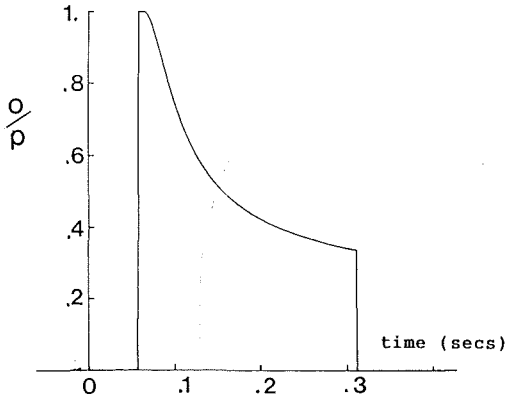

Fig. 5 Exact analog *o/p* for step input in heat flux

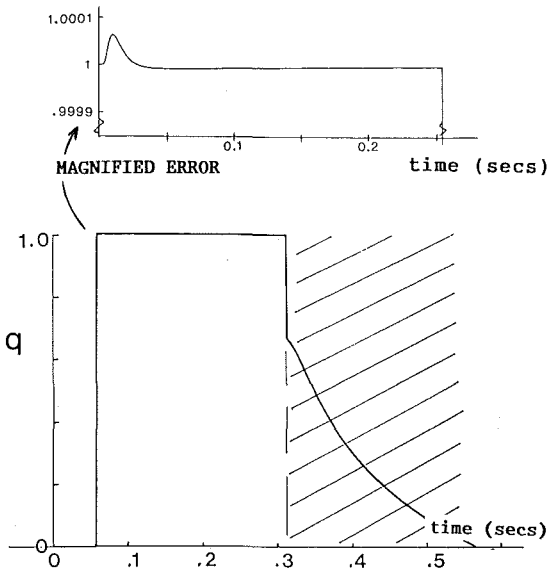

Fig. 6 Heat flux calculated by FFT convolution of exact *g(t)* and analog *o/p*

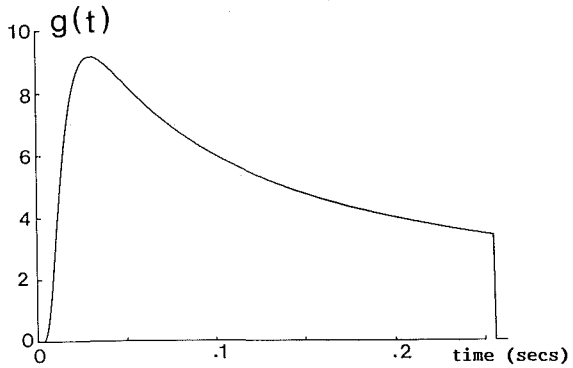

Fig. 7 Exact impulse response of post processing filter

The predicted signal is extended to double its original length by zero padding and the processed heat transfer rate using equations (15), (16), (19), and (20), is shown in Fig. 6. The impulse response of the post processing filter, g, is shown in Fig. 7. The maximum error in recovering the step in heat transfer is only 0.006 percent (Fig. 6*b*).

4.2 Processing Filter Specified by Sampling Frequency Transfer Function. For a general frequency boosting circuit with a prescribed frequency transfer function, it may not be possible to perform a straightforward inversion, as in 4.1, to obtain the correction filter. The following section describes an alternative approach in which samples of the frequency transfer function are used to specify the Fourier coefficients of the required filter; the technique is again illustrated using the analog as a boosting circuit.

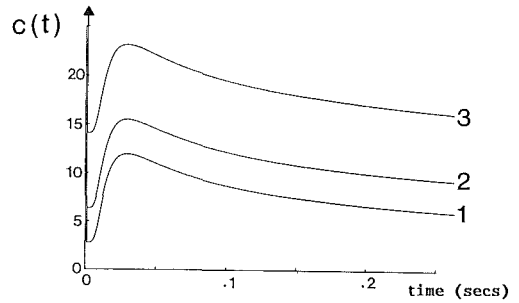

Fig. 8 Aliased impulse response *c(t)* for various amounts of zero padding: (1) impulse response of *c(t)* extended to *8N* samples; (2) impulse response of *c(t)* extended to *4N*; (3) impulse response of *c(t)* extended to *2N*

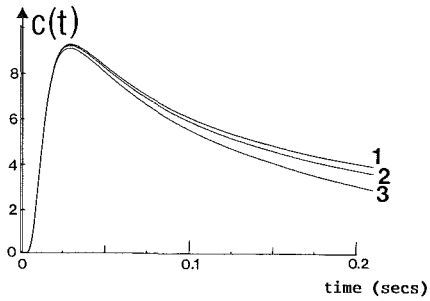

Fig. 9 Effect of removing constant offset from aliased impulse response: (1) impulse response of (1 + *G(w)*) filter: 2048 pts—8 N; (2) impulse response of (1 + *G(w)*) filter: 1024 pts—4 N; (3) impulse response of (1 + *G(w)*) filter: 256 pts

Writing jw for s in equations (10) and (11) shows that the Fourier transform of the surface heat flux equals the transform of the (analog) boosted temperature signal times the transfer function of the conversion filter $\bar{c}(jw)$. If the boosted temperature signal (of length N samples) is extended to M samples (where $M \geq 2N$) by zero padding, and the DFT taken, one could attempt to evaluate the surface heat flux as

$$\dot{q}_0(t) = K \cdot \mathrm{IDFT}\left\{\mathrm{DFT}(v_a) \cdot \sum_{r=0}^{M-1} \bar{c}(jw)\delta(w - rw_0)\right\} \qquad (21)$$

(i.e., the discrete transform of v_a is multiplied by the values of the exact transfer function $\bar{c}(jw)$ evaluated at the M frequency samples, and the inverse taken to yield $\dot{q}_0$). This could however yield a totally inaccurate result for q, particularly at the low-frequency end of the spectrum, depending on the characteristic of the filter $\bar{c}(jw)$. The cause of the error and the remedy can be illustrated using the $\bar{c}(jw)$ particular to the analog, defined by equation (11).

From equation (11) note that the frequency components of the filter c change very rapidly near $w = 0$, so that insufficiently closely spaced frequency samples result in aliasing of the impulse response in the time domain. Thus, the boosted temperature signal is effectively convolved in equation (21) with an aliased impulse response. The effect of the aliasing can be diminished by extending the length of the boosted temperature signal by progressively more zeros. [As the frequency intervals of the discrete transformed signal are proportional to $1/M$, increased zero padding in the time domain corresponds to more closely spaced frequency estimates (Rabiner and Gold, 1975).]

Alternatively, from equation (16) of the last section, it is clear that the exact impulse response of $c(jw)$ is given by

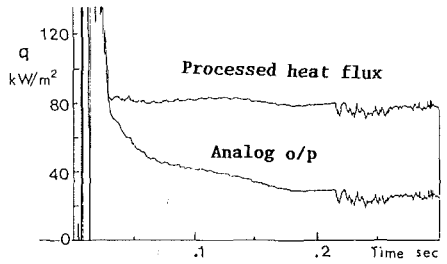

Fig. 10 Circular cylinder stagnation point q calculated using frequency sampled post processing filter

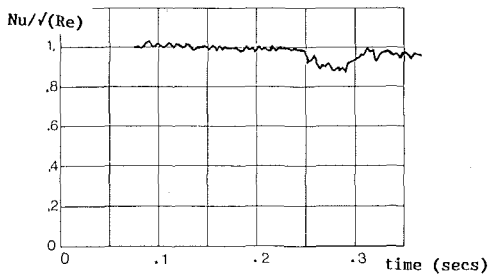

Fig. 11 Plot of $Nu/\sqrt{(Re)}$ for cylinder

$$c(t) = \hat{\delta}(t) + g(t) \tag{22}$$

$c(t)$ does not diminish to zero within any finite interval $M\tau$, but can be made as small as desired by increasing the interval by extra zero samples. In practice, an inordinate amount of zero padding may be required to reduce $c(t)$ sufficiently close to zero for the typical longest time scale (0.5 s) of experimental interest. The asymptotic decay of $c(t)$, which causes this, however, also ensures that as the amount of zero padding is increased, so the effect of aliasing on the first N samples of the extended trace tends toward the addition of a constant offset.

Figure 8 shows the aliased $c(t)$ for various amounts of zero padding, and Fig. 9 shows the result when the initial offset is subtracted. Although there is still significant aliasing when the signal is extended by eight times, Fig. 9 shows that, when the initial offset is subtracted, the impulse response is then graphically indistinguishable from that calculated by exact inversion, over the time of interest. In practice for a general boosting circuit, either the impulse response may be found by the above technique and applied in the manner of section 4.1, or, alternatively, an equivalent procedure to subtracting the offset from the impulse response is to extend the boosted temperature signal with an initial negative portion of equal area and equal or shorter duration, followed by zeros. Equation (21) may then be applied directly. A typical operation count for the procedure would be either $16N \log 8N$ to get the impulse response, followed by three times $2N \log 2N$ to apply the impulse response by convolution, or $16N \log(8N)$ to transform the extended and negatively cancelled boosted temperature signal, apply $c(jw)$ directly, and invert. The maximum inaccuracy decreases as the amount of zero padding increases, and is less than 0.5 percent for an eight times extended signal.

Experimental Results Processed Using the Method of Section 4.2: (*a*) *Circular Cylinder Data.* As reported by Doorly (1985) and Doorly and Oldfield (1986a), a two-layered circular cylinder model instrumented with thin film gages was tested in the Isentropic Light Piston Tunnel (I.L.P.T.) at Oxford, along with a machinable glass cylinder. This was done to check on the relative accuracy of the new and old gage systems, and also the absolute accuracy, by comparing the stagnation point heat transfer rate with the accepted experimental correlations and the theoretical predictions of

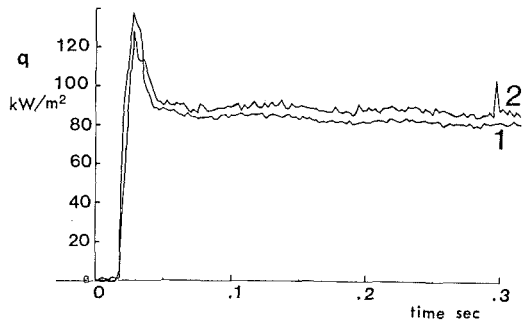

Fig. 12 (1) Heat flux from enamel blade; (2) heat flux from machinable glass blade

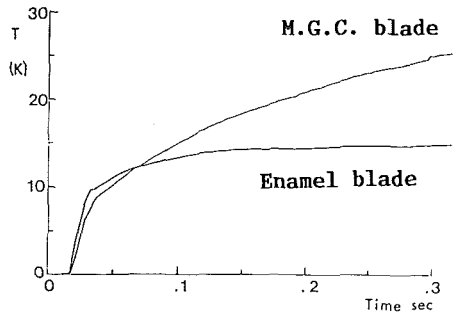

Fig. 13 Reconstructed surface temperatures

Lowery and Vachon (1975), Traci and Wilcox (1975), Kayalar (1968), and Schlichting (1979), giving $Nu/\sqrt{(Re)} = 1.01$ for $Tu = 0.0$. The analog output from one wind tunnel test and corresponding heat transfer rate, calculated using the frequency sampled post processing filter of section 4.2, are shown in Fig. 10. The corrected heat transfer rate is indistinguishable from that calculated using the time convolution procedure of equation (7) (reported by Doorly and Oldfield, 1986a), although a considerable saving in computational time has been achieved. Figure 11 shows a plot of $Nu/\sqrt{(Re)}$ calculated using the new procedure, confirming the absolute accuracy of the new gage calibration and processing. The disturbance in the traces of Figs. 10 and 11 at about 0.25 s is caused by the well-known "cold vortex," which is formed ahead of the piston in the I.L.P.T. Data obtained over this latter part of the run are not evaluated.

(*b*) *Blade Heat Transfer Rate.* An enamel-coated metal blade, instrumented with thin film gages, was placed in a cascade, along with a corresponding machinable glass blade to obtain a direct comparison between the single-layer technique and the two-layer technique. The heat transfer from the warm air to the model surface results in a significant rise in the surface temperature of the model, during the test time. The surface temperature history is needed so as to correct for the drop in heat flux, which results from the decrease in driving temperature ratio, or equivalently, in order to calculate the Nusselt number. The corrected heat transfer rate is given by

$$\dot{q}_{\text{corr}} = \dot{q}(t)_{\text{meas}} \cdot \left[\frac{T_\infty - T_{\text{init(blade)}}}{T_\infty - T(t)_{\text{blade}}} \right]$$

Further correction may be made for the thermal property changes as discussed in Doorly (1985).

The processed heat transfer rate from the enamel/steel blade using the method of Section 4.2 from a pressure surface film gage is shown in Fig. 12. The signal has been corrected for the decrease in driving temperature ratio, by using the calculated surface temperature rise in Fig. 13. A corresponding trace from a gage on the machinable glass blade is superimposed in Fig. 12; again this has been corrected for the drop in driving temperature, using the corresponding surface

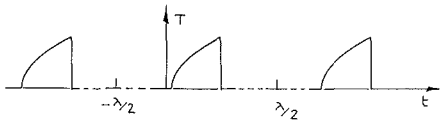

Fig. 14

temperature history. The agreement between the traces is very good, considering that the two gages are not positioned at exactly the same location on the blade surface, and allowing for some passage-to-passage variation. (The slight fall in both signals with time is due to a gradual decrease in the wind tunnel pressure, as the flow was not exactly matched.)

5 Direct Temperature to Heat Flux Processing

Instead of attempting to calculate the surface heat flux by further processing the digitally recorded boosted temperature signal as in Sections 4.1 and 4.2, an alternative is to deboost the signal digitally, recovering the original temperature (although uncorrupted by quantization errors), and then doing a straight T to $\dot{q}$ calculation. The digital deboosting procedure represents a form of low pass filtering, for which FFT techniques are particularly well suited. Such procedures are very straightforward and Rabiner and Gold (1975) describe FFT filtering techniques in great detail.

Concerning the T to $\dot{q}$ conversion, the main procedure examined also uses the FFT. The solution again makes the constant property assumption, however, for the typical temperature rise of the enamel coated model (Fig. 13), the process is considered sufficiently accurate (about 1 percent) for the present. The well-known method of lines (using the classical fourth-order Runge–Kutta time discretization) to solve the full linear or nonlinear partial differential equation (Mikhlin and Smolitsky, 1967) has been used to check the FFT based results. An explicit procedure for matching boundary conditions on the enamel/metal interface, using finite difference schemes, was given by Doorly (1985). Comparisons of finite difference methods with the FFT schemes are given by Doorly (1987), to be published.

Using the FFT, the surface heat flux may be calculated for a prescribed periodic surface temperature. Thus to calculate the heat flux for a temperature described by a finite-time duration function, the temperature is approximated by an equivalent long time periodic signal, which is extended by zero padding. The application of the FFT to solve the periodic problem follows. Note that it is possible to process the entire spectrum of the temperature fluctuations using this procedure.

The equations and boundary conditions for the problem are given in Doorly and Oldfield (1986a). The prescribed finite duration surface temperature is, however, given by

$$T(0, t) = T_0(t) \quad \text{for } |t| < \lambda/2$$
$$T(0, t) = 0 \quad \text{for } |t| \geq \lambda/2 \tag{22}$$

The temperature field $T(x, t)$ is first made periodic with period λ (Fig. 14) by convolution with the impulse train $i(t)$, where

$$i(t) = \lambda \sum_{r=-\infty}^{\infty} \delta(t - r\lambda) \tag{23}$$

i.e., using T_λ to represent the periodically extended temperature

$$T_\lambda(x, t) = T(x, t) * i(t) \tag{24}$$

Then, taking the continuous Fourier Transform (since $T(0, t)$ satisfies the Dirichlet conditions)

$$\Rightarrow \bar{T}_\lambda(x, f) = \bar{T}(x, f)\bar{i}(f) \tag{25}$$

$$= \bar{T}(x, f) \sum_{n=\infty}^{\infty} \delta(f - nf_0) = \sum_{n=-\infty}^{\infty} \bar{T}(x, nf_0)\delta(f - nf_0) \tag{26}$$

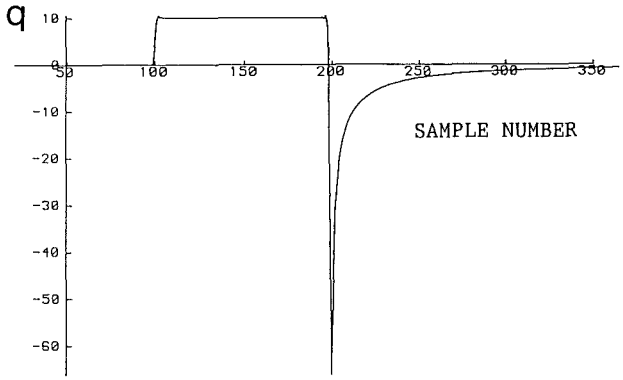

Fig. 15 FFT processed truncated parabolic temperature signal (extended by factor eight with zeros)

where $2\pi f_0 = 1/\lambda$, and so the discrete spectrum is obtained.

But

$$\bar{T}(x, nf_0) = \int_{-\infty}^{\infty} T(x, t)e^{-j2\pi nf_0 t}dt$$

$$= \int_{-\lambda/2}^{\lambda/2} T_\lambda(x, t)e^{-j2\pi nf_0 t}dt \tag{27}$$

since T is zero outside $(-\lambda/2, \lambda/2)$, and equal to T_λ within $(-\lambda/2, \lambda/2)$. Assuming we have expanded $T(x, t)$ so $T_\lambda(x, \lambda/2) = 0 = T_\lambda(x, -\lambda/2)$ then integration by parts and use of a zero initial condition gives an identical result to that for the usual Fourier transform, i.e.,

$$\int_{-\lambda/2}^{\lambda/2} \frac{\partial}{\partial t}(T_\lambda(x, t))e^{-j2\pi nf_0 t}dt = j2\pi nf_0 \bar{T}_\lambda(x, f) \tag{28}$$

Applying the boundary conditions and following an analysis similar to that performed in terms of the Laplace transform as in Doorly (1985)

$$\bar{q}_\lambda(0, f) = K\bar{D}(j2\pi nf_0)\bar{T}_\lambda(0, f) \tag{29}$$

where $\bar{D}(j2\pi nf_0) = \sqrt{(j2\pi nf_0)}\ \bar{c}(j2\pi nf_0)$ and $\bar{c}(j2\pi f)$ is given in terms of s in equation (11).

If only the N discrete sampled values of $T_\lambda(0, t)$ are taken, then as shown (Brigham, 1974) this reduces the integral in equation (27) to a finite sum, so

$$\bar{T}_\lambda(0, f) = \sum_{k=0}^{N-1} T_0(k\tau)e^{-j2\pi kn/N} \tag{30}$$

The DFT may then be used to obtain the periodic heat flux corresponding to the imposed periodic temperature, by inverting equation (29). The amount of zero padding required can be estimated analytically as follows. The truncated temperature signal may be written

$$T_0(t) = \sum_{n=1}^{N} a_n U(t - n\tau) - A_N U(t - (N+1)\tau) \tag{31}$$

where $a_n = T_0(n\tau) - T_0(n-1)\tau$, and $A_n = \sum_1^N a_n$.

Solution by Laplace transform yields

$$\dot{q}_0(t) = \sum_{n=1}^{N} \frac{a_n}{\sqrt{(\pi(t - t_n))}} - \frac{A_{N+1}}{\sqrt{(\pi(t - t_{N+1}))}}, \quad t > t_N \tag{32}$$

Figure 15 shows the heat flux obtained using the DFT to invert equation (29). The second term on the right of equation (32) is

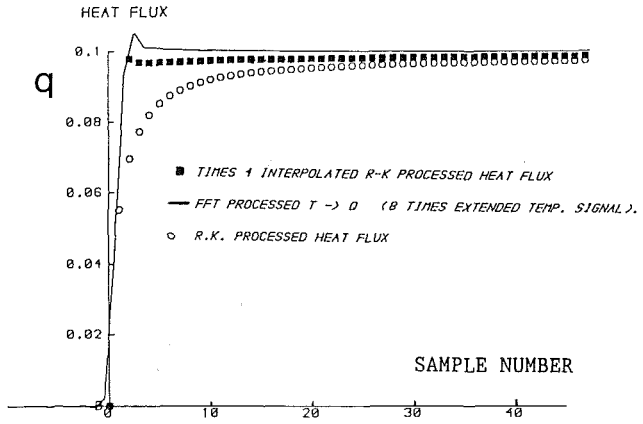

Fig. 16 Comparison between the FFT and Runge-Kutta calculated heat flux for a parabolic temperature input from a single-layered gage

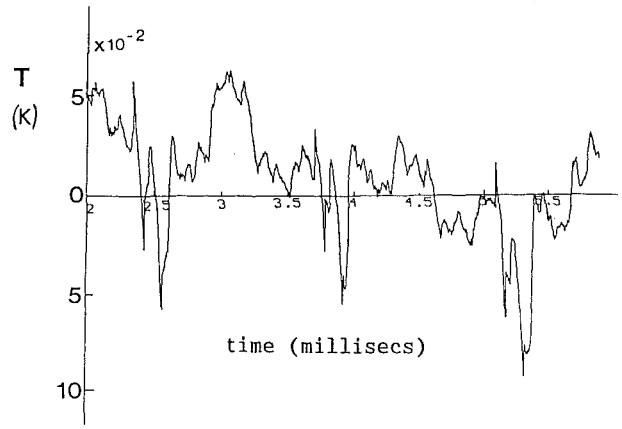

Fig. 17 Deboosted surface temperature (from unsteady heat transfer rate measured using analog)

responsible for the sharp negative impulse after the heat flux step. The difference between the terms in equation (32) decays asymptotically, so that if the original signal is extended to $8N$, the heat flux calculated over the first N samples is constant to within 0.1 percent.

The accuracy of the FFT processing was checked (Fig. 16) by calculating the heat flux corresponding to a surface temperature given by $T(t) = 2\sqrt{(t/\pi)}$, for which the analytic result is a constant step. To avoid Gibbs oscillations, a simple three-point Hanning smoothing (Rabiner and Gold, 1975) was applied to the eight times extended temperature trace before processing. Also shown in Fig. 16 is the heat flux calculated by a Runge–Kutta second-order finite difference scheme evaluated using only the prescribed temperature samples, and one where intermediate values were obtained by linear interpolation. As is clear, the FFT performs very well.

An example of the application of the technique to process experimental data follows. The temperature signal from a thin film gage on the surface of a coated metal turbine blade undergoing simulated engine unsteady flow [using the wake-generator at Oxford (Doorly and Oldfield, 1985a)] was passed through an electrical analog circuit to boost the high-frequency content. The analog output was digitally recorded using a Datalab DL2800 transient recorder. The recorder was operated in split timebase mode (as described by Doorly, 1983), whereby the signal was sampled at a slow rate of 1 ms/sample before the run up until a point about 75 ms after the flow initiation. A burst of 3500 samples at 2 μs/sample was then recorded to capture the unsteady flow effects.

The recorded signal was then deboosted, although not using FFT techniques since this would merely result in an identity in this case, and would not provide a suitable validation. Instead, a standard numerical integration was used (Doorly, 1985). The deboosted signal was then divided into the 596-point-long slow-speed sampled record, and the second 3500-point high-speed record.

Processing of the slow-speed sampled record to yield the mean heat transfer level (at the instant the high-speed burst of samples was recorded), was accomplished as described above,

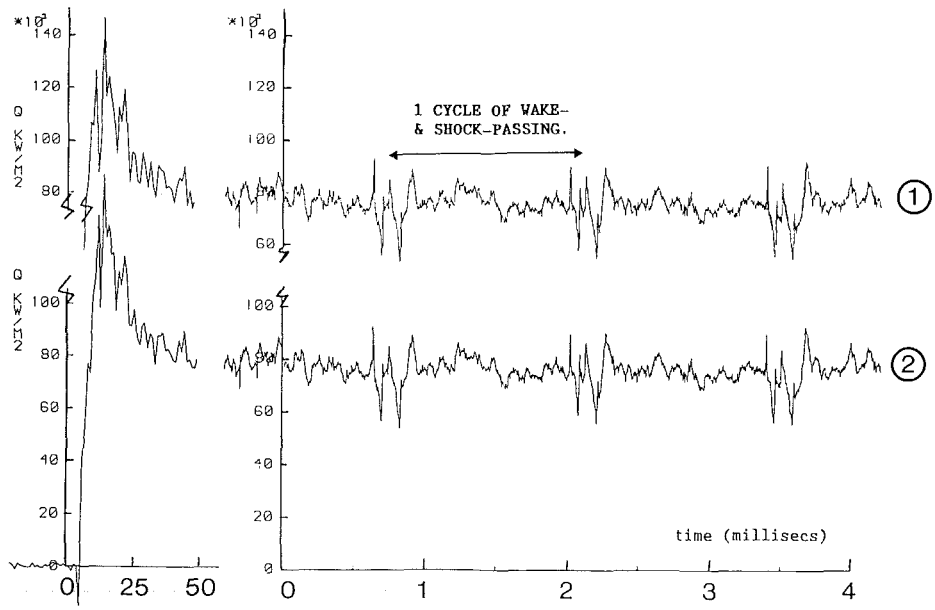

① **Fig. 18 Heat flux q calculated from surface temperature obtained by deboosting analog signal (as described in section 5)**

② **Fig. 19 Heat flux calculated by applying digital correction filter to analog signal (as described in section 4.2)**

using equation (29) and the inverse FFT. The high-speed signal was offset to zero mean value, extended to 4096 points by zero padding, and directly processed.

The deboosted surface temperature is shown in Fig. 17. The high-speed part of the heat transfer record in Fig. 18 is that obtained from the temperature trace of Fig. 17. Figure 19 shows the original analog output trace, where the low-speed data were processed by the method of section 4.2 to obtain the mean level of q. As can be seen, the high-speed traces of Figs. 17 and 18 are in excellent agreement, since $\bar{D}(jw)$ in equation (29) reduces to $\sqrt{(jw)}$ at high frequency. The minor differences in the low-speed traces are due to the smoothing applied to the FFT processed results to avoid Gibbs oscillations. (In any event, the fluctuations in the low-speed section are not meaningful, as the sampling rate is too slow.) The high-speed data were not smoothed at all.

6 Conclusions

1 Enamel-coated turbine blades have been satisfactorily produced and instrumented. Testing under steady and unsteady flow regimes has yielded accurate heat transfer rate measurements.

2 Various processing procedures to obtain the heat transfer rate from gages on single or multilayered substrates have been developed and evaluated. The recommendations for the choice of the most appropriate method are as follows:

If an electrical analog is used as the boosting circuit, then the method of section 4.1 should be adopted. If an alternative boosting circuit is used, then the impulse response should be derived analytically if possible and a similar procedure to that of section 4.1. utilized. If this is not straightforward, then the FFT may be used as in section 4.2 to obtain the required filter. Finally, for maximum flexibility, the boosted temperature signal may be deboosted. The heat flux may then be calculated either by the FFT based method of section 5, or an alternative full pde solver, e.g., the method of lines, may be employed to process results where nonlinear effects are significant.

Acknowledgments

Grateful thanks to Denis Doorly for advice on the analysis, Dr. M. L. G. Oldfield, for helpful discussions, and Dr. R. W. Ainsworth for his interest in this work. Rolls Royce plc and the Royal Aircraft Establishment (Pyestock) provided financial support for the work, which is gratefully acknowledged.

References

Ainsworth, R. W., 1976, D. Phil. Thesis, Oxford University, Oxford, United Kingdom.

Brigham, E. O., 1974, *The Fast Fourier Transform*, Prentice-Hall, pp. 94–108, Ch. 7.

Burrus, C. S., and Parks, T. W., 1985, *DFT/FFT and Convolution Algorithms*, Wiley, New York.

Chapman, D. R., and Rubesin, M. W., 1949, "Temperature and Velocity Profiles in the Compressible Laminar Boundary Layer With Arbitrary Distribution of Surface Temperature," *Jnl. Aero Sci.*, Vol. 16, No. 9, p. 547.

Cook, W. J., and Felderman, E. J., 1966, "Reduction of Data From Thin Film Heat Transfer Gauges. A Concise Numerical Technique," *AIAA Jnl.*, Vol. 4, No. 3, p. 561.

Crank, 1979, *The Mathematics of Diffusion*, Oxford, United Kingdom, pp. 266–285.

Doorly, D. J., 1983, D. Phil. Thesis, University of Oxford, Oxford, United Kingdom.

Doorly, D. J., and Oldfield, M. L. G., 1985, "Simulation of the Effects of Shock Wave Passing on a Turbine Rotor Blade," ASME *Journal of Engineering for Gas Turbines and Power*, Vol. 107, pp. 998–1006.

Doorly, J. E., 1985, D. Phil Thesis, Oxford University, Oxford, United Kingdom.

Doorly, J. E., and Oldfield, M. L. G., 1986a, "New Heat Transfer Gages for Use on Multilayered Substrates," ASME JOURNAL OF TURBOMACHINERY, Vol. 108, pp. 153–160.

Doorly, J. E., and Oldfield, M. L. G., 1986b, "The Theory of Advanced Heat Transfer Gauges," to be published in *Int. J Heat Mass Transfer.*

Doorly, J. E., 1987, to be published.

Dunn, M. G., 1986, "Heat-Flux Measurements for the Rotor of a Full-Stage Turbine: Part I—Time-Averaged Results," ASME JOURNAL OF TURBOMACHINERY, Vol. 108, pp. 90–97.

Dunn, M. G., George, W. K., Rae, W. J., Woodward, S. H., Moller, J. C., and Seymour, P. J., 1986, "Heat-Flux Measurements for the Rotor a Full-Stage Turbine: Part II—Description of Analysis Technique and Typical Time-Resolved Measurements," ASME JOURNAL OF TURBOMACHINERY, Vol. 108, pp. 98–107.

Epstein, A. H., Guenette, G. R., Norton, R. J. G., and Cao Yuzhang, 1986, "High Frequency Response Heat Flux Gauge for Metal Blading," AG-CPP-390 Paper No. 30.

Jones, T. V., Schultz, D. L., Oldfield, M. L. G., and Daniels, L. C., 1979, "A New Transient Facility for the Measurement of Heat Transfer Rates," in: *High Temperature Problems in Gas Turbine Engines*, AGARD CP-229, Ankara, Turkey.

Kayalar, L., 1969, "Experimentelle und Theoretische Untersuchungen uber den Einfluss des Turbulenzgrades auf den Warmeubergang in der Umgebung des Staupunktes eines Kreiszylinders," *Forschg. Ing.-Wes*, Vol. 35, pp. 157–167.

Kays, W. M., 1966, *Convective Heat and Mass Transfer*, McGraw-Hill, New York.

Lowery, G. W., and Vachon, R. I., 1975, "The Effect of Turbulence on Heat Transfer From Heated Cylinders," *Int. J. Heat Mass Transfer*, Vol. 18, pp. 1229–1242.

Meyer, R. F., 1960, "A Heat Flux Meter for Use With Thin Film Surface Thermometers," NRC Canada, Aero. Rep. LR-279.

Mikhlin, S. G., and Smotlitsky, K. L., 1967, *Approximate Methods for the Solution of Differential and Integral Equations*, Elsevier, New York.

NAG Numerical Algorithms Group, Oxford, United Kingdom.

Oldfield, M. L. G., Jones, T. V., and Schultz, D. L., 1978, "On-Line Computer for Transient Turbine Cascade Instrumentation," *I.E.E.E. Transactions on Aerospace and Electronic Systems*, Vol. AES-14, No. 5, pp. 738–749.

Oldfield, M. L. G., Burd, H. J., and Doe, N. G., 1982, "Design of Wide-Bandwidth Analogue Circuits for Heat Transfer Instrumentation in Transient Tunnels," *16th Symposium of I.C.H.M.T.*, Dubrovnik, Hemisphere.

Rabiner, L. R., and Gold, B., 1975, *Theory and Application of Digital Signal Processing*, Prentice-Hall, New Jersey.

Reynolds, W. C., Kays, W. M., and Kline, S. J., 1958, "Heat Transfer in the Turbulent Incompressible Boundary Layer II; Step Wall-Temperature Distribution," NASA TM 12-2-58W.

Rubesin, M. W., 1951, "The Effect of an Arbitrary Surface Temperature Variation Along a Flat Plate on the Convective Heat Transfer in an Incompressible Turbulent Boundary Layer," NACA TN 2345.

Schlichting, H., 1979, *Boundary Layer Theory*, 7th ed.

Schultz, D. L., and Jones, T. V., 1973, "Heat Transfer Measurements in Short Duration Hypersonic Facilities," AGARD AG-165.

Traci, R. M., and Wilcox, D. C., 1975, "Freestream Turbulence Effects on Stagnation Point Heat Transfer," *AIAA Journal*, Vol. 13, No. 7.

Vibration Amplitudes of Mistuned Blades

D. Afolabi
Assistant Professor of Mechanical Engineering,
School of Engineering and Technology,
Purdue University,
Indianapolis, IN 46223

Due to the mistuning effect, the nominally identical blades on a rotor are forced to vibrate with greatly unequal amplitudes under certain circumstances. It is, therefore, desirable to have the capability of predicting the highest responding blades so that such blades may be instrumented during engine tests. However, the predictions of various investigators in this regard are apparently inconsistent. Usually, the inconsistency is attributed to differences in mathematical models. By using modal analysis, it is shown that the various results are really not in conflict, but merely reflect the local and contrasting features in the global characteristics of a typical bladed disk. Good agreement is obtained when the results of this study, which is based on a model with structural coupling, are compared with those of other investigators utilizing models with aerodynamic and structural coupling. It is concluded that if the primary resonance being excited is not in a "crossover" zone, the highest responding blades are most likely to be those with extreme mistuning.

1 Introduction

An important objective in the design and operation of turbomachinery is to prevent excessive vibration amplitudes. However, amplitude prediction for a typical rotor is complicated by the mistuning effect. Mistuning refers to the nonuniformity in the structural properties of blades, and is usually described in terms of the "blade alone frequency" of each blade in a given mode of vibration: first flap wise (1F), second edge wise (2E), first torsional (1T), etc. It is well known that when even a small amount of mistuning is present, blade amplitudes generally become unequal under engine order excitations, whereas all the blades in a tuned assembly have equal amplitudes. Moreover, a very small number of blades in a mistuned system may be vibrating at excessively high levels while, at the same time, all other blades on the same disk may be virtually at rest – a situation that could lead to rogue blade failure (Afolabi, 1988).

In order to avoid such failures, it is important to preidentify those few blades which could have unusually large amplitudes. The identified blades may then be monitored closely during engine tests, when only a very small number may be strain-gaged. Although various research results have consistently predicted that blade amplitudes in mistuned assemblies could be greatly unequal, there is apparently no consensus on how the blades with the largest amplitudes may be identified. For instance, El-Bayoumy and Srinivasan (1975) and, later, Griffin and Hoosac (1984) concluded from their studies that the blades with cantilever frequencies close to the coupled blade-disk resonance usually respond the greatest. However, Afolabi's findings (1982) are that the blades with extreme detune are most likely to vibrate with the largest amplitudes in many bladed disk assemblies. This conclusion was also later reached by Ewins and Han (1984). In general, different blades are predicted from different theoretical studies.

In view of such apparent inconsistencies, the few blades to be instrumented during engine tests are still selected at random. However, in such a way, the high responding blades are as likely to be left out of the limited sample as any other blades, so that the successful completion of a test run may not necessarily yield accurate estimates of the largest amplitudes. There is therefore a need for further investigation of this important problem, so that the present confusing state may be clarified. In an earlier study (Afolabi, 1985b), an attempt was made in this direction to reconcile the apparently inconsistent findings of various investigators. This study is an extension of the earlier effort.

2 Theoretical Modeling

Many mathematical models have been devised by various authors for studying the mistuning problem. These include models with aerodynamic coupling (Bendiksen, 1980; Hoyniak and Fleeter, 1985; Kaza and Kielb, 1984; Srinivasan and Cutts, 1985; Whitehead, 1966), structural coupling (Afolabi, 1985a; Ewins, 1973; Fabunmi, 1978; Griffin and Hoosac, 1984), friction damping (Griffin and Sinha, 1985; Muszynska and Jones, 1983), etc. Generally, the equations of motion of turbomachine blades that are coupled structurally via the flexibility of the rotor disk, and rotating in a medium which admits of aerodynamic coupling, may be put in matrix form:

$$[M]\{\ddot{x}\}+([C]+\Omega[G])\{\dot{x}\}+([K]+\Omega^2[R]+j[H])\{x\}+[A(\omega, V)]\{x\}=\{f\} \quad (1)$$

Here, $\{x\}$ is the vector of generalized coordinates and $\{f\}$ is that of external loading; ω is the excitation frequency, Ω the speed of rotation, V the fluid velocity; while the square matrices represent the mass $[M]$; viscous damping $[C]$;

Contributed by the Gas Turbine Division for publication in the JOURNAL OF TURBOMACHINERY. Manuscript received at ASME Headquarters May 29, 1987.

gyroscopic action [G]; elastic stiffness [K]; centrifugal stiffness [R]; hysteretic damping [H]; and aerodynamic coupling [A]. For tuned models in which each blade is assumed to influence all other blades, the square matrices in equation (1) are circulant, except [G] which is skew symmetric. If only near-neighbor interaction is assumed, or if the system is mistuned, then the circulant matrices are reduced to having simple symmetry. Assuming sinusoidal motions, i.e., $x_i = X_i e^{j\omega t}$, time dependence may be removed from equation (1) to yield

$$[K_D(\omega, \Omega, V)]\ \{x\} = \{f\} \tag{2}$$

where $[K_D]$ is the complex, dynamic stiffness matrix of the system.

The specific nature of the matrices to be included in K_D depends on the degree of refinement desired by the analyst. For instance, the structural matrices may be derived from finite elements, lumped parameters, or receptance methods. Also, the aerodynamic coupling matrix may be formulated for various kinds of flow. Further, the dynamic stiffness matrix may include more factors than given in equation (1), or only a few of those factors may be considered. No matter what type of model is used in analyzing the complete system, provided it is admissible, the resulting equation (2) with null $\{f\}$ is an eigenvalue problem, which may be solved for $[\Lambda]$ and $[\Phi]$. These eigenmatrices are complex in the general case, giving rise to a modal frequency $\mathrm{Im}(\lambda_n)$, modal damping $\mathrm{Re}(\lambda_n)$, and modal vector $\{\phi\}_n \equiv \{\phi_R\}_n + j\{\phi_I\}_n$, for every mode of the system. Depending on the nature of [A], some system modes may be unstable. If all $\mathrm{Re}(\lambda_n) < 0$, then the stability of the system is assured, and steady-state vibration amplitudes may be calculated from

$$\{x\} = [\Phi]\ [G]^{-1}[\Phi]^H \{f\} \tag{3}$$

where the superscript H denotes a hermitian matrix transpose, and the matrix $[G] = [\Lambda] - \omega^2\ [\mathrm{I}]$. From modal analysis theory, equation (3) may be written in series form over all the M modes of the system as

$$\{x\} = \sum_{n=1}^{M} \frac{\{\phi\}_n^H\ \{f\}\ \{\phi\}_n}{(\omega_n^2 - \omega^2 a_n) + jb_n} =$$

$$\frac{c_1}{d_1(\omega)}\ \{\phi\}_1 + \frac{c_2}{d_2(\omega)}\ \{\phi\}_2 + \ldots + \frac{c_M}{d_M(\omega)}\ \{\phi\}_M \tag{4}$$

where a_n, b_n, c_n, and d_n are modal constants. The dependence of vibration amplitudes on various mathematical models may be investigated by using equation (4) and exploiting the orthogonality between $\{f\}$ and most of the system mode shapes.

2.1 Significance of Mode Shapes. In the tuned state, each mode shape may be written as a pure sine or cosine function of the blade slot number and a nodal diameter index. Thus, the ith element of the nth nodal diameter mode shape is

$$\phi_i = A_n \cos 2\ \pi ni/N + j \sin 2\pi ni/N \tag{5}$$

where A_n is a modal normalizing constant. In contrast, several nodal diameters are present simultaneously in a mistuned mode shape. Thus, if $M' = \mathrm{int}\ \{N/2\}$, then the ith element of the nth nodal diameter mode of a mistuned system is of the general form

$$\phi_i = \sum_{n=0}^{M} A_n(\cos 2\ \pi ni/N + j \sin 2\ \pi ni/N) \tag{6}$$

For both tuned and mistuned assemblies, the excitation on the ith blade by the mth engine order (EO) force may be written as

$$(f_m)_i = B_m \exp(j\beta), \quad \beta = 2\pi mi/N \tag{7}$$

where B_m is the amplitude of the force, β is the interblade phase angle, and N is the number of blades in the row. For a tuned system, the orthogonality of $\{f\}_m$ and $\{\phi\}_n$ $(n \neq m)$ is evident, by inspection of equations (5) and (7). The modal constant c_n in equation (4) therefore becomes

$$c_n = \{\phi\}_n^H\ \{f\}_m = D_{mn}\delta_{mn} \tag{8}$$

where D_{mn} is some norm and δ_{mn} is the Kronecker delta. Therefore, equation (4) is no longer a modal summation, since only one term, c_m, in the series does not vanish. The vector of tuned response amplitudes is then simply a scalar multiple of the symmetric mode shape, and may be written as

$$\{x\} = \frac{c_m}{d_m(\omega)}\ \{\phi\}_m \tag{9}$$

so that the ith element becomes

$$x_i(\omega) = A_m c_m / d_m(\omega) \cdot [\cos 2\pi mi/N + j \sin 2\pi mi/N] \tag{10}$$

resulting in equal magnitudes for the blades, and a constant interblade phase angle, at any given excitation frequency.

In the mistuned system, however, the mode shape is no longer symmetric, while the mth EO is still as described in equation (7). The response amplitude is then given by

$$\{x\} = \sum_{n=0}^{M} \frac{c_n'}{d_n} A_n\ \{\phi\}_n \tag{11}$$

where

$$c_n' = \sum_{n=0}^{M} A_n B_m\ (\cos 2\ \pi ni/N + j \sin 2\ \pi ni/N)$$

$$\cdot(\cos 2\ \pi mi/N + j \sin 2\ \pi mi/N)$$

As in the tuned state, all other terms except $c_m' = D_{mm}'$ must vanish due to orthogonality. Equation (11) may be rewritten (cf. equation (9)) as:

$$\{x\} = \frac{D_{mm}}{(\omega_m^2 - \omega^2 a_m) + jb_m}\ (A_1\ \{\phi\}_1 + A_2\{\phi\}_2 + \ldots + A_M\ \{\phi\}_M) \tag{12}$$

where the A_n are amplitudes of the Fourier decomposition of the mth mode shape, equation (6).

It is evident from the foregoing that the factor most responsible for the vastly contrasting features in the forced response characteristics of tuned and mistuned assemblies is the circular content of the system's eigenvectors, which may be determined from a Fourier analysis. In turn, the eigenvectors of a given mistuned system are strongly dependent on certain key elements in the system's physical characteristics. In their study of the mode shapes of a mistuned system of coupled pendula, Hodges and Woodhouse (1983) have shown that it is not merely the degree of mistuning (as measured, for instance, by the range or standard deviation of blade 1F) that determines the nature of system eigenvectors. Another important parameter is the strength of coupling, i.e., disk stiffness. Thus, it is the *ratio* of disorder to coupling strength that is very important. Since mode shapes are very sensitive to changes in a system's physical characteristics, it is very important to make a harmonic analysis to determine the nodal diameter content of the dominant eigenvectors before making predictions regarding forced response amplitudes. In an earlier paper (Afolabi, 1985b), it is shown that one may broadly identify three different types of eigenvectors. The classification was based on the relative magnitudes of the A_n resulting from a Fourier decomposition of mode shapes. Figure 1 shows a summary of the various response patterns and other vibration characteristics in each class. Class 1 mode shapes are almost like those of the tuned system, so that only one Fourier coefficient, A_m, is approximately nonzero. Class 2A modes have a few nonzero coefficients in addition to the dominant A_m. Also, the dominant mth mode is relatively well separated from

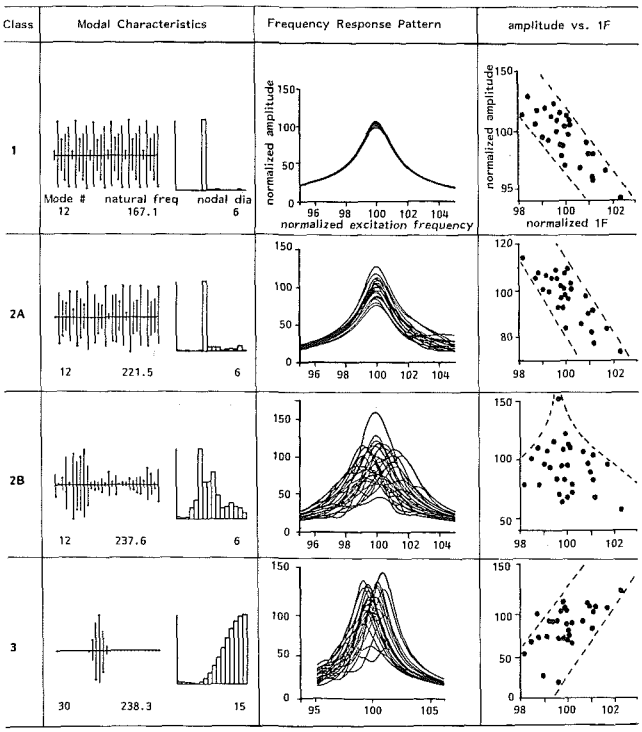

Fig. 1 Classification of vibration characteristics

other resonances, and all the blades reach their maximum amplitudes at the primary resonance ω_n. It is well known in modal analysis (e.g., Ewins, 1984), that when a mode is well separated from other modes, vibration amplitudes at the isolated resonance are not significantly influenced by the distant modes. In such a case the contributions by other modes to vibration amplitudes at the *primary resonance* are negligible, since A_n $(n \neq m) \cong 0$. The situation in Class 2A is also similar to this, except that more nonzero coefficients exist. Again, it is usually blades with extreme detune, e.g., lowest 1F, that vibrate with the largest amplitude in this class. Class 2B mode shapes have more Fourier coefficients, or nodal diameters, than those of Class 2A. As a result of this, and also due to the "crossover" phenomenon which has been described in detail by Afolabi (1985a), it is difficult to predict the particular slots of the blades likely to vibrate with the largest amplitude, although in principle they should be blades that are subject to the tuned absorber effect. Class 3 mode shapes are severely distorted from the symmetric shapes of the equivalent tuned system. However, the dominant resonances are clustered together within a much narrower band than in class 2B, so that there is considerable interference among the closely coupled modes. In general, the highest responding blades at a Class 3 mode are usually those with extreme detuning, e.g., highest 1F.

2.2 *Different Mathematical Models.* Any differences in response characteristics predicted by various models will depend on the extent to which the parameters used in the modal analysis ($\{f\}$, $[\Lambda]$, and $[\phi]$) are predicted differently by those models. If the parameters are predicted with qualitative similarity, then the calculated response patterns will also be qualitatively similar. For engine order excitations, virtually all the different methods model $\{f\}$ in terms of a constant interblade phase angle, equation (7). Similarly, most of the various models qualitatively predict $\{\phi\}_n$ alike; thus, tuned system modes are always pure sine or cosine forms as in equation (5). Because the different models used by various authors agree that the tuned $\{\phi\}_n$ and $\{f\}_m$ are as described in equations (5) and (7), respectively, identical response patterns have always been obtained for tuned systems. However, the eigenvalues (λ_n) in equation (4) may differ substantially in different models depending on the nature of the matrices retained in equation (1). Nevertheless, if the dynamic stability of the system is assured, such differences would not necessarily lead to considerable qualitative differences. For example, most models still predict similar frequency splits in the mistuned system, a cluster of eigenvalues near the blade cantilever frequency, etc., even though the actual magnitudes of the predicted frequencies may differ substantially.

No matter what type of mathematical model is used, three important conditions essentially govern the relative amplitudes of blades from modal analysis considerations, equation (4). They are:

(*a*) a qualitatively realistic prediction of $\{\phi\}_n$;
(*b*) orthogonality between some or most of $\{\phi\}_n$ and $\{f\}$;
(*c*) the relative location of λ_n in the eigenvalue spectrum, where λ_n is the dominant resonance excited by $\{f\}$. Therefore, when only a basic understanding of amplitude distribution is sought, the specific nature of the mathematical method used in obtaining the modal parameters is not of crucial importance, provided the parameters are qualitatively realistic. Thus, they may be determined by using any theoretical method, or from experimental tests – as described by Fabunmi (1978) and Ewins (1984) – or a combination of both.

Not all the terms in equation (1) are always considered in one study. Usually, some of the matrices are dropped, according to the underlying assumptions being made in the theoretical model, or the degree of refinement desired by the analyst. For instance, if the dynamic stability of the rotor is of prime consideration, then the aerodynamic coupling matrix $[A]$ cannot be ignored. In some other machines, it is assumed that the system is dynamically stable, and it is only necessary to make assessments of forced response amplitudes, in which case the aerodynamic coupling matrix $[A]$ may be ignored while some form of nonnegative aerodynamic damping may be included in $[C]$.

3 Results and Discussion

In the mathematical model employed for the present study, only structural coupling of the blades is accounted for. The model has been described in detail (Afolabi, 1984a) when a 30-bladed disk was used. In this instance, 72 blades are present in each of the four rotors. The datum, Rotor I, is the same rotor previously studied by Griffin et al. (1984, 1985) who used a model that includes both aerodynamic and structural coupling. Figure 2, which is divided into cells, gives a summary of the spectral characteristics of the lowest 20 modes of Rotor I. Each cell has two figures: The leftmost gives the relative amplitudes in free vibration, while the histogram displays the nodal diameter content of that mode shape. The dominant nodal diameter is indicated below the histogram. In each cell, the leftmost number is the serial number of that resonance in the system's eigenvalue spectrum, while the resonant frequency in cycles per second is given in the middle. The primary excitation used by Griffin et al. is the fifth engine order. An examination of the modal data of the rotor (modes 10 and 11 in Fig. 2) shows that the 5E0 modes are of Class 2B type. This means that the maximum amplitudes are likely to occur in a crossover zone, in which case the highest responding blades would depend to a large extent on the relative development of the crossover. If the dominant resonance is closer to class 2A, then the lowest 1F blades will still vibrate most. If, on the other hand, the dominant resonance is closer to class 3, then the highest 1F blades will have the largest amplitudes (see Fig. 1). In the most general case of Class 2B, it is difficult, in this author's experience, to correctly predict the slot numbers of the high-amplitude blades.

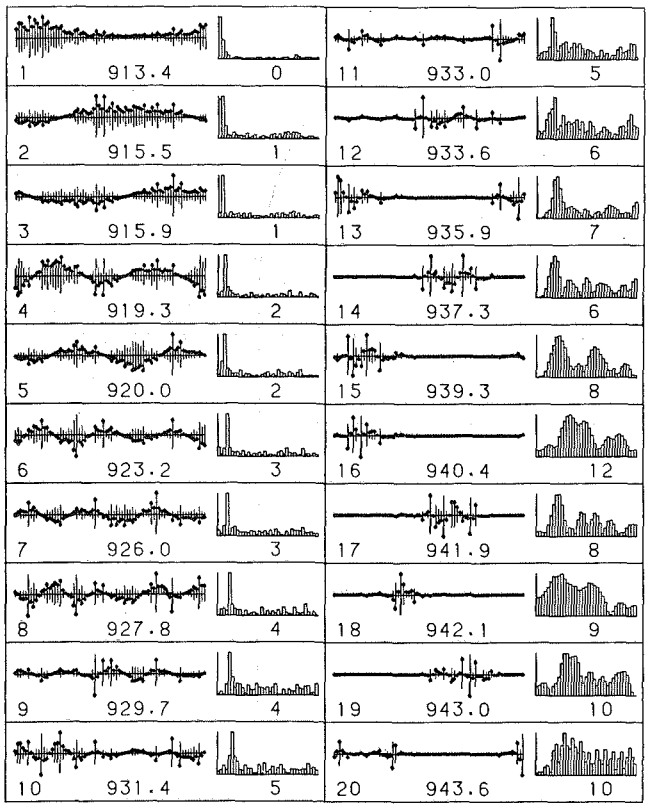

Fig. 2 Natural frequencies and mode shapes of Rotor I (modes 1-20)

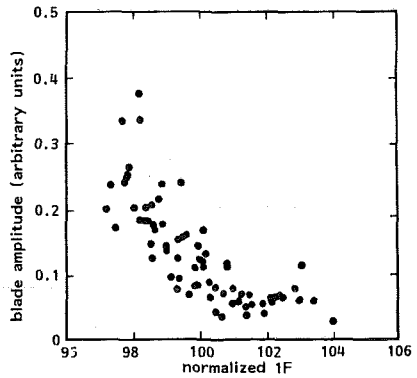

Fig. 3 Peak amplitudes of Rotor I in 5EO forced response (Griffin et al.)

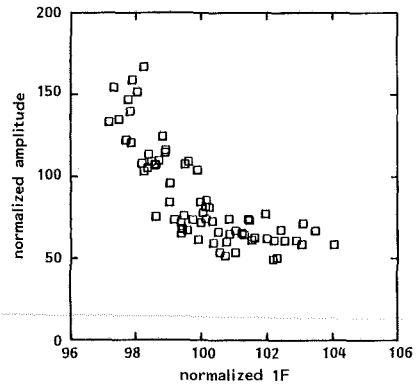

Fig. 4 Peak amplitudes of Rotor I in 5EO forced response (present study)

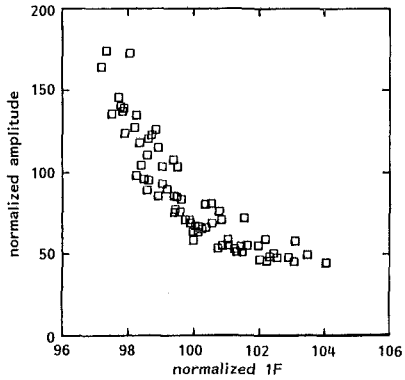

Fig. 5 Peak amplitudes of Rotor I in 3EO forced response (present study)

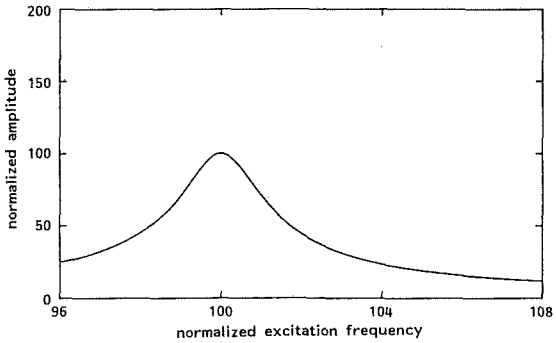

Fig. 6 5EO response of tuned Rotor I

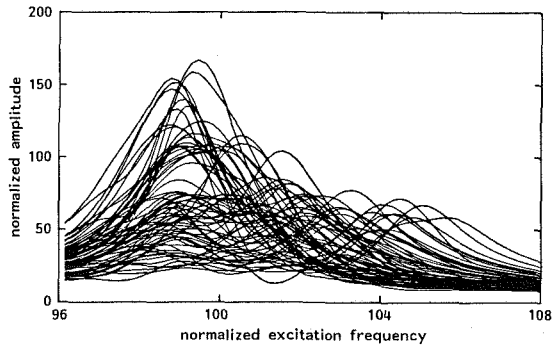

Fig. 7 5EO response of all blades in Rotor I

3.1 Relationship Between 1F and Peak Amplitudes. The scatter diagram in Fig. 3 shows the peak amplitudes ($\hat{x}$) versus mistuning (1F) for Rotor I, as calculated by Griffin et al. Figure 4 shows the data of the present investigation, which is based on a different model, for the same bladed disk. It is evident that the predictions of both models are qualitatively similar. The coefficient of correlation between $\hat{x}$ and 1F in both cases is -0.78. Because this class 2B resonance is close to the transition from class 2A, a relatively good correlation between amplitude and 1F is still obtained.

In general, Class 1 modes show the least complication from the tuned state. However, an examination of Fig. 2 shows that there is no Class 1 mode in this assembly. Instead, many Class 2A modes may be excited, for instance by a 3EO forcing. Since a reasonably accurate prediction of slot number may be made for class 2A modes, a simulation of the third order forcing of the assembly was carried out. The peak amplitude results are shown in Fig. 5. The coefficient of correlation between $\hat{x}$ and 1F is now significant, being $r = -0.87$. Nevertheless, it is still advisable to collect data for as many blades with extreme detune as possible, for more reliable inferential statistics.

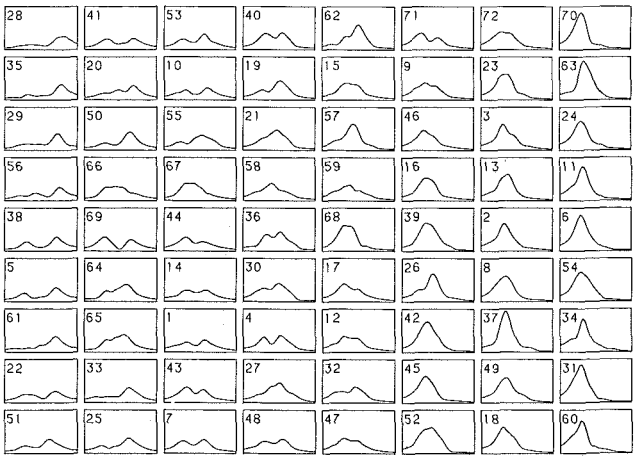

Fig. 8 5EO response of individual blades in Rotor I (plotted in order of blade 1F: 28, 35, 29, ..., 31, 60)

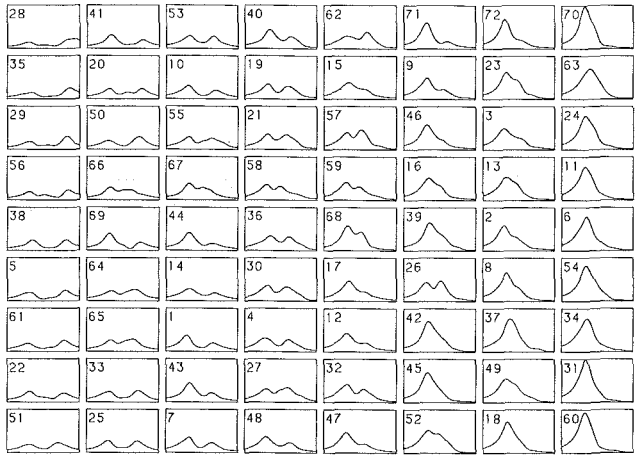

Fig. 9 3EO response of individual blades in Rotor I

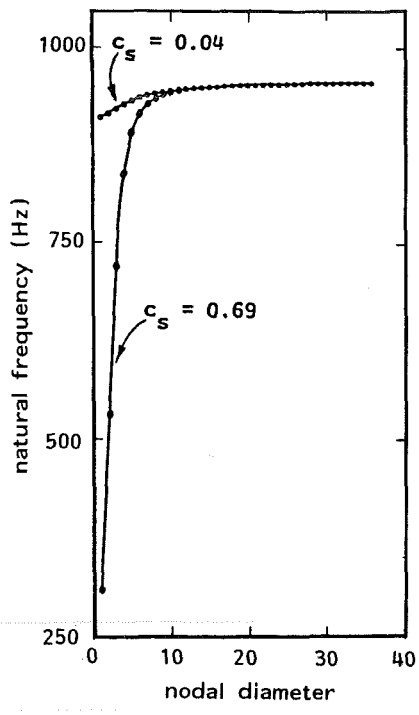

Fig. 10(*a*) Effect of coupling strength on eigenvalue spectrum

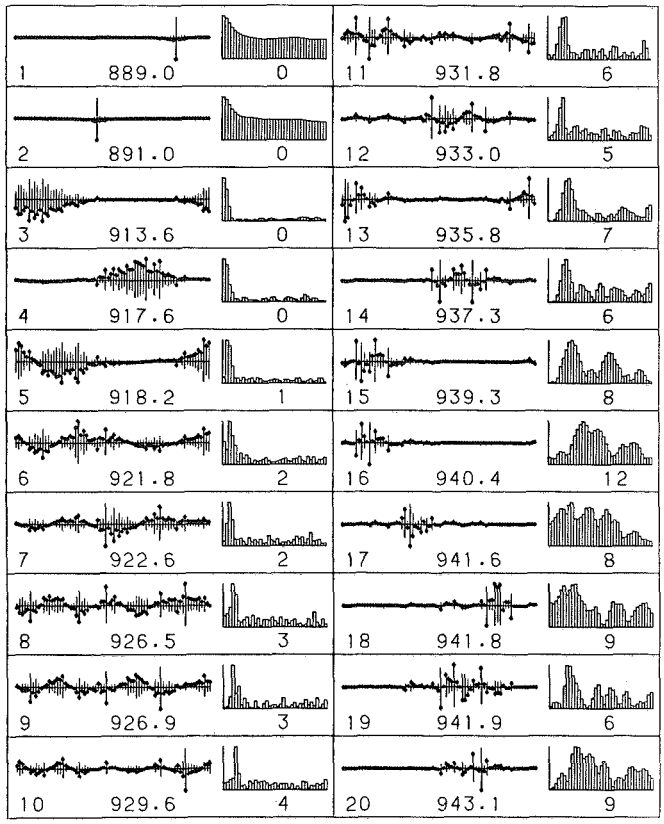

Fig. 10(*b*) Natural frequencies and mode shapes of Rotor III (modes 1-20)

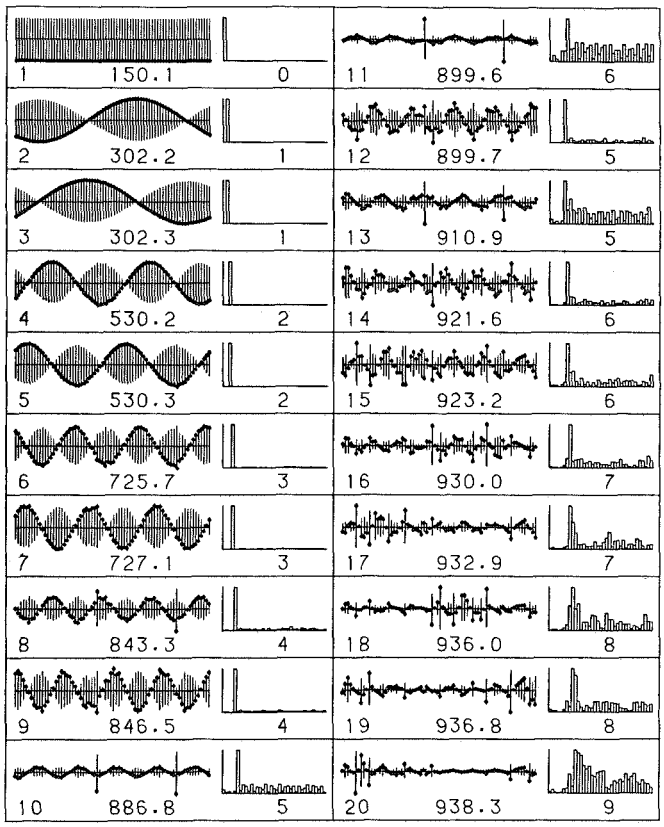

Fig. 10(*c*) Natural frequencies and mode shapes of Rotor IV (modes 1-20)

3.2 Frequency Response. The complicating effects of mistuning on vibration amplitudes may be appreciated from Figs. 6 and 7, which show, respectively, the 5EO response data for tuned and mistuned Rotor I. In the tuned system, all blades have equal amplitudes at each excitation frequency. They also reach their peak amplitudes at the primary resonance of the system. In contrast, the blades in the mistuned rotor reach their amplitudes at different frequencies (Fig. 7). By making reference to Fig. 1, it is seen that this type of response pattern is characteristic of Class 2B. The data shown in Fig. 7 are difficult to assimilate, and may be reprocessed as shown in Fig. 8. In the latter figure, the response of one blade is plotted at a time. The figure is also divided into cells. In each cell, the slot number of the blade being featured is given. The cells are ordered according to blade ranking in a descending order of 1F. Thus, the blade on slot 28 has the highest 1F, while the lowest 1F blade is on slot 60. It may be observed that low amplitude blades occupy the leftmost column of Fig. 8, while the highest responding blades are in the rightmost column. Thus, the limited correlation between peak amplitude and mistuning for this Class 2B resonance, which was observed in Fig. 4, is more clearly in evidence here. Figure 9 shows a similar presentation for the 3EO resonance, which is of Class 2A. As expected of this class, the blades with extreme detune have extreme amplitudes.

3.3 Effect of Frequency Scatter and Disk Stiffness. In their study of a mistuned pendula system, Hodges and Woodhouse (1983) have shown that the extent to which the mode shapes of a mistuned system deviate from the symmetric tuned form is dependent mainly on the ratio of disorder to coupling strength. For a mistuned rotor, the range of disorder is measured by $(1F_{max} - 1F_{min})/1F_{tuned}$, while the coupling strength c_s is equal to the ratio $(\omega_{max} - \omega_{1dia})/\omega_{max}$, where ω_{max} is the upper frequency of the pass band, and is practically equal to $1F_{tuned}$ in this case. A system with $c_s = 0$ has "weak" coupling, while $c_s = 1$ represents a rotor with extremely "strong" coupling. In this section, it is desirable to investigate the effect of disorder and coupling strength on vibration characteristics by creating three new rotors from the datum system. The datum, Rotor I, has a 1F disorder between 97 and 104 percent, while the coupling strength has a value of $c_s = 0.04$. In Rotor II, only the coupling strength is changed; all other parameters remain exactly as they were in Rotor I. The coupling strength was changed by making the disk more flexible, using a disk grounding stiffness of 429.5 N/m ($c_s = 0.69$), instead of 42,950 N/m as in Rotor I. Rotor III has the same coupling strength as Rotor II, but the 1F of blades 28, 31, 35, and 60 are changed to 1043.4, 900.6, 1033.3, and 898.5 Hz, respectively. This represents a range of 1F disorder between 93.2 and 108.3 percent. The 1F of all other blades remain as they were in Rotors I and II. Finally, Rotor IV has the coupling strength of Rotor I but the disorder of Rotor III. The eigenvalue curves for the tuned versions of the stiff (Rotors I and IV) and flexible (Rotors II and III) disks are shown in Fig. 10(*a*).

As predicted by Hodges and Woodhouse, it is not merely the extent of disorder in 1F that is important. Rather, it is the combined effect of disorder and coupling strength. Thus, the eigenvectors of Rotors III and IV which are shown in Figs. 10(*b*, c) are very much different from those in Fig. 2 for Rotor I. The 5EO responses of Rotors II–IV are shown in Figs. 11–13, respectively. Figures 11 and 12 are clearly of Class 2A and, as expected, the highest responding blades are those with extreme mistuning. Figure 13 shows that the 5EO response of Rotor IV is of lower Class 2B, as is that of Rotor I. The highest responding blade is therefore not a blade with extreme mistuning. This is due to the existence of the primary resonance in a crossover zone (Fig. 13*b*). However, by

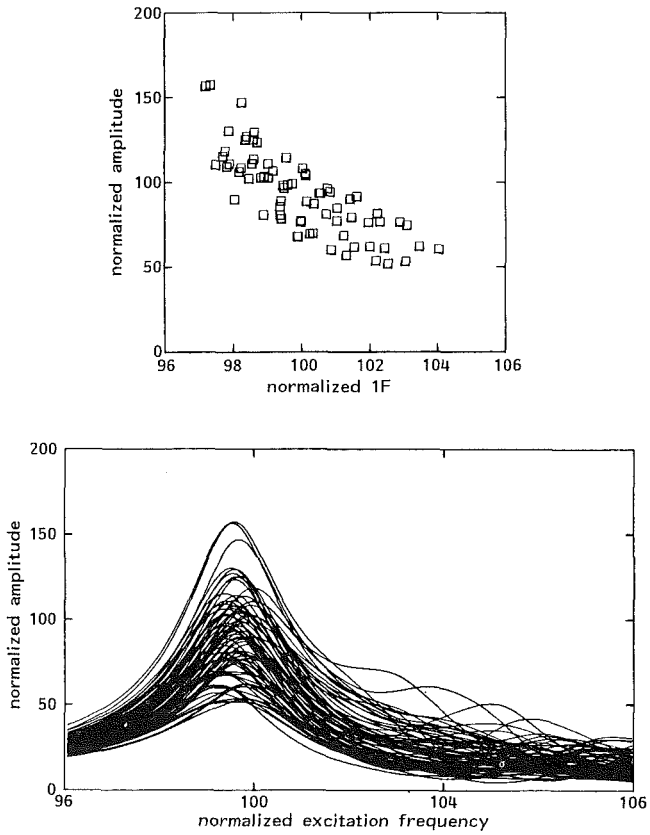

Fig. 11 5EO response of Rotor II: (*a*) peak amplitude, (*b*) frequency response

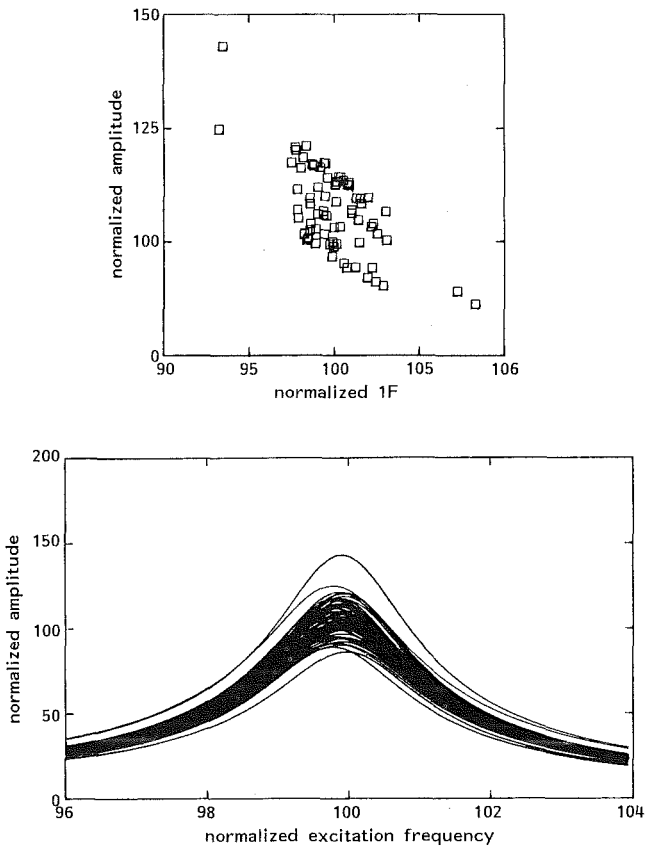

Fig. 12 5EO response of Rotor III: (*a*) peak amplitude, (*b*) frequency response

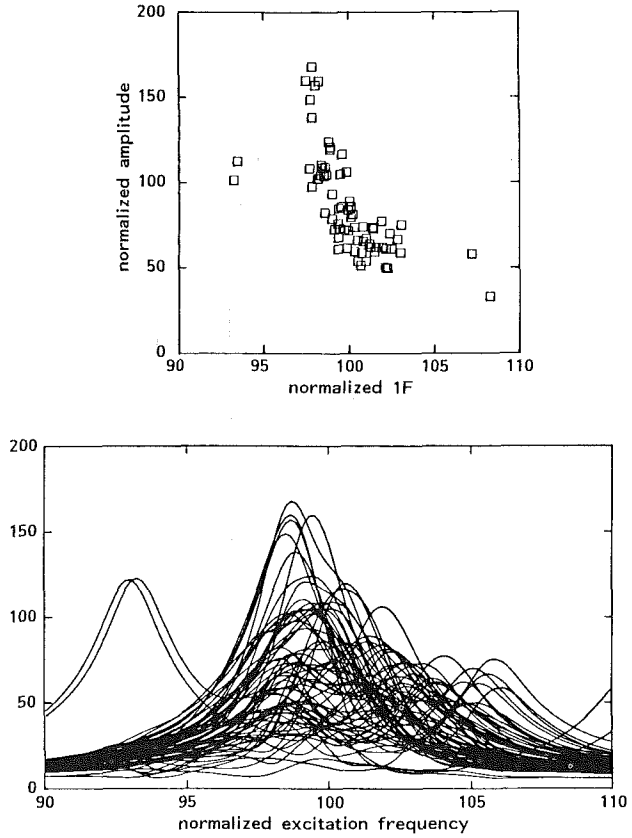

Fig. 13 5EO response of Rotor IV: (*a*) peak amplitude, (*b*) frequency response

monitoring a larger number of blades with extreme mistuning than in Class 2A, for example 8 out of 72 blades, one can still estimate the highest amplitude in Rotor IV accurately. It may also be noted that the lowest responding blades, even in Rotor IV, are those at the other extreme end of mistuning.

4 Conclusions

The three parameters that govern vibration amplitudes in any structural system are the complex eigenvalues and vectors of the system and the excitation force. The eigenparameters are sensitive to changes in system variables such as aerodynamic or structural coupling strength, range of 1F disorder, etc. For bladed disk assemblies exposed to engine order excitations, a critical factor is the orthogonality between system eigenvectors and excitation force. If the eigenvectors are predicted to reflect this orthogonality in a similar way by different mathematical models, then the amplitude predictions will also be similar, qualitatively. The application of different mathematical modeling does not necessarily lead to inconsistent results.

Contrasting characteristics may be observed in the response of a bladed disk at different segments of its eigenvalue spectrum, depending on the nature of the dominant eigenvectors at those segments. In order to make an accurate prediction of the high responding blades, it is important to predetermine the type of resonance likely to be excited. By making a Fourier analysis of the eigenvectors, one may determine the class of the dominant resonance. If Class 1 resonances are expected, then the variation of peak amplitudes among the blades may be ignored, since the scatter in response amplitudes will be rather small. For a resonance in Class 2A, the scatter is larger, but a good correlation usually exists between amplitudes and mistuning. It is, therefore, advisable to monitor blades with extreme detune for this class of resonance. In Class 2B, it is not easy to predict the particular blade that will have the largest amplitude. If the primary resonance is close to the transition from Class 2A – or, on the other hand, to Class 3 – then the high responding blades would still be those with the lowest or highest 1F, although more blades would have to be included in the sample than in Class 2A. In Class 2B, it is generally necessary to monitor a larger number of blades than in all other classes.

Acknowledgments

The cooperation of Professor J. H. Griffin of Carnegie-Mellon University in making his data available for comparison with the present study is gratefully acknowledged. Computation resources were provided by the Computer Center of Indiana University-Purdue University at Indianapolis.

References

Afolabi, D., 1983, "Vibration of Mistuned Bladed Disc Assemblies," PhD Thesis, University of London, United Kingdom.

Afolabi, D., 1985a, "The Frequency Response of Mistuned Bladed Disk Assemblies," in: *Vibrations of Blades and Bladed Disk Assemblies*, R. E. Kielb and N. F. Rieger, eds., ASME, New York, pp. 14–21.

Afolabi, D., 1985b, "The Eigenvalue Spectrum of a Mistuned Bladed Disk," in: *Vibrations of Blades and Bladed Disk Assemblies*, R. E. Kielb and N. F. Rieger, eds., ASME, New York, pp. 23–29.

Afolabi, D., 1988, "The Rogue Failure of Turbine Blades," *Journal of Sound and Vibration*, Vol. 122, in press.

Basu, P., and Griffin, J. H., 1985, "The Effect of Limiting Aerodynamic and Structural Coupling on Models of Bladed Disk Vibration," in: *Vibrations of Blades and Bladed Disk Assemblies*, R. E. Kielb and N. F. Rieger, eds., ASME, New York, pp. 30.

Bendiksen, O. O., and Friedman, P., 1980, "Coupled Bending-Torsion Flutter in Cascades," *AIAA Journal*, Vol. 18, pp. 194–201.

Crawley, E. F., and Hall, K. C., 1985, "Optimization and Mechanism of Mistuning in Cascades," ASME JOURNAL OF ENGINEERING FOR GAS TURBINES AND POWER, Vol. 107, pp. 418–426.

Dugundji, J., and Bundas, D. J., 1984, "Flutter and Forced Response of Mistuned Rotors Using a Standing Wave Analysis," *AIAA Journal*, Vol. 22, pp. 1652–1661.

El-Bayoumy, L. E., and Srinivasan, A. V., 1975, "Influence of Mistuning on Rotor Blade Vibration," *AIAA Journal*, Vol. 13, pp. 460–464.

Ewins, D. J., 1973, "Vibration Characteristics of Bladed Disk Assemblies," *Journal of Mechanical Engineering Science*, Vol. 15, pp. 165–186.

Ewins, D. J., 1984, *Modal Testing: Theory and Practice*, Wiley, New York.

Ewins, D. J., and Han, Z. S., 1984, "Resonant Vibration Levels of a Mistuned Bladed Disk," ASME *Journal of Vibrations, Acoustics, Stress and Reliability in Design*, Vol. 106, pp. 204–210.

Fabunmi, J. A., 1978, "Forced Vibrations of a Single Stage Axial Compressor Rotor," Ph.D. Dissertation, MIT, Cambridge, MA.

Griffin, J. H., and Hoosac, T. M., 1984, "Model Development and Statistical Investigation of Turbine Blade Mistuning," ASME *Journal of Vibrations, Acoustics, Stress and Reliability in Design*, Vol. 106, pp. 204–210.

Griffin, J. H., and Sinha, A., 1985, "The Interaction Between Mistuning and Friction Damping in the Forced Response of Bladed Disk Assemblies," ASME JOURNAL OF ENGINEERING FOR GAS TURBINES AND POWER, Vol. 107, pp. 205–211.

Hodges, C. H., and Woodhouse, J., 1983. "Vibration Isolation From Irregularity in a Nearly Periodic Structure: Theory and Measurements," *Journal of the Acoustical Society of America*, Vol. 74, pp. 894–905.

Hoyniak, D., and Fleeter, S., 1985, "Forced Response Analysis of an Aerodynamically Detuned Supersonic Turbomachine Rotor," in: *Vibrations of Blades and Bladed Disk Assemblies*, R. E. Kielb and N. F. Rieger, eds., ASME, New York, pp. 1–13.

Kielb, R. E., and Kaza, K. R. V., 1984, "Effects of Structural Coupling on Mistuned Cascade Flutter Response," ASME JOURNAL OF ENGINEERING FOR GAS TURBINES AND POWER, Vol. 106, pp. 17–24.

Muszynska, A., and Jones, D. I. G., 1983, "On Tuned Bladed Disk Dynamics: Some Aspects of Friction Related Mistuning," *Journal of Sound and Vibration*, Vol. 86, pp. 107–128.

Srinivasan, A. V., and Cutts, D. G., 1985, "Aerodynamically Excited Vibrations of a Part-Span Shrouded Fan," ASME JOURNAL OF ENGINEERING FOR GAS TURBINES AND POWER, Vol. 107, pp. 399–407.

Whitehead, D. S., 1966, "Effects of Mistuning on the Vibration of Turbomachine Blades Induced by Wakes," *Journal of Mechanical Engineering Science*, Vol. 8, pp. 15–21.

Temperature Effect on Particle Dynamics and Erosion in Radial Inflow Turbine

W. Tabakoff

A. Hamed

Department of Aerospace Engineering and Engineering Mechanics, University of Cincinnati, Cincinnati, OH 45221-0070

This paper presents the results of an investigation of the particle dynamics and the resulting blade erosion in radial inflow turbine rotors. In order to determine the influence of the temperature, the computations were performed for cold and hot inlet flow conditions. The results indicate that the trajectories of these small 5-μm ash particles are quite sensitive to the flow temperatures. In addition, gas turbines operating under hot flow are subjected to higher local blade erosion rates compared to cold flow conditions.

Introduction

Many industrial engines that utilize radial inflow turbines are often operated in dusty environments, or exposed to combustion gases of newly developed synthetic fuels or heavy oils. The growing concern for the precise determination of the erosive effects on the turbine components also coincides with the increased interest in burning different kinds of new fuels in industrial gas turbines. The unique characteristics of radial inflow turbines result in much higher rates of erosion than are normally experienced in axial flow turbines; this is due to higher particle concentrations consistently impacting relatively small metal areas. In addition, the very high centrifugal forces prevent the larger particles from going through the rotor of radial turbines.

Several studies have been conducted to investigate particle dynamics in axial flow turbomachines [1–5], but very few data are available in the literature for particle dynamics in radial inflow turbines [6]. Reference [7] describes a test program that was performed to relate the loss in a radial turbine operating lifetime to the amount and sizes of ingested particles. This study indicated that particles as small as 2–3 μm can still cause a serious loss in the engine operating lifetime. Reference [8] describes several design modifications to reduce the erosion in radial inflow turbines, but the test results of the same reference suggest only a slight improvement in the erosion, with their implementation. The analytical study of [6] presents similarity parameters for relating the particle trajectories in equivalent gas flow fields for different particle material densities and particle sizes. These parameters can be used to analyze trajectories for several particle characteristics from one set of computed trajectories.

The erosion of metals by solid particle laden flow has been investigated experimentally [9–11] to determine the parameters affecting the erosion rate. The results of these investigations demonstrate that for a given particle target material combination, the erosion rate is affected by the impacting velocity, impingement angle, and by the metal and gas temperatures [10, 11]. Their effects can be accurately simulated by experiments in carefully designed erosion tunnels where the gas particle stream conditions can be controlled [10]. Erosion cascade tunnels have also been used to determine experimentally the change in compressor cascade performance due to erosion [12]. A special code was developed to predict the blade erosion and was used to investigate the blade erosion in axial flow compressors [3] and turbines [2, 3]. The blade erosion in radial inflow turbines differs significantly from that in axial machines because of the unique particle blade impact locations and the difference in the impacting velocities and impingement angle relative to the blade surfaces. To the best of the authors' knowledge there are no data in the open literature that show the detailed erosion analysis on the blade surfaces in radial inflow turbines.

This paper presents the results of an analytical study of particle dynamics and blade erosion in radial inflow turbines under hot and cold flow operating conditions. The results of the trajectory calculations are presented for 5-μm fly ash particles. The results indicate that the high centrifugal forces on the particle, which oppose the drag forces at the turbine inlet, highly influence the trajectories of the small particles as they cross the turbine rotor and consequently affect the particle blade impact conditions and the resulting blade erosion. The particle blade impact locations and the magnitude and direction of the particle impacting velocity relative to the blade surfaces as determined from three-dimensional particle trajectory calculations are used in the analysis of the blade surface erosion. The blade surface erosion computations are based on these particle blade impact statistics and the experimental results of blade material erosion. The study reveals that under hot flow conditions, the internal turbine surfaces are subject to more than double the erosion encountered under cold flow conditions.

Contributed by the Gas Turbine Division of THE AMERICAN SOCIETY OF MECHANICAL ENGINEERS, and presented at the 32nd International Gas Turbine Conference and Exhibit, Anaheim, California, May 31–June 4, 1987. Manuscript received at ASME Headquarters February 10, 1987. Paper No. 87-GT-123.

Particle Dynamics

In the particle trajectory computation, it is assumed that the particles move only under the influence of aerodynamic forces, while the electrostatic forces are neglected. The general forms of the equations of motion of particles immersed in a fluid are written in a rotating frame of reference using cylindrical coordinates. The three components of the equations of motion are given by

$$\frac{\delta^2 r}{\delta t^2} - r\left(\frac{\delta\theta}{\delta t}\right)^2 - 2r\omega\frac{\delta\theta}{\delta t} - r\omega^2 = \frac{1}{2}\frac{\rho V^2 A C_D}{m}\frac{V_r}{|\bar{V}|} - g\cos(\theta+\sigma)\cos\phi \tag{1}$$

$$r\frac{\delta^2\theta}{\delta t^2} + 2\frac{\delta r}{\delta t}\frac{\delta\theta}{\delta t} + 2\omega\frac{\delta r}{\delta t} = \frac{1}{2}\frac{\rho V^2 A C_D}{m}\frac{V_\theta}{|\bar{V}|} + g\sin(\theta+\sigma)\cos\phi \tag{2}$$

$$\frac{\delta^2 z}{\delta t^2} = \frac{1}{2}\frac{\rho V^2 A C_D}{m}\frac{V_z}{|\bar{V}|} - g\sin\phi \tag{3}$$

In the above equations, ω is the angular velocity of the rotating frame about the z axis, ϕ is the angle between the turbine axis and the horizontal plane, and σ is the angular position of the reference axis $\theta = 0$ from the vertical direction.

The first term on the right-hand side of the equations (1)–(3) represents the drag force on the particles, which is dependent on the relative velocity of the gas with respect to the particles $\bar{V}$. The three components of this relative velocity vector are

$$V_r = w_r - \frac{\delta r}{\delta t}$$

$$V_\theta = w_u - \frac{r\delta\theta}{\delta t}$$

$$V_z = w_z - \frac{r\partial\theta}{\delta t} \tag{4}$$

where w_r, w_u, and w_z are the radial, tangential, and axial components of the gas velocity relative to the rotor, and $\delta r/\delta t$, $r\delta\theta/\delta t$, and $\delta z/\delta t$ are the radial, tangential, and axial velocity components of the particle velocity in the rotating reference frame.

The drag coefficient of a spherical particle is well known from the experimental measurements over a wide range of Reynolds numbers. Because of the significance of C_D in equations (1), (2), and (3), a description of the drag coefficient in algebraic form is necessary for the numerical solution of the particle trajectories. The value of C_D was determined using the following relations:

$$C_D = 4.5 + \frac{24}{\mathrm{Re}} \qquad \mathrm{Re} < 1.0 \tag{5a}$$

$$C_D = 28.5 - 24.0(\log \mathrm{Re}) + 9.0682(\log \mathrm{Re})^2 - 1.7713(\log \mathrm{Re})^3 + 0.1718(\log \mathrm{Re})^4 - 0.0065(\log \mathrm{Re})^5 \qquad 1.0 < \mathrm{Re} < 3000 \tag{5b}$$

$$C_D = 0.4 \qquad 3000 < \mathrm{Re} < 2.5\times 10^{-5} \tag{5c}$$

The Reynolds number is expressed as

$$\mathrm{Re} = \frac{\rho_g |\bar{V}| D_p}{\mu_g} \tag{6}$$

The particle trajectories are determined from the numerical integration of the equations of motion of the solid particles in the appropriate flow field [9, 14]. In the case of radial inflow turbines, the particle trajectories are computed through the scroll, the nozzle, and the rotor, thus requiring a knowledge of the different flow fields in these components. The influence of gravitational forces is generally minimal compared to the aerodynamic forces in axial flow machines, and in the rotor of radial machines. However, gravity can have a significant influence on particle trajectories in the scroll where the flow velocity can be very low.

Particle Blade Impacts and Blade Material Erosion. The experimental measurements in the erosion tunnel provide erosion data for a given particle target material combination. The target erosion is known to depend on the particle impact velocity, impingement angle, and the flow and target temperature for a given particle target material combination. The same tunnel is also used for measuring the particle rebounding characteristics using laser-Doppler velocimetry through a specially equipped window. These measurements are used to derive correlations for the restitution ratio, i.e., the ratio between the rebounding and incoming velocities. These correlations are used in the particle trajectory computations to determine the particle rebound conditions after blade impacts.

Experimental measurements were obtained in the erosion tunnel for fly ash particles impacting RENE 41 sample material at different impacting velocities, impingement angles, and target temperatures. The following empirical equations for the tangential and normal rebounding restitution ratios were derived from the experimental measurements of the particles impact and rebounding velocities using the laser-Doppler velocimeter:

Nomenclature

A = particle cross-sectional area
C_D = particle drag coefficient
D_p = particle diameter
e_T = tangential rebounding restitution ratio
e_N = normal rebounding restitution ratio
g = gravitational acceleration
m = particle mass
r = radial coordinate
Re = Reynolds number
t = time
V = particle relative velocity to the gas
V_1 = particle relative impact velocity
w = gas velocity
z_t = axial coordinate
β_1 = particle relative impingement angle
γ = particle blade impact frequency, number of impacts/m^2/number of particles
ϵ = target material erosion parameter, mg/g
ϵ_b = blade surface specific mass erosion parameter, mg/m^2/g
θ = angular coordinate
μ_g = gas coefficient of dynamica viscosity
ρ_g = gas density
ω = rotor speed, rad/s

Subscripts

g = gas
p = particle
r = component in radial direction
z = component in axial direction
θ = component in circumferential direction

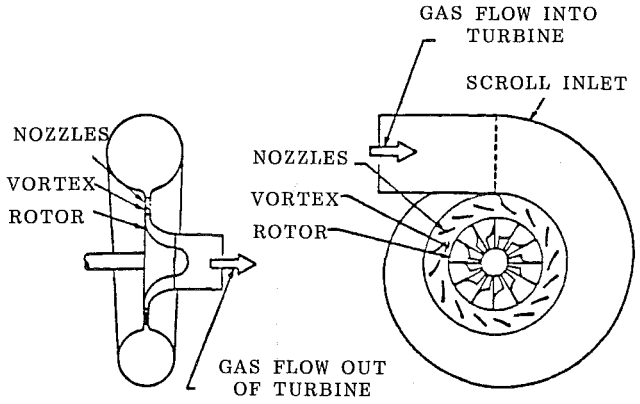

Fig. 1 Turbine model used in analytical study

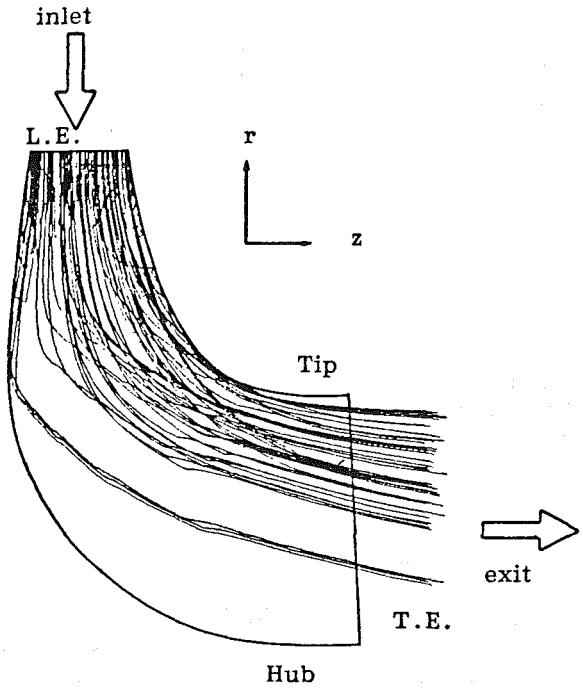

Fig. 2 Projection of particle trajectories in the *r*–*z* plane for cold flow

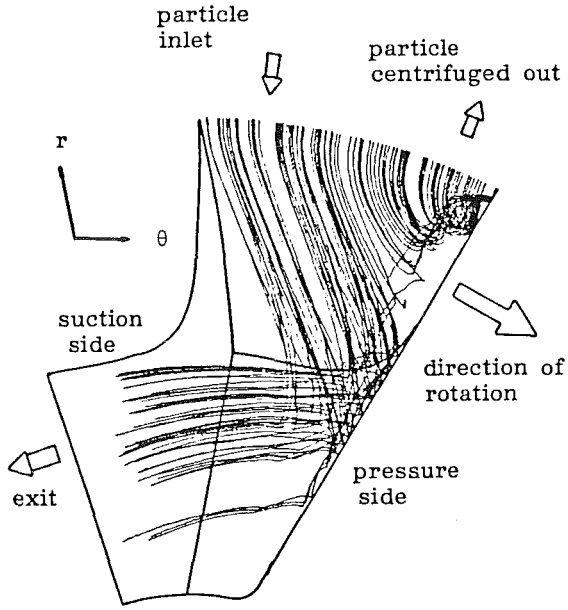

Fig. 3 Projection of particle trajectories in the *r*–*θ* plane, for cold flow

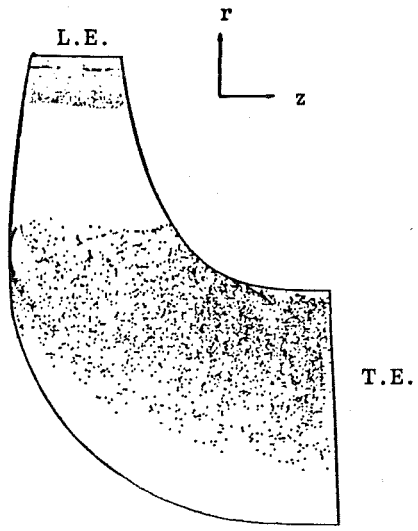

Fig. 4 Particle impact locations on the rotor pressure surface for cold flow

$$e_T = 1.01029 - 1.34759\beta_1 + 4.59474\beta_1^2 - 6.56109\beta_1^3 + 3.05952\beta_1^4$$

$$e_N = 1.00577 - 1.78169\beta_1 + 2.88518\beta_1^2 - 2.49243\beta_1^3 + 0.76224\beta_1^4 \quad (7)$$

where V_1 and β_1 are impact velocity and impingement angles, respectively. The experimental data from the erosion tests were used to obtain the following empirical equation for the erosion mass parameter ϵ, which is defined as the ratio of the eroded mass of target material to the mass of impinging particles:

$$\epsilon = 8.19 \cdot 0.00377 F(T)\left[\left(\frac{V_1}{100}\right)^{2.19}\cos^2\beta_1(1-e_T^2) + 0.053\left(\frac{V_1}{100}\right)^{2.24}\sin^2\beta_1(1-e_N^2)\right] \quad (8)$$

In the above equation $F(T)$ is a parameter that expresses the influence of the temperature in the erosion equation. It takes into account the variation of the target material yielding strength with its temperature and is given by

$$F(T) = \left[\left(\frac{Y_{srt}}{Y_s}\right)^{3.869} + \left(\frac{Y_s}{Y_{srt}}\right) - 1\right] \quad (9)$$

where Y_s is the yielding strength of the target material at the elevated temperature, and Y_{srt} is the yielding strength of the target material at room temperature.

The empirical correlations for the restitution ratios (equations (7)) are used in the particle trajectory code to determine the particle rebound conditions after each blade, hub, or casing impact. The blade erosion computations combine the empirical correlation for the mass erosion parameter (equations (8) and (9)) with the results of the particle trajectory calculations in the form of impact velocities and impingement angles, for a large number of particle trajectories.

Computation Procedures. The flow computations were performed for a typical radial inflow turbine model as shown

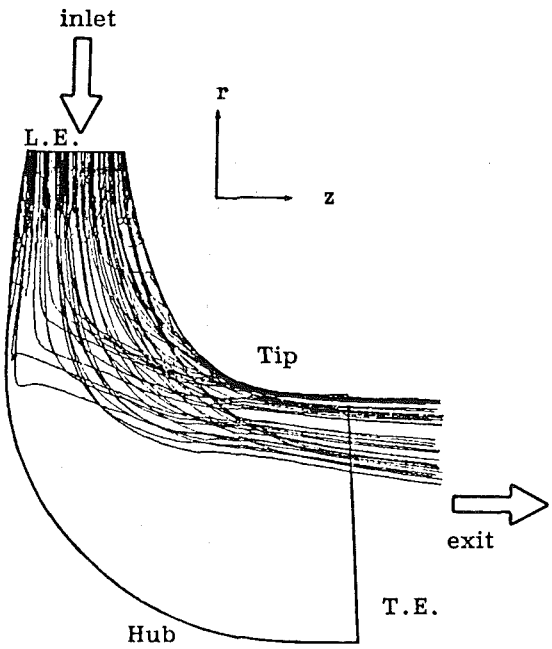

Fig. 5 Projection of particle trajectories in the r–z plane for hot flow

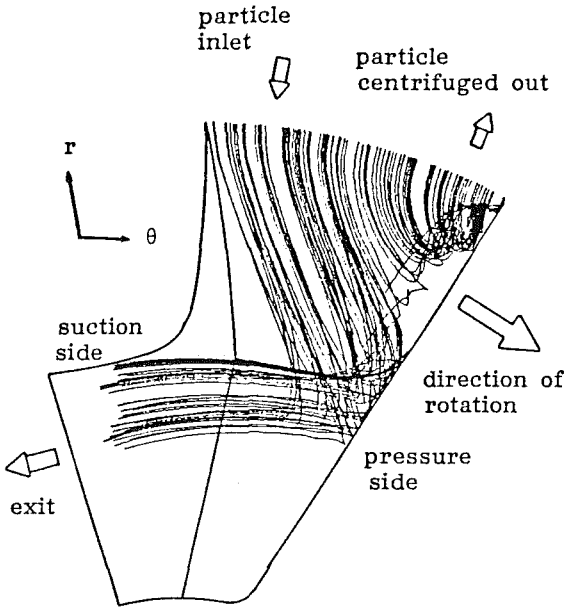

Fig. 6 Projection of particle trajectories in the r–θ plane for hot flow

in Fig. 1. The rotor tip diameter is equal to 11.43 cm and the mass flow rate was taken equal to 0.6 kg/s at 51,500 rpm. The rotor flow field was calculated using the code of [15]. The midchannel hub-to-tip stream surface solution provides the gas density and the relative gas velocity components in the radial, circumferential, and axial directions at the computational grid points. The velocity gradient in the circumferential direction is also determined in the flow solution and used to represent the blade-to-blade flow field variation as described in [4]. The flow field computations in the radial inflow turbine rotor were performed for two points corresponding to hot and cold operating conditions. The inlet temperatures and pressures were 328 K and 2.86 atm for cold flow and 810 K and 4 atm for hot flow. Significant differences were observed between the flow fields in the two cases, particularly in the

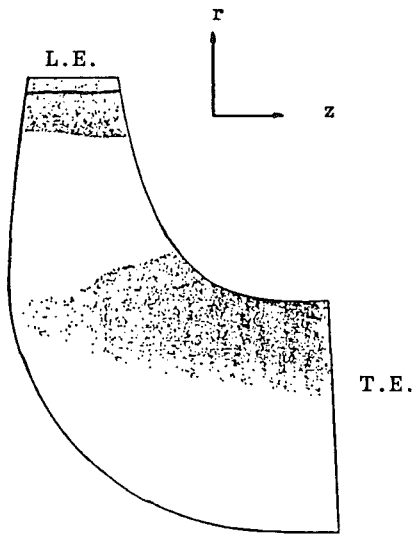

Fig. 7 Particle impact locations on the rotor pressure surface for hot flow

computed hub-to-tip flow density variation in the meridional plane. The computed flow fields were then used in the computations of the particle trajectories for the 5-μm ash particles through the radial turbine rotor. The difference of the flow field between hot and cold inlet total conditions was found to change the trajectory of the 5-μm particles significantly.

Results and Discussion

Particle trajectory computations were performed for 5-μm particles through the radial inflow turbine rotor under cold and hot flow operating conditions. Detailed results are presented for the particle trajectories in both cases as well as in the form of figures showing particle impact locations with the blade surface. The results are also presented for the blade erosion data as determined from the impact conditions for a large number of particles in cold and hot flow fields.

Figures 2–4 present the results of the particle trajectory calculations through the turbine rotor in the case of the cold flow field. Figure 2 shows the projection of the 5- μm particle trajectories in the z–r plane, while Fig. 3 shows the projection of the same trajectories in the θ–r plane. One can see from Fig. 3 that the trajectories of the particles in the rotor fall into two different categories depending on their circumferential location at the rotor inlet. Approximately half the particles, which enter the rotor toward the blade suction side, continue their trajectory through the rotor and leave at the rotor exit. The other half, entering the rotor toward the pressure surface, initially move in the radially inward direction, then later reverse the direction of their radial motion under the influence of the centrifugal forces. These particles leave the rotor tip at the blade surface after impacting that part of the blade during their radial outward motion. The particles that go through the rotor also impact the pressure surface but much farther inward radially. Figure 4 shows the impact location of the 5-μm particles with the blade pressure surface. Two distinct bands of high impact intensities can be clearly seen near the blade tip. The impacts in these bands are by the particles returning toward the tip. The rest of the impacts are more distributed over the pressure surface with higher intensities toward the casing. These impacts are by the particles that complete their trajectory in the rotor and leave at the rotor exit are more distributed. Very few particles impact the suction surface near the tip to warrant presentation.

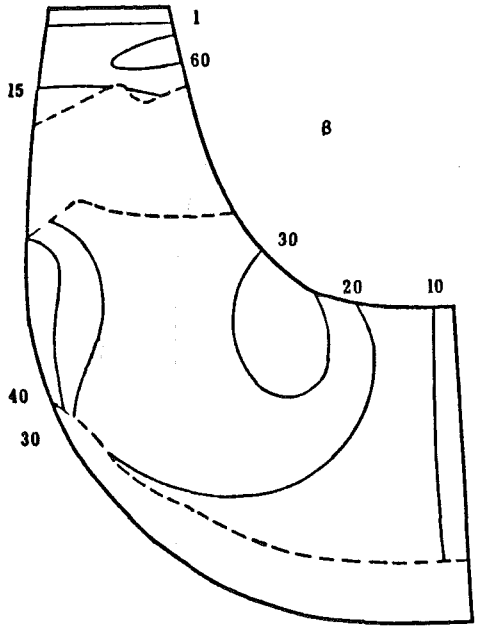

Fig. 8(*a*) Particle impingement angle on the rotor blade pressure surface for cold flow

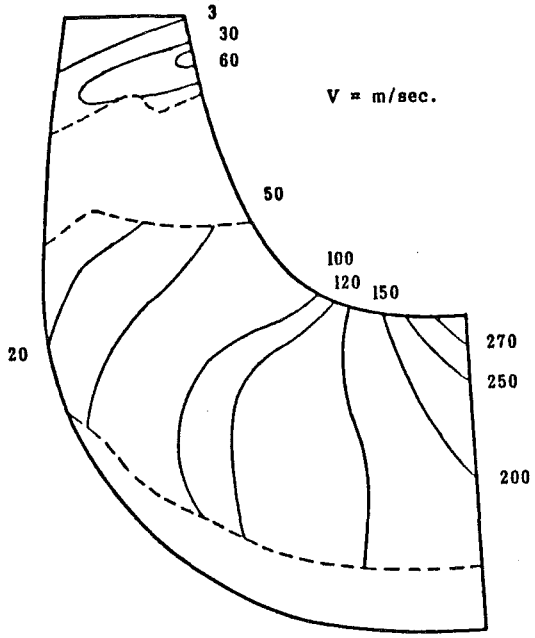

Fig. 9(*a*) Particle impact velocity on the rotor blade pressure surface for cold flow

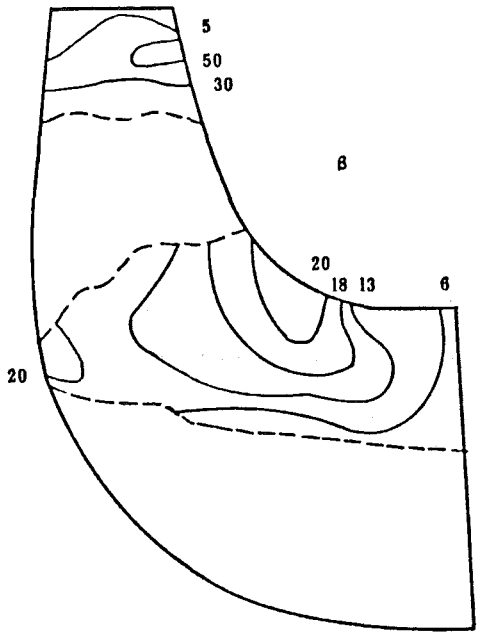

Fig. 8(*b*) Particle impingement angle on the rotor blade pressure surface for hot flow

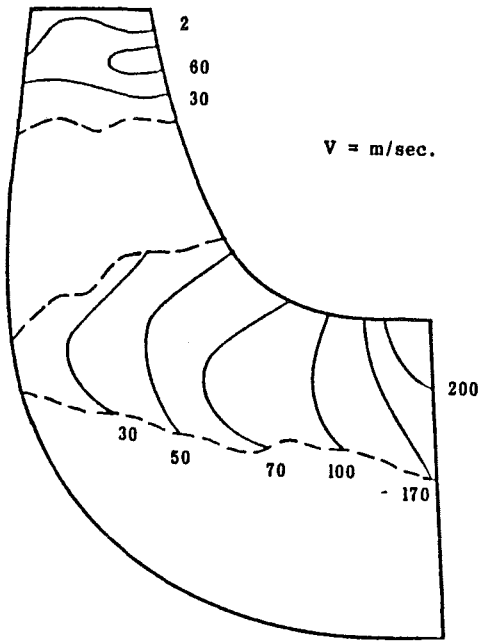

Fig. 9(*b*) Particle impact velocity on the rotor blade pressure surface for hot flow

Figures 5–7 show similar results for the particle trajectories through the high temperature rotor flow field. Comparing Figs. 2 and 5, it can be seen that the particles are more concentrated toward the casing as they leave the rotor under hot flow conditions. A thorough examination of the computed hot and cold flow fields revealed higher radial velocities at inlet, and lower axial velocities close to rotor exit in the case of hot flow conditions. The circumferential gas velocities were similar, however, since the rotational speed is the same in both cases. The lower drag forces in the axial direction and the same centrifugal forces acting on the particles result in more particle radial migration in the hot flow field. Comparing Fig. 6 to Fig. 3, one can see that the projection of the particle trajectories in the r–θ plane, in the case of high-temperature flow, are almost the duplicate of that found for the cold flow in the outer radial part. Figure 7 shows the impact location of the 5-μm ash particles on the pressure side of the turbine rotor, for the high-temperature flow field. This figure shows bands of high particle impact concentrations at the rotor tip as in the case of cold flow, but the more distributed impacts as the flow starts to turn in the axial direction are more concentrated in the area near the casing.

The results of the erosion study of the turbine rotor pressure side are presented in the rest of figures for cold and hot flows. Only the turbine rotor pressure surface is considered since the suction surface does not encounter a significant amount of impacts. The distribution of the blade erosion parameters, name-

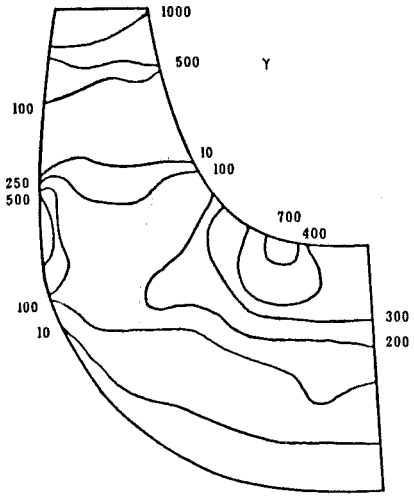

Fig. 10(*a*) Particle impact frequency on the rotor blade pressure surface for cold flow

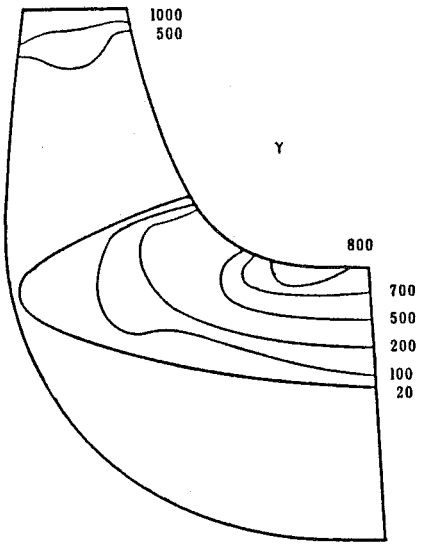

Fig. 10(*b*) Particle impact frequency on the rotor blade pressure surface for hot flow

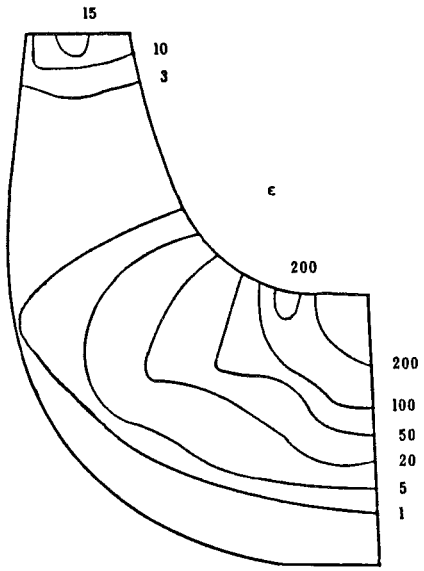

Fig. 11(*a*) Erosion parameter on the rotor blade pressure surface for cold flow

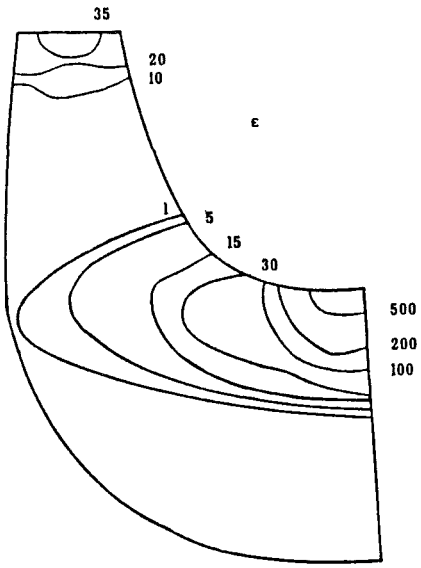

Fig. 11(*b*) Erosion parameter on the rotor blade pressure surface for hot flow

ly particle impinging angle (β), particle impact velocity (V), frequency of particle impact (γ), and blade mass erosion parameter (ϵ_b), are presented in Figs. 8–11. Figures. 8(a) and 8(b) present the distribution of the particle impact angles on the pressure side of the turbine rotor for the cold and hot flow. One can see from these figures that the particle impact angle distributions are somewhat similar for hot and cold flows. The highest impingement angles are at the casing near the tip, but they do not correspond to the maximum erosion. The second region of high impingement angles on the pressure side near the casing at the turn corresponds closely to the impact angle of maximum erosion (35 deg) in the case of cold flow, but they are lower in the case of hot flow.

The impact velocity distribution patterns over the pressure side for the cold-hot flow fields are shown in Figs. 9(a) and 9(b), respectively. The two patterns are also similar with higher impacting velocities over most of the blade surface for the case of cold flow field.

The particle impact frequency parameter γ is defined as the number of particle impacts per unit area, divided by the total number of ingested particles. Its distribution over the pressure side of the turbine is presented in Fig. 10 for the cold and hot cases. The patterns are somewhat different because of the difference in the second half of the particle trajectories between hot and cold flows. The impacts are more concentrated toward the casing near the exit in the case of the high-temperature flow field.

Figure 11 presents the distribution of the blade mass erosion parameter over the pressure side of the turbine rotor for the two flow fields under consideration. The erosion parameter is defined as the mass of blade material removed in milligrams per unit area of blade surface per unit mass (g) of ingested particles. The figure demonstrates that larger areas of the blade surfaces are subjected to erosion in the case of cold flow but that for hot flow the blade is locally subject to higher erosion, which is almost more than double that of the cold flow. This large difference is attributed mainly to the temperature effect on the erosion rate, which appears as the temperature parameter $F(T)$ in the erosion equation (equation (7)). The higher frequencies also contribute to the higher erosion rates encountered under higher temperature operating conditions.

Conclusion

The presented results for the particle trajectory through the radial inflow turbine rotor show that the flow temperature has a significant effect on the particle trajectories and the blade erosion. Almost half the 5-μm particles complete their trajectory through the rotor, while the other half are centrifuged back to the rotor inlet. A small band on the blade pressure surface erosion rates are predicted at the blade pressure surface near the rotor tip is subject to the highest impact frequencies by those returning particles; however, the blade erosion at the tip is not serious because of the very low particle velocities. The highest blade surface erosion rates are predicted at the blade pressure surface near the casing at the exit where the impact velocities are high and the impingement angles are close to those corresponding to maximum erosion. The blade erosion in this region is two and half times higher in the case of hot flow compared to cold flow conditions. Furthermore, the erosion pattern of the blade pressure surface is affected by the flow temperature with more of the blade surface subjected to less severe erosion in the case of the cold flows.

Acknowledgments

This research work was sponsored by the U.S. Department of Energy, Contract No. 19X-89628C, Oak Ridge National Laboratory, Oak Ridge, TN.

References

1 Tabakoff, W., Hamed, A., and Mansour, M. L., "The Dynamics of Suspended Solid Particles in a Two-Stage Gas Turbine," ASME JOURNAL OF TURBOMACHINERY, Vol. 108, 1986, pp. 298–302.

2 Hamed, A., and Tabakoff, W., "Turbine Erosion Exposed to Particulate Flow," ASME Paper No. 86-GT-258, 1986.

3 Tabakoff, W., and Hamed, A., "Installed Engine Performance in Dust-Laden Atmosphere" AIAA Paper No. 84-2488, 1984.

4 Hamed, A., "Particle Dynamics of Inlet Flow Fields With Swirling Vanes," *Journal of Aircraft*, Sept. 1982, pp. 707–712.

5 Tabakoff, W., "Review—Turbomachinery Performance Deterioration Exposed to Solid Particles Environment," *Journal of Fluids Engineering*, June 1984.

6 Clevenger, W. B., and Tabakoff, W., "Similarity Parameters for Comparing Erosive Particle Trajectories in Hot Air and Cold Air Radial Inflow Turbines," ASME JOURNAL OF ENGINEERING FOR POWER, Vol. 96, 1974.

7 Montgomery, J. E., and Clark, J. M., Jr., "Dust Erosion Parameters for a Gas Turbine," SAE Paper No. 538, June 1962.

8 Shoemaker, H. E., and Shumate, C. P., "Techniques for Reducing Sand and Dust Erosion in Small Gas Turbine Engines," SAE Paper No. 700706, Sept. 1970.

9 Grant, G., and Tabakoff, W., "Erosion Prediction in Turbomachinery Due to Environmental Solid Particles," *Journal of Aircraft*, Vol. 12, No. 5, 1975, pp. 471–478.

10 Tabakoff, W., Hamed, A., and Ramachandran, J., "Study of Metals Erosion in High Temperature Coal Gas Streams," ASME JOURNAL OF ENGINEERING FOR POWER, Vol. 102, 1980, pp. 148–152.

11 Tabakoff, W., and Hamed, A., "Investigation of Gas Particle Flow in Erosion Wind Tunnel," presented at the 7th Annual Conference on Materials for Coal Conversion and Utilization, National Bureau of Standards, Gaithersburg, MD, Nov. 16–18, 1982.

12 Tabakoff, W., Hamed, A., and Balan, C., "Performance Deterioration of an Axial Flow Compressor Stage With Presence of Solid Particles," *Proceedings of 15th International Symposium on Airbreathing Engines*, 1980.

13 Beacher, B. F., and Mansour, M. L., "Erosion of a Coal-Burning Gas Turbine by Ash Particles," presented at the AIAA/ASME 4th Joint Fluid Mechanics, Plasma Dynamics and Lasers Conference, Atlanta, GA, May 12–14, 1986.

14 Tabakoff, W., and Hussein, M. F., "Trajectories of Particles Suspended in Fluid Flow Through Cascades," *AIAA Journal of Aircraft*, Jan. 1971.

15 Katsanis, T., and McNally, W. D., "Revised Fortran Program for Calculating Velocities and Streamlines on the Hub-Shroud Mid Channel Stream Surface of an Axial, Radial or Mixed Flow Turbomachine or Annular Duct," Vols. 1 and 2, NASA TN D-8430 and NASA TN D-8431, 1977.

Verification of Compressor Data Accuracy by Uncertainty Analysis and Testing Methods

N. D. Poti

D. C. Rabe

Aero Propulsion Laboratory,
Air Force Wright
Aeronautical Laboratories,
Wright-Patterson AFB,
OH 45433

A transonic compressor designed and instrumented by the General Electric Company was recently evaluated during several test programs in the Compressor Research Facility at Wright-Patterson Air Force Base. An analytical uncertainty analysis was performed for the individual measurements, as well as the calculated performance parameters. During the tests, the experimental values of precision uncertainty were compared to the analytical predictions. The spatial variation of the individual discharge measurements was evaluated for its effect on the uncertainty of the measured parameters and calculated performance. Through the comparison of the analytical and measured uncertainty and the evaluation of spatial variation, a final uncertainty of the measured performance is presented, and the overall quality of the test results is assessed. Through these data reviews, a more accurate understanding of the performance of the test compressor is obtained.

Introduction

A transonic unswept compressor test vehicle designed and built by the General Electric Company was recently evaluated during several test programs in the Compressor Research Facility (CRF) at Wright-Patterson Air Force Base. The compressor test vehicle was built to demonstrate a mechanically simple compression system with a pressure rise per stage above the current state of the art (Fig. 1). The compressor consists of a two-stage design with a flight-weight rotor and slave casing. The low aspect ratio first-stage integrally bladed rotor (blisk), is followed by a second-stage bladed disk. This compressor has no inlet guide vanes and utilizes a first-stage variable stator flap for part speed performance improvements (Fig. 2). The test vehicle was instrumented with 614 channels including pressure, temperature, vibration, strain, angular position, oil flow, clearance, and air velocity in order to measure overall and stage performance as well as for monitoring the mechanical integrity of the vehicle. The vehicle was used for three test programs. Two builds of the compressor were for steady-state performance evaluations, and a third investigated distortion sensitivity of the compressor. Prior to the first test program, an analytical uncertainty analysis was performed that determined the precision and bias uncertainties of the measurement system and then propagated those errors through the performance calculations. During the steady-state testing, data were obtained that experimentally measured the precision error, and that error is compared to the pretest prediction. Test data are presented that show the repeatability of steady-state data relative to the pretest analysis, both during constant test conditions on a given day, as well as from day

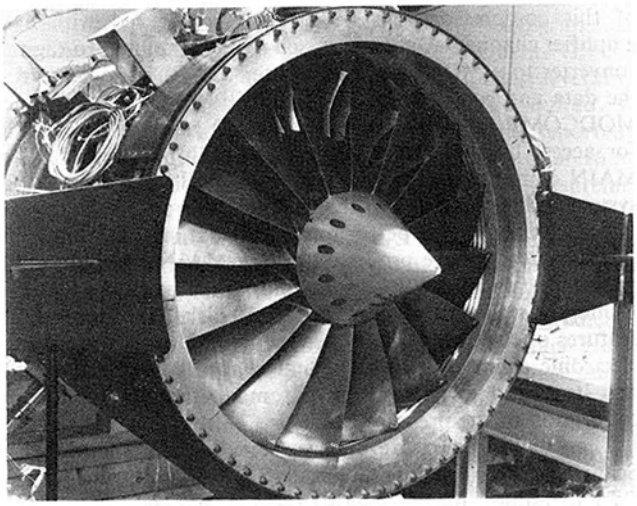

Fig. 1 Compressor test rig

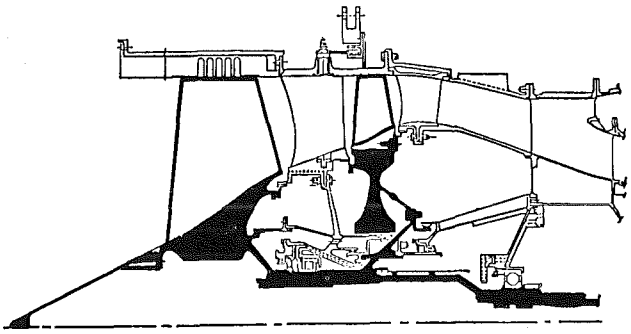

Fig. 2 Compressor test rig schematic

Contributed by the Gas Turbine Division of THE AMERICAN SOCIETY OF MECHANICAL ENGINEERS and presented at the 32nd International Gas Turbine Conference and Exhibit, Anaheim, California, May 31–June 4, 1987. Manuscript received at ASME Headquarters February 17, 1987. Paper No. 87-GT-165.

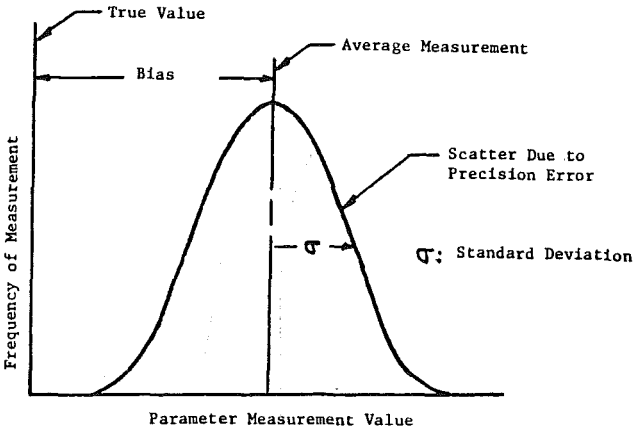

Fig. 3 Bias and precision errors

to day throughout the test programs. Discharge profiles of temperature and pressure will be discussed for steady-state operation. The impact of these profiles on the overall stated performance will be shown. A method will be presented that incorporates experimental results with the predicted uncertainty to determine a final test uncertainty. The overall quality of CRF data will be demonstrated, and a more accurate representation of the uncertainty in the compressor test data will be presented.

CRF Data Acquisition

The CRF acquires measurements of pressure and temperature from experimental vehicles through its digital data acquisition system. The system acquires data from a Preston analog-to-digital converter and multiplexer at a rate which approaches 50,000 samples per second. For the testing of this compressor, the system was configured with 640 amplifier channels. Data are passed from the analog-to-digital converter to a MODCOMP computer (DAC) which acquires the data and controls the data acquisition system. A second MODCOMP auxiliary computer (AUX) reformats the data for access by the IBM 4341 Main (MAIN) computer. The MAIN computer is the heart of the digital data acquisition system and performs all of the channel calibrations, engineering conversions, and performance calculations. On-line and steady-state data are processed by the MAIN computer and transmitted to IBM 3277 display monitors, an IBM 1401 line printer, as well as stored on ITEL 3330 disks. Two important features of the MAIN computer are its ability to perform an electronic calibration of all digital channels (channel check) and its ability to perform an automatic five-point pressure calibration of the pressure channels.

The digital pressure measurements are made with Scanivalve Zero Operate Calibrate (ZOC) block transducers. Each transducer blocks together eight measurements and provides for a common switching valve and calibration source. The calibration source is provided by a series of eight Mensor quart pressure controllers. These Mensors provide a highly stable and accurate pressure source and are controlled by inputs from the MAIN computer. The MAIN computer steps the controllers through a five-point calibration routine and determines linearity, offset, and hysteresis of each pressure channel. The calibrations are then stored and used for the on-line and steady-state engineering value calculations.

The CRF temperature measurement system consists of beaded thermocouple measurements which are terminated in Uniform Temperature Reference (UTR) blocks. The temperature of a UTR block is measured with a Resistance Temperature Dector (RTD). The MAIN computer determines the nonlinearity and offset of each temperature channel by applying a known voltage source in place of the thermocouple during channel check. In addition, two thermocouples referenced to each UTR block are immersed in a Hy-Cal Engineering temperature well and displayed as a temperature measurement channel for automatic, as well as visual, comparisons.

Prior to initial rotation, an exhaustive checkout of the data system is performed. The channel check and pressure calibration ensure the proper functioning of the digital data system; however, possibilities still exist for errors. End-to-end checks are performed from the test article measurement source to the output devices, such as the static data print-out and the on-line monitoring screens. An actual known pressure or temperature change is introduced as close to the measurement source as possible, and the output is compared to the input value. Through this procedure, the actual measurement is verified for proper location and wiring connection as well as proper display formating.

Uncertainty Analysis

Performance parameters used to assess compressor performance are calculated using measured values of basic quantities such as pressure and temperature. Measurement errors occur in the process of acquiring data, and those errors are propagated through the calculations yielding uncertainty in the results. In order to understand better the calculated performance quantity, the uncertainty of the calculation must be determined. Measurement uncertainty has been reported in many published works, such as [1]. Measurement uncertainty can be defined as the maximum error which might be expected between a measurement and the true value of the measured parameter. This uncertainty can be influenced by two sources of errors, precision (random) and bias (fixed). Precision error is the scatter observed in the measurement that develops into a Gaussian distribution about a mean value in multiple samples. Statistical analysis shows that the standard deviation of the distribution is the value which best represents the measure of precision. Bias error is the difference between the measured mean value and the true value. Bias error remains constant for a given test configuration (Fig. 3). The precision and bias errors are combined and presented as a single number as defined below:

$$U = \pm(B + t_{.95}S)$$

The value shown as $t_{.95}$ depends on sample size. It is defined as the 95th percentile point for the two-tailed Students "t" distribution, and for sample sizes of 30 or more, a value of 2.0 is generally used.

Bias and precision errors exist for all equipment used to obtain measured values. The entire data path from the measure-

Nomenclature

B = measurement bias error
B_c = calculation bias error
b_k = elemental bias error
N = number of elemental error sources
S = measurement precision error
S_s = calculation precision error
S_k = elemental precision error
U = measurement uncertainty
U_c = calculation uncertainty
$\partial c/\partial M_k$ = partial derivative of the calculated with respect to the measured value

Table 1 Predicted measurement uncertainty

Parameter	Precision Error	Bias Error	Uncertainty
PS2	±0.14% M[1]	±0.44% M	±0.72% M
PD2	±0.32% M[1]	±0.10% M	±0.74% M
PT3	±0.44% M	±0.21% M	±1.09% M
TT0	±0.05% M	±(0.20% M+1.8 R)[2]	±(0.30+1.8 R)
TT3	±0.05% M	±(0.20% M+3.0 R)	±(0.30+3.0 R)

[1]Where M represents the measured value
[2]Where R represents degrees Rankine.

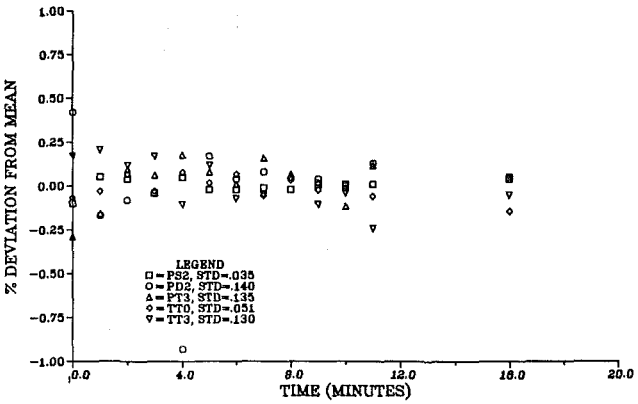

Fig. 4 Experimental measurement precision during constant test conditions

ment source to the output device, including probes, transducers, amplifiers, signal conditioning equipment, power supplies, computers, and calibration sources, must be studied to determine individual error contributions. Most of the component errors can be derived from data sheets listing manufacturer's specifications. Each individual error component is combined to yield an overall system measurement error by the following:

$$B=\sqrt{\sum_{k=1}^{N}(b_k)^2} \qquad S=\sqrt{\sum_{k=1}^{N}(S_k)^2}$$

The accuracy level of most devices varies throughout the measurement ranges. For example, pressure transducer errors are larger in their low range of measurement than at the full-scale reading. The value used in determining the measurement error must consider where in the measurement range the device is going to be used. The measurement uncertainty of the primary compressor inlet and exit measurements is shown in Table 1.

Any performance parameter calculated from measurements has an associated uncertainty due to the measurement errors. The sensitivity of the performance to individual measurement errors can vary greatly and can only be determined by propagating the measurement bias and precision errors through the calculations. These performance sensitivities are found by determining the partial derivatives of the performance parameters with respect to the measurements. Two methods used for this determination can be found in [2, 3]. The partial derivatives are then multiplied by corresponding measurement errors and combined into calculation bias and precision terms as follows:

$$B_c=\sqrt{\sum_{k=1}^{N}\left(\frac{\partial c}{\partial M_k}b_k\right)^2}$$

$$S_c=\sqrt{\sum_{k=1}^{N}\left(\frac{\partial c}{\partial M_k}S_k\right)^2}$$

The final calculation uncertainty is then found from

$$U_c=\pm(B_c+t_{.95}S_c)$$

A measurement uncertainty analysis can affect the data acquisition process. For example, in this compressor test, the inlet total pressure and the pressure measurements for the mass flow calculations were made with the same probes. Only two of the quantities of inlet total, static, and dynamic pressures could be measured directly. The resulting total pressure ratio and mass flow calculations are affected by which two of these pressures are measured directly. The calculation uncertainty analysis determined that the more accurate method was to measure inlet static and dynamic pressure. The measurement uncertainty analysis propagation for compressor mass flow, pressure ratio, and efficiency for the testing programs is shown in Table 2. The data presented in Tables 1 and 2 do not account for multiple measurements used to determine averaged values; instead they are for single measurements only.

Experimental Uncertainty

The theoretical uncertainty is the worst-case approximation of the experimental error within the stated confidence level. Since the precision error is a measure of the random fluctuations in a measurement, this error can be experimentally verified with multiple samples of this measurement. The compressor operating point was held constant during several test phases, and multiple digital data points were acquired. The primary compressor inlet and exit measurements reported in Table 1 are plotted for 13 data points over a span of 16 min (Fig. 4). The data presented are for an individual measurement port, and the resulting scatter is representative of the precision of the measurements. The standard deviations determined from this plot indicate that all of the listed pressure measurement precision errors are lower than the predictions. The inlet temperature precision agrees fairly well with prediction; however, the discharge temperature precision is much greater than predicted. This could be the result of the unsteadiness due to upstream blade wakes and will be discussed in more detail in the following section.

The determination of calculation uncertainty presupposes that each measurement error combines to yield a total error larger than the components; however, this rarely happens in practice. Precision errors from one measurement often cancel errors from other measurements when used jointly in an engineering calculation. Careful evaluation of experimental test data can evaluate this canceling effect. Performance parameters corresponding to the data previously presented for constant test conditions can be compared to the predicted calculation uncertainty (Fig. 5). The resulting data scatter is representative of the precision error of the calculations. The standard deviations of the data are listed, and all fall well below the predicted precision errors shown in Table 2. This is consistent with the result of measured precision errors being lower than the predictions.

The previous results can be combined into a final demonstrated performance uncertainty. The precision errors of the calculation uncertainty can be combined with the predicted bias errors. Since the sample size for this data field is

Table 2 Predicted calculation; uncertainty in percent of design

Parameter	Precision Error	Bias Error	Uncertainty
Mass flow	±0.17	±0.29	±0.63
Pressure ratio	±0.45	±0.42	±1.34
Efficiency	±0.48	±1.85	±2.82

Table 3 Final performance uncertainty in percent of design value

Parameter	Precision Error	Bias Error	Uncertainty
Mass flow	±0.06	±0.29	±0.43
Pressure ratio	±0.04	±0.42	±0.51
Efficiency	±0.22	±1.85	±2.33

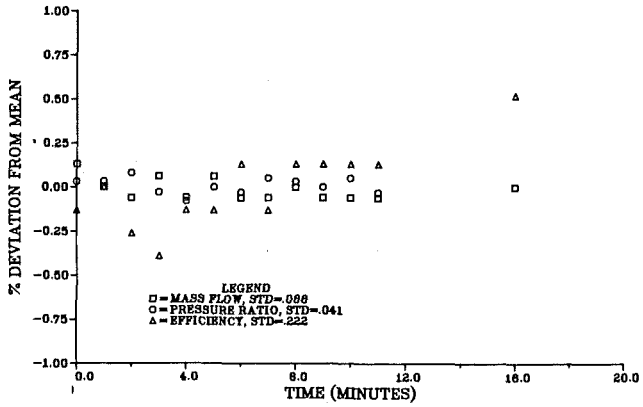

Fig. 5 Experimental calculation uncertainty during constant test conditions

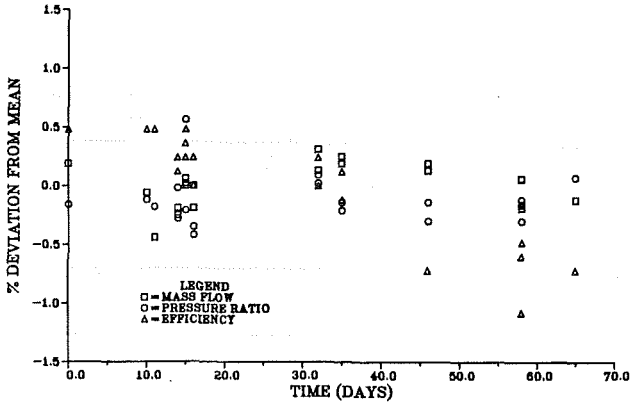

Fig. 6 Deviation of calculated performance from day to day

13, the $t_{.95}$ percentile value is 2.179. The final performance uncertainties listed in Table 3 show that all of the values are lower than predicted, with the greatest improvement being in the calculation of pressure ratio, which was less than half of the expected value.

Another method of determining data system accuracy uses test checkpoints. The performance of any compressor at a single operating point can be characterized by corrected speed, pressure ratio, and corrected mass flow. During the compressor test program, data were repeated at precise speed and pressure ratio setpoints throughout the test. The setpoints were repeated during each test period, and the efficiency and mass flow were compared (Fig. 6). The use of this method is all-inclusive in that it not only evaluates the measurement capability of the data system, but also accounts for the facility's capability for accurately controlling and repeating a

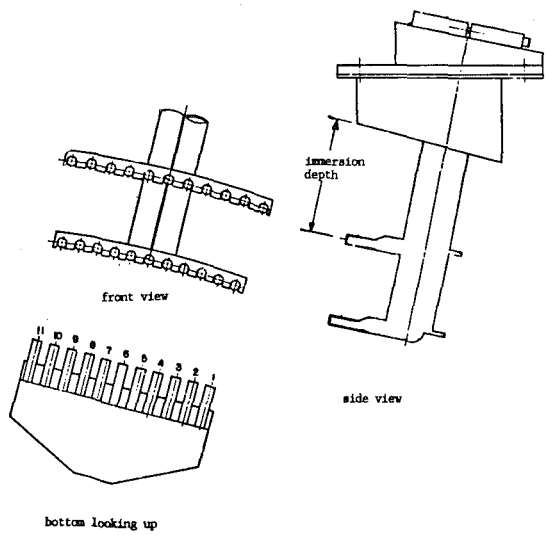

Fig. 7 Discharge rake schematic

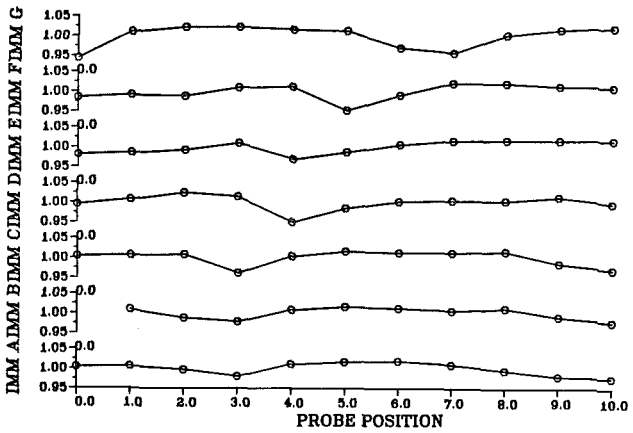

Fig. 8 Compressor discharge pressure profiles including blade wakes

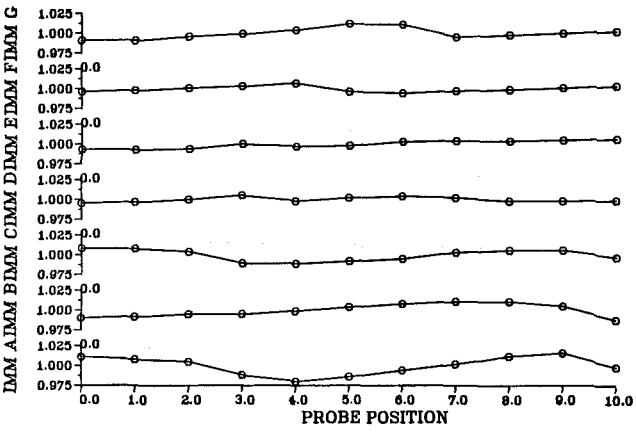

Fig. 9 Compressor discharge temperature profiles including blade wakes

compressor operating point. The data show that throughout the tests the checkpoints repeated mass flow and pressure ratio within 0.50 percent. The efficiency showed a general decreasing trend with a step change after day 35. The total drop observed was 1.50 percent and was attributed partly to minor damage sustained by the second-stage blades, which was discovered upon post-test teardown.

Planar Profile Variations

Planar station values of properties throughout compressor

test vehicles are often measured as the average of several ports distributed circumferentially and radially throughout the measurement plane. Pressure and temperature rakes are used to characterize profiles, and their measurements are averaged simply or by a weighted method such as an area or mass-averaged method. For steady-state testing, the profiles entering the bellmouth section of the test compressor should exhibit classical boundary layer profiles with no circumferential variations. The CRF inlet has been studied [4] and exhibits a low turbulence level, uniform flow into the test compressor. During steady-state operation, the discharge pressure and temperature profiles in a compressor are affected wakes of the upstream blade rows. The test compressor was instrumented with circumferential arc rakes (Fig. 7). The angular extent of the rakes was designed to cover one-blade spacing and, therefore, measure the pressure and temperature variation in the wake region. Pressure and temperature profiles were measured by the discharge rakes at the compressor design point (Figs. 8 and 9). It can be seen that if the wake region at this operating point was not included in the average, the value of pressure ratio would have been 0.95 percent greater, and likewise the temperature ratio would have been 0.55 percent lower. This, in turn, would have resulted in a value of efficiency 1.90 percent higher than that calculated by including the wake effects. This difference represents about 20 percent of the efficiency range of modern compressors.

Discussion

A theoretical uncertainty analysis was performed in accordance with classical procedures to determine the uncertainty in the CRF data acquisition system. The bias and precision indices were determined and then were propagated through the performance calculations which yielded uncertainties of 0.63, 0.46, and 2.83 percent for compressor mass flow, pressure ratio, and efficiency, respectively. The pretest uncertainty propagation analysis resulted in a data system configuration that measures inlet static and dynamic pressures instead of the inlet total pressure.

Measurement uncertainty can be experimentally verified through careful test planning and execution. Calibration of transducers can reduce the bias errors associated with the measurement of pressures. Channel checks, as performed in the CRF, can reduce the bias errors of the thermocouple measurement system. Evaluation of test data acquired during test programs can experimentally verify predicted precision uncertainty values. The data presented show precision errors taken during extended periods at the same operating point, as well as test checkpoints from day to day throughout the test program. The experimental values for precision errors can be used as a value of post-test uncertainty. The final uncertainties for mass flow, pressure ratio, and efficiency are 0.44, 0.51, and 2.33 percent, respectively. The measurement of compressor discharge properties must include provisions for the measurement of upstream blade wakes. Ignoring the wake effects in the recent CRF tests would have resulted in a pressure ratio error of 0.55 percent and an efficiency error of 1.90 percent.

Acknowledgments

The test programs described within this report were conducted by the Technology Branch of the Turbine Engine Division at the Aero Propulsion Laboratory. The authors wish to acknowledge the contributions of all of those co-workers whose participation made the testing and subsequent data analysis possible. The authors also wish to acknowledge the employees of the General Electric Company who, under Air Force contract, developed the compressor test vehicle, and provided guidance throughout the test.

References

1 Abernethy, R. B., and Thompson, J. W., Jr., "Handbook Uncertainty in Gas Turbine Measurements," AEDC-TR-73-5, Feb. 1973.

2 Boedicker, C. A., "Uncertainty Analysis," United States Air Force Academy Research Paper, 1982.

3 Perry, M. S., "Compressor Research Facility Compressor Performance Calculation Uncertainty Analysis," Air Force Wright Aeronautical Laboratories, Wright-Patterson AFB, OH.

4 Rabe, D. C., "Effects of Downstream Distance on Turbulence Decay for the Compressor Research Facility Flow Conditioning System," AFWAL-TR-80-2023, Air Force Wright Aeronautical Laboratories, Wright-Patterson Air Force Base, OH, Mar. 1980.

Application of Advanced Computational Codes in the Design of an Experiment for a Supersonic Throughflow Fan Rotor

J. R. Wood

J. F. Schmidt

R. J. Steinke

R. V. Chima

W. G. Kunik

NASA Lewis Research Center,
Cleveland, OH 44135

Increased emphasis on sustained supersonic or hypersonic cruise has revived interest in the supersonic throughflow fan as a possible component in advanced propulsion systems. Use of a fan that can operate with a supersonic inlet axial Mach number is attractive from the standpoint of reducing the inlet losses incurred in diffusing the flow from a supersonic flight Mach number to a subsonic one at the fan face. The data base for components of this type is practically nonexistent; therefore, in order to furnish the required information for assessment of this type fan, a program has been initiated at the NASA Lewis Research Center to design, build, and test a fan rotor that operates with supersonic axial velocities from inlet to exit. This paper describes the design of the experiment using advanced computational codes to calculate the unique components required. The fan rotor has constant hub and tip radii and was designed for a pressure ratio of 2.7 with a tip speed of 457 m/s. The rotor was designed using existing turbomachinery design and analysis codes modified to handle fully supersonic axial flow through the rotor. A two-dimensional axisymmetric throughflow design code plus a blade element code were used to generate fan rotor velocity diagrams and blade shapes. A quasi-three-dimensional, thin shear layer Navier–Stokes code was used to assess the performance of the fan rotor blade shapes. The final design was stacked and checked for three-dimensional effects using a three-dimensional Euler code interactively coupled with a two-dimensional boundary layer code. A translating nozzle was designed to produce a uniform flow parallel to the fan up to the design axial Mach number of 2.0. The nozzle was designed with the three-dimensional Euler/interactive boundary layer code. The nozzle design in the expansion region was analyzed with a three-dimensional parabolized viscous code, which corroborated the results from the Euler code. A translating supersonic diffuser was designed using these same codes.

Introduction

Recent renewed interest in high-speed flight has focused attention on possible power plants to sustain efficient supersonic cruise or to act as boosters to accelerate a vehicle to moderate supersonic velocities where transition to propulsion might take place by a subsonic ramjet for subsequent acceleration to hypersonic velocities. One such power plant was discussed by Boxer [1] who proposed a high bypass ratio turbofan engine/ramjet combination, which utilized a variable pitch supersonic axial inflow fan. Cascade tests were performed with supersonic inflow air operating at 2144 K and adequate cooling was maintained. Spin pit tests were also conducted on a single blade to test a proposed mechanism for varying the pitch of the fan blades at the design tip speed of 448 m/s with good success.

Contributed by the Gas Turbine Division of THE AMERICAN SOCIETY OF MECHANICAL ENGINEERS and presented at the 32nd International Gas Turbine Conference and Exhibit, Anaheim, California, May 31–June 4, 1987. Manuscript received at ASME Headquarters February 17, 1987. Paper No. 87-GT-160.

Cycle studies have indicated that substantial improvements can be obtained by using a fan that was capable of accepting a supersonic axial component in a turbofan engine at supersonic cruise conditions. Ferri [2] was the first to point out the potential advantages of eliminating the subsonic portion of the supersonic inlet and providing a fan capable of accepting supersonic axial inflow.

Franciscus [3] compared the performance of several supersonic throughflow fan engines to a reference turbofan engine for a Mach 2.32 all supersonic cruise mission and concluded that use of a supersonic throughflow fan equipped engine could reduce specific fuel consumption by 12 percent, which could lead to an improvement in range of 20 percent. Tavares [4] considered a mission for a supersonic transport operating at Mach 2.7 and concluded that a fan efficiency of 68 percent would be necessary to have performance advantage over a turbojet engine with the same core.

All of the cycle studies to date have suffered from a severe lack of experimental data to confirm assumptions concerning

the fan performance. Only two experiments dealing with supersonic axial inflow to an axial flow rotor are known to the authors. Savage [5] showed a single plot of efficiency versus pressure ratio for a transonic rotor that was operated at tip speeds considerably above the design value in conjunction with a Mach 1.5 annular flow nozzle to study the rotor starting characteristics with a shadowgraph technique. The most thorough experiment to date for this type of rotor was conducted by Breugelmans [6]. He designed and tested an isolated rotor with a design inlet axial Mach number of 1.5. Because of a mechanical failure, extensive data were not taken; however, the rotor did start as anticipated and a total–total pressure ratio of about 2 at 80 percent design speed was attained. Based upon the measured data the rotor appeared to be operating with an internal shock that produced subsonic axial flow out of the rotor.

Because of the possible advantages of incorporating a supersonic throughflow fan into the propulsion system for high-speed vehicles, NASA Lewis embarked upon a program to develop the computational capability to analyze and design turbomachinery with supersonic axial inlet Mach numbers. Recent developments in turbomachinery analysis codes [7, 8] and modern high-speed computers have combined to provide the turbomachinery designer with sophisticated computational tools to guide him in attaining a desirable design. The state of the art, however, in computational capability in turbomachinery would suggest that even though a great deal of the physics of the flow process is modeled, not all of the details of the flow can be resolved. Thus, computational tools available today must be thoroughly tested against experiments to "calibrate" them for design purposes. The intent of this paper is to describe the design using advanced computational codes of an experiment to investigate the flow in a supersonic throughflow fan rotor. An experimental program is anticipated that will obtain both overall performance and detailed internal flow patterns to provide necessary "calibration" data for this type of turbomachine.

Computational Codes

A variety of codes ranging from a one-dimensional meanline compressor code to a three-dimensional viscous parabolized code were used to design the fan stage and several critical elements of the facility. It was necessary to modify all the turbomachinery codes to handle axial supersonic velocities since their traditional use has been for subsonic axial flow. All these codes had been previously tested against turbomachinery data in the relative Mach number range around 1.4 but had not been applied in the range of interest for this paper. Since no data base existed to test the codes adequately at the Mach number range of interest, where possible, codes using different algorithms were used to obtain solutions on the same element in order to increase confidence in the final design. The codes used are described in the following subheadings.

Meanline Code (STGSTK). The STGSTK code by Steinke [9] is a one-dimensional inviscid code used to estimate off-design performance once design point performance is estimated. The code uses the estimated design point performance and correlations based upon transonic blade element data to predict the off-design performance. The code was modified to allow calculation of single blade rows, stages, and counterrotating rotors having supersonic axial velocity. The results from STGSTK were used to check matching of the facility speed and power requirements and to give a perspective on how an operating line might look for this type of turbomachine.

Axisymmetric Compressor Design Code (CDP). The CDP code by Crouse and Gorrell [10] uses the streamline curvature method to compute velocity diagrams at the blade edges for two-dimensional inviscid axisymmetric flow. This code provides flow solutions at the leading and trailing edge of the blades that satisfy the desired pressure ratio, mass flow, and radial equilibrium. The code also stacks an arbitrary blade shape from hub to tip and prints output data for subsequent analysis by more advanced codes. The code requires input for blade element incidence, loss, and deviation angle. Each subsequent blade element that satisfies the input conditions is described using fourth-order polynomials for the blade angle and thickness distributions. CDP generates blade element geometry, which can be used in a detailed blade element analysis code. The blade geometry can be iterated until the deviation predicted by the viscous code and the deviation used in CDP are the same.

The CDP was modified to calculate supersonic axial flow; however, because the code uses the streamline curvature method it was necessary to incorporate damping on the calculated curvatures in order to obtain converged solutions.

Thin-Shear-Layer Viscous Code (RVCO3). The RVCO3 code by Chima [8] solves the Euler and thin shear layer Navier–Stokes equations for a quasi-three-dimensional flow. The convergence is enhanced by use of variable timesteps, multigridding, and vectorization for application to the NASA Lewis Cray XMP. The code uses a C-type grid generated by a modified form of the GRAPE code grid generator by Sorenson [11]. The RVCO3 was used as a "numerical test cell" to screen blade designs and aid the designer in evaluating the desirability of one blade design over another.

The RVCO3 is relatively new but results [12] have compared well to laser anemometry measurements made at NASA Lewis on a transonic compressor rotor as indicated in Fig. 1. The experimentally measured static pressure was used as the downstream boundary condition on RVCO3. The shock location and downstream Mach number contours predicted by the code agree quite well with the data. RVCO3 was adapted for supersonic axial flow by holding the inlet conditions constant and extrapolating the flow quantities to the downstream boundary.

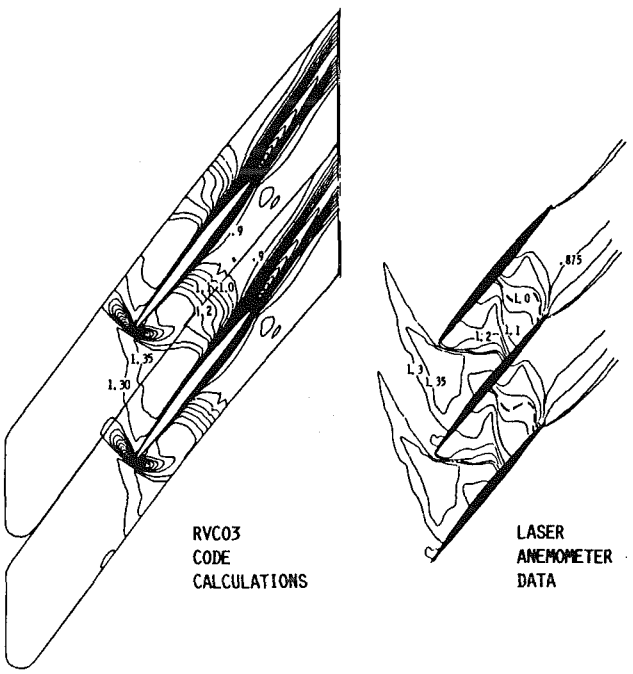

Fig. 1 Relative Mach number contours for NASA rotor 33 from RVCO3 code (using experimental back pressure for downstream boundary condition) compared to laser anemometer data

Three-Dimensional Euler Code With Interactive Two-Dimensional Boundary Layer Code (D3DVBL). The D3DVBL code consists of the three-dimensional finite volume code developed by Denton [7] and an interactive boundary layer calculation [13], which is continually updated as the time unsteady solution proceeds to a final steady-state value. The method models only the displacement effect of the boundary layer on the flow by injecting additional mass into the flow path in the proper proportion to simulate a physical displacement of the wall surface equal to the calculated displacement thickness. The external conditions for the boundary layer are taken as the velocity at the blade surface and the boundary layer is assumed to be affected only by the component of velocity that lies along a streamwise grid line, i.e., no strong three-dimensional flows are present in the channel. The original boundary layer routine was a simple solution to the von Karman integral equation using a constant shape factor and skin friction coefficient, which was shown by Pierzga and Wood [14] to improve the calculated results significantly when compared to experimental laser anemometry data on a transonic fan. In order better to model the boundary layer the method of Sasman and Cresci [15] as developed by McNally [16] for turbulent boundary layers was added to the code by Liu [17]. The method solves the momentum and moment of momentum integral equations for a compressible turbulent boundary layer to obtain the momentum thickness and shape factor. The boundary layers are always assumed to be turbulent. The original paper by Sasman and Cresci modeled the integral of the shear stress through the boundary layer as a function of incompressible shape factor and the incompressible skin friction coefficient. Comparison of the results of the Sasman and Cresci model to flows with large decelerations where the incompressible shape factor is large indicates that separation is predicted much too early by the method. Wood and Schmidt [20] modified the expression for the shear stress integral so that the prediction of shape factor growth near separation more closely modeled data (see for example Moses' Case 5 in the Stanford conference on incompressible turbulent boundary layers [19]). Calculations for flows that were not near separation indicated the modified expression did not adversely affect the results. All the results obtained with the D3DVBL code presented herein for the nozzle, fan, and diffuser design use the Sasman and Cresci equations with the modification by Wood and Schmidt.

The D3DVBL code was used to check the three dimensionality of the rotor flow after the design was completed. It was shown by Wood et al., [20] that the D3DVBL code prediction of shock three dimensionality agreed very well with laser anemometry data taken on a transonic fan stage. In order to confirm that differences between the quasi-three-dimensional results from the RVCO3 code and the D3DVBL code were indeed due to three-dimensional effects, the D3DVBL code was run on the mean and tip section in a two-dimensional mode (i.e., only a very thin streamsheet was analyzed with the hub and tip boundary layer calculations turned off). These two-dimensional calculations were compared to the results from the RVCO3 code and the D3DVBL three-dimensional calculations to assess whether three-dimensional affects were a significant factor in the final design.

The D3DVBL code was modified so that the inlet axial velocity at the hub was held constant and the gradient of the

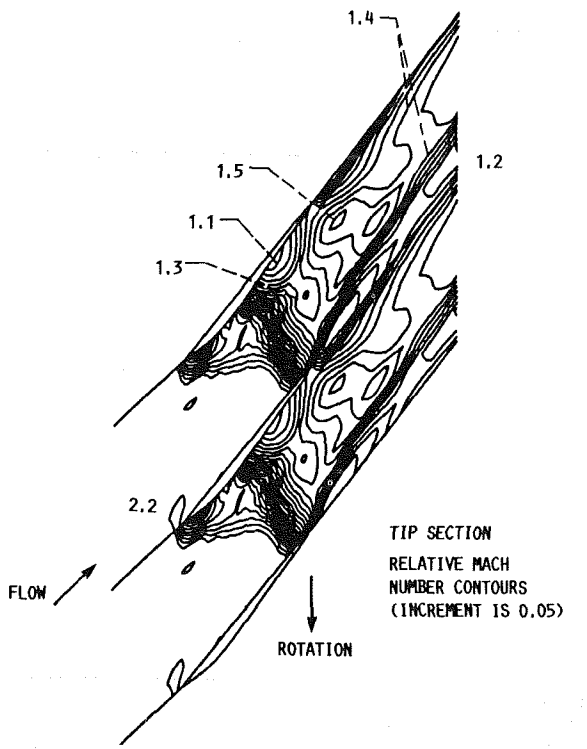

Fig. 2 Calculated results from the D3DVBL code on the supersonic throughflow rotor tested by Bruegelmans [6]

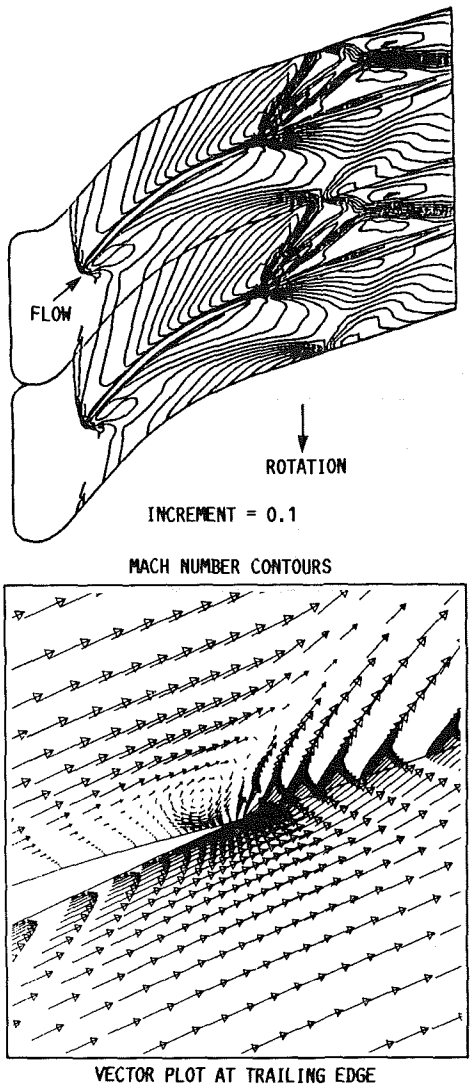

Fig. 3 Results obtained with the RVCO3 code on an initial blade shape used to check codes for supersonic axial inflow: inlet axial Mach number of 1.5 and tip speed of 488 m/s

radial velocity in the streamwise direction was constant. Radial equilibrium with the assumption of no streamline curvature was used to establish the pressure gradient from hub to tip at the inlet plane and thus the velocity field. No downstream condition was imposed on the solution for flow with all supersonic axial velocities. The code may also be run with a downstream static pressure imposed to calculate a shock-in-rotor flow when the incoming axial flow is supersonic. The supersonic throughflow fan tested by Breugelmans [6] was analyzed with the D3DVBL code. The nonaxisymmetric hub of the test rotor was modeled as an axisymmetric hub with the same contraction ratio across the rotor. The results of the calculation for the rotor are shown in Fig. 2 for the tip section. The calculations indicate that the oblique shock from the leading edge is contained inside the blade passage with no strong shocks emanating from the trailing edge.

During modification of the RVCO3 and D3DVBL codes for supersonic throughflow, a design with a typical transonic rotor tip solidity and an inlet axial Mach number of 1.5 was analyzed. MCA blades with typical transonic maximum thickness-to-chord ratios were used. The results of the analysis using the RVCO3 code and the D3DVBL code run as a two-dimensional code on the section and as a three-dimensional code on the entire rotor are shown in Fig. 4. Because of the solidity chosen, the wave system is not contained inside the passage and shocks pass into the downstream flow field. The agreement between the RVCO3 and D3DVBL codes is excellent.

Three-Dimensional Parabolized Viscous Supersonic Code (PEPSIS). The PEPSIS code is a three-dimensional parabolized viscous code, which has been used extensively at NASA Lewis to calculate supersonic flows for mixed compression inlets and benchmark-type experiments [21, 22]. Results from the code for flows at supersonic Mach numbers similar to those encountered in the nozzle and diffuser show that the viscous layers and the shock/boundary layer interaction effect are well predicted by the code. Details of the code development are described in the paper by Buggeln [23]. The code was used to analyze the final designs for the translating nozzle and diffuser. Several diffuser designs that the D3DVBL code indicated were separated (incompressible shape factor exceeding 2.4) were analyzed with the PEPSIS code. In all cases the PEPSIS calculations became unstable in approximately the same location where separation was predicted by the D3DVBL code.

Overall Fan Design Conditions

Since the intent of the research program on this supersonic throughflow fan is to develop the computational technology to design/analyze this unusual type of turbomachine for possible future applications, there were several overall guidelines that impacted the final design. They are as follows:

1 Since viscous effects can be important in terms of the secondary flows generated when the shock waves interact with the hub and tip boundary layers and a three-dimensional viscous code is not available for turbomachinery design, it was decided to limit possible severe three-dimensional effects by maintaining the hub and tip radii constant through the rotor. This has the additional advantage that the spacing between the rotor and a subsequent stator design can be easily varied to determine its effect on stage performance.

2 A moderate overall pressure ratio at moderate tip speed was selected to be representative of the pressure ratio that might be required for a high-speed power plant but not so agressive as to require large blade turning for this initial experiment.

3 The blade span should be representative of that required for possible inlet matching but be large enough to allow detailed spanwise surveys with laser anemometry.

The overall facility, showing the location of the translating nozzle, fan rotor, and translating diffuser, is shown in Fig. 5. The inlet plenum can be connected to an atmospheric intake or to the NASA Lewis central air supply system. By means of an upstream throttle valve, the inlet plenum pressure can be varied from subatmospheric up to several atmospheres. The collector can be connected to either an atmospheric exhaust or to the NASA Lewis altitude exhaust system. The rotor has a design pressure ratio of 2.7, an inlet axial Mach number of 2.0, and a tip speed of 457.2 m/s. The estimated design absolute Mach numbers are shown in Fig. 6. Because there is no contraction in the flow path the Mach number increases from the inlet value of 2.0 to a value at exit of about 3.1 at the hub and 2.7 at the tip. These Mach number distributions were calculated from the CDP code. The streamlines predicted by

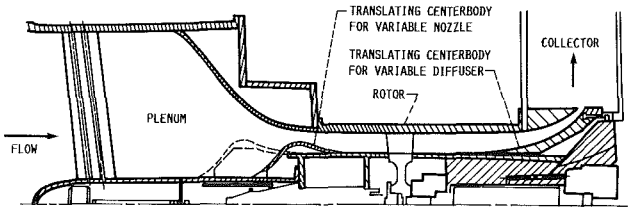

Fig. 5 Proposed test facility for supersonic throughflow fan rotor

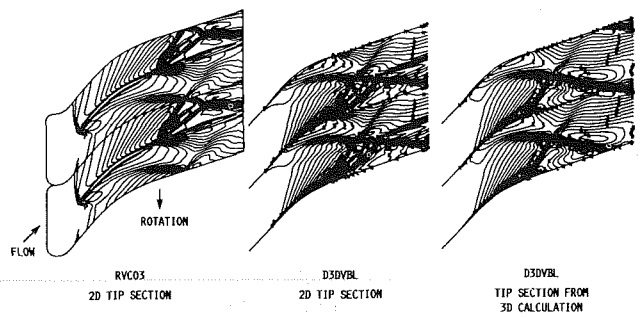

Fig. 4 Results obtained with RVCO3 code and D3DVBL code on an initial blade shape used to check codes; Mach number contours with 0.1 increment

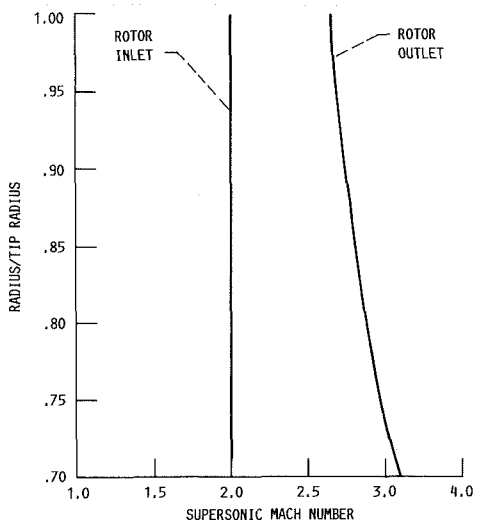

Fig. 6 Calculated distributions of supersonic absolute Mach number through fan rotor using the CDP code

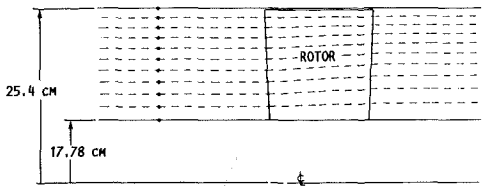

Fig. 7 Fan flowpath with rotor and calculated streamlines from the CDP design code

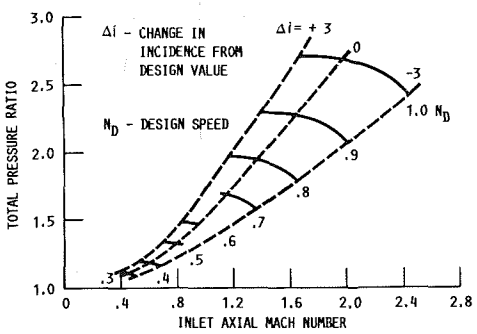

Fig. 8 Fan stage off-design performance prediction from the STGSTK meanline code

the CDP code are shown in Fig. 7 and were used to generate streamsheet thickness distributions for the RVCO3 viscous code.

Once design point performance was estimated, the STGSTK program was used to estimate the off-design performance map shown in Fig. 8 for a stage. Supersonic axial Mach numbers occur at speeds above 60 percent of design. The loci of operating points for zero incidence to the suction surface of the meanline blade are shown on the map to indicate a possible operating line for the experimental test. Envelope lines at positive and negative 3 deg of incidence are also shown on the figure to indicate the range available over a 6 deg incidence change. Further analysis by the RVCO3 would be necessary to indicate whether or not this range is reasonable. This operating line would certainly require a variable nozzle and might possibly require variable blading as well.

Translating Nozzle Design

In order to test the fan over a range of inlet Mach numbers from subsonic to the design inlet value of Mach 2, it was necessary to design an annular nozzle that would deliver a uniform, parallel flow at the fan face. Since the facility selected to serve as the test bed for the fan used an overhung bearing mount, it was desirable to hold the axial length and movement of the nozzle to a minimum. The D3DVBL code was used for the design since it allowed calculation of the entire flow field from very low subsonic Mach numbers to the design value of 2. The shroud portion of the nozzle starts at the inlet plenum radius of 60.96 cm and is faired into a superellipse, which subsequently fairs into the constant radius section in front of the fan. This allowed a great deal of flexibility in balancing between the requirement for a short stroke on the nozzle and control of the surface curvatures. The lower surface started at the sting radius of 9.525 cm and was faired into a point that was determined from the required throat area calculated from one-dimensional considerations to produce the desired nozzle Mach number. A control point was used with a cubic spline fairing to determine the distribution of the wall slope from the throat to the constant radius hub section. An initial geometry based primarily upon the one-dimensional area ratio was analyzed with the D3DVBL code. If an acceptable solution was not obtained, the initial geometry was

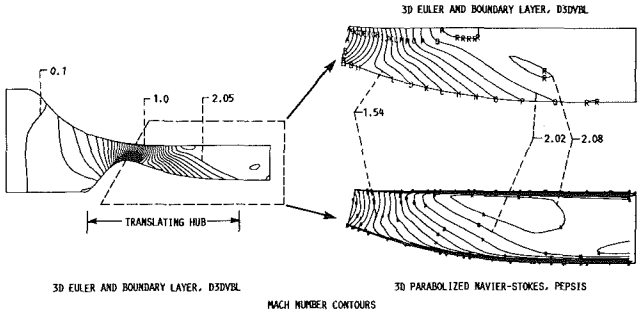

Fig. 9 Mach number contours calculated for the translating nozzle using the D3DVBL and PEPSIS codes

perturbed and the previous solution used as the initial starting point for the next solution. Depending upon the degree of change in the geometry, the next solution could be obtained in a relatively short number of time steps. After obtaining a satisfactory solution with the D3DVBL code, the nozzle was analyzed using the PEPSIS viscous code. The code is for all supersonic flow so the results from the D3DVBL code just past the throat were used as the initial starting profile. The results from the D3DVBL analysis for the entire nozzle are shown in Fig. 9, along with the results obtained with the PEPSIS viscous code in the supersonic region. The flow smoothly accelerates into the throat and expands rapidly with a compression wave emanating from the hub where the wall begins to turn back toward axial. The wave is canceled on the shroud wall and the flow attains a Mach number slightly higher (2.08) than the desired value of 2.0. Comparison of the D3DVBL code results with the PEPSIS viscous code results shows that the agreement is excellent. The clustering of contour lines near the walls in the viscous code results indicates the extent of the wall boundary layers.

Figure 10(*a*) shows the distribution of Mach number versus spanwise distance at the fan face. The free-stream values predicted by the two codes agree very well with the viscous code indicating boundary layer thicknesses on each wall of about 10 to 14 percent of the passage height. Also shown in the figure is the distribution of Mach number relative to the fan blade. This was obtained by adding the blade speed at any radial location to the axial velocity predicted by the viscous code. Figure 10(*b*) is a plot of the difference in the flow angle relative to the blade obtained with the inviscid profile from the Euler code and from the viscous profile. This represents the skewness in the relative velocity profile as a result of the inlet boundary layer. This effect is, of course, present in all turbomachine rotors, but for this case the skewness occurs at Mach numbers of about 1.6 or higher and has the potential to trigger flow separation from the blade, which could possibly result in an unstart of the rotor.

In order to insure the nozzle would deliver a desirable flow over the range of translation, the geometries for six different axial settings of the translating hub part of the nozzle were analyzed with the D3DVBL code. Figure 11 shows the results obtained. Each case analyzed showed that the flow delivered by the nozzle was uniform. The results are compatible with fan speed lines from 70 to 102 percent of design speed, which have supersonic axial inflow as presented in Fig. 8.

Mechanical considerations dictated that the nozzle design on the hub would have to be modified to end in about a 7 deg wedge instead of the smoothly varying slope used in the final design. Analysis of this modification predicted a wave emanating from the intersection of the translating part with the stationary part with a Mach number variation across the wave of about 0.1, which was judged acceptable for the experiment.

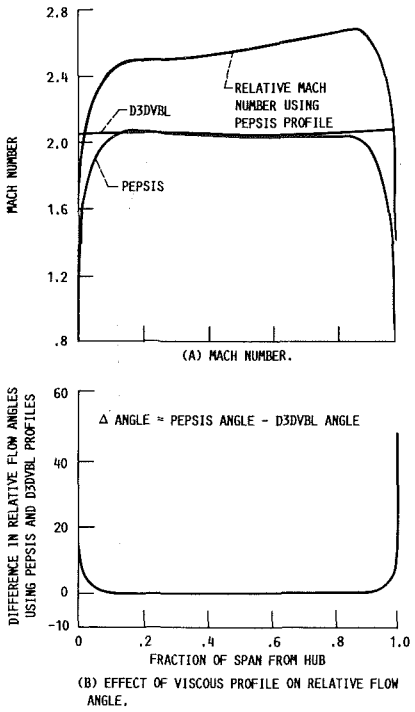

Fig. 10 Calculated conditions at the fan face using the D3DVBL and PEPSIS codes

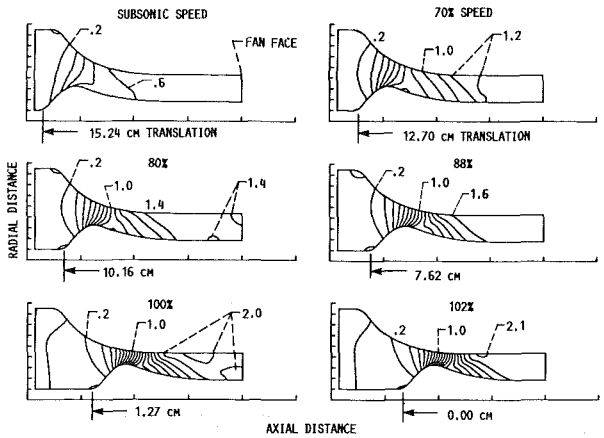

11 Mach number contours calculated for the translating nozzle with the D3DVBL code

Detailed Fan Rotor Blade Design

The detailed fan rotor was designed by Schmidt [24] using the CDP and RVCO3 codes described earlier. Details of the fan rotor design such as deviation, blade number, blade solidity, and blade thickness resulted from analysis of prospective blade shapes using the RVCO3 code for guidance. Five sections from hub to tip were designed with the RVCO3 code and stacked using the CDP code to form a three-dimensional blade. The mean section designed by Schmidt was analyzed with the grid shown in Fig. 12. The results shown in Fig. 13 indicate that the wave system is contained inside the passage and the flow exits the blade smoothly. The static pressure distribution closes at the trailing edge, indicating that the flow on both sides of the blade has been turned equally. Details of the bow shock at the leading edge and the flow vectors at the trailing edge are shown in Fig. 14.

The near-hub blade section was analyzed by Schmidt with the RVCO3 code at +5 deg and −5 deg of incidence to the

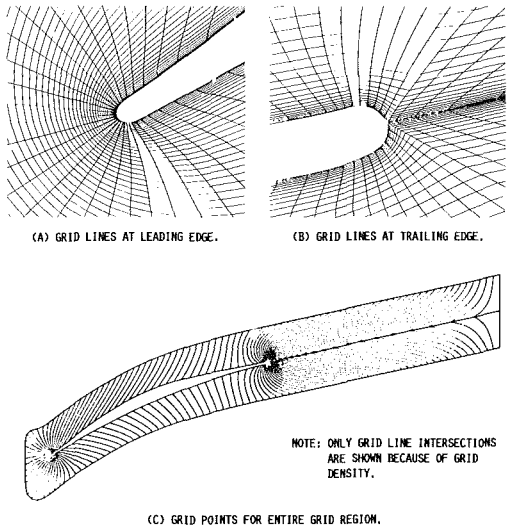

Fig. 12 The 161 × 65 C-grid used for the RVCO3 code

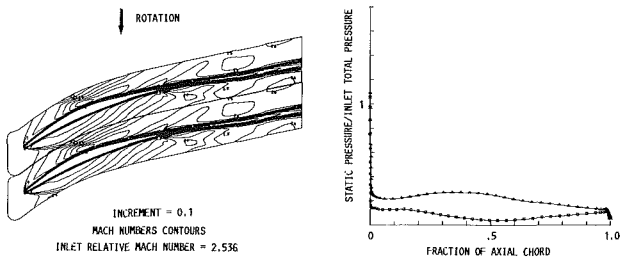

Fig. 13 Results obtained with the RVCO3 code on the mean section of a rotor designed for an inlet axial Mach number of 2.0 and a tip speed of 457 m/s

suction surface. No global flow breakdown that might indicate a possible unstart situation was indicated. These off-design calculations indicate that the incidence range envelope of +3 deg to −3 deg shown in Fig. 8 is reasonable.

In order to check the flow three dimensionality, the final stacked blade from the CDP program was analyzed with the D3DVBL code. As indicated earlier the D3DVBL code was run on a two-dimensional section so that comparisons for three-dimensional effects would not be code dependent. Static pressure distributions for the mean section are shown in Fig. 15. Both two-dimensional and three-dimensional results from the D3DVBL code show slightly more compression on the pressure surface at about 20 to 40 percent chord than do the results for the RVCO3 code. The difference in static pressures is apparently due, primarily, to the viscous treatment used. RVCO3 allows transition from laminar to turbulent flow, whereas D3DVBL assumes a fully turbulent boundary layer. Calculations using both codes with no viscous effects included yielded static pressure distributions, which were in much better agreement (6.9 percent difference versus 19 percent difference with viscous effects). The results for the D3DVBL code on the mean section run in the two-dimensional and three-dimensional mode agree closely except on the suction surface from about 75 percent chord to the trailing edge. This difference can be attributed to the three-dimensional nature of the flow. It is obvious that there are no significant three-dimensional effects present. Three-dimensional effects in terms of pressure-driven secondary flows where the endwall boundary layers are subjected to transverse pressure gradients are not calculated by the D3DVBL code and cannot be estimated for this rotor. The predicted relative Mach number contours for the mean section using the RVCO3 code and the

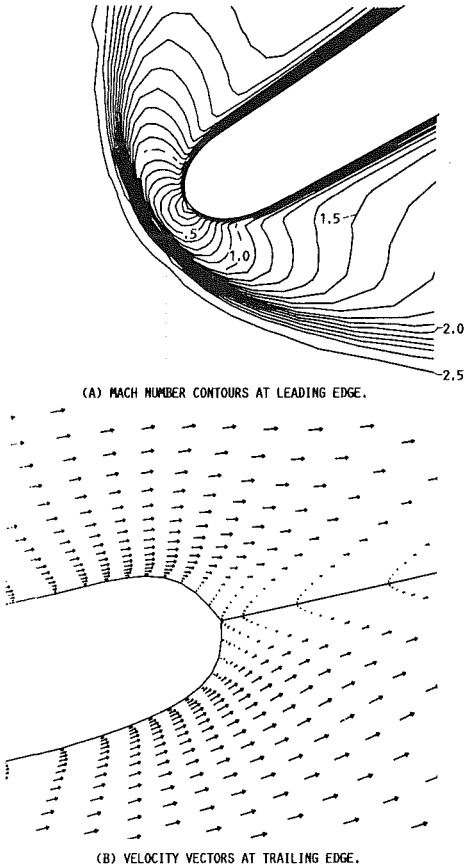

Fig. 14 Detailed flow analysis by the RVCO3 code of the fan rotor at the mean section

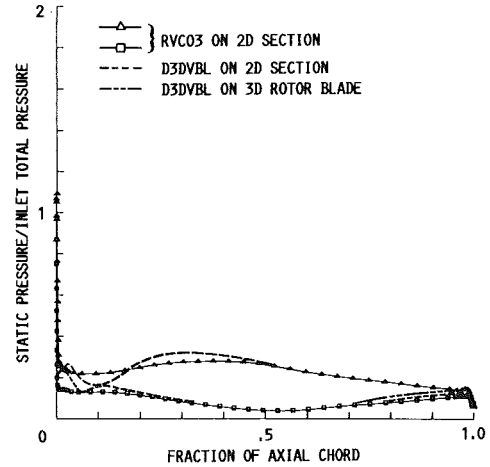

Fig. 15 Comparison of static pressures at mean section of the fan rotor calculated with the RVCO3 and D3DVBL codes for the two-dimensional section and calculated with the D3DVBL code for the full three-dimensional blade

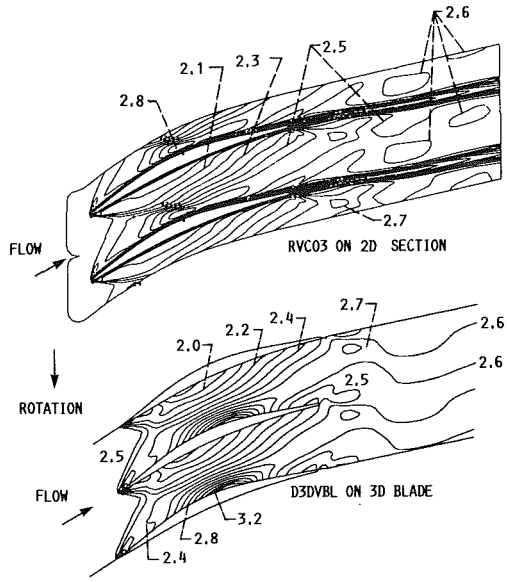

Fig. 16 Comparison of calculated relative Mach number contours on the mean section using the RVCO3 and D3DVBL code

D3DVBL code are shown in Fig. 16. The results from D3DVBL are for the three-dimensional calculations on the full rotor blade. The exit Mach number is about 2.6 for both codes with the overall agreement being quite good. The three-dimensional nature of the flow is indicated in Fig. 17, which shows the relative Mach numbers calculated with D3DVBL on three meridional surfaces. The only appreciable three-dimensional effect is on surface 3 (the suction surface) where the shock is leaning in the meridional plane at about 30 deg from the radial direction. The obliquity of the shocks in the blade-to-blade plane significantly reduce the effect of the radial lean. The grid used for the three-dimensional calculations is also shown in the figure. The two-dimensional solution with D3DVBL was run with the same blade-to-blade grid as used for the three-dimensional calculation. The growth in hub and shroud boundary layer displacement thickness as calculated at midgap using the D3DVBL code is shown in Fig. 18. The calculated increase across the rotor is about 50 percent of the inlet value. It should be noted that the endwall region contains some very complex flows, which are being modeled by a two-dimensional boundary layer method, and that the calculated boundary layer growth serves only as an indicator of the level of blockage to be expected. A full treatment of this region would obviously require a three-dimensional viscous analysis.

Total conditions across the rotor as predicted by RVCO3 and D3DVBL codes are shown in Fig. 19. The free-stream total–total pressure ratio predicted by the RVCO3 code is about 2.9 to 3.4 with the integrated value, which includes the wake at the downstream boundary, being about 2.82. The D3DVBL code prediction of total–total pressure ratio is about 2.7 to 3.1. Both calculations indicate that the rotor pressure ratio will be achieved.

In order to assess the impact of blade number, the number of blades was changed from the design value of 58 to 54. The results (Fig. 20) from the D3DVBL code run on the rotor indicate that the shock on the suction surface increases in strength and is not fully contained on the tip section. This could produce shocks from the trailing edge, which would propagate downstream.

Translating Diffuser Design

Since it was desired to operate the fan over its entire operating range from subsonic inlet/subsonic outlet to supersonic inlet/subsonic outlet to supersonic inlet/supersonic outlet, it was necessary to design a diffuser capable of operating over this range. The design was compounded considerably by a restriction on available length and maximum movement that would be available without a major redesign of the experimental facility. However, since static pressure in the downstream collector can be maintained at about 0.21 bar with an exhauster, it is not necessary for the diffuser to recover a significant amount of the incoming dynamic head.

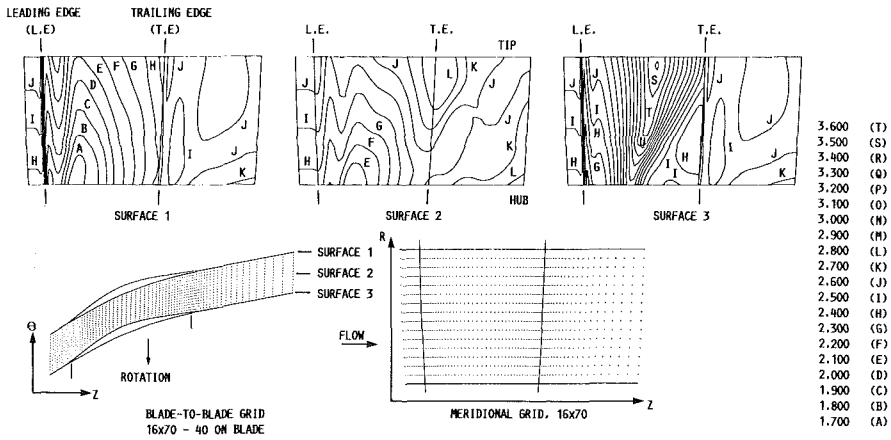

Fig. 17 Computation grid and relative Mach number contours calculated using the D3DVBL code

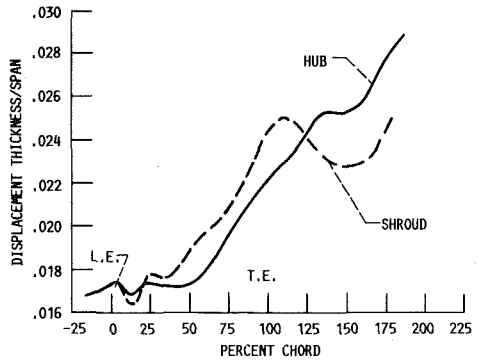

Fig. 18 Growth of displacement thickness along the midgap line at hub and shroud for the fan rotor as calculated with the D3DVBL code

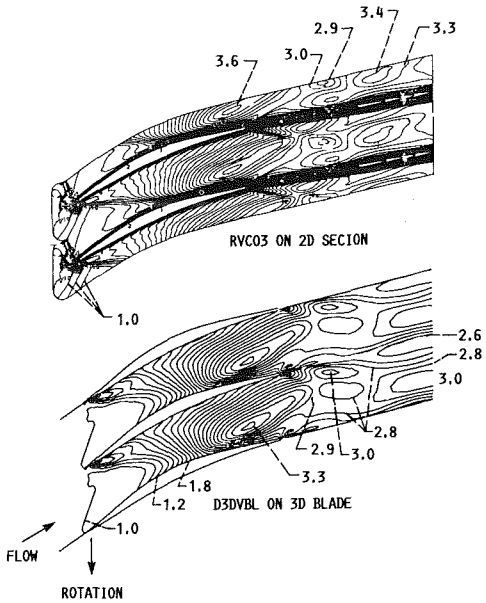

Fig. 19 Comparison of absolute total pressure ratio calculated with the RVCO3 and D3DVBL codes for the rotor mean section

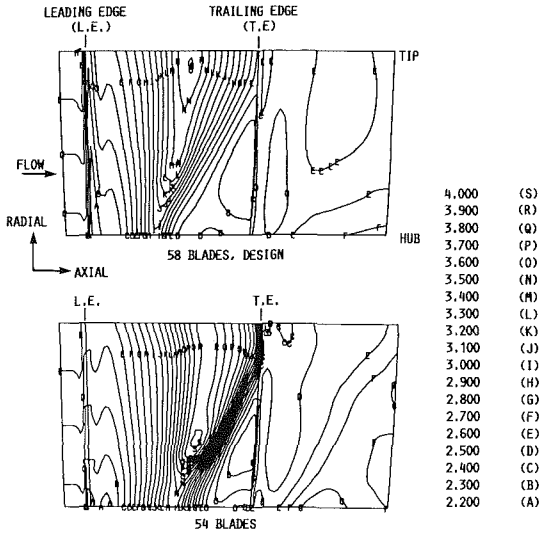

Fig. 20 Results from the D3DVBL code showing the effect of reducing blade number on the relative Mach number contours on the meridional projection of the suction surface

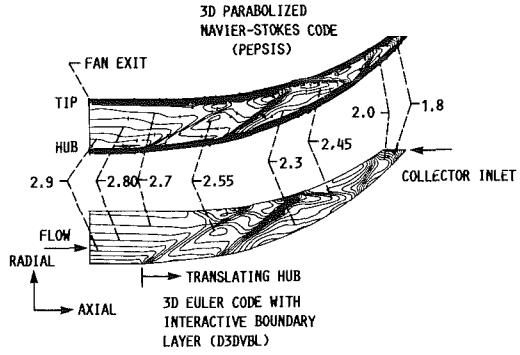

Fig. 21 Mach number contours calculated with the D3DVBL and PEPSIS codes for the translating diffuser at the design setting; flow angle from axial is 27 deg at the hub and 21 deg at tip

Given the restrictions on the geometry and the range, it was decided to design the diffuser to recover only a moderate amount of dynamic head with the main goal being to maintain a started diffuser over the Mach number range from 1.4 to the design rotor outlet values of about 3.1 at the hub and 2.7 at the tip. The predicted amount of swirl in the rotor outlet air varies from about 27 deg at the hub to 21 deg at the tip. The diffuser was designed for rotor exit conditions since the initial experiment is to be conducted without the stator in place.

As in the case of the nozzle design the diffuser was designed using a basic geometry generating program and the D3DVBL

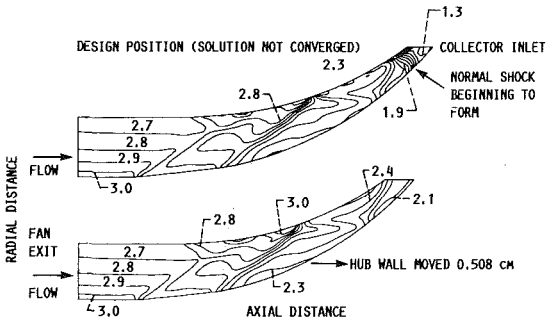

Fig. 22 Mach number contours calculated with the D3DVBL code showing the effect of doubling the fan exit blockage and the relief gained by translating the inner wall

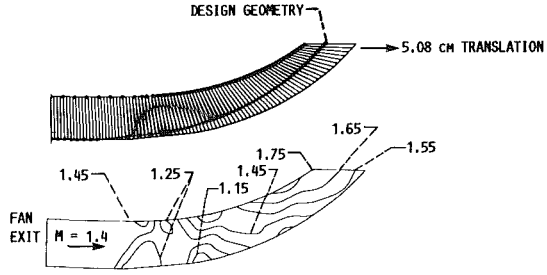

Fig. 23 Mach number contours calculated with the D3DVBL code showing translation required to maintain supersonic flow for operation at an inlet Mach number of 1.4

code. The blockage at the inlet to the diffuser was assumed to be the same as that calculated for the inlet to the rotor since no experimental data exist for endwall blockage growth through a supersonic throughflow fan. It was felt that any increase in blockage could be handled with the variable geometry. The translating part of the diffuser makes up the hub contour from just downstream of the blade row to the inlet of the collector. A 6 deg wedge was used to begin the translating section and to initiate the first oblique shock. This wedge angle was chosen because the shock at a 6 deg deflection should remain attached down to a Mach number of about 1.28. At this Mach number the shock should detach from the wedge and the flow should shock to subsonic through a normal shock near the wall. The static pressure rise across the shock at 1.28 should not be strong enough to cause boundary layer separation. Boundary layer bleed will be provided at the junction of the translating part and the stationary part to help stabilize the boundary layer and avert a gross flow separation. The results obtained with the D3DVBL code and the results obtained with the PEPSIS viscous code using the design fan rotor exit Mach number and flow angle distributions from hub to tip as upstream conditions are shown in Fig. 21. The oblique shock is not canceled on the shroud because the shroud contour begins to increase in radius just upstream of where the wave hits. This was necessary because otherwise the restriction on axial movement would lead to a terminal shock occurring in the converging portion of the diffuser at the desired lower operating limit of Mach 1.4. The second wave system emanating from the hub results from transition from the 6 deg wedge to a modified circular arc used to control the area distribution and turn the flow into the collector. As can be seen the agreement between the two numerical results is excellent with a Mach number of about 1.8 predicted at the collector inlet by both codes. The dark areas near the walls for the Navier–Stokes code results indicate the extent of the boundary layers. Both solutions were obtained with the design swirl anticipated at the exit of the rotor.

Since the endwall boundary layer growth across the rotor is not known with certainty, an off-design calculation was performed with the D3DVBL code. The inlet boundary layer displacement thickness was doubled on both walls and the design geometry analyzed. The results are shown in Fig. 22. the solution was not stable as a result of the formation of a terminal shock in the diffuser near the collector inlet. The calculations were restarted from the solution shown and allowed to continue. This resulted in a normal shock moving through the diffuser into the constant area section. The translating hub was moved 0.508 cm and the calculations were restarted with the same inlet blockage and the diffuser remained started as indicated in the figure. No calculations were made at axial movements less than 0.508 cm since the numerical results indicated that the diffuser could be maintained in a started condition.

The off-design results obtained at Mach 1.4 are shown in Fig. 23. As can be seen in the contour plot, the Mach number behind the first oblique shock is 1.25, which indicates that a terminal shock would form if the wave were allowed to reflect from a constant radius tip. This off-design flow point as mentioned previously made it necessary to begin increasing the tip radius farther upstream than desired for the design point operation in order to keep the diffuser started for the Mach 1.4 condition. The calculation is for an axial movement of 5.08 cm. The results for an axial movement of 4.445 cm indicated a terminal shock did form and move upstream into the constant area section. Initial research runs will be conducted with only the nozzle and diffuser installed in order to check the operating characteristics of each component. Consequently, these two calculations were run with no inlet swirl to the diffuser.

The design geometry was also analyzed with the expected collector pressure obtainable with the altitude exhaust system imposed as a downstream boundary condition for the D3DVBL code. The results indicated that the diffuser Mach contours were acceptable for subsonic operation. Sonic conditions were predicted at a location just before the collector inlet with a Mach number of about 0.3 in the constant area section.

Concluding Remarks

This paper has described the use of advanced computational codes to design an experiment to study a supersonic axial inflow fan rotor in detail. The philosophy taken in order to maximize the possibility of success of the experiment was to perform duplicate calculations using different codes. Where feasible, an existing supersonic viscous code was used to check the design of the experimental components. Application of a quasi-three-dimensional viscous code and a three-dimensional Euler code with an interactive two-dimensional boundary layer code to model the viscous effects for the supersonic throughflow fan rotor has resulted in almost identical solutions for the blade elements. The three-dimensional code indicated that no significant three-dimensional effects due to shock lean in the meridional plane were present.

Use of advanced codes that model much of the physics of the flow in this experiment—but certainly not all of it—to "test" various configurations before commitment to hardware has the potential to reduce significantly the time and expense required to develop the technology to produce high-efficiency supersonic throughflow components for advanced propulsion systems. In order to gain confidence that the physics is modeled properly in the codes, it is necessary to conduct experiments such as the one anticipated to collect detailed internal flow data, which will help us to assess the accuracy of the codes and to understand the physics of this unique turbomachinery component.

References

1 Boxer, E., "The Variable-Pitch Supersonic Inflow Compressor and Its

Application in a Hypersonic Engine," *Conference on Hypersonic Aircraft Technology*, NASA SP-148, 1967, pp. 401–416.

2 Ferri, A., "Problems Related to Matching Turbojet Engine Requirements to Inlet Performances as Function of Flight Mach Number and Angle of Attack," *Air Intake Problems in Supersonic Propulsion*, J. Fabri, ed., AGARDograph No. 27, AGARD, France, 1956.

3 Franciscus, L. C., "Supersonic Through-Flow Fan Engines for Supersonic Cruise Aircraft," NASA TM-78889, 1978.

4 Tavares, T. S., "A Supersonic Fan Equipped Variable Cycle Engine for a Mach 2.7 Supersonic Transport," NASA CR-177141, 1985.

5 Savage, M., Boxer, E., and Erwin, J. R., "Resume of Compressor Research at the NACA Langley Laboratory," ASME JOURNAL OF ENGINEERING FOR POWER, Vol. 83, No. 3, 1961, pp. 269–285.

6 Breugelmans, F. A. E., "The Supersonic Axial Inlet Component in a Compressor," ASME Paper No. 75-GT-26, Mar. 1975.

7 Denton, J. D., "An Improved Time-Marching Method for Turbomachinery Flow Calculations," ASME JOURNAL OF ENGINEERING FOR POWER, Vol. 105, No. 3, 1983, pp. 514–524.

8 Chima, R. V., "Development of an Explicit Multigrid Algorithm for Quasi-Three-Dimensional Viscous Flows in Turbomachines," AIAA Paper No. 86-0032, Jan. 1986.

9 Steinke, R. J., "STGSTK: A Computer Code for Predicting Multistage Axial Flow Compressor Performance by a Meanline Stage Stacking Method," NASA TP-2020, 1982.

10 Crouse, J. E., and Gorrell, W. T., "Computer Program for Aerodynamic and Blading Design of Multistage Axial-Flow Compressors," NASA TP-1946, 1981.

11 Sorensen, R. L., "A Computer Program to Generate Two-Dimensional Grids About Airfoils and Other Shapes by the Use of Poisson's Equation," NASA TM-81198, 1980.

12 Chima, R. V., "Inviscid and Viscous Flows in Cascades With an Explicit Multiple Grid Algorithm," *AIAA Journal*, Vol. 23, No. 10, 1985, pp. 1556–1563.

13 Denton, J. D., Lecture Notes, ASME Turbomachinery Institute Course on Fluid Dynamics of Turbomachinery, July 18–27, 1983.

14 Pierzga, M. J., and Wood, J. R., "Investigation of the Three-Dimensional Flow Field Within a Transonic Fan Rotor: Experiment and Analysis," ASME JOURNAL OF ENGINEERING FOR GAS TURBINES AND POWER, Vol. 107, No. 2, April 1985, pp. 436–449.

15 Sasman, P. K., and Cresci, R. J., "Compressible Turbulent Boundary Layer With Pressure Gradient and Heat Transfer," *AIAA Journal*, Vol. 4, No. 1, 1966, pp. 19–25.

16 McNally, W. D., "FORTRAN Program for Calculating Compressible Laminar and Turbulent Boundary Layers in Arbitrary Pressure Gradients," NASA TN D-5681, 1970.

17 Liu, J. S., "Numerical Models for Transonic Inlet Rotor Stages of Axial Flow Compressors," M. S. Thesis, Case Western Reserve University, 1984.

18 Wood, J. R., Strazisar, A. J., and Simonyi, P. S., "Shock Structure Measured in a Transonic Fan using Laser Anemometry," presented at the AGARD Symposium on Transonic and Supersonic Phenomena in Turbomachine Propulsion and Energetics Panel 68th Specialists Meetings, Munich, Sept. 1986; NASA TM-88910.

19 Coles, D. E., and Hirst, E. A., eds., *Proceedings of the AFOSR-IFP-Stanford Conference on Computation of Turbulent Boundary Layers—1968*, Stanford University, Aug. 1968; AFOSR-69-2713TR,-696082.

20 Wood, J. R., and Schmidt, J. F., NASA Lewis Research Center, Cleveland, OH, Personal Communications.

21 Anderson, B. H., "Three Dimensional Viscous Design Methodology for Advanced Technology Aircraft Supersonic Inlet Systems," AIAA Paper No. 84-0194, Jan. 1984.

22 Anderson, B. H., and Benson, T. J., "Numerical Solution to the Glancing Sidewall Oblique Shock Wave/Turbulent Boundary Layer Interaction in Three-Dimensions," AIAA Paper No. 83-0136, Jan. 1983.

23 Buggeln, R. C., McDonald, H., Levy, R., and Kreskovsky, J. P., "Development of a Three-Dimensional Supersonic Inlet Flow Analysis," NASA CR-3218, 1980.

24 Schmidt, J. F., "Design of a Supersonic Through-Flow Fan Stage," NASA TM-88908.

Journal of Turbomachinery

Discussion

Influence of the Reynolds Number on the Performance of Centrifugal Compressors[1]

L. Sapiro.[2] I would like to reiterate and expand the comments I made to Dr. Casey in Anaheim during his oral presentation of this paper.

There is a contradiction in Fig. 6 of the proposed allowable range of application of the correction formula for Reynolds number. The lower limit of tolerance shown on that figure does not correlate with the upper limit of tolerance.

Consider a compressor to be tested at a lower Reynolds number than at the operating conditions. If the operating Reynolds number is 5.0×10^5, the lower curve indicates that the accuracy of the correction formula is valid down to 10 percent of that value, which is 5.0×10^4.

Assume now that the same compressor is to be tested at a higher Reynolds number than at the operating conditions. If the operating Reynolds number is 5.0×10^4, the upper curve indicates that the accuracy of the correction formula is valid only up to about 3.5 times that value, which is 1.6×10^5.

One would expect the obtain a value of 10. This would be the required value to make the test Reynolds number equal to the original Reynolds number of 5.0×10^5 in the previous example. Similar discrepancies occur at other values.

For consistency, the upper curve should be much steeper or the lower curve should reach the 10 percent ratio at a higher Reynolds number value (more conservative) than 5.0×10^5. The second approach appears to be the obvious one. Figure 7 shows the lower curve that correlates with the upper curve.

It should be noted that the same discrepancy between upper and lower curves appears on the equivalent figure of Wiesner's paper ([1], Fig. 8). That figure is more conservative than Fig. 6 in this paper, as shown in the comparison of Fig. 8. On the upper curve, the difference is substantial. At a value of 7.7×10^5, the map in Fig. 6 indicates a limit of 100 times, whereas the map in Fig. 8 of [1] indicates 8.5. To obtain correlation between the upper and lower curves of his Fig. 8, Wiesner's lower curve should be modified as shown on Fig. 9. A comparison of Fig. 6 and Wiesner's Fig. 8, as modified, is presented in Fig. 10.

I would appreciate any comments on the reasons for the upper curve of Fig. 6 being so much more optimistic than the upper curve in Fig. 8 of [1], and I recommend that equations be given for these curves of Fig. 6 to allow their use in computerized procedures.

I agree fully with the additional limitation imposed on the lower curve of Fig. 6. The minimum ratio between the Reynolds number at test and the specified value should never be lower than 10 percent, even at the highest specified Re.

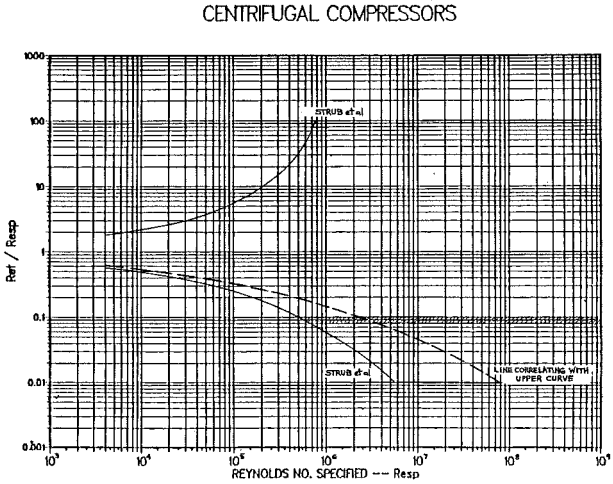

Fig. 7

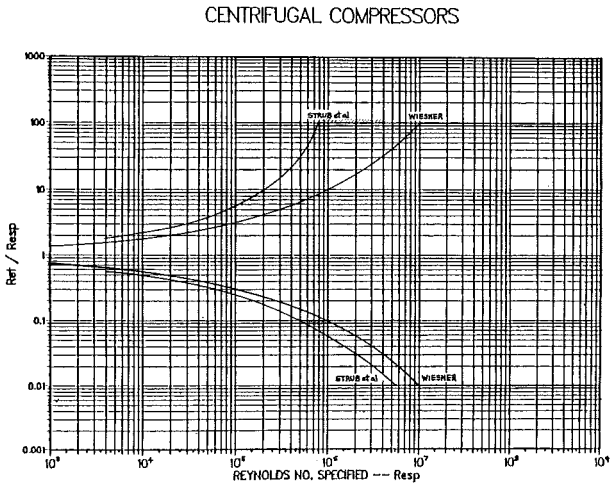

Fig. 8

That prevents excessive measurement inaccuracy when the reduction in Reynolds number is accomplished by lower suction pressure and, thus, lower mass flow and power. My own experience has been that this inaccuracy tends, in most cases, to produce overly optimistic efficiency values [10].

This paper's formula for correcting efficiency, regardless of its accuracy or its comparison with other proposed formulae, has the inconvenience of being an implicit equation. It would be desirable to simplify it and convert it to an explicit form.

When considering the formula for correcting the flow coefficient, it is arguable whether a correction for use in the ASME PTC-10 is justified at all. Although the flow position at peak efficiency may vary with the Reynolds number, in most cases

[1] By R. A. Strub, L. Bonciani, C. J. Borer, M. V. Casey, S. L. Cole, B. B. Cook, J. Kotzur, H. Simon, and M. A. Strite, published in the October 1987 issue of the JOURNAL OF TURBOMACHINERY, Vol. 109, No. 4, pp. 541–544.

[2] Consulting Design Engineer, Solar Turbines Incorporated, San Diego, CA 92138; Mem. ASME.

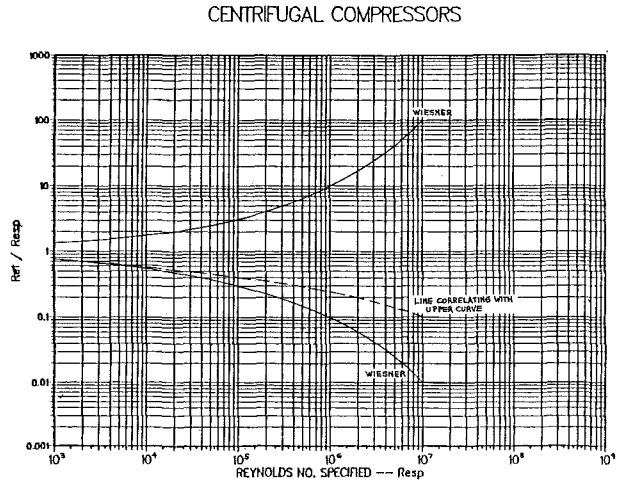

Fig. 9

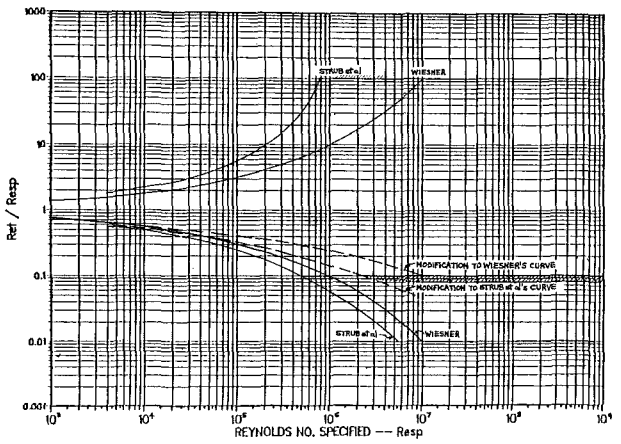

Fig. 10

the efficiency curve at both sides of the peak value does not slope fast enough to require an adjustment of meaningful magnitude. Applications at machine Mach numbers below 0.8, using vaneless diffuser staging, fit into that category.

The same argument about the justification of correcting the flow coefficient, given the generalization of the correcting formulae, applies to the work factor. After predicting and testing more than 3000 compressors at ambient air conditions and then in closed loop or field conditions, I have found no reason also to correct the flow coefficient or the work factor value. I simply apply the same correction to the head coefficient as to the efficiency. However, my approach is to include this effect of Reynolds number in the performance prediction prior to the test, to affect the stage matching, rather than as a correction of results after the test. My correction formulae take into consideration the specific speed of each stage ([10, 11], and discussion of Wiesner's paper [1], pp. 394–395).

In all, the authors of this paper have made a commendable contribution to the still unresolved debate about which formulae and allowable ranges should be adopted to replace the formulae and allowable ranges in the present ASME PTC-10.

References

10 Sapiro, L., "Review of Factory Aerodynamic Tests for Verification of Centrifugal Gas Compressor Field Performance Prediction," ASME Paper No. 85-GT-154, 1985.

11 Sapiro, L., "Preliminary Staging Selection for Gas Turbine Driven Centrifugal Gas Compressor," ASME Paper No. 73-GT-31, 1973.

Authors' Closure

The authors are very grateful to Dr. Sapiro for his kind remarks and very useful comments on several aspects of their paper.

Sapiro points out an inconsistency in Fig. 6 concerning the proposed allowable range of application of the correction formulae. This inconsistency is purely academic in nature and has no influence on the application of the correction method. The same inconsistency is also present in nearly all previous recommendations on allowable range of application of correction formulae for Reynolds number effects (see, for example, Wiesner [1] and Davis [6]). In all practical cases, workshop acceptance tests are carried out with reduced suction pressure and inlet density and the test Reynolds number is invariably lower than the specified Reynolds number. Acceptance tests at higher inlet density and pressure are not usual because of mechanical limitations from the casing and pipework design pressure or the power required from the driver. As a result only the lower half of Fig. 6 (with $\mathrm{Re}_t/\mathrm{Re}_{sp} < 1.0$) has any practical significance for centrifugal compressor acceptance tests.

The allowable range given in the lower part of Fig. 6 has been derived by noting that the ICAAMC correction formula for efficiency is most accurate when the losses $(1-\eta)$ do not change by more than 20 percent from those at the test conditions. It can be shown from the equations given in the paper that the allowable range of Reynolds number variation for a 20 percent change in losses is a function of the relative roughness (Ra/b_2) of the stage. Strictly speaking, there is a whole series of curves for the allowable range, each of which depends on the relative roughness. In the interests of simplicity a single curve has been selected that corresponds to a typical relative roughness. The allowable range in the upper part of Fig. 6 has been chosen as a compromise between that determined from the accuracy of the correction formula and that determined from mechanical considerations (available driving power, casing and pipework design pressure, etc.). Other compromises are possible for both the upper and the lower curves in Fig. 6, and for this reason we do not think it is worthwhile to give equations for the allowable range. We do feel, however, that a smaller allowable range, as suggested by the various limits given in Figs. 7–10 of Sapiro, is not necessary when using the very accurate correction formulae given in the paper.

Sapiro mentions that the formula for correcting the efficiency is somewhat inconvenient as it is implicit. In fact, there is no difficulty in writing an explicit form of the formula for correcting the efficiency (equation (4)), as follows:

$$\eta_{sp} = 1 - (1-\eta_t)\frac{(0.3+0.7\lambda_{sp}/\lambda_{cr})}{(0.3+0.7\lambda_t/\lambda_{cr})}$$

It is the Colebrook–White equation for friction factor (equations (6) and (7)) that is inconvenient, as the value of the friction factor appears on both the right and left-hand sides of the equation. This was discussed in our committee meetings, and we decided to adopt the Colebrook–White formula because it is generally accepted as accurate by all fluid dynamicists and no accurate and simple alternative was available at the time. The inconvenience of an implicit formula is of no concern in most computerized test procedures, as a straightforward iteration can be incorporated. Since the last meeting of our working group (Oct. 1982), a suitable explicit formula for the friction factor of a turbulent pipe flow has been published [12], as follows:

$$1/\sqrt{\lambda} = -1.8\log_e[\{6.9/\mathrm{Re}\} + \{k_s/(3.7D_h)\}^{1.11}]$$

This gives excellent agreement with the Colebrook–White equation, the maximum error being less than ± 1.5 percent, and is ideally suitable for quick calculations on a pocket calculator.

Sapiro suggests that a correction of the flow coefficient is not justified because the efficiency characteristic is always very flat at the peak efficiency point. We do not agree. The correction of the flow coefficient applies not only at the peak efficiency point but also at other points along the characteristic, for example at the choke point where the efficiency characteristic is steep. The increase in the volume flow of stage with increasing Reynolds number is most likely caused by a decrease in the blockage of the boundary layers. A change in boundary layer blockage can also have an effect on the work input of the stage. These effects are clearly shown in the experimental data presented in the most recent publications on the effects of Reynolds number (see, for example, Fig. 1 of Wiesner [1], Figs. 4 and 5 of Simon and Bülskämper [7], and Fig. 1 of Casey [9]). The very accurate measurements available to the working group showed clearly that corrections for efficiency, head, and volume flow are necessary.

Sapiro comments that he applies his own correction method for Reynolds number effects to the individual stage characteristics prior to stage-stacking calculations rather than as a correction of results after the test. The standard design procedure for multistage compressors used by most manufacturers takes into account the effect of Reynolds number on the stage matching in this way. Although the equations presented in the paper could be used for this purpose, the paper does not concern itself with this design problem. The main objective of the working group was to propose suitable formulae to correct the measured performance for the effect of a difference in Reynolds number between the workshop acceptance test and the specified conditions. This correction has to be applied to the global performance data of each casing and not to the individual stage characteristics. Despite the many simplifications involved, the very good agreement between measurements and predictions presented in the paper (Fig. 3) show that the results of the ICAAMC correction equations are within the range of accuracy of the measurements.

References

12 Haaland, S. E., "Simple and Explicit Formulas for the Friction Factor in Turbulent Pipe Flow," ASME *Journal of Fluids Engineering*, Vol. 105, 1983, pp. 89–90.